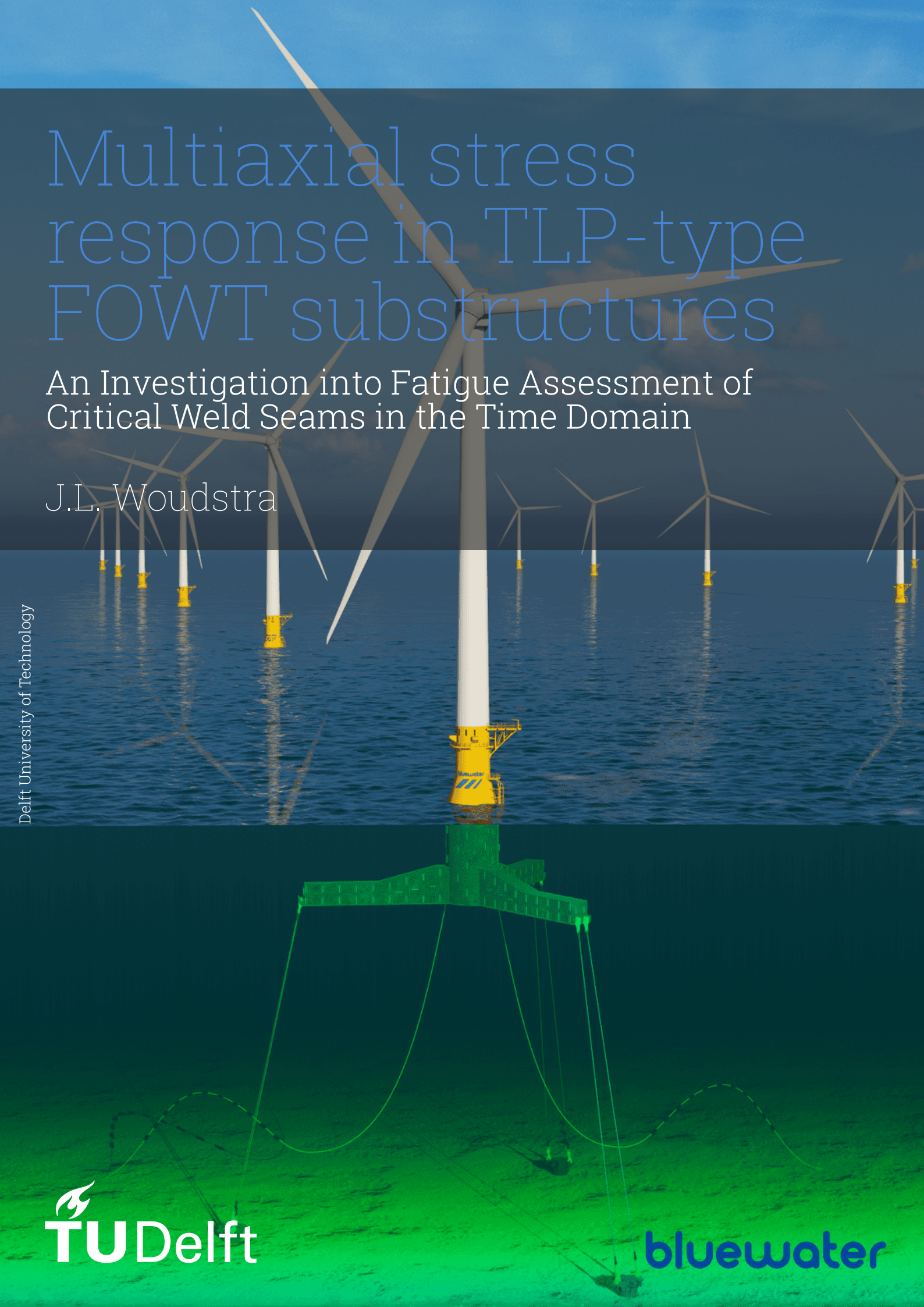
Multiaxial stress response in TLP-type FOWT substructures

An Investigation into Fatigue Assessment of Critical Weld Seams in the Time Domain

J.L. Woudstra

Delft University of Technology



TU Delft

bluewater

Multiaxial stress response in TLP-type FOWT substructures

An Investigation into Fatigue Assessment of Critical Weld Seams in the Time Domain

by

J.L. Woudstra

Student number: 4722744

Project duration: April 24, 2023 – May 23, 2024

Thesis committee:

Dr. ir. J.H. den Besten,	TU Delft, supervisor
Dr. H. C. Seyffert,	TU Delft, committee member
Ir. R. Slange,	TU Delft, committee member
Ir. R. Donk,	Bluewater, supervisor

Cover: Bluewater TLP concept render (Modified)

TU Delft

bluewater

Preface

Dear reader,

This thesis on "Multiaxial stress response in TLP-type FOWT substructures" finalises the master Offshore Offshore & Dredging Engineering and marks an end to my time at the Delft University of Technology. The work was performed under the guidance and supervision of Henk den Besten and Rick Donk.

Coming from a maritime engineering background, my interests did not always lie in the offshore renewables industry. It was in the transitionary period, working at Bluewater between my BSc and MSc, that I was introduced to the challenges posed by offshore floating wind as a source of renewable energy. The enthusiasm of colleagues was contagious and instilled an interest in the complex multidisciplinary challenge posed by FOWT. When the opportunity presented itself to conduct research on this subject matter, the choice was an easy one. It would, however, not have been possible to complete this research without the contributions of the following people.

I would like to express my deepest gratitude to my daily supervisor at Bluewater, Rick Donk, whose unconditional support and guidance were instrumental in realising this research. Your feedback was invaluable, and hands-on experience with the subject matter made sparring sessions incredibly productive, ensuring that I would always walk out with new ideas.

I also want to express my gratitude to Henk den Besten, my supervisor at the TU Delft, for guiding me. Your attention to detail and encouragement for critical scientific thinking, combined with thorough feedback, pushed me to scrutinize my work while still maintaining the creative freedom to tackle the problem as I saw fit.

I would also like to thank Gabriele Bufalari for providing me with his work and time, prior to publishing, which allowed me to relate the abstract nature of my findings into real world terms.

Furthermore, I would like to express my thanks to my colleagues and the rest of the team at Bluewater, who provided support during welcome coffee breaks or with the engineering-related challenges of this investigation.

Finally, I would like to thank my family, friends and girlfriend who have supported me through this endeavour, listening to my struggles and questions and providing me with the needed distraction during this period.

J.L. Woudstra
Delft, May 2024

Summary

In an era where global energy consumption has been rising steadily, the demand and supply of renewable energy sources have become increasingly important. Offshore wind is a promising renewable energy source, which has been actively developed in the last decades in the form of bottom-founded offshore wind, bound to shallow water. Floating Offshore Wind Turbines (FOWT) offer a solution for countries without shallow coastal waters with an abundance of wind potential. In a competitive market with different solutions, Bluewater Energy Services (Bluewater) has developed a tension leg platform (TLP) type substructure to support a 15MW turbine.

These FOWT installations are subject to the random nature of environmental loading which is highly stochastic in terms of amplitude, frequency and phase angle and is hence considered multiaxial non-proportional (random) variable amplitude loading. Multiaxial loading does not, however, guarantee a multiaxial stress response. One of the considerations for offshore structures subject to repetitive loading is fatigue lifetime estimation, which is predominantly done using uniaxial assessment methods. This is not an issue if the stress response is dominantly uniaxial, however, literature has demonstrated that evaluating a specimen subject mode-{I,III} multiaxial stress response using uniaxial (mode-{I}) assessment methods can lead to a significant overestimation of the fatigue lifetime.

To investigate the (multiaxial) stress response of fatigue-critical weld seams in TLP-type FOWT substructures, a new simulation methodology needed to be developed, which allowed for the structure's rigid body motions and elastic deformations to be captured. This methodology was built on an existing hybrid rigid-flexible modelling approach. It was improved upon by considering local (panel-based) hydrodynamic pressure and kinematic structural boundary conditions in order to conduct coupled (aerodynamic-hydrodynamic-mooring) analysis with integrated structural analysis. This approach allowed for the system motion and structural response to a dynamic metocean environment to be simulated using a range of commonly occurring seastates. The integrated coupled analysis was completely conducted within the Ansys environment.

Next, time-varying mode-{I,III} stress signals were reconstructed from the structural analysis model using a traction-based structural stress assessment method. In order to assess the extent to which fatigue-critical weld seams are subject to multiaxial stress response, a damage accumulation calculation should be conducted. However, given the added computational expense of such a calculation, a screening method was first considered in order to better understand the characteristics of stress response behaviour. The screening method considered was based on a Minimum-Circumscribed Ellipse method.

From this screening method, it was found that stress response behaviour is predictable and can be related to specific loading & response frequencies. Furthermore, it was found that parts of the considered structure were subject to significant levels of multiaxial non-proportional stress response and that applying uniaxial fatigue assessment criteria risks overestimating lifetime estimation and misplacing the governing fatigue hotspot. Finally, it was concluded that fatigue-critical weld seams in a FOWT TLP-type substructure are subject to multiaxial stress to the extent that multiaxial damage accumulation models should be considered. If this is not possible, a multiaxial stress response screening should be conducted to identify fatigue governing locations in the welds, as well as locations subject to multiaxial stress.

Contents

Preface iii

Symbols xxiii

1 Introduction 1
1.1 Motivation . . . 1
1.2 Outline . . . 2

2 Project definition 3
2.1 Problem statement . . . 3
2.2 Research question . . . 3
2.3 Scope . . . 4
2.4 Research goal . . . 4
2.5 Relevance . . . 4

I Literature Review 7

3 Environment 9
3.1 Wind statistics . . . 9
3.1.1 Wind speed . . . 9
3.1.2 Wind shear . . . 10
3.1.3 Turbulence . . . 10
3.1.4 Wake interaction . . . 11
3.2 Wave statistics . . . 11
3.2.1 Regular waves . . . 11
3.2.2 Irregular waves . . . 12
3.2.3 Non-linear waves . . . 12
3.2.4 Short term statistics . . . 12
3.2.5 Long term statistics . . . 13
3.2.6 Time domain formulation . . . 13
3.2.7 Kinematic profile extension . . . 14
3.3 Current statistics . . . 14

4 Loading 17
4.1 Aerodynamic loading . . . 17
4.1.1 Sources . . . 17
4.1.2 Damping . . . 19
4.1.3 Load models . . . 19
4.1.4 Blade Element Momentum . . . 20
4.1.4.1 Tip and hub loss . . . 20
4.1.4.2 Skewed inflow . . . 20
4.1.4.3 Dynamic stall . . . 20
4.1.4.4 Tower effects . . . 20
4.1.5 Controller . . . 21
4.1.5.1 Pitch-regulated variable speed controllers . . . 21
4.1.5.2 Floating Wind Controller Challenges . . . 22
4.1.5.3 ROSCO controller . . . 22
4.2 Hydrodynamic loading . . . 22
4.2.1 Hydrostatics . . . 23
4.2.2 First-order hydrodynamics . . . 23

4.2.2.1 Froude-Krilov . . . 24
4.2.2.2 Diffraction . . . 24
4.2.2.3 Radiation . . . 25
4.2.3 Second-order hydrodynamics . . . 25
4.2.3.1 Near field method . . . 26
4.2.3.2 Middle field method . . . 26
4.2.3.3 Newman approximation . . . 26
4.2.3.4 Far field method . . . 26
4.2.3.5 Viscous effects . . . 26
4.2.3.6 Springing . . . 27
4.2.4 Third-order hydrodynamics: Ringing . . . 27
4.2.5 Morison's formulation . . . 27
4.2.6 CFD . . . 28
4.2.7 Vortex induced oscillations . . . 29
4.3 Mooring loading . . . 29
4.3.1 Tendon construction . . . 29
4.3.2 Tendon modelling . . . 29
4.3.2.1 Static . . . 29
4.3.2.2 Quasi-static . . . 30
4.3.2.3 Quasi-dynamic . . . 30
4.3.2.4 Dynamic . . . 30
4.3.2.5 Coupled and uncoupled . . . 31
4.3.3 TLP mooring analysis . . . 31
4.3.4 Mooring induced torsion . . . 32

5 Motions & Response **33**
5.1 Coupled motion analysis . . . 33
5.2 Rigid body formulation . . . 34
5.2.1 Potential added mass and damping matrices . . . 34
5.2.2 Inertia contribution . . . 34
5.2.3 Damping contribution . . . 35
5.2.3.1 Potential damping . . . 35
5.2.3.2 Quadratic damping . . . 35
5.2.4 Stiffness contribution . . . 35
5.3 Flexible body formulation . . . 35
5.3.1 Mass matrix . . . 36
5.3.2 Damping matrix . . . 36
5.3.3 Stiffness matrix . . . 36
5.4 Hybrid flexible-rigid formulation . . . 37
5.4.1 Drawbacks of Hybrid Method . . . 38
5.4.2 Benefits of Hybrid Method . . . 39
5.5 Aero-elasticity . . . 39
5.6 Hydro-elasticity . . . 40

6 Multiaxial Fatigue **41**
6.1 Fundamentals . . . 41
6.1.1 Damage modes . . . 42
6.1.2 Welded joint hotspot types . . . 43
6.1.3 Weld notch stress distribution . . . 43
6.1.4 Mean stress . . . 44
6.1.5 Residual stress . . . 44
6.1.6 Multiaxial sources . . . 45
6.1.6.1 Material . . . 45
6.1.6.2 Geometry . . . 45
6.1.6.3 Loading . . . 45
6.2 Fatigue resistance . . . 45
6.2.1 Wöhler curves . . . 46

6.2.2 Constant and Variable Amplitude Loading . . . 46
6.2.3 Loading signal shape . . . 47
6.3 Failure criterion . . . 47
6.3.1 Von Mises . . . 48
6.3.2 Modified Gough Ellipse . . . 48
6.3.3 Effective Equivalent Stress Hypothesis . . . 48
6.3.4 Modified Carpinteri and Spagnoli . . . 49
6.3.5 Minimum Circumscribed Ellipse . . . 49
6.3.6 Response level dependency . . . 49
6.3.7 Summary . . . 50
6.4 Assessment Concepts . . . 50
6.4.1 Nominal Stress Concept . . . 51
6.4.2 Hot Spot Structural Stress Concept . . . 52
6.4.2.1 Surface extrapolation . . . 52
6.4.2.2 Subsurface identification . . . 52
6.4.2.3 Traction-based structural stress . . . 53
6.4.3 Effective Notch Stress Concept . . . 54
6.4.4 Summary . . . 54
6.5 Damage plane selection . . . 54
6.6 Cycle counting . . . 55
6.6.1 Multiaxial rainflow . . . 55
6.6.2 Virtual . . . 55
6.6.3 Path-dependent maximum range . . . 55
6.7 Non-proportionality . . . 56
6.7.1 Moment of Load Path . . . 57
6.8 Damage accumulation . . . 58
6.8.1 Palmgren-Miner . . . 58
6.9 Recommendations in design guidelines . . . 59
6.9.1 Bureau Veritas . . . 59
6.9.2 American Bureau of Shipping . . . 59
6.9.3 European Committee for Standardization: Eurocode 3 . . . 59
6.9.4 International Institute of Welding . . . 59
6.9.5 Det Norske Veritas . . . 60

7 Methodology **63**
7.1 Research gap . . . 63
7.2 Research hypothesis . . . 64
7.3 Research setup . . . 64
7.3.1 Phase 1: Coupled System Dynamics . . . 64
7.3.2 Phase 2: Dynamic Structural Analysis . . . 64
7.3.3 Phase 4: Application . . . 64
7.3.4 Phase 5: Results and evaluation . . . 64

II Modelling **65**

8 Coupled System Dynamics **67**
8.1 System overview . . . 67
8.2 Rigid Body Properties . . . 67
8.2.1 Floater . . . 68
8.2.2 Tower . . . 68
8.2.3 Rotor Nacelle Assembly . . . 69
8.2.4 Tendons . . . 70
8.2.5 Total FOWT System . . . 71
8.2.6 Tendon elastic stiffness . . . 71
8.2.7 System Natural Modes . . . 72
8.3 Hydrodynamic model . . . 72

8.3.1 Hydrodynamic mesh . . . 72
8.3.2 First Order Hydrodynamics: Diffraction analysis . . . 74
8.3.2.1 Model setup . . . 74
8.3.2.2 Mesh convergence and validation . . . 74
8.3.3 Second-order Hydrodynamics: QTF analysis . . . 76
8.3.4 Viscous damping . . . 77
8.4 Aerodynamic model . . . 78
8.4.1 BEM Model: AeroDyn . . . 78
8.4.1.1 Blade . . . 78
8.4.1.2 Tower . . . 79
8.4.1.3 Turbine . . . 79
8.4.1.4 Azimuth angle . . . 79
8.4.2 Control systems . . . 79
8.4.3 Power take-off . . . 80
8.5 Mooring model . . . 82
8.6 Coupled Dynamic Model . . . 82
8.6.1 Flexible Tower Dynamics . . . 84
8.7 Summarising statement . . . 84

9 Dynamic Structural Analysis 85
9.1 Structural model . . . 85
9.1.1 Geometry . . . 85
9.1.2 Mesh . . . 85
9.1.3 External load mapping . . . 86
9.1.4 Boundary conditions . . . 88
9.1.5 Time discretisation . . . 90
9.2 Traction based structural stress . . . 90
9.2.1 Nodal forces and moments . . . 90
9.2.2 Open and closed welds . . . 90
9.2.3 Critical weld seams . . . 91
9.2.4 Nodal sorting algorithm . . . 92
9.2.5 Local force and moment transformation . . . 92
9.2.6 Weld seam assessment . . . 93
9.2.7 Line Forces . . . 94
9.2.8 Line Stresses . . . 95
9.3 Stress history . . . 95
9.4 Minimum Circumscribed Ellipse . . . 96
9.5 Screening Criteria . . . 97
9.5.1 Level of multiaxiality . . . 97
9.5.2 Level of Non-Proportionality . . . 97
9.5.3 Equivalent stress range . . . 97
9.5.3.1 MCE Major axis . . . 97
9.5.3.2 Maximum stress range . . . 98
9.5.3.3 DNV mean stress correction . . . 98
9.5.3.4 Modified Carpinteri-Spagnoli . . . 98
9.5.3.5 Walker's mean stress correction . . . 99
9.5.4 Damage indicator . . . 100
9.6 Spectral Decomposition . . . 100
9.7 Summarising statement . . . 101

10 Case study 103
10.1 Environmental conditions . . . 103
10.1.1 Wind & Waves . . . 103
10.1.2 TLP orientation to metocean environment . . . 104
10.2 Load cases . . . 104
10.2.1 Seastates . . . 106
10.2.2 Special cases . . . 108

10.3 Temporal discretization . . . 108
10.3.1 Time step . . . 109
10.3.2 Simulation duration . . . 109
10.3.3 Filtering transient effects . . . 109
10.3.4 Simulated vs Target spectrum . . . 110
10.4 Summarising statement . . . 111

III Results 113

11 Results 115
11.1 Spectral decomposition . . . 115
11.1.1 Loading . . . 115
11.1.2 Response . . . 117
11.2 Load dominance . . . 118
11.3 Multiaxial Stress Response . . . 119
11.3.1 General Stress Behaviour . . . 119
11.3.2 Mean stress correction . . . 121
11.3.3 Spatial distribution of stress behaviour . . . 122
11.3.4 Effects of power controls . . . 124
11.3.5 Fatigue conscious design implications . . . 125
11.4 Damage accumulation . . . 128

IV Conclusions and Recommendations 135

12 Conclusion 137
12.1 Conclusion . . . 139
12.2 Discussion . . . 140
12.3 Implications . . . 141

13 Recommendations 143

References 145

A Potential theory 155
A.1 Deriving the potential . . . 155
A.2 Solving for the unknown potential . . . 157

B Hydrodynamic Mesh Convergence 159

C Spectral Decomposition Results 163
C.1 Loading . . . 163
C.2 Response . . . 164

D Stress behaviour in weld seams 173

List of Figures

3.1 Wind speed spectrum over a wide range of frequencies. The dotted line in the turbulence zone indicates turbulence magnitude for low winds (adapted from [134, p .32]). 9
3.2 Mean wind speed distribution over height, plotted in a dotted line, clearly showing that the mean wind speed increases over height. [134, p .33]). 10
3.3 Shown on the left, a regular wave frozen in time. Shown on the right is a regular wave time signal at a fixed location. Both illustrations indicating key wave parameters [70, p. 154]. 11
3.4 Representation of irregular sea as a composition of infinite harmonic wave components [70, p. 153]. 12
3.5 Valid range for different wave theories, waves considered in this thesis indicated with the dark blue shaded area (adapted from [100]). 12
3.6 Converting a surface elevation to an equivalent spectrum [70, p. 190]. 13
3.7 2D wave spectrum on the North Sea, clearly showing the difference between local wind sea and swell waves incident from different angles ([61, p .48]) 13
3.8 Kinematic comparison of various stretching theories illustrating the variance in the vertical distribution of horizontal particle velocity [70, p. 178]. 15

4.1 Example of a PSD plot for a simulated turbine in uniform wind conditions showing the blade edgewise and tower top contributions separately (adapted from [47, p. 3] to maintain consistency in notation). 18
4.2 Blade root edgewise bending moment PSD for low turbulence, above-rated wind conditions. Shown for reference illustrating a much cleaner signal [135, p. 8] 18
4.3 Tower base bending moment PSD for low turbulence, above-rated wind conditions.[135, p. 7] 18
4.4 Example of power output for different wind speeds for pitch and stall regulated wind turbines. ([51, p. 3]). 21
4.5 Total loading can be considered as a superposition of linearly decoupled excitation and radiation sources ([45, p. 40]). 24
4.6 Depiction of the discretisation of the continuous mooring line into lumped masses[37, p. 21] 30
4.7 Situation in which mooring lines are not equally loaded on a given pontoon, resulting in a net torsional moment applied to the pontoon, as well as the weld seam. 32

5.1 Flow chart of general approach as presented by Luan et al ([91, p .89]) 38
5.2 Flow chart of proposed changes to the analysis approach as presented by Luan et al ([91, p .91]) 38
5.3 Discretization of FOWT. Shown is one of three pontoons and surface piercing columns (adapted from [91, p .92]) 38

6.1 Range of scales at which fatigue physics can be considered [20, p. 2]. 42
6.2 Crack surface displacing modes [66, p. 25]. 43
6.3 Hotspot types as defined by Fricke [48] (higher resolution figure adapted from [117, p. 5]). 43
6.4 Weld toe notch stress distribution of a DS welded T-joint and DS welded cruciform joint in a tubular structure. The total resulting stress can be decomposed into an equilibrium equivalent (membrane and bending component) and a self-equilibrating stress part, for both mode-{I,III} [23, p. 7]. 44
6.5 Different parameters to characterise a stress cycle [125, p. 142]. 46
6.6 Different load signal shapes (adapted from [125, p. 46]). 47
6.7 Response level dependent shear strength coefficient [23, p. 4]. 50

6.8 Overview of fatigue assessment methods grouped by stress, strain and energy-based methods for intact or cracked geometries. The assessment methods considered in this thesis are outlined in blue (adapted from [18, p. 5]). . . . 51
6.9 Welded joint normal force and bending moment induced stress distributions, clearly separating the nominal stress distribution and structural hotspot stress distributions [18, p. 6]. Only mode-{I} is depicted here. . . . 51
6.10 Linear HSSSC extrapolation based of two reference points. This figure also clearly shows that although it includes more local information than NSC, the weld stress contribution is still ignored [147, p .3]. . . . 52
6.11 Crosssection, zoomed in perspective from figure 6.9 showing subsurface extrapolation method to determine hotspot structural stress. Clearly shown is the transition from weld notch to far-field stress-dominated region, at which S_n is calculated [19, p .26]. . . . 52
6.12 Curved weld in space depicting global and local axis systems [40, p .2] . . . 53
6.13 Structural stress definitions at weld toe with respect to local coordinate system (adapted from [41, p .3]) . . . 53
6.14 PDMR cycle counting methodology (adapted from [23, p .5]). . . . 56
6.15 Proportional and non-proportional CA load paths for mode I and mode III (adapted from [62]). . . . 56
6.16 Load paths plotted in nominal stress plane (adapted from [102]). . . . 56
6.17 Different types of proportional and non-proportional CA load paths for mode I and mode III (adapted from [82]). Note that strain is plotted. . . . 57
6.18 Different types of proportional and non-proportional (random) VA load paths for mode I and mode III [30]. Note that strain is plotted. . . . 57
6.19 MLP concept visualized [101, p. 3]. . . . 57
6.20 MLP method for an arbitrary non-proportional stress path between two points in a stress cycle [101, p. 4]. . . . 57
6.21 Maximum principal stress used by DNV regulations for multiaxial stress states. Also clearly showing direction of crack propagation [10, p .23]. . . . 60

7.1 The considered research will investigate the structural stress response in 8 critical weld seams, 2 closed and 6 open. . . . 63

8.1 Axis system for the different subsystems considered, as well as the total combined system 68
8.2 Cross section of the IEA-15-240-RWT hub and nacelle, turbine blades are not rendered (based on geometry from GitHub repository [17]) . . . 69
8.3 Radial flanges between pontoons, connected to the central column. Also, serves as structural support for power export cables. . . . 72
8.4 Tendon connectors structural configuration. . . . 72
8.5 Hydrodynamic plate structure used for the meshing process . . . 73
8.6 Importance of refined mesh control in order to avoid undesirable mesh behaviour . . . 73
8.7 Longest wave that can be considered for each water depth using deep water theory . . . 74
8.8 Zoomed in mesh heave RAO from AQWA illustrating the mesh convergence . . . 75
8.9 Approach for integrating flexible tower effects into diffraction analysis by replacing rigid tower by a number of subsystems connected by springs and dampers. . . . 76
8.10 Illustration of the challenge of assigning an equivalent drag diameter for non-cylindrical bodies . . . 77
8.11 Different Morison element diameters modelled along the length of the pontoon to account for the structure's taper, as well as a separate element for the central column. . . . 78
8.12 Rotor plane precone and shaft tilt angle are two design considerations to increase blade-tower clearance and prevent tower striking [146] . . . 79
8.13 NREL controller for the IEA-15-240-RWT turbine considered in this thesis. As can be seen, the pitch controller is inactive in Region 2, between wind speeds of 6.98-10.59 m/s (adapted from [49, p. 19]) . . . 80
8.14 Rotor thrust across the wind range. Also depicted is the wind window applied in this thesis (adapted from [49, p. 19]) . . . 80
8.15 Example of the relationship between wave energy and significant wave height [3] . . . 80

8.16 True generator torque and modelled torque plotted for angular velocity. Clearly, in Region 2, when the blade pitch remains constant, the rotor torque and rotational speed share a linear relationship . . . 81
8.17 Overview of global integrated load analysis process . . . 82
8.18 Flowchart describing the coupled dynamic model. . . . 83

9.1 FEA model mesh refinement. Gray depicts a rough mesh of 900x900mm, and blue depicts a refined mesh of 200x200mm. . . . 86
9.2 FEA model mesh refinement showing rough mesh of 900x900mm and area of refined mesh of 200x200mm. . . . 86
9.3 Cross section of FEA model mesh refinement. Gray depicts a rough mesh of 900x900mm, and blue depicts a refined mesh of 200x200mm. . . . 86
9.4 Close-up cross-section of FEA model mesh refinement. . . . 86
9.5 Load mapping of forces and moments onto the TLP-tower interface . . . 87
9.6 Load mapping of forces onto TLP-tendon interface . . . 87
9.7 Load mapping hydrodynamic pressure to nodal loads for unequal mesh sizes . . . 88
9.8 Hydrodynamic pressure mapping from 1000mm diffraction mesh to a finer, variable-size structural mesh. . . . 88
9.9 Distribution of mass and inertia representing all non-structural steel items in the FEA model. These non-structural steel items are generally items such as ladders, deck grating and supports, which are concentrated in the central column. . . . 89
9.10 Continuous weld seam connecting the deck to hull due to the weld access holes in the stiffeners. . . . 90
9.11 Example of a discontinuous weld seam along hull and deck, between stiffeners. The stiffeners are the continuous member and weld access holes are located in the deck plating. 90
9.12 Critical weld seams between column and pontoons, considered in this thesis. . . . 91
9.13 Welded geometry represented using shell elements. At the nodes at the centre of the weld seam, 3 shell plates can be seen to come together. These are referred to as element sets of the considered weld . . . 91
9.14 Top weld (TW) cross section showing 4 element sets . . . 91
9.15 Bottom weld (BW) cross section showing 3 element sets . . . 91
9.16 Vertical welds (VW1-6) cross section showing 3 element sets . . . 91
9.17 Importance of nodal sorting algorithm visualized . . . 92
9.18 Nodal sorting algorithm . . . 93
9.19 Tube to flange model considered by Rick Donk [42] used to validate nodal sorting algorithm and rotation matrix algorithm . . . 94
9.20 Example of a very rough mesh producing a mixture of triangular and quadrilateral mesh elements, which was used to demonstrate mesh insensitivity of implemented algorithms 94
9.21 Example of a two-component mode-{I,III} stress history as well as the history projection into the stress space. It can be seen that the stress history is of the variable amplitude non-proportional type. . . . 95
9.22 Various stress response time traces projected into the stress space, clearly showing different stress response behaviour. . . . 95
9.23 MCE applied to a non-proportional multi-axial stress response, enclosing all stress states 96
9.24 DNV mean stress correction, as can be seen only a reduction in effective stress range is realised (adapted from [8]). . . . 98
9.25 Modified correction coefficient used in Walker's mean stress correction as proposed by Besten [20], using $\gamma = 0.92$ . . . 100
9.26 Comparison between FFT and Welch's method for spectral decomposition of a short signal.101

10.1 Wave rose plot for the case study site in the Korean Straight. The colour gradient is used to indicate wave height. As can be seen, waves predominantly originate from the northeast104
10.2 Total wind rose plot for case study site in the Korean Straight. The colour gradient is used to indicate wave height. As can be seen, wind predominantly originates from the southwest-northeast hemisphere. . . . 104
10.3 Wave scatter plot for all measured seastates, measured at hub height, 150m above sea level105

10.4 Measured wind speed probability distribution 150m above sea level. Also plotted in green is the operational wind window to which simulation must be restricted due to the absence of a controller. Within the green area, 29.8% of measured windspeeds can be found in this window. 105
10.5 Wave scatter plot for sea states that can be simulated without an aerodynamic controller. For the turbine considered in this thesis, this wind window is $6.98 \leq V_{\infty,150m} \leq 10.59$ m/s at the hub height, 150m above sea level. Considered seastates are highlighted in blue. 105
10.6 FLS 1.1-3 are a set of simulated seastates based on the most likely to occur combination of wind and waves within the wind window. 107
10.7 FLS 2 is chosen to provide an even spread in the choice of seastates from the site-specific scatter plot. 107
10.8 FLS 3 aligns maximum angular frequency with the peak frequency of the incoming wave to concentrate external excitation energy in a narrow spectral bandwidth. 107
10.9 FLS 4 provided a baseline to investigate changes to a single parameter in the system. . . 107
10.10 FLS 5 is the design case that results in very high statistical damage. 107
10.11 FLS 6 studies the effect of short wave systems on structural loading and response. . . . 107
10.12 Addition of external fatigue brackets installed between the pontoons and column on the outer hull. These fatigue brackets seek to reduce hotspot stress, especially at the hard points between the corners of the pontoon-column connection. 108
10.13 Convergence of time step discretisation for an AQWA motion analysis. 109
10.14 Example of a motion analysis conducted, clearly showing startup effects in the first part of the simulation, using tendon tension as an indicator. After a maximum of 300 seconds, the simulation stabilises. 110

11.1 Spectral decomposition of external forces for FLS 2 116
11.2 Spectral decomposition of external forces for FLS 6 116
11.3 Spectral decomposition of external forces for FLS 4 without any rotor power controls, showing a significant increase in rotor angular velocity and corresponding spectral shift in tendon tension. 116
11.4 Spectral decomposition of weld stress response for FLS 2 117
11.5 Spectral decomposition of weld stress response for FLS 6 118
11.6 Example of varying multiaxial stress state in different weld element sets for the same node in the same weld. This case is in the top weld for FLS5 119
11.7 Distribution of degree of non-proportionality and equivalent stress range, excluding a mean stress correction. 120
11.8 Distribution of degree of non-proportionality and damage importance, excluding a mean stress correction. 120
11.9 Distribution of mean stress concentration 121
11.10 Effect of Walker mean stress correction on the equivalent stress range. 121
11.11 Distribution of degree of non-proportionality and damage importance, including a mean stress correction. 121
11.12 Distribution of degree of non-proportionality and damage importance, showing the relative effect of the mean stress correction. 122
11.13 Damage importance throughout the top critical weld seam, showing a clear pattern. . . 123
11.14 Illustration of the scissor effect caused by mooring line loads acting out of the radial pontoon plane of symmetry. Outward buckling of the central column can be seen in the highlighted area. Deformations are exaggerated for illustration purposes 123
11.15 Effect of power controls on the damage importance throughout the considered critical welds. 124
11.16 Spectral decomposition of normal and shear stress for FLS4 without power controls. . . 124
11.17 Variation of average equivalent stress range $\Delta\sigma_{eq,Walker}$ in the top weld for various seastates, with and without fatigue brackets 125
11.18 Effect of fatigue brackets on the general stress behaviour of nodes in the top fatigue critical weld 125
11.19 Effect of fatigue brackets on the damage importance throughout the top circular weld, broken down by element set. 126

11.20Variation of average normal $\Delta\sigma_{Walker}$ and shear $\Delta\tau$ stress range in the top weld for FLS5, with and without fatigue brackets . . . 127
11.21Mode-{I,III} single slope SN curves from Bufalari et al. [23], with proposed mode-{I} slope change amendment. . . . 128
11.22Variation in $\beta(N)$ for reference single-slope, and proposed dual-slope resistance curves. 128
11.23Distribution of damage throughout weld fatigue governing top weld seam. Note that distribution is plotted at a logarithmic scale to provide an overview. . . . 129
11.24Effect of fatigue brackets on hourly accumulated damage. . . . 130
11.25Comparison between two proposed damage indicators and multiaxial damage calculation on a normalised scale. . . . 131
11.26Comparison between input signal types for state-of-the-art damage accumulation and design guideline type of stress information. . . . 132
11.27Comparison between full MA stress signal processed with a state-of-the-art damage accumulation model, compared to the same signal converted to a design guideline type and processed with a state-of-the-art damage accumulation model. . . . 132

12.1 Observed data scatter band for growth dominant to initiation controlled [117, p. 3] . . . 141
12.2 Welded tube to flange connection [23] . . . 141

B.1 Mesh convergence study and comparison between ANSYS AQWA and HydroStar for surge motion RAO . . . 159
B.2 Mesh convergence study and comparison between ANSYS AQWA and HydroStar for sway motion RAO . . . 160
B.3 Mesh convergence study and comparison between ANSYS AQWA and HydroStar for heave motion RAO . . . 160
B.4 Mesh convergence study and comparison between ANSYS AQWA and HydroStar for roll motion RAO . . . 161
B.5 Mesh convergence study and comparison between ANSYS AQWA and HydroStar for pitch motion RAO . . . 161
B.6 Mesh convergence study and comparison between ANSYS AQWA and HydroStar for yaw motion RAO . . . 162

C.1 Spectral decomposition of external forces for FLS1.1 . . . 163
C.2 Spectral decomposition of external forces for FLS 1.2 . . . 163
C.3 Spectral decomposition of external forces for FLS 1.3 . . . 164
C.4 Spectral decomposition of external forces for FLS 2 . . . 164
C.5 Spectral decomposition of external forces for FLS 3 . . . 164
C.6 Spectral decomposition of external forces for FLS 4 . . . 165
C.7 Spectral decomposition of external forces for FLS 4 without power take off . . . 165
C.8 Spectral decomposition of external forces for FLS 5 . . . 165
C.9 Spectral decomposition of external forces for FLS 6 . . . 166
C.10 Spectral decomposition of normal and shear stress response for FLS1.1 . . . 166
C.11 Spectral decomposition of normal and shear stress response for FLS 1.2 . . . 167
C.12 Spectral decomposition of normal and shear stress response for FLS 1.3 . . . 167
C.13 Spectral decomposition of normal and shear stress response for FLS 2 . . . 168
C.14 Spectral decomposition of normal and shear stress response for FLS 3 . . . 168
C.15 Spectral decomposition of normal and shear stress response for FLS 3 with fatigue brackets 169
C.16 Spectral decomposition of normal and shear stress response for FLS 4 . . . 169
C.17 Spectral decomposition of normal and shear stress response for FLS 4 with fatigue brackets 170
C.18 Spectral decomposition of normal and shear stress response for FLS 4 without power take off . . . 170
C.19 Spectral decomposition of normal and shear stress response for FLS 5 . . . 171
C.20 Spectral decomposition of normal and shear stress response for FLS 5 with fatigue brackets 171
C.21 Spectral decomposition of normal and shear stress response for FLS 6 . . . 172

D.1 Damage importance throughout the top critical weld seam, showing a clear pattern. . . . 173
D.2 Damage importance throughout the bottom critical weld seam, showing a clear pattern. 174

D.3 Damage importance throughout the vertical critical weld seams, showing a clear pattern. 174
D.4 Effect of fatigue brackets on the damage importance throughout the top circular weld, broken down by element set. 175

List of Tables

4.1 Overview of mooring modelling and analysis methods in the literature, compiled from various sources . . . 31

8.1 Substructure rigid body properties . . . 68
8.2 Scaled NREL fixed tower rigid body properties . . . 69
8.3 IEA-15-240-RWT RNA rigid body properties [17] . . . 70
8.4 Coordinates of tendon connectors and anchors, expressed in body boud coordinate system with the origin at SWL . . . 70
8.5 Tendon rigid body properties, expressed in body boud coordinate system with the origin at SWL . . . 70
8.6 Summary of rigid body properties, expressed in body boud coordinate system with the origin at swl of the complete FOWT system . . . 71
8.7 Frequency and period for first natural frequency for the rigid system modes . . . 72
8.8 Maximum resolvable frequency depending on mesh element size . . . 76
8.9 Morison element diameter and drag coefficients . . . 78
8.10 Turbine input parameters . . . 79

9.1 FEA extra point mass properties . . . 89
9.2 Nomenclature used to refer to critical welds and their location in the structure. The coordinate system is shown in figure 9.12. . . . 92

10.1 Summary of seastates considered in this investigation . . . 106
10.2 Summary of special cases . . . 108
10.3 Comparison of generated and target wave spectra . . . 110

11.1 Comparison of generated and target wave spectra . . . 118

Glossary

ABS American Bureau of Shipping.
AW as welded.

BEM Blade Element Momentum.
BV Bureau Veritas.
BW backward whirling.

CA Constant Amplitude.
CFD Computational Fluid Dynamics.
COG Center of Gravity.

DNV Det Norske Veritas.
DOF degree of freedom.
DS dual slope.

EESH Effective Equivalent Stress Hypothesis.
ENSC Effective Notch Stress Concept.

FEA Finite Element Analysis.
FEM Finite Element Method.
FFT Fast Fourier Transform.
FOWT Floating Offshore Wind Turbine.
FSI Fluid Structure Interaction.
FW forward whirling.

HCF High Cycle Fatigue.
HFL high-frequency limit.
HPC High Performance Cluster.
HSSSC Hot Spot Structural Stress Concept.

IIW International Institute of Welding.

LC Load Carrying.
LCF Low Cycle Fatigue.
LDR Linear Damage Rule.

MCE Minimum Circumscribed Ellipse.
MCF Medium Cycle Fatigue.
MCS Modified Carpinteri-Spagnoli.
MLP Moment of Load Path.
MSL mean surface level.
MVEE Minimum Volume Enclosed Ellipse.

NLC Non Load Carrying.
NREL National Renewable Energy Laboratory.
NSC Nominal Stress Concept.

O&G Oil & Gas.

PDMR Path-dependent-maximum range.
PRVS pitch-regulated variable speed.
PSD Power Spectral Density.
PTO power take-off.

QTF Quadratic Transfer Function.

RAO Response Amplitude Operator.
RNA Rotor Nacelle Assembly.
ROSCO reference open-source controller.

SCF Stress Concentration Factor.
SDG sustainable development goals.
SPAR Single Point Anchor Reservoir.
SR stress relieved.
SS single slope.
swl still water line.
SWT Smit-Watson-Topper.

TLP Tension Leg Platform.

UN United Nations.

VA Variable Amplitude.
vim vortex induced motions.
vio vortex induced oscillations.
viv vortex induced vibrations.

WTG Wind Turbine Generator.

Symbols

Latin

Symbol	Definition	Unit
$\mathbf{A}$	Added mass matrix	
$\mathbf{B}$	Damping matrix	
$\mathbf{C}$	Stiffness matrix	
C_D	Drag coefficient	[-]
C_M	Inertia coefficient	[-]
D	Diameter	[m]
D	Accumulated damage	[-]
D_{imp}	Damage importance indicator	[Pa^3]
$\mathbf{F}$	Force & moment vector	[N, Nm]
f_i	Nodal force component i	[N]
G_{np}	Degree of non-proportionality	[-]
$\mathbf{M}$	Mass matrix	
m_i	Nodal moment component i	[Nm]
N	Number of cycles	[-]
P	Power	[W]
r_{lr}	Loading & response ratio	[-]
t	Time	[s]
t, t_p	Plate thickness	[m]
T	Wave period	[s]
T	Tendon tension	[N]
T_n	Natural period	[s]
V	Wind speed	[m]
x	Surge displacement	[m]
y	Sway displacement	[m]
z	Heave displacement	[m]
Z_0	Wind speed reference height	[m]

Greek

Symbol	Definition	Unit
α_{shear}	Wind shear power law coefficient	[-]
β	Shear stress coefficient	[-]
γ	Wave spectrum peak enhancement factor	[-]
γ	Walker material coefficient	[-]
ζ_a	Wave amplitude	[m]
η	Wave surface elevation	[m]
Θ	Degree of multiaxiality	[°]
θ	Roll rotation	[°]
θ_{wind}	Wind incident angle	[°]
θ_{waves}	Waves incident angle	[°]
k	Wave number	[1/m]
λ	Wavelength	[m]
ρ	Density	[kg/m^3]

Symbol	Definition	Unit
σ_s	Normal structural stress (mode-{I})	[Pa]
σ_m	Normal membrane stress	[Pa]
σ_b	Normal bending stress	[Pa]
τ_s	Shear structural stress (mode-{III})	[Pa]
τ_m	Shear membrane stress	[Pa]
τ_b	Shear bending stress	[Pa]
ϕ	Wave phase angle	[rad]
ϕ	Pitch rotation	[°]
ψ	Yaw rotation	[°]
ω	Circular wave frequency	[rad/s]
ω_n	Natural frequency	[rad/s]
ω_i	Natural frequency system DOF i	[rad/s]

1 Introduction

A floating wind turbine installation is subject to variable multiaxial loading, as the loading of the structure by the environment is typically multiaxial in nature as wind, waves, and current may be incident at different heading angles. Even within wave loading, there is a component of multiaxiality as swell and wind seas may also have different headings. The fatigue limit state typically governs marine structures, such as floating wind turbines. Welded joints are often critical connections and can dictate design considerations. This chapter will preface an investigation to capture potential multiaxial stress response in these critical weld seams.

1.1. Motivation

In an era where global energy consumption has been rising steadily, the demand and supply of renewable energy sources have become increasingly more important [36] to meet the clean and affordable energy goal set by the United Nations (UN) [138]. Although more difficult in operational maintenance and installation, offshore wind is a promising renewable energy source, which has been actively developed in the last decades in the form of bottom-founded offshore wind, also referred to as fixed wind. However, due to installation feasibility, this type of Wind Turbine Generator (WTG) is limited to about 60m of water depth [7]. Floating Offshore Wind Turbine (FOWT) offers a solution for countries without shallow coastal waters with an abundance of wind potential, such as France and Norway, *"for these countries, offshore wind means floating wind"* [141]. Although operating far offshore introduces new challenges, an almost inexhaustible list of successful long-term offshore oil and gas deployments shows this is possible, even in remote waters.

Different platform types are distinguished by the most dominant source of hydrostatic stability in pitch and roll. These sources may be buoyancy, ballast or mooring. The latter type is unique in that it depends on mooring tendons for stability when installed. The buoyancy of the substructure keeps the mooring tendons under tension, providing a restoring force through the elasticity of the lines. These stiff mooring lines provide a righting force when a displacement or rotation is applied. This stiff mooring configuration results in the lowest motion response at the turbine relative to other substructure types supporting an equal turbine. This behaviour is desired for continual power production and turbine fatigue lifetime.

Although seeming trivial, the analysis of a floating substructure introduces a whole new set of challenges compared to bottom-founded monopiles. One of these challenges is the integrated load assessment, which becomes very complex considering that a combination of aerodynamics, hydrodynamics and finite element analysis must be considered, each of which concerns a separate set of physics. These systems are tightly linked and interact with each other (non) linearly. Although dynamic motion analysis of FOWT is not new, the integration with structural load assessment is a mismatch in underlying assumptions between motion and structural response models, which poses a challenge for this integration.

Loading and response of a structure can be divided into three modes: I, II, and III. These modes may be considered individually for uniaxial application. Response (and fatigue) may be considered as multiaxial when a subject is loaded in two or three directions (modes). For thin-walled constructions, the in-plane shear or sliding mode (mode II) may be neglected as the through-thickness shear forces are negligible. Hence, a multiaxial stress response consists of a mode-{I,III} response.

These FOWT installations are subject to the random nature of environmental loading which is highly stochastic in terms of amplitude, frequency and phase angle and is hence considered multiaxial non-proportional (random) variable amplitude loading. Multiaxial loading does not, however, guarantee a multiaxial stress response. One of the considerations for offshore structures subject to repetitive loading is fatigue lifetime estimation, which is predominantly done using uniaxial assessment methods. This is not an issue if the stress response is dominantly uniaxial, however, literature has demonstrated that evaluating a specimen subject mode-{I,III} multiaxial stress response using uniaxial (mode-{I}) assessment methods can lead to a significant overestimation of the fatigue lifetime. There is, however, very little research published on fatigue in FOWT for reasons that will become evident in the literature review. Furthermore, no published investigations are available on multiaxial fatigue assessment for FOWT.

1.2. Outline

In this thesis, a multi-disciplined problem will be addressed in different phases. To start with, the problem will be defined, along with an investigative approach in chapter 2. Subsequently, in part I, a thorough review of the state-of-the-art environmental representation (chapter 3), loading (chapter 4), dynamic (chapter 5) and response (chapter 6) analysis will be presented. In the second phase, in part II, the considered model will be presented, consisting of a coupled dynamics model (chapter 8) and a structural response analysis model (chapter 9). This model is subjected to a number of environmental load cases (chapter 10). The findings from these simulations will be covered in part III and chapter 11. Finally, the conclusions and recommendations are presented in part IV.

2

Project definition

Having established the context of the proposed issue, the problem can be framed. Starting with the problem statement and research question in sections 2.1 and 2.2. After which, scope and research goal will be defined in sections 2.3 and 2.4. Finally, the relevance of the proposed area of research is discussed in section 2.5.

2.1. Problem statement

In a situation in which the fatigue limit state becomes governing for the design of FOWT substructures such as a Tension Leg Platform (TLP), accurate damage assessment models are required. As FOWT is subject to a dynamic ocean environment consisting of multiaxial, variable amplitude and out-of-phase loading between wind and wave excitation, which suggests that stress response may have similar characteristics. Applying uniaxial fatigue assessment methods to a structure with a highly multiaxial stress response will lead to a significant overestimation of design life. In order to establish if a (point in) a structure is subject to multiaxial fatigue, a representative stress response signal must be derived. This presents a challenge as the total response of a FOWT substructure to the environmental loads is a superposition of rigid body motions and elastic deformations. Furthermore, as the multiaxial stress response is subject to local stress influences, the stress response model must account for a combination of rigid body motions and local elastic deformations. Therefore to assess if the considered structure is subject to multiaxial stress response, first a representative model must be derived which maintains stress response signal integrity, such that it can be processed with the appropriate tools.

2.2. Research question

The problem statement presents the following research question.

Research question:
To what extent are fatigue-critical weld seams in an offshore floating wind TLP-type substructure in multi-directional mixed wind-wave loading conditions subject to a multiaxial stress response?

The following subquestions have been formulated to aid the investigation throughout the various phases. These phases are based on the structure of the problem described in section 2.1, and will be covered in section 7.3.

SQ1: What types of environmental loading is a FOWT subject to, and what loading components must be considered?

SQ2: How can the dynamic wind-wave environment be expressed as input for a fatigue sea state?

SQ3: Which stress assessment parameter and fatigue failure criterion can be used to assess multiaxial stress response in combination with time domain finite element analysis?

SQ4: How can the multi-disciplinary, multi-physics submodels be coupled in order to conduct coupled dynamic analysis consisting of a rigid motion and elastic deformation component?

SQ5: How can *'the amount'* of multiaxial response be quantified and allow for a comparison between locations in the structure?

SQ6: Are critical weld seams in an offshore floating wind TLP-type substructure in mixed wind-wave conditions subject to mean stress effects?

SQ7: At what stage in design and analysis can predictions of multiaxial stress behaviour be made?

SQ8: What are the effects of fatigue brackets on (multiaxial) stress behaviour of a TLP in mixed wind-wave conditions?

2.3. Scope

To propose a feasible study, this research will be limited to investigating the loading and response of a TLP type substructure using a time-domain coupled simulation. The simulated structure will be subject to linear waves and linear elastic mooring response, and an existing linear aerodynamic turbine model will be applied. Hence, the research will be restricted to the numerical characterization of the dynamic environment, the loads this environment produces, and the resulting motions and structural responses to these forces.

2.4. Research goal

This thesis seeks to assess the extent of multiaxial stress response in a selection of weld seams. It is of interest to assess if these locations are subject to a complex stress state, which must be evaluated as such. In other words, is it essential to consider the multiaxial component(s) of the stress state at a point in the structure, or can uni-axial fatigue assessment methods be applied? In order to perform this assessment, a new type of model needs to be derived, which allows for motions, loading, and stress response to be included. Hence, the goal of this thesis can be considered in two parts.

Research goal:

1. Construct and validate a temporal analysis model that takes the numerical characterization of the metocean environment as input and allows for the structural stress response to be derived.

and

2. Demonstrate the (lack of) presence of multiaxial stress response in a TLP- type substructure for FOWT. Establish to what extent critical weld seams are subject to multiaxial stress response.

The investigation can be considered successful if both goals are met. For the first goal, this can be assessed if a deliverable of the specified type is produced. The second goal is met if a multiaxial stress response behaviour is constituted and its implications can be quantified. The investigation can also be considered successful if the absence of a multiaxial stress response is constituted.

2.5. Relevance

Several implications, spanning different facets, must be considered before starting this investigation. These are discussed below.

Practical

As discussed, current design and analysis practices do not allow for a complete multiaxial fatigue assessment. Due to this, it is also not possible to provide evidence that multiaxial stress components may be neglected. The practical implementations of the research presented in this literature review may affirm design and analysis practices at Bluewater or require the revision of (some) design practices regarding fatigue for FOWT.

Scientific

As most of the tools required to conduct the type of analysis outlined in this section are (very) expensive to license for both companies and scientific institutions, and others are entirely unavailable for non-commercial use, the prospective results are effectively locked behind a paywall. This investigation seeks to provide meaningful insight into the degree to which multiaxial fatigue assessment methods are

required to evaluate lifetime damage accumulation. In addition to this, TU Delft is actively taking charge in the field of multiaxial fatigue research, especially in the field of offshore and maritime engineering.

Societal and Environmental

Within the context of FOWT, societal and environmental relevance are closely related. An investigation into multiaxial fatigue in FOWT may contribute to understanding the structural response of TLP-type structures. This will contribute to the construction of resilient infrastructure and sustainable industry, which is sustainable development goals (SDG) 9 posed by the UN for 2030 [138]. Understanding the structural response mechanisms allows for efficient and safe designs. Safe structures with a low failure rate also pose a lesser threat to the environment to which they are alien. This contributes to SDG 14, which is to conserve and sustainably use our oceans [138]. Furthermore, the availability of renewable energy in production industries allows for environmentally sustainable production and consumption (goal 12), thus reducing greenhouse gas emissions and combatting climate change (goal 13) [138].

Ethical

The development and implementation of renewable energy sources, such as FOWT, play a role in reducing reliance on fossil fuels and mitigating climate change. The adverse impacts of wind power, such as bird and bat mortality or aesthetic concerns, are minor compared to the effects of climate change on health, ecological systems, and safety [22]. Although production and installation of FOWT is an energy-intensive process currently highly reliant on fossil fuels, this footprint is minor to the added benefit of large-scale renewable energy production.

Part I

Literature Review

3 Environment

The first step towards a fatigue assessment of an offshore floating structure is an environmental representation. This section aims to provide a complete portrayal of the dynamic wind-wave-current environment, as well as its numerical implementation. As this thesis considers both linear and nonlinear approaches, it is important to distinguish these approaches as the term *linearised* may have more than one interpretation. In the context of this investigation, linearisation allows for the use of superposition, meaning that the problem can be split up into all of the force components separately, which can be added together to determine the total loading. Therefore, the linear theory may be used to describe a time-varying constant amplitude potential flow, as it adheres to the above assumptions [61, 70]. This chapter will consider the statistical representation of wind and waves separately in sections 3.1 and 3.2.

3.1. Wind statistics

Wind is a constantly changing phenomenon composed of components with low-frequency, as well as high-frequency turbulence [74, 134]. This section serves as a means to represent this highly dynamic environment by individually considering the various aspects of modelling a wind field. In section 3.1.1, wind speed is discussed, followed by wind shear in section 3.1.2. Next, in section 3.1.3 will be discussed, followed by wake interaction effects in section 3.1.4.

3.1.1. Wind speed

As the velocity of the wind is constantly changing, it is mainly quantified by its mean. This can be done over short intervals for gusts (3-10s) or as 10-minute, daily, monthly or yearly mean [134]. For these more extended measurements, the time-varying component of the wind can be represented in a wind spectrum, as shown in figure 3.1. An important feature in the wind speed spectrum is the spectral gap separating the mesometeorological and micrometeorological ranges. This gap shows that the mean over 10-minute or 1-hour periods may be considered constant, although the instantaneous wind speed varies due to a high frequency time-varying turbulent component [74, 134].

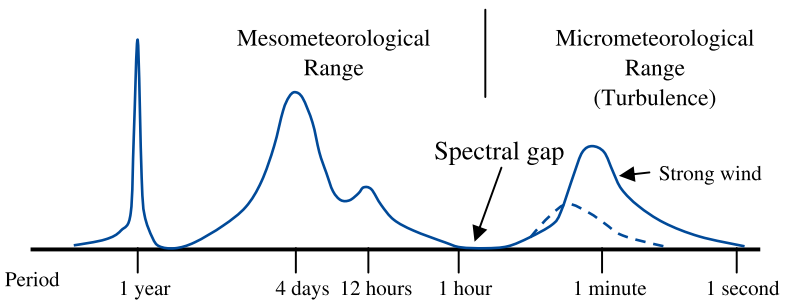


Figure 3.1: Wind speed spectrum over a wide range of frequencies. The dotted line in the turbulence zone indicates turbulence magnitude for low winds (adapted from [134, p .32]).

3.1.2. Wind shear

In the bottom 2 kilometres of the earth's atmosphere, the flow of air interacts with the surface, creating a boundary layer [74, 95, 134, 142]. This is pictured in figure 3.2, where it can be clearly seen that despite the variations in instantaneous velocity, the mean wind speed increases with elevation. The shape of this boundary layer depends on the surface roughness of the earth, as the effects of a forested area are noticeable at a higher altitude than the equivalent for a meadow or stretch of ocean [142]. It is important to know how the wind speed profile is distributed as most wind measurements are conducted at 10m above sea level, and one would like to determine the wind speed at hub height. Furthermore, the distribution of wind speed across the height of the rotor plane, as well as the tower, is important to accurately determining the total loading [142].

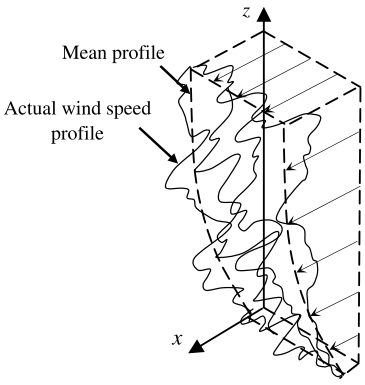


Figure 3.2: Mean wind speed distribution over height, plotted in a dotted line, clearly showing that the mean wind speed increases over height. [134, p .33]).

For engineering purposes, there are two common methods: the logarithmic profile or the power law profile as shown in equations (3.1) and (3.2) below [95, 134].

$$V(z) = V_{w,r}\left(\frac{\ln\frac{z}{z_0}}{\ln\frac{z_r}{z_0}}\right) \qquad (3.1) \qquad V(z) = V_{w,r}\left(\frac{z}{z_r}\right)^{\alpha_{shear}} \qquad (3.2)$$

Where $V(z)$ is the wind velocity at height z and $V_{w,r}$ at reference height z_r, in turn, z_0 is the surface roughness length and α_{shear} the power law coefficient. As these formulations differ, their outcomes can also be expected to differ. Tempel states that this difference is not important as long as all parties agree on which model to implement and stick to this. This is because most turbine loading software requires a hub height and profile as input [134]. Generally, the logarithmic profile is most suitable below 60m, and power law is most suitable for heights above 100m [142]. As the hub height of the turbine is well above 100m, the power law profile in equation (3.2) should be used for further modelling.

3.1.3. Turbulence

The high-frequency, time-varying component of wind is turbulence, which also depends on altitude and surface roughness. The turbulence intensity is defined as the standard deviation of the time-varying wind speed divided by the mean wind speed, in percentage [25, 95, 134].

$$I_t = \frac{\sigma}{V}\,[\%] \qquad (3.3)$$

Values for turbulence intensity depend on location and altitude and can be found in design standards and may differ per classification society. Apart from a longitudinal component, turbulence also contains vertical and lateral components [95, 134]. It is common to negate this vertical component [13].

Furthermore, as Tibaldi [135] concludes, it is important to consider low/no turbulence in the analysis for fatigue analysis. This is because, in low turbulence intensity, resonant vibrations are allowed to build

up, allowing for proper identification. In high turbulence intensity conditions, the rotor speed varies more. Hence, the turbine will be in and out of resonance; thus, not enough time will be available for vibrations to build. This will be discussed further in section 4.1.1.

3.1.4. Wake interaction

As the rotating turbine interacts with the incoming wind field, it further disturbs this Windfield and leaves a highly turbulent flow downstream of the turbine. This is referred to as a wake. This wake gradually mixes back into the surrounding flow. These effects are important for large-scale turbine deployments, as another turbine may interact with the wake of one or more other turbines [142]. If only a single installation is considered, wake effects do not need to be modlled.

3.2. Wave statistics

One of the most prominent loading sources for a floating structure at sea is waves. Waves at sea are composed of many components travelling in different directions. Waves also interact with their environment, be it other waves, tides, currents, sea floor or coastlines [13]. Waves out at sea can be generated in several ways: a moving floating body, tidal fluctuations, earthquakes and interaction between wind and sea surface. The last source of loading will be considered in this thesis. Waves generated by wind can be further divided into two categories [61, 70]:

- **Wind seas**: Waves generated by local wind field. Waves are generally short and highly irregular. Wave crests are generally quite short and have no shared heading angle. This type of sea is often interpreted as chop on the water.
- **Swell**: Swell is composed of waves that have propagated out of the wind field they were generated in and are capable of propagating hundreds of kilometres. These waves are more regular, and the crests are more rounded than the waves of a wind sea. This is the type of wave surfers chase.

This thesis will not consider the mechanisms that drive wave generation and propagation. In this section, the approach to conducting fatigue analysis based on statistical data will be explained. In order to do this, regular and irregular linear waves as well as nonlinear waves, will be discussed in sections 3.2.1 to 3.2.3. Based on these fundamentals, short and long-term statistics will be explained in sections 3.2.4 and 3.2.5 such that the process of acquiring a representative time domain signal for wave elevation can be achieved in section 3.2.6. Finally, in section 3.2.7, the methods for describing particle kinematics above the mean water level will be covered.

3.2.1. Regular waves

Regular linear harmonic waves can be described in time travelling in $+x$ direction using a sinusoidal function characterised by wave amplitude ζ_a, wave number k, and circular wave frequency ω equation (3.4).

$$\eta(x,t) = \zeta_a \cos(kx - \omega t) \tag{3.4}$$

with;

$$k = \frac{2\pi}{\lambda} \qquad \text{and} \qquad \omega = \frac{2\pi}{T} \tag{3.5}$$

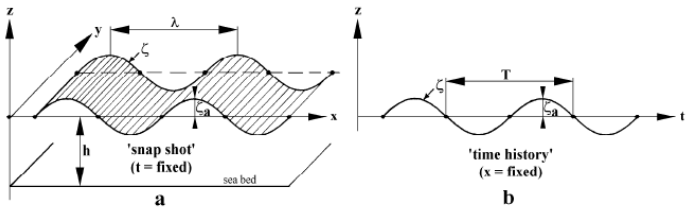


Figure 3.3: Shown on the left, a regular wave frozen in time. Shown on the right is a regular wave time signal at a fixed location. Both illustrations indicating key wave parameters [70, p. 154].

3.2.2. Irregular waves

As anyone who has stood on the beach can confirm, the sea looks nothing like figure 3.3. Instead, the surface appears to be constantly changing, never to repeat itself. Considering linear theory, the surface elevation may be considered as the sum of the elevations of a large number of linear harmonic wave components at an instant, as illustrated in figure 3.4 [13, 61]. Using this simple linear assumption to describe a complex process, an irregular sea can be described. This is referred to as the random phase/amplitude model. Wave statistics are built upon this assumption and apply Fourier transformations to compose or decompose an irregular sea surface elevation signal.

3.2.3. Non-linear waves

The regular and irregular wave description provided above is built on the assumption that wave components are harmonic and independent of each other [61]. This assumption is valid as long as the waves do not become too steep or propagate through shallow water as nonlinearities increase the height and sharpness of wave crests and make troughs shallower and flatter [61]. Different theories should be applied depending on the type of nonlinearities in a particular wave (e.g. steepness or breaking). This can be seen without studying the details of figure 3.5.

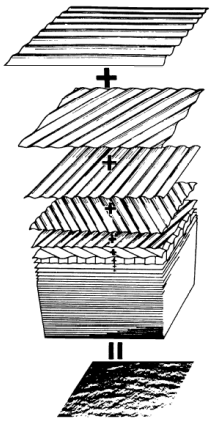


Figure 3.4: Representation of irregular sea as a composition of infinite harmonic wave components [70, p. 153].

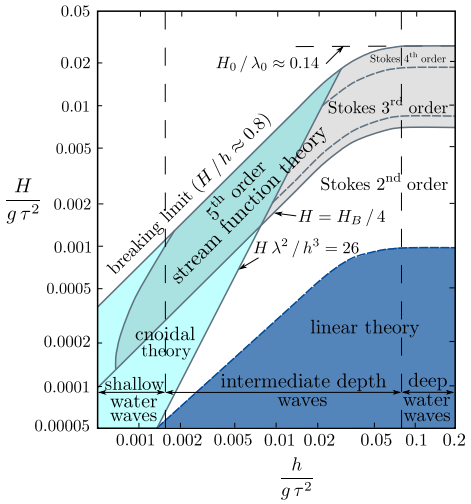


Figure 3.5: Valid range for different wave theories, waves considered in this thesis indicated with the dark blue shaded area (adapted from [100]).

Other than adding extra computational expenses, some nonlinear theories inhibit using linear potential flow theory. Water is considered deep when the surface wave is unable to 'feel' the seabed. In other words, the seabed does not inhibit wave propagation. Deep water can be characterised if the water depth h is greater than half of the wavelength as $h/\lambda > 2$ [61, 70].

3.2.4. Short term statistics

Ocean waves can be described using a spectrum by considering the sea surface as a stochastic process. In other words, all possible observations are captured in the spectrum [61]. Given a wave/surface elevation record $\eta(t)$ and the assumption that any wave record can be reproduced by a sum of a large number of harmonic wave components N as shown in equation (3.6);

$$\eta(x,y,t) = \sum_{i=1}^{N}\sum_{j=1}^{M} \zeta_{a_{i,j}} \cos(\omega_i t - k_i \cos(\theta_j)x - k_i \cos(\theta_j)y + \phi_{i,j}) \tag{3.6}$$

Where ζ_a and ϕ are the wave amplitude and phase, respectively, most wave records have a uniformly distributed phase angle in deep water, and hence, the wave record is characterised by the amplitude spectrum. As each component has been generated and travelled independently of each other, they may be considered independent random variables [61]. According to the central limit theorem, which in short states that the sum of a large number of independent random variables is

normally distributed (Gaussian), it follows that the surface elevation should be normally distributed (Gaussian). Measurements also support this theory, but not for nonlinear events, such as steep or high waves in shallow water [61]. As linear wave loading is a much more dominant contribution to fatigue loading than rare nonlinear waves, those events do not need to be considered in a fatigue analysis.

Over a period of time, it may be said that the statistical characteristics of the wave are independent of time, and thus, the process may be considered stationary. A wave spectrum is generated from many 15-30 minute wave records, each transformed separately. As illustrated in figure 3.6, the wave signal is decomposed into many harmonic signals. The phase angle is discarded in the spectral approach and can be justified by the apparent uniform distribution of phase angles between $0 \leq \phi \leq 2\pi$. The wave amplitude is approximately Rayleigh distributed for each frequency [61]. Using these distributions, a total *amplitude spectrum* can be generated. Although an amplitude spectrum provides enough information to describe the sea surface, an *energy density spectrum* is even better. As nature does not work in discrete frequencies, a continuous energy density spectrum must be determined. The steps described above are visually represented in figure 3.6 for a *1D* wave spectrum (i.e. wave angle is not considered).

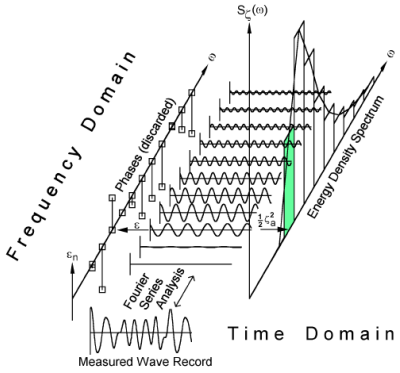


Figure 3.6: Converting a surface elevation to an equivalent spectrum [70, p. 190].

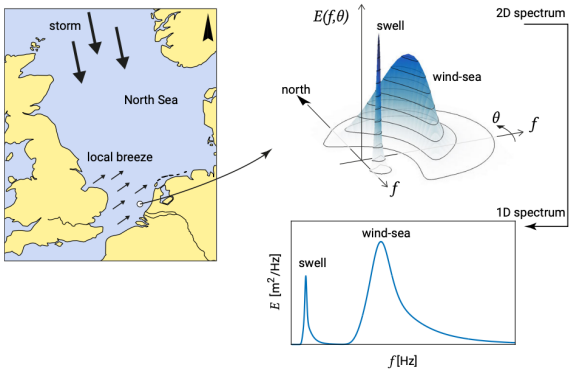


Figure 3.7: 2D wave spectrum on the North Sea, clearly showing the difference between local wind sea and swell waves incident from different angles ([61, p .48])

Repeating these steps for all wave angles θ, a 2D wave spectrum can be generated. An example of this is shown in figure 3.7. Using these spectra, average parameters such as significant wave height H_s and significant wave period T_s can be used to characterise a wave record [61]. The application of this will be apparent from the use of long-term statistics in section 3.2.5.

3.2.5. Long term statistics

For long-term statistics (10+ years), the conditions may no longer be considered stationary, and the approach must be changed. As it is not feasible to generate a 10-year time signal, instead, each stationary condition is replaced by significant wave height H_s, significant period T_s and mean wave direction $\bar{\theta}$. This information is summarised in wave scatter diagrams, each with its own probability of occurrence [61, 70]. Depending on the level of detail required there are several ways of further discretising the data. First of all, by incoming wave direction, wave scatter diagrams are plotted for each $\Delta\theta$ [70]. Common engineering practice is to discretise according to the 16-point wind rose (i.e. N-NNE-NE-ENE-E for the first quadrant). As the wave climate varies throughout the year, scatter plots may also be further divided per month or season. Regardless of the choice of further discretising the scatter diagram, wind and swell components can remain separated.

3.2.6. Time domain formulation

As will be established at several points throughout this literature review, (multiaxial) fatigue assessment for a FOWT requires a time domain simulation, which also requires long-term wave statistics. Any offshore structure will encounter a vast number of waves of different sizes and frequencies throughout its lifespan. Fortunately, the original time signal does not need to be reproduced as long as the simulated waves are statistically indistinguishable from the original data [13, 70]. This can be checked by generating

a wave spectrum from the generated signal in order to verify that the energy density spectrum is maintained. In engineering practice, it is common to divide all of the waves a structure will encounter into sea-states and use a mixture of short-term wave statistics to generate an energy density spectrum for each sea state and to use long-term statistics to determine how frequently each sea-state occurs and the heading angle [2]. In order to generate a time signal equation (3.6) requires the following information;

- θ: Follows from the wave scatter diagram for a chosen θ
- ω_n: Chosen at equally spaced intervals $\Delta\omega$ of the spectrum. Note that the time series will repeat itself after $2\pi/\Delta\omega$ seconds, which may result in simulations after $t = 2\pi/\Delta\omega$ to be redundant.
- ζ_a, n: The wave amplitude follows from the area under the spectrum at a particular frequency according to $\zeta_a, n = 2\sqrt{S_\zeta(\omega_n) \cdot \Delta\omega}$
- k_n: Wave number follows from wave frequency according to dispersion relation. As it has already been established that only deep water will be considered, the dispersion relation can be simplified to the following: $k_n = \omega_n^2/g$
- ϕ: As phase angle information is lost in spectral analysis, it needs to be generated. As previously established, the phase angle is uniformly distributed over $0 \leq \phi \leq 2\pi$. Hence, ϕ is to be randomly drawn.

3.2.7. Kinematic profile extension

Thus far, this literature review has only considered linear wave theory, which allows for efficient computations to be run on a structure in irregular waves. However, as linear wave theory is formally only valid for very small waves, it is unable to capture the kinematics of the wave above the mean surface level (MSL) [111]. As the wave crest contains points with the highest kinematic velocity and acceleration, neglecting the kinematics above the MSL would result in a misrepresentation of the wave kinematics. Using profile stretching, the kinematics of wave particles above the MSL can be represented. As these methods are derived for linear theory, they are all applicable to linear irregular waves. There are three available methods for kinematic stretching [70, 111].

- **Exponential extrapolation:** Linear wave theory depth decay function is extrapolated exponentially above the mean water level. Kinematics below the MSL remains unaffected. The exponential extrapolation does cause the kinematics at the wave crest to be grossly over-estimated.
- **Linear extrapolation:** Using the gradient of the depth decay function at the MSL, the kinematics of the wave particles can be described with a lower degree of over-estimation. This is due to the growth rate of a linear function compared to an exponential function. Kinematics below MSL are unaffected
- **Constant extension:** Another very simple to implement extension method is to state that all particles above the MSL share the same kinematics of the particle at the water surface. Hence, kinematics below MSL are unaffected. This is a popular method for hand calculations.
- **Wheeler stretching:** The most popular implementation of kinematic profile extensions. Simply put, the negative z-axis extends from the instantaneous surface elevation $\eta(t)$ to the seabed. This means that in all formulations, global coordinate z is replaced by a computation z' where d is the local water depth.

$$z' = \left(\frac{d}{d + \eta(t)}\right) z + d\left(\frac{d}{d + \eta(t)} - 1\right) \tag{3.7}$$

  Despite the extra computational step, this method is very efficient and can be easily implemented.

Several profile stretching methods are compared in figure 3.8, illustrating how the horizontal particle velocity differs between methods.

3.3. Current statistics

At a global scale, currents are driven by a multitude of factors that may be any combination of wind-driven, temperature-driven, tides, storm surge, river discharge or global weather patterns [2, 61]. However, at an installation site level, current can be considered a speed and direction and hence be

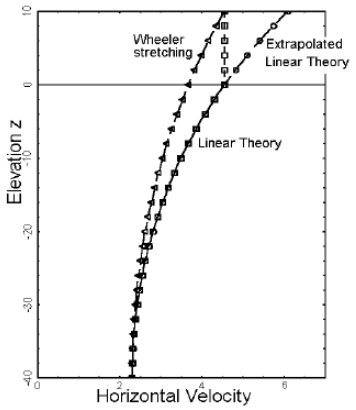


Figure 3.8: Kinematic comparison of various stretching theories illustrating the variance in the vertical distribution of horizontal particle velocity [70, p. 178].

decoupled from the global forces driving current. It is at this level that current can be considered in this literature review. According to ABS, current loads may be regarded as static, although a flow may induce dynamic effects such as vortex induced oscillations (vio), which will be considered separately in section 4.2.7

Currents vary over time, as well as water depth, due to tide and interaction effects with the seabed. For installations at offshore sites, it is common practice to conduct an environmental study, which will include a report on the current depth decay, direction, and velocity, which may be further broken down by time of year.

As a current may be considered a static load, no associated potential function needs to be determined. Instead, the total velocity of the fluid at any point may be considered as the superposition of current and wave contributions to the fluid velocity.

4

Loading

Throughout the lifespan of a FOWT, a substructure is subject to a multitude of loading sources from construction to transport & installation and operation. For feasibility purposes, this literature review will only consider the loading during the day-to-day operational lifespan of the structure. These loads are due to wind, waves, and currents. Incidentally, these loads dominate the mechanical loading and response of a marine structure [18]. In sections 4.1 and 4.2, aerodynamic and hydrodynamic loading will be discussed, respectively.

4.1. Aerodynamic loading

In this section, the aerodynamic loading will be discussed in detail. In section 4.1.1, the various aerodynamic excitation sources will be discussed, after which sources of aerodynamic damping will be discussed in section 4.1.2. Subsequently, in section 4.1.3, the modelling methods of aerodynamic forces will be discussed, one of which is discussed in detail in section 4.1.4. Finally, in section 4.1.5, the aerodynamic controller and its effects on the system dynamics will be considered.

4.1.1. Sources

Even when considering constant velocity laminar incoming flow, aerodynamic loading also contains cyclical components at various frequencies. As an aerodynamic loading time trace does not provide a clear separation between load sources, this section will refer to the Power Spectral Density (PSD) plot. These plots are derived from a load signal by decomposing into all of the frequency components using a Fourier Transformation, in the same way as wave spectra are derived, as explained in section 3.2.4. The resulting spectrum contains peaks at different excitation frequencies. These excitations occur at multiples of the rotational frequency P (interchangeably referred to as ω) or blade passing frequency $3P/3\omega$ (for a three-bladed turbine). In figure 4.1 below, an example of a PSD plot is shown for a simulated turbine in uniform wind conditions, showing several labelled peaks.

The clear separation between energy peaks in the PSD plot can be seen, which contain the following harmonic loading sources can be found in a three-bladed turbine:

- **Aerodynamic imbalance:** Occurs when the loading across all of the blades is not equal, for example, due to different pitch angles of the blades. This causes the centre of thrust to move out of line with the central axis of the hub. This imbalance causes a load variation with $1P$ frequency [142].
- **Mass imbalance:** Slight differences in the production process may cause an imbalance in the blade masses, again shifting the centre of gravity away from the central axis of the hub. This imbalance causes a load variation with $1P$ frequency [142].
- **Rotational sampling:** While a blade rotates, it samples different characteristics of the wind field over one rotation. These differences may be caused by wind shear, yaw misalignment and tower shadow effect. This causes a load variation with $3P$ frequency and multiples [142].

Although not harmonic, turbulence is also a source of variant loading. Due to the random nature of the turbulence in the flow, the variation in loading is also random, as was discussed in section 3.1.3. The

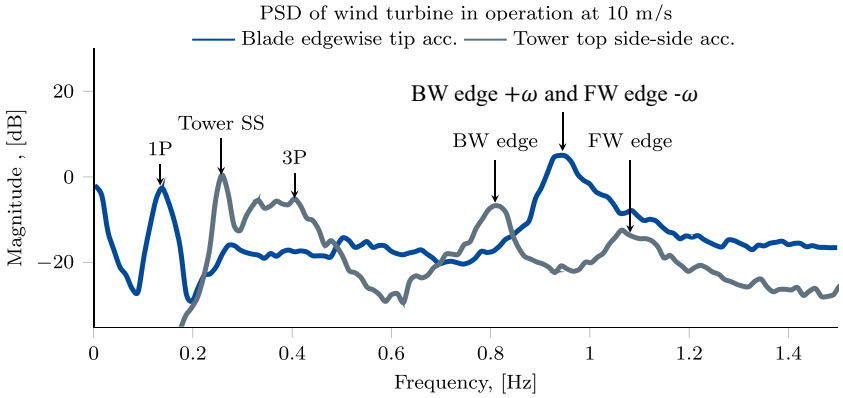


Figure 4.1: Example of a PSD plot for a simulated turbine in uniform wind conditions showing the blade edgewise and tower top contributions separately (adapted from [47, p. 3] to maintain consistency in notation).

turbulence causes the 'grassy' signal. One of the excitation sources displayed in figure 4.1 that has not been explained is backward whirling (BW) and forward whirling (FW). When considering the blade spectrum (blue), two clear peaks can be observed at $1P$ and $7P$, the last of which corresponds to an accumulation of energy from BW edge + ω and FW edge - ω modes. For the side-side tower mode, a clear peak can be seen at its first natural frequency, followed by two less logical peaks due to whirling. Here ω represents the rotational frequency [47, 135, 56]

Whirling is caused by an imbalance of the rotor due to deformations and also depends on the rotational velocity due to centrifugal stiffening. Whirling frequency follows from an eigenfrequency analysis. If the rotational frequency ω (previously also referred to as P) equals the blade vibration frequency, f_{blade} the centre of gravity becomes static. If $\omega > f_{blade}$, then the centre of gravity moves with the rotational direction of the rotor, resulting in FW. If $\omega < f_{blade}$, then the centre of gravity moves against the rotational direction of the rotor, resulting in BW [47]. These are aeroelastic effects.

Granting that figure 4.1 very clearly shows the PSD distribution for blades, tower and the superposed system, the peaks shown are from a simulation concerning turbulent wind, and the measurements are only considering the tower top and blade tips. As this literature seeks to investigate contributing sources to (considers) multiaxial fatigue in the TLP substructure, the PSD distribution at the tower base is more interesting. Furthermore, as Tibaldi [135] concludes, it is important to include low turbulence intensity conditions in the analysis. This is because, in low turbulence intensity, resonant vibrations are allowed to build up, allowing for proper identification. In high turbulence intensity conditions, the rotor speed varies more. Hence, the turbine will be in and out of resonance; thus, not enough time will be available for vibrations to build.

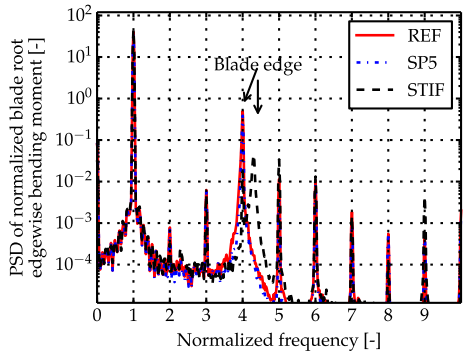


Figure 4.2: Blade root edgewise bending moment PSD for low turbulence, above-rated wind conditions. Shown for reference illustrating a much cleaner signal [135, p. 8]

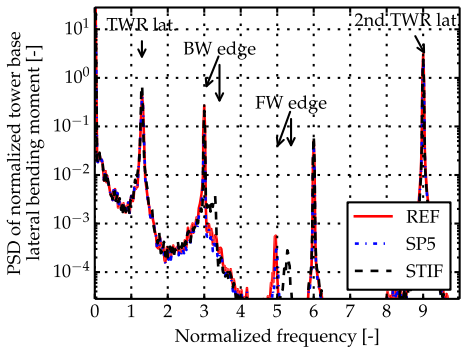


Figure 4.3: Tower base bending moment PSD for low turbulence, above-rated wind conditions.[135, p. 7]

In figures figures 4.2 and 4.3, the blade root edgewise bending moment and tower base bending moment PSD are shown respectively. Both plots display simulation results for the above-rated, low-turbulence wind conditions for three different blade configurations, the details of which are not important to this investigation. Plot 4.2 is included to show that the pronounced peaks at nP are conserved, but the signal has become less 'grassy' due to the lower turbulence. In figure 4.3, it can clearly be seen that $1P$ and $3nP$ loads are governing present at the base, with a small peak at $5P$ due to forward blade whirling. There is also energy at $6P$ and $9P$ due to second and third-order effects happening at a frequency of $3P$

4.1.2. Damping

Wind turbines experience structure motions due to deformations of the tower, and for FOWT due to the motions of the substructure. These motions induce a velocity component on the blades, and thus fluctuating thrust, resisting the motion of the nacelle due to the moving components of the tower and substructure [74, 134]. This is known as aerodynamic damping. Previous works reviewed by Tempel showed that aerodynamic damping plays an important role in structural dynamics and that damping in operational conditions is very different from parked conditions due to the thrust on the blades [134]. Damping is inherently included in temporal simulations and does not need to be accounted for separately, unlike spectral simulations [74, 86, 94, 134]

4.1.3. Load models

As this literature review seeks to investigate multiaxial fatigue in the TLP substructure, the exact physics applied to model the aerodynamics of a WTG is out of the scope of this investigation. However, there are multiple modelling philosophies available for application, of which a short overview is given below [57, 143]:

- Blade Element Momentum (BEM) is the most common tool to calculate the aerodynamic loading of a WTG. The method considers each blade as a number of independent sections that may each be considered in 2D and assumes there is no mutual interaction between sections. Using vector mathematics, all of the incident wind velocity components can be determined, such that an incident wind velocity and angle of attack can be established for each section. The total blade load can be determined by integrating the length of the blade. This method is applicable in the temporal domain and is able to include dynamic wake and inflow, yaw misalignment, dynamic stall and a finite number of blades due to tip corrections. The BEM method heavily relies on accurate airfoil data.
- Vortex models have been developed to improve models of the wake dynamics of a wind turbine. Trailing and shed vortices are modelled by lifting lines or surfaces. Potential theory is applied, and therefore, viscous effects cannot be captured. Compared to BEM, vortex models are more computationally intensive, and simulations tend to diverge due to singularities in the wake. Simulations have been shown to provide much more accurate predictions of wind turbine wakes than the empirical BEM methods.
- Actuator-type models are probably the simplest type of models and apply 1D actuator disk theory. Although BEM is a much more sophisticated application of actuator disk theory, the actuator disk problem can be directly solved using Euler or Navier-Stokes equations. This type of model is more computationally expensive than BEM but does not provide more accurate answers than BEM.
- Computational Fluid Dynamics (CFD) presents the final method to evaluate forces on a wind turbine. CFD inherently takes viscous effects into account, including other effects such as vorticity in the airflow. This is done by directly solving the Navier-Stokes and continuity equations at thousands of points in the fluid. It does not require any aerofoil data to work accurately. Meshing the complex 3D shape of the blades accurately also poses issues. Finally, this method is highly computationally expensive but provides the highest level of detail with respect to dynamic effects in the temporal domain.

Striking a balance between accuracy and computational efficiency, BEM is a very popular engineering tool to compute aerodynamic loads on a WTG. Much like Finite Element Analysis (FEA), BEM is a method for which various companies and institutes have developed their own computer programs. One of these programs is OpenFast (previously FAST), which has been in development for a long time.

OpenFast is widely accepted and has been implemented directly into widely trusted industrial software such as SESAM (by Det Norske Veritas (DNV)), OrcaFlex (by Orcina) and Workbench (by ANSYS), to name a few. Due to the established open-source nature of OpenFast, this investigation will consider this software package as a suitable and appropriate toolset.

4.1.4. Blade Element Momentum

As a full breakdown of aerodynamic models does not fall within the scope of this literature review and the overview discussed in section 4.1.3 provides a sufficient introduction, the rest of this section will consider a number of important aerodynamic modelling considerations, and how these are handled by BEM models, and specifically AeroDyn.

4.1.4.1 Tip and hub loss

One of the drawbacks of BEM is that it is unable to capture tip or hub loss effects. Tip loss is caused when air flows from the pressure side to the suction side of the blade over the blade tip. This reduces the pressure difference and hence the lift at the tip; a vortex is also shed at the tip [57, 95, 143]. Several empirical models have been suggested, but Prandtl's correction factor has been shown to provide accurate results without inhibiting computational speed [95, 104].

Hub loss is caused by vortices shed at the connection between the nacelle hub and the blade. Modified Prandtl correction factors exist to account for this [95, 104].

4.1.4.2 Skewed inflow

When the normal to the rotor plane is not perfectly aligned with the incoming wind, the inflow is skewed. This can be caused by a yaw misalignment of the Rotor Nacelle Assembly (RNA) or due to a yaw response in a FOWT. For engineering practices, yaw/tilt models are used to redistribute the induced velocities such that the induced velocity is higher when the blade is passing deep through the wake, as opposed to moving upstream. This causes an imbalance in the rotor loading, which results in a correcting yaw moment. If the tower does not allow for the rotor plane to yaw into the incoming flow, this moment is transferred to the substructure [57, 143]. This is interesting for multiaxialresponse and fatigue.

Another aspect contributing to skewed inflow is wind shear, an effect causing the flow to shear due to surface friction, as described in more detail in section 3.1.2.

4.1.4.3 Dynamic stall

Dynamic stall is a nonlinear unsteady aerodynamic effect due to a rapid change in the angle of attack of the turbine blade [95, 143]. The wind, as experienced by a point on the blade, is in a constant state of change due to wind shear, yaw misalignment, tower effects and atmospheric turbulence. For the considered point on the blade, this is experienced as a fluctuation in the magnitude of the incident wind as well as the angle of attack [13, 57, 143]. The response to this change lags behind with a time delay depending on the blade profile. This can be translated to the lift coefficient curve, where, once flow separation starts to occur, an increase in the angle of attack no longer leads to a linearly increasing lift coefficient. Once the maximum lift coefficient has been achieved, the aerofoil has stalled until the flow has reattached [142]. This effect can be modelled using empirical methods available in AeroDyn.

4.1.4.4 Tower effects

As the wind must also pass the tower that supports the RNA, it has an effect on the local flow upwind from the turbine. As the blade travels through this altered flow, the generated lift fluctuates. For a three-bladed turbine, this occurs at a frequency of 3ω. The change in flow velocity due to the presence of the tower can be modelled using potential flow around a cylinder. Textbook solutions are available [57, 95, 104].

The influence of the tower can also be seen downwind in the wake. Apart from reducing the velocity of the flow locally, the tower also has aerodynamic drag [13, 95]. As discussed in section 3.1.4, wake interaction is outside of the scope of this investigation. Tower drag may become important in extreme wind situations when the rotor is parked [13]. However, in normal operating conditions, the force contribution is so small that it may even be neglected entirely.

4.1.5. Controller

Power production using a wind turbine (farm) effectively cannot take place without a control system [95]. Generally, a controller seeks to find an optimum between (1) maximising energy production within operational restraints, (2) preventing extreme loads, including resonance, (3) ensuring acceptable power quality output to the grid, and (4) ensuring safe operation. There are three types of controllers employed in wind farms: a wind farm controller, a supervisory controller for each turbine and dynamic controllers for the subsystems in each turbine. The first coordinates with various supervisory turbine controllers, i.e., tells each turbine how much power should be produced. The second type is the supervisory controller. This controller can respond to commands from the wind farm controller to safely start up or shut down operations [13, 95]. These types of controllers will not be considered in this investigation.

Instead, dynamic controllers will be used to control the various subsystems in the turbine, such as torque or blade pitch [13, 95]. This investigation will consider a three-blade, upwind, pitch-regulated, direct drive horizontal axis wind turbine which predominantly employs pitch-regulated variable speed (PRVS) controllers [13].

4.1.5.1 Pitch-regulated variable speed controllers

PRVS wind turbines can regulate turbine operation through speed changes and blade pitch changes. As this literature does not seek to research the development of a WTG controller, this subsection will not consider a detailed explanation. Instead, a global introduction limited to PRVS controllers will be given.

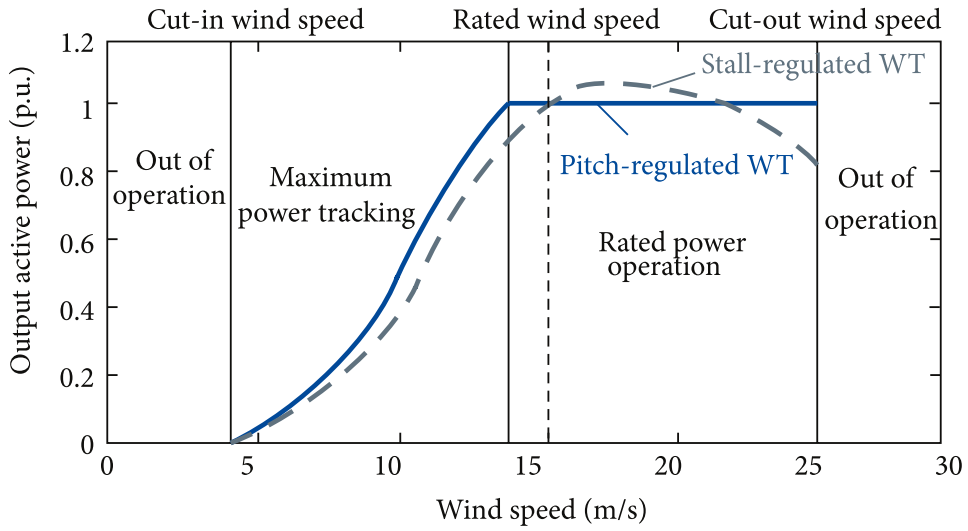


Figure 4.4: Example of power output for different wind speeds for pitch and stall regulated wind turbines. ([51, p. 3]).

A wind turbine exists in four regions, of which it can produce power in two operational regions: below-rated and above-rated wind speed as can be seen in figure 4.4 [13]. PRVS typically use pitch control, only above rated wind speed, but use generator torque control over the whole operating range of the turbine [105]. For below-rated wind speeds, the blade pitch remains constant, and the generator torque is controlled such that the optimal C_p is reached and maximum power output is achieved [13, 95, 105]. This is also known as the variable speed operational window, as the inertia of the turbine rotor helps to smooth out shaft speed by storing energy during acceleration and releasing energy during deceleration. In short, if the aerodynamic power is greater than the outgoing generator power, the rotor speeds up and vice versa [13, 95, 105].

When operating in the above-rated wind speed window, a variable pitch is used to regulate the aerodynamic power generated. This is done by feathering the blade such that the produced lift, and hence power, decreases, such that the rotor rotational speed can be kept constant. During gusts, electrical power output can be maintained while rotor speed increases, in the same way as the below-rated speed [13, 95, 105]. In between regions, the control logic is applied to smoothly transition between regions [1].

4.1.5.2 Floating Wind Controller Challenges

Unlike fixed wind, floating wind nacelles move due to the motions of the substructure, adding an extra challenge to the control system. Platform motions induce an extra velocity component as experienced by the blades. When applying a traditional wind pitch controller, which has a relatively slow response bandwidth compared to the fixed turbine, no special behaviour is seen. However, as (depending on substructure) FOWT generally has a very low response period, the controller is relatively fast compared to motions [13, 148]. In above-rated wind speeds, the pitch controller will respond to this perceived increase (decrease) in relative wind speed due to motions by increasing (decreasing) the pitch in order to shed (increase) generated thrust. This decrease (increase) in thrust will cause an amplified motion response upwind (downwind), thus causing negative damping [13, 148].

For a TLP, the pitch frequency is usually higher than the control frequency, meaning that no modifications to the control system would be needed [13]. On the other hand, the surge natural frequency is significantly lower than the controller frequency, which can lead to instability, as Matha observed [96]. Matha concluded that TLPs generally have enough hydrodynamic surge damping to overcome the negative damping in an unstable situation. Bachynski could apply land-based turbine controllers to five different TLPs without issues.

4.1.5.3 ROSCO controller

The reference open-source controller (ROSCO) is a general wind turbine controller designed for fixed and floating wind applications by National Renewable Energy Laboratory (NREL) [1]. It is also the only available open-source turbine controller applicable for FOWT application. An extra benefit of ROSCO is that it can be integrated easily with OpenFast and the considered IEA-15-240-RWT turbine. It is also accompanied by a Python-based toolbox that allows for tuning and implementing a controller model.

4.2. Hydrodynamic loading

A moored floating body at sea is subject to hydrodynamic loading components from waves, the current and the tidal range. Hydrodynamic loading is one of the main sources of loading on any floating structure, including FOWT and is paramount for the structural loading and response analysis. In this section, the various methods to determine the hydrodynamic loading will be discussed, starting hydrostatic loading in section 4.2.1. Next, in sections 4.2.2 to 4.2.4, the potential theory will be discussed, including the linear and non-linear loading terms. In section 4.2.5, an alternative formulation in Morison's work will be discussed, after which in sections 4.2.6 and 4.2.7 CFD and vortex-induced oscillations are discussed.

The hydrodynamic loading for any floating body, including FOWT, follows from the pressure exerted by the fluid. This pressure follows from Bernoulli's law, and total potential Φ as presented in equation (A.1);

$$p = -\rho g z - \rho \frac{\partial \Phi}{\partial t} - \frac{1}{2}\rho |\vec{\nabla}\Phi|^2 \tag{4.1}$$

As the derivation of potential theory is thoroughly covered in several textbooks, it will not be discussed in detail in this literature review. However, in appendix A, the mathematical derivation of potential theory is given as discussed in this literature review. Formally, one would use a potential function of the same order as the highest-order force that needs to be determined. This is done in order to consider all coupling terms present in the equation. As will become evident in section 4.2.4, loads up to the second are required for analysis. Hence, the considered potential function is built up from a first and second-order potential. Substituting this into the non-linear Bernoulli equation results in various pressure contribution terms varying from 0^{th} - 4^{th} order terms. Terms above 2^{nd} order are to be neglected. This results in the following pressure, where X denotes the displacement vector;

$$p = -\rho g \left[X_3^{(0)} + X_3^{(1)} \right] - \rho \left[\varepsilon \frac{\partial \Phi^{(1)}}{\partial t} + \varepsilon \vec{X}^{(1)} \cdot \varepsilon \vec{\nabla} \frac{\partial \Phi^{(1)}}{\partial t} + \varepsilon^2 \frac{\partial \Phi^{(2)}}{\partial t} \right] - \frac{1}{2}\rho |\varepsilon \nabla \Phi^{(1)}|^2 \tag{4.2}$$

In order to calculate the load this pressure exerts on a body, equation (4.3) and equation (4.4) must be applied for force and moments, respectively.

$$\vec{F} = -\iint_S p \cdot \vec{n}\, dS \tag{4.3}$$

$$\vec{M} = -\iint_S p \cdot \left(\vec{r} \times \vec{n}\right)\, dS \tag{4.4}$$

The double integral seen in equations (4.3) and (4.4) over wetted surface S considers area A and a vertical component due to the instantaneous wave elevation $\zeta(t)$. The contribution due to the dynamic wave elevation can be considered a linear superposition over constant part S_0 up to the static waterline and an oscillating part s describing the intermittent wetting zone.

This allows for the integral in equation (4.3) and equation (4.4) to be rewritten. In order to reduce perceived clutter, only the equation for force is shown. The product with $\vec{n}$ needs to be replaced with $\left(\vec{r} \times \vec{n}\right)$ in order to calculate moments.

$$\begin{aligned}\vec{F} = &\int_{-S_0}^{0} \Bigg[\underbrace{\rho g X_3^{(0)}}_{0^{th}\text{ Order}} + \underbrace{\varepsilon\rho\left(g X_3^{(1)} + \frac{\partial \Phi^{(1)}}{\partial t}\right)}_{1^{st}\text{ Order}} + \underbrace{\rho\left(\varepsilon \vec{X}^{(1)} \cdot \varepsilon\vec{\nabla}\frac{\partial \Phi^{(1)}}{\partial t} + \varepsilon^2 \frac{\partial \Phi^{(2)}}{\partial t} + \frac{1}{2}|\varepsilon \nabla \Phi^{(1)}|^2\right)}_{2^{nd}\text{ Order}} \Bigg] \cdot \vec{n}\, dz \\ + &\int_{0}^{s} \Bigg[\underbrace{\rho g X_3^{(0)}}_{1^{st}\text{ Order}} + \underbrace{\varepsilon\rho\left(g X_3^{(1)} + \frac{\partial \Phi^{(1)}}{\partial t}\right)}_{2^{nd}\text{ Order}} + \underbrace{\rho\left(\varepsilon \vec{X}^{(1)} \cdot \varepsilon\vec{\nabla}\frac{\partial \Phi^{(1)}}{\partial t} + \varepsilon^2 \frac{\partial \Phi^{(2)}}{\partial t} + \frac{1}{2}|\varepsilon \nabla \Phi^{(1)}|^2\right)}_{3^{rd}\text{ Order}} \Bigg] \cdot \vec{n}\, dz\end{aligned} \tag{4.5}$$

As can be seen, the introduction of a time-varying function in the upper bound of the integral increases the order of the source terms by one. This results in the total hydrodynamic load due to the incoming wave being a superposition of 0^{th}-3^{rd} order terms. Each contributing term in equation (4.5) will be discussed in the sections below by order of the term.

4.2.1. Hydrostatics

The 0^{th} order term considers the hydrostatic contribution. Hydrostatics considers the pressure loading due to a fluid at rest. The first term in Bernoulli's equation equation (4.1) considers the static pressure. This pressure contribution in the fluid is only affected by the depth of the fluid z. As the fluid is non-viscous, it cannot exert any shear stress on the submerged structure. Therefore, the loading component is normal to the surface.

Apart from applying a load to the submerged structure, the hydrostatic pressure dictates the buoyancy of a floating object. If the platform is considered a rigid body, the hydrostatic contribution to the system stiffness follows from waterline geometry, the centre of buoyancy and the centre of gravity [13]. Section section 5.2.4 will provide more information about the hydrostatic stiffness matrix.

4.2.2. First-order hydrodynamics

First-order potential flow theory, based on the previously described linear wave theory, is able to determine dominant wave loading on offshore structures [45]. These first-order wave forces are linearly proportional to the wave height ζ_a and are of the same frequency as the incident wave [115].

The first-order wave force contribution can be expressed as shown in equation (4.6). The first term is a cross-term between hydrostatic pressure and the oscillatory component of normal vector $\vec{N}$. The second term is the first-order potential contribution to the first-order force. The final term presented is the time-varying buoyant force due to the varying wave elevation, which is equal to zero.

$$\vec{F}^{(1)} = \int_{-S_0}^{0} \left[\varepsilon\rho g X_3^{(1)} + \varepsilon\rho\frac{\partial \Phi^{(1)}}{\partial t}\right] \cdot \vec{n}\, dz + \int_{0}^{s} \cancel{\rho g X_3^{(0)}} \cdot \vec{n}\, dz \tag{4.6}$$

The aforementioned first-order potential contribution to the first-order force can be broken down further into its components. One of the previously defined assumptions of linear analysis means that the total force can be considered as the sum of separate loading sources. This assumption is applied

when the wave loading and motion response are decoupled [145]. As the forces on the structure due to its motion response are assumed independent of the wave, and the forces on the structure due to the wave are independent of the motion response. Faltinsen is able to visualise this in figure 4.5 below, showing that the excitation loads can be considered by evaluating the loads when constraining the structure, whereas the radiation loads can be evaluated for the waves radiating from the body for a forced oscillation.

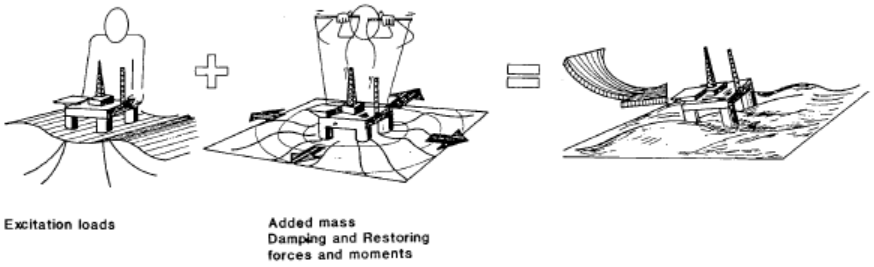


Figure 4.5: Total loading can be considered as a superposition of linearly decoupled excitation and radiation sources ([45, p. 40]).

Therefore, the potential contribution to the total first-order hydrodynamic load can be expressed as the sum of the force due to the incident wave (F_w), diffraction force (F_d) and radiation force (F_r), which will be discussed individually below.

$$\int_{-S_0}^{0} \rho \frac{\partial \Phi^{(1)}}{\partial t} \cdot \vec{n}\, dz = \vec{F_{exc}} + \vec{F_R} = \vec{F_w} + \vec{F_d} + \vec{F_r} \tag{4.7}$$

4.2.2.1 Froude-Krilov

Forces due to incident waves are very easily evaluated [99]. The Froude-Krilov force contribution is the force due to the pressure in the fluid, assuming the fluid is not affected by the presence of the ship [145]. In reference to equation (4.8) this contribution can be isolated to;

$$\vec{F_w} = -\int_{S_0} \rho \frac{\partial \Phi_w}{\partial t} \cdot \vec{n}\, dS \tag{4.8}$$

Here we consider the potential of the incoming wave Φ_w as the potential of the undisturbed incoming wave.

4.2.2.2 Diffraction

The diffraction potential represents a correction to the abovementioned Froude-Krilov force from section 4.2.2.1 to account for the fact that the fluid is disturbed by the presence of the structure [145]. In order to satisfy the boundary condition of the hull being watertight the incoming fluid velocity normal to the hull must be equal and opposite to the 'outgoing' fluid velocity of the diffracted wave. In A.8, the origin of this boundary condition is derived.

$$\frac{\partial \Phi_w}{\partial t} + \frac{\partial \Phi_d}{\partial t} \left(= \frac{\partial \Phi_0}{\partial t} + \frac{\partial \Phi_7}{\partial t} \right) = 0 \tag{4.9}$$

As the potentials in equation (4.9) are time and space-dependent, the unknown potential cannot be directly solved. Just as for the radiation potential, Φ_0 and Φ_7 need to be split up into a time and space-dependent part. These time-dependent parts can simply be eliminated against one another, resulting in;

$$\frac{\partial \phi_0}{\partial t} = -\frac{\partial \phi_7}{\partial t} \tag{4.10}$$

Where ϕ_0 is the space-dependent part of the undisturbed incoming wave potential and ϕ_7 is the unknown space-dependent part of the diffracted wave potential. This unknown space-dependent component is to be solved separately and is explained in appendix A.2.

4.2.2.3 Radiation

The radiation force contribution follows from the force exerted on the structure due to its motion response to the incoming wave. This force follows from the radiation potential Φ_r, describing the dynamics of the fluid due to the response motion. To visualise this, one can consider the situation where external forcing causes a body to move. This movement induces a *radiating* wave in the surrounding fluid, dissipating energy from the system and can be denoted as shown in equation (4.11) for all six degree of freedom (DOF). It is not possible to directly solve for a time and space-dependent potential. Instead, it needs to be separated into a separate time and space-dependent variable for each degree of freedom [70].

$$\Phi_r(x,y,z,t) = \sum_{j=1}^{6} \Phi_j(x,y,z,t) = \sum_{j=1}^{6} \phi_j(x,y,z) \cdot v_j(t) \tag{4.11}$$

As previously defined, the flow potential is a mathematical expression whose derivative in any direction equals the flow velocity in that direction. Hence, the normal velocity to the surface of the structure can be rewritten as:

$$\frac{\partial \Phi_r}{\partial n} = \sum_{j=1}^{6} \frac{\phi_j}{n} \cdot v_j(t) \tag{4.12}$$

The solution for the unknown potential is described in appendix A.2 as the methodology is largely the same.

4.2.3. Second-order hydrodynamics

Floating objects are also subject to second-order, mean, low-frequency and high-frequency wave forces proportional to the square of the wave height ζ_a^2. When subject to these forces, a floating object will perform a slow and steady drifting motion in the direction of wave propagation, hence known as the wave drift force [115]. One of the primary functions of a mooring system is to offset this force in order to keep a floating object in place (stationkeeping). It has been demonstrated that the dynamic component of the wave drift force could excite large amplitude motions of a moored structure in irregular waves [115], resulting from the interaction between two waves of frequencies outside of the wave excitation range [13]. These components carry frequencies $2\omega_1, 2\omega_2, \omega_1 \pm \omega_2$. Isolating the second-order contributions from equation (4.5) results in equation (4.13). It is relevant to note that the second-order potential is composed of the same components as the first-order potential, being wave and diffraction excitation forces and radiation forces. The second-order radiation potential may be disregarded [70]. The hydrostatic pressure contribution at the oscillating surface is also equal to zero and can be disregarded [70].

$$\vec{F}^{(2)} = \int_{-S_0}^{0} \rho \left(\varepsilon \vec{X}^{(1)} \cdot \varepsilon \vec{\nabla} \frac{\partial \Phi^{(1)}}{\partial t} + \varepsilon^2 \frac{\partial \Phi^{(2)}}{\partial t} + \frac{1}{2} |\varepsilon \nabla \Phi^{(1)}|^2 \right) \cdot \vec{n}\, dz + \int_{0}^{s} \varepsilon \rho \left(g \cancel{X_3^{(1)}} + \frac{\partial \Phi^{(1)}}{\partial t} \right) \cdot \vec{n}\, dz \tag{4.13}$$

This formulation shows a clear distinction between the in and out-of-phase contributions, denoted by P and Q, respectively. The superscript $^-$ and $^+$ also indicated the high and low frequency or sum and difference frequency terms.

$$\begin{aligned} F^{(2)} = &+ \sum_{i=1}^{N} \sum_{j=1}^{N} \zeta_i \zeta_j P_{ij}^{-} \cos\left(\left(\omega_i - \omega_j\right) t + \left(\epsilon_i - \epsilon_j\right) \right) \\ &+ \sum_{i=1}^{N} \sum_{j=1}^{N} \zeta_i \zeta_j Q_{ij}^{-} \sin\left(\left(\omega_i - \omega_j\right) t + \left(\epsilon_i - \epsilon_j\right) \right) \\ &+ \sum_{i=1}^{N} \sum_{j=1}^{N} \zeta_i \zeta_j P_{ij}^{+} \cos\left(\left(\omega_i + \omega_j\right) t + \left(\epsilon_i + \epsilon_j\right) \right) \\ &+ \sum_{i=1}^{N} \sum_{j=1}^{N} \zeta_i \zeta_j Q_{ij}^{+} \sin\left(\left(\omega_i + \omega_j\right) t + \left(\epsilon_i + \epsilon_j\right) \right) \end{aligned} \tag{4.14}$$

Where a first-order Response Amplitude Operator (RAO) approach considers the response of a floating structure to an individual wave component, a Quadratic Transfer Function (QTF) considers the contribution of a pair of waves. Depending on the resonance frequency of the moored structure, either the sum or difference frequencies are of importance. For a catenary moored system, the stiffness and, hence, the resonance frequencies are expected to be low, resulting in the low-frequency difference frequencies being of particular interest. For a TLP moored structure, the stiffness and resonance frequencies are expected to be high, and hence the high-frequency sum frequency forces are important [45, 97, 115, 103]. Just as with the first-order potential problem, the above formulation for the second-order loading is solved using diffraction software, resulting in equation (4.14). These pieces of software employ one of the following three methods presented in decreasing included detail and computational load.

4.2.3.1 Near field method

The near field method is the most computationally expensive method but is able to calculate the entire QTF matrix by evaluating equation (4.13) at the boundary of the surface. This method calculates all components of the QTF matrix in all 6 degrees of freedom but has poor mesh convergence properties. Proper application of this method requires highly refined mesh near the mean free surface and sharp corners to converge, more so than required for first-order analysis [43]. This means that for practical purposes, two sets of meshes are required to conduct near-field analysis efficiently.

4.2.3.2 Middle field method

The middle-field method is derived from the far-field method and uses a variant of Stoke's theorem [35]. It also applies the conservation of momentum but for a finite volume bounded by the body, free surface and outer wall. The outer wall can be set at a finite distance from the surface but also infinitely far from the body surface. Unlike the far-field method, the middle-field method can be used to calculate the high and low-frequency components of the second-order drift force. This method is able to calculate the QTF matrices for all 6 degrees of freedom with a more stable and superior mesh convergence than the near-field method. In this situation, stability refers to the sensitivity of the final result to the roughness of the input mesh [35].

4.2.3.3 Newman approximation

Full QTF data is not always available for all wave component directions and frequencies, and calculating them is highly computationally expensive. The approximation derived by Newman [107] addresses this issue. Using the diagonal terms of QTF matrices for wave pairs of equal direction, the off-diagonal terms representing unequal wave directions and frequencies can be estimated [111]. Experiments have shown that this approximation yields accurate results for deep water but underestimates forces in shallow water [114].

4.2.3.4 Far field method

The fastest and simplest method to determine part of the QTF matrices is using the far field method. As the name may suggest, the far-field method is evaluated far away from the object. This method considers the contribution to the rate of change of momentum through all boundaries of the control volume bounded by the free surface, the body boundary and the wall of an infinitely large cylinder [145]. This method is only suitable to calculate the diagonal terms of the QTF matrices and is hence only applicable to the mean wave drift force [145].

4.2.3.5 Viscous effects

The above derivation of the second-order hydrodynamic force contribution shares the same assumptions as the potential theory used to derive said forces. This means that no viscous effects are included. Faltinsen [45] states that as wave drift forces become small, viscous effects become increasingly more important. This is especially important for slender, surface-piercing structures, such as semi-submersibles or TLPs. This is because although the waves are considered small, their amplitude is relatively large compared to the cross-sectional dimensions of the hull [45]. These effects can be taken into account using Morison's drag term [13, 45].

$$F_d = -\int_S \rho C_D V_r |V_r| \, dS \tag{4.15}$$

4.2.3.6 Springing

A previously undiscussed phenomenon associated with second-order loading in TLP-type structures is springing. There does not seem to be a consensus on the most important forcing mechanism for ringing, which comes from second, third, fourth, or even infinite-order wave load effects. This is one of the reasons why studying ringing is difficult. Springing is a steady state response in vertical and/or bending modes of the tendons caused by the continuous excitation from high-frequency first-order wave components and sum frequency terms [53]. Most of the research conducted on springing in TLP considers Oil & Gas (O&G) application, which is distinctly different from FOWT due to the lack of a turbine attached to the structure. It needs to be considered that the presence of the WTG reduces the resonance frequency of the total structure due to the added damping due to the turbine, especially in operational conditions. This reduction of resonance frequency may put it in the range of first-order wave excitation. In section 4.1.2 it was demonstrated that when operational, the turbine introduces a significant component of damping to the dynamic system. In engineering practice, it is accepted that the most critical source of springing comes from the second-order sum frequency excitation [50]. Due to the continuous nature of springing, it is an essential component in tendon design for long-term fatigue resistance [50]. As springing is highly local to the tendons, it is not necessary to consider for structural design.

4.2.4. Third-order hydrodynamics: Ringing

When considering a velocity potential consisting of first and second-order terms, the third-order hydrodynamic loading can be expressed as a function of a set of terms evaluated in the splash zone of the structure. If potential were to be considered, including a third-order part, $\vec{F}^{(3)}$ would also consist of a component on the mean submerged area. However, as will become evident in this section, it is not necessary to include this level of complexity. Isolating the third order terms from equation (4.5) results in the expression below;

$$\vec{F}^{(3)} = \int_0^s \rho \left(\varepsilon \vec{X}^{(1)} \cdot \varepsilon \vec{\nabla} \frac{\partial \Phi^{(1)}}{\partial t} + \varepsilon^2 \frac{\partial \Phi^{(2)}}{\partial t} + \frac{1}{2} |\varepsilon \nabla \Phi^{(1)}|^2 \right) \cdot \vec{n} \, dz \tag{4.16}$$

In engineering practice, third-order loading is not used in dynamic analysis but is of importance in tendon fatigue analysis.

Ringing is a transient response in the vertical and/or bending modes at frequencies substantially higher than the incident wave frequencies [45] and is only observed in severe sea states during the passing of high, steep waves. Gurley has also demonstrated that ringing was not a result of first-order resonant effects [53]. Bachynski also demonstrated that viscous effects had a negligible effect on ringing response but did note that the influence of the added damping of the turbine could be important to consider [12]. Ringing is an important phenomenon to consider in tendon design due to the high loads induced in the mooring lines; it is, however, not an important phenomenon to consider for fatigue as it is a response to rare events and hence does not contribute to fatigue.

4.2.5. Morison's formulation

As an alternative to potential theory, Morison's formulation is also available to determine the hydrodynamic loading on a structure in waves and unlike potential theory, is able to capture viscous force contributions. Morison's formulation is valid for slender structures such that the incoming wavelength λ is large relative to a characteristic dimension D of a structure. For a TLP, for example, D can be considered the diameter of the surface piercing column and $\lambda > 5D$ [13, 45]. It was initially specifically developed for circular structures but can be adapted to different shapes.

Morison's equation can be modified for a moving circular cylinder as follows [45, p. 255];

$$f = \underbrace{\frac{\rho \pi D^2}{4} \dot{u}}_{\text{Froude-Krilov}} + \underbrace{\frac{1}{2} \rho C_D D (u - v)|(u - v)|}_{\text{Viscous drag}} - \underbrace{(C_m - 1) \frac{\rho \pi D^2}{4} (\dot{u} - \dot{v})}_{\text{Inertia}} \tag{4.17}$$

Where u and v are the undisturbed incoming particle velocity and body velocity, respectively, expressed in the global axis system. C_M and C_D are the inertia and drag coefficients. Equation 4.17 also

remains valid for inclined members by decomposing the incident flow velocity into a tangential and normal component to the cylinder. The tangential component can be used in the above formulation, and the normal component is disregarded [45].

From the above, Morison appears to be a very promising approach to calculated forces on the structure. However, the condition of $\lambda > 5D$ may pose a large problem, depending on site location. In order to quantify this, we can explore how much of the dynamic environment can be modelled using Morison's formulation. As the surface piercing column has a constant diameter $D = 11$m, the smallest allowable wave number $k = 2\pi/\lambda = 0.1142$ rad/m. Applying the dispersion relation allows for the shortest wave incident on the structure that can be resolved.

$$\omega = \sqrt{kg \tanh(kh)} = 1.059 \text{ rad/s}, \quad T = 5.93 \text{ s} \tag{4.18}$$

Considering the wave environment at the base case location, a scatter plot quantifies the fraction of the wave environment. Only 61% of waves have a longer period than 5.93s and can be modelled using Morison's formulation, assuming static conditions.

A FOWT, however, cannot be considered static. Although the lower for Morison's formulation is defined as $\lambda > 5D$, the actual limit is defined by the flow regime downstream of the tubular member, which must be laminar and attached. For higher λ/D ratios, the flow may start to detach or become turbulent (or both) [70], and hence Morison's wave force formulation becomes less accurate. Apart from increasing the diameter, it is also possible to increase flow detachment or turbulence by increasing the perceived velocity of the fluid. Wave height, current and structure motions influence this perceived velocity. As the FOWT substructure moves in the water, the flow velocity increases and may detach or become turbulent.

Another issue posed by the use of Morison's formulation is that loads it was meant for cylindrical shapes. Other geometries may be considered by applying a representative mass (C_m) and drag (C_D) coefficient to the structure [70]. Forces are calculated at discrete nodes along the axial direction of a structure and are hence mapped onto discrete points along a line. This poses the issue as the total forces on a section are lumped on a single point. This means any force distribution along the chord of a section is completely lost and cannot be recovered. To place this in the context of the problem presented in this literature review, this is not an issue for a motion solver, but if the local loading of a submerged structure needs to be resolved, Morison's formulation provides no representative solution.

In conclusion, the aforementioned limit of Morison is a very optimistic estimate, resulting in Morison's formulation being applicable in less than 61% of simulated scenarios. Of this reduced number of scenarios, Morison's formulation does not provide enough detail to resolve the local loading of the submerged structure.

4.2.6. CFD

CFD presents another alternative method to calculate hydrodynamic loading. CFD inherently takes viscous effects into account and allows for all of the considered forces discussed above to be taken into account in all six degrees of freedom for a fully coupled system. CFD also allows for normal and tangential force components to be evaluated and allows for accurate simulation of the air-water fluid boundary. Other effects, such as vorticity in the flow, can also be modelled using CFD, unlike the aforementioned potential theory and Morison methods. This is done by directly solving the Navier-Stokes and continuity equations [88, 121]. In order to accurately simulate a FOWT using CFD, fine hydro- and aerodynamic meshes and small timesteps are required in order to allow for the simulation to converge. This inherently makes the simulations incredibly computationally expensive. This is also reflected in the pricing of CFD software licences. Due to this, most of the research on FOWT conducted using CFD approaches considers regular waves instead of irregular wave conditions [121]. Aligned wind-wave conditions are also often applied.

Although CFD application in coupled dynamic FOWT seems to yield the most accurate results, it is the computational load and shortcomings of regular wave conditions that justify abandoning further review in this method as an application in multiaxial loading does not appear fruitful at this time.

4.2.7. Vortex induced oscillations

When a fluid flows over a structure, an unsteady flow pattern due to vortex shedding may emerge [11, 70]. This change in flow pattern introduces a dynamic lift component that oscillates over the body, causing the structure to oscillate in a direction crosswise to the flow and is hence referred to as vio. This oscillatory response can be divided into excitation of the rigid body motions vortex induced motions (vim) and structural vibrations vortex induced vibrations (viv).

DNV states that it should be included when considering coupled analysis for FOWT [9, p. 50]. DNV continues by stating that as these conditions are not considered by the models applied, they must be evaluated separately and disregarded if it is demonstrated that vim is unlikely to occur at the installation site.

4.3. Mooring loading

In a dynamic environment such as the ocean, a floating structure is subject to wind, wave and current loads. A mooring system is designed to keep a floating structure on the station in order to allow for onboard activities to occur safely [93]. For FOWT applications, the allowances are governed by the bending restriction of the electrical export cable and the nacelle accelerations due to dynamic actions of the platform [93]. Mooring of FOWT takes shape after the vast experience from O&G and hence adopts the same mooring types. Next, the construction of tendons and their properties will be discussed in section 4.3.1 before an in-depth review of mooring modelling techniques in section 4.3.2. In section 4.3.3, the discussed theory will be applied to TLP mooring in order to formulate an approach. Finally, in figure 4.7 a multiaxial loading mechanism specific to TLP mooring that is not symmetrical to the pontoon's longitudinal axis of symmetry.

4.3.1. Tendon construction

Mooring tendon lines may be constructed from different materials and take on different weaving patterns. The material choices are limited to steel and synthetic fibres but may also exist in a combination of both, allowing for the tendon characteristics to be tuned [70, 93]. For the scope of this investigation, only mooring line angle and mooring line stiffness are required for the analysis, as will become evident in section 4.3.3.

Relevant to note is that depending on the type of construction of the mooring line, the tension in the line can induce a torsional moment in the line. This has implications for the connection point between the line and the pontoon. As the scope of this investigation excludes this mating point, the multiaxial response will not be investigated at this location. Relevant to note is that the optimal design of this interface can resolve multiaxial stress response issues. An investigation of this nature will be recommended for further analysis.

4.3.2. Tendon modelling

As with aerodynamic and hydrodynamic loading, there are also multiple ways of modelling TLP mooring, allowing for various levels of detail. There are two approaches when considering dynamic mooring modelling: linear and non-linear. Jain states that linear analysis is cheap and easy but has a major drawback that any non-linear effects are neglected [65]. Therefore, one must be certain that the system is linear when applying this approach. Alternatively, a non-linear approach may be used, of which the drawback is that it needs to be conducted in the time domain. These approaches will be discussed one by one. For linear approaches, these are static analysis in section 4.3.2.1 and quasi-static analysis in section 4.3.2.2. Next, the non-linear approaches quasi-dynamic in section 4.3.2.3 and dynamic analysis in section 4.3.2.4 will be discussed.

4.3.2.1 Static

Static models only consider constant loads such as gravity, buoyancy, constant current and wind and the mean wave drift force. A static model derives equilibrium between external loads and restoring forces due to the mooring at each time step but does not consider the process between timesteps. This type of model usually applies a single set of springs to represent the mooring. Static analysis is often useful for conceptual design or to identify aspects for further analysis for structures in the harbour or benign offshore conditions, where waves are not critical [37, 80]. However, due to the availability of more sophisticated mooring analysis software, this method is no longer common practice. This approach is

not suitable for coupled dynamic analysis.

4.3.2.2 Quasi-static

The quasi-static method assumes that the system moves in a linear manner between two static positions in time. The mooring line shape and tension are derived from analytical formulations. Using an iterative process, the state of the system can be solved. Although more detailed than the static analysis, dynamic effects such as added mass and damping due to the acceleration of fluid surrounding the mooring line are ignored [37, 80]. Although these effects do influence the response of the moored system, Jonkman argues this is justified as the typical weight of a mooring system is about 8% of the total mass of the floater, tower and RNA for a catenary moored system. From experience [69], only about 25% of the inertia of the mooring system delivers a contribution to the dynamic response of the system. This means that the total contribution of the mooring system inertia to the dynamic response is 2%, which justifies ignoring the mooring system inertia. As a tensioned leg mooring configuration is lighter and stiffer, the damping and inertia contributions are likely even smaller.

4.3.2.3 Quasi-dynamic

The quasi-dynamic models each line as a single DOF non-linear spring-dashpot and is hence able to include drag and inertia forces on the lines, both due to material and geometric as well as line motions. Due to the inclusion of non-linearities in the system, this method is bound to the time domain. This method includes all six DOF [80] and uses precalculated RAO for the vessel motions and fairlead loads based on the position and orientation of the floating structure. It, therefore, includes hydrodynamics (including added mass and damping), wave drift, current, wind and mooring loads [80].

4.3.2.4 Dynamic

Dynamic modelling solves Newton's second law of motion in time and allows for non-linearities in all terms of the equation of motion as discussed in section 5.2. For coupled dynamic mooring analysis, all dynamic loads for the mooring system, as well as the vessel motions, are considered. This type of analysis is particularly important in deep water due to the long mooring lines and high mass of the mooring system. As the shape of the mooring line may be challenging to formulate analytically, the line must either be linearised or discretised. The two types of spatial discretisation are discussed below.

Lumped mass

The lumped mass approach lumps all effects due to mass, external force and internal reactions at a finite number of nodes per mooring line. Hence, each mooring line is divided into n segments and $n+1$ concentrated nodes (lumped masses), which are connected by spring dashpots. The shape of the line is assumed from the position of the fairlead with respect to the anchor [37, 149].

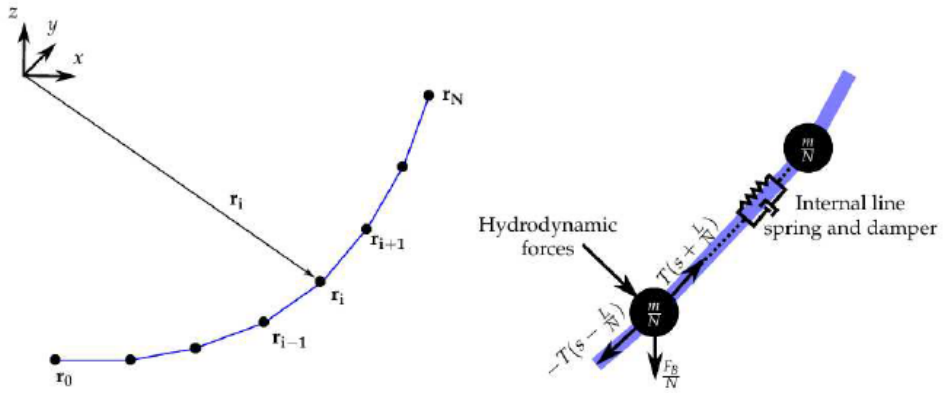


Figure 4.6: Depiction of the discretisation of the continuous mooring line into lumped masses[37, p. 21]

Finite Element Method

The Finite Element Method (FEM) method also discretises the mooring line into n segments but sets itself apart by analytically integrating over each element [37, 73]. Each line segment is subject to its own

weight and external forces due to wave or current-induced water flow, and motion is determined using Morison's formula or CFD. These forces and moments are denoted with M_i and f_i. As mooring lines are extremely slender structures, the stress inside the cable will be dominated by axial stresses, and thus bending stress can be neglected [54], this simplification results in a few degrees of freedom being ignored. Each element will have potential energy such as strain energy due to torsion, kinetic energy, external work and length constraint. Solving the potential of this system for the minimum energy will lead to the nodal displacement of each node.

Interesting to note is that Davidson states that a FEM analysis requires fewer nodes to reach accurate results compared to the lumped mass approach; however, no claims on computation time are made [37].

4.3.2.5 Coupled and uncoupled

In the same way that the aerodynamics and floating structure are intrinsically coupled, the floating structure and its mooring are intrinsically coupled as well. In an uncoupled analysis, the dynamics of the floating structure and the mooring system are calculated separately and superposed over each other [37]. The uncoupled analysis does offer reduced complexity and superior numerical stability [37]. For a coupled dynamic analysis, a solver iterates over the mooring lines until a compatible solution is reached. This has to be done for every timestep. Omberg and Larsen were one of the first to implement coupled analysis and concluded that uncoupled analysis was prone to severely underpredict mean offset and overpredict low-frequency motions, especially in deep water [112]. This dependency on coupled analysis in deep water is due to inertia in the mooring line for extended length, as the bottom of the mooring line does not immediately feel loading at the top of the line. This effect is mainly applicable to catenary mooring, which is not considered for TLP application.

4.3.3. TLP mooring analysis

Having defined and briefly described the different modelling approaches for offshore mooring a closer look may be taken at the applied methodology of different works on TLP analysis. Table 4.1 below shows an overview of work done in dynamic FOWT analysis. All considered analyses were for coupled mooring and hydrodynamic analysis.

Table 4.1: Overview of mooring modelling and analysis methods in the literature, compiled from various sources

Author	Year	Source	Stucture type	Static	Quasi-static	Quasi-dynamic	Dynamic Lumped Mass	FEM
Jain	1997	[65]	TLP		x			
Chen	2006	[32]	TLP					x
Robertson	2011	[124]	TLP		x			
Kvittem	2012	[75]	SS					x
Bae	2013	[15]	TLP					x
Ren	2014	[121]	TLP			x		
Bachynski [1]	2014	[13, 12]	TLP		x			x
Nematbakhsh	2015	[106]	TLP					x
Shen	2016	[127]	TLP				x	
Lui	2017	[88]	SS					x
Ren	2022	[122]	TLP		x			
Ren	2023	[123]	TLP		x			

As can be seen from table 4.1, the quasi-static approach is not applied in dynamic FOWT analysis, for obvious reasons, as discussed in section 4.3.2.1. The quasi-dynamic and lumped mass approaches are rarely used for TLP approaches. This is likely as quasi-dynamic and lumped mass approaches make more sense for simplified time-domain calculations of catenary mooring due to the shape of the mooring line requiring it to be solved. Although superior, FEM analysis may be too computationally expensive for large catenary moored simulations. However, as TLPs have highly loaded tendons, the shape of the tendon may be approximated as a straight line [12, 13, 127]. For FEM analysis, this provides a close solution to the actual line form, thus requiring relatively few iterations to solve for the line shape

[1] The work of Bachynski considered a comparison between linear and non-linear analysis, and hence two modelling methods were used

for every time step. Although solving for the line shape also needs to be done for quasi-dynamic and lumped mass approaches, FEM analysis provides better tension results in the lines. This is especially important for tendon design. FEM also allows for easier integration of the power export cable into the dynamic model. The importance of including this component is not established

The above conclusion based on table 4.1 does not explain the number of publications using quasi-static models. It has been established that the tendons may be considered straight lines and that TLPs receive their restoring force from the elastic properties of the tendons. Hence, as long as the tendons are loaded in the elastic region of the stress-strain curve the tendons effectively behave as springs. Operating under this set of assumptions, quasi-static models appear to do a very good job of representing the mooring systems as an alternative to the more computationally expensive time domain dynamic methods. This conclusion is confirmed by DNV in the guide for coupled analysis [9].

The limitations of quasi-static mooring models are as follows:

- **Slack line events:** When the tension in the line becomes negative, a spring can provide a restoring force. A line, however, does not have this ability, and hence, the mooring line will become slack. This is a huge issue as once the mooring line becomes loaded once again, it will snap into place, issuing a shock load to the system.
- **Tendon overload:** When the tendon is overloaded into the plastic region of the stress-strain curve, the line does not break. As with any material, plastic deformation will take place before fracture. In a highly loaded tendon, this deformation causes the tendon to extend in length, thus reducing the tension in the line and creating an imbalance in the mooring response. Theoretically, this can be solved by re-tensioning the affected mooring line. However, a tensioner must be on board the structure, which may not be the case [93].

4.3.4. Mooring induced torsion

In this section, a scenario will be sketched, which requires some imagination from the reader. Take the Bluewater TLP as an example, where each pontoon has two mooring lines mounted symmetrically but out of line with the pontoon axis of symmetry. A situation may arise where the two mooring lines on a given pontoon are not under equal tension, for example, when the platform rotates about the axis of symmetry of a pontoon. If one decomposes each of the mooring vectors into the outer-facing plane (denoted in purple in figure 4.7), it becomes evident that the greater force contribution of one of the mooring lines results in a net torsional moment applied over the cross-section. This will in turn induce a torsional moment in the cross-section and the critical weld joining each pontoon to the central column. This process is described in figure 4.7.

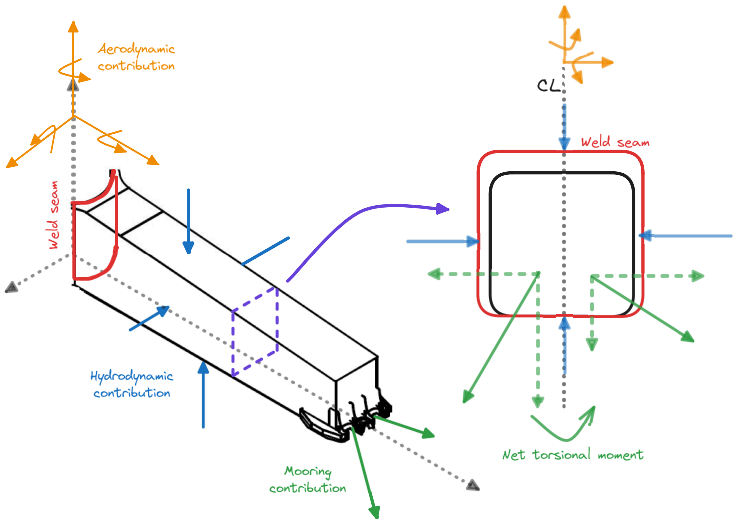


Figure 4.7: Situation in which mooring lines are not equally loaded on a given pontoon, resulting in a net torsional moment applied to the pontoon, as well as the weld seam.

5

Motions & Response

According to our laws of physics, any object subject to an external influence will react to said influence. The quantification of these loads was extensively discussed in chapter 4. Under the influence of these loads, the structure reacts by displacing at a global level and a local level. This chapter will clearly distinguish between motions and response, where motions consider dynamic displacements of the structure, whereas response will consider the structural (stress) response to external loading.

In this section, it will first be established why a FOWT system must be considered as a coupled system in section 5.1. After this, two separate approaches are considered for the modelling of FOWT in wind-wave conditions in section 5.2 and section 5.3 followed by a combined approach of these two in section 5.4.

5.1. Coupled motion analysis

Literature about FOWT analysis often considers coupled motion analysis, implying there is also uncoupled analysis. The coupling referred to is the dependency or coupling of the hydrodynamic (floater and mooring) and aerodynamic (tower and RNA) components. The two sets of components are evaluated separately and do not affect one another. This approach is insufficient for FOWT applications as the components are strongly coupled [9]. DNV states two examples of this coupling effect [9]. The first is that forces on the turbine affect the floater motions as well, thus completing the feedback loop. The second is that the motions of the floater induce aerodynamic inflow on the rotor and introduce inertial loads on the turbine, which is confirmed in the work of Tran [137]. In this paper, the author demonstrated that for surge motions of the platform, the generated force on the blades and the power output was unsteady. This was in part contributed to the turbine moving up and downstream due to the platform motions, but also due to the turbine interacting with its own wake more than a fixed turbine [137]. This unsteady force component may be of special relevance to multi-axial fatigue, as will be discussed in section 6.2 where non-proportionality of loading and response will become evident.

The importance of considering a FOWT system as coupled partially depends on the type of substructure. However, DNV explicitly states that due to the strong coupling of rigid body motions and tower structural modes, TLPs must be considered as a coupled system [9].

Within coupled analysis, there is also a distinction to be made between fully (strongly) coupled and loosely (weakly) coupled [98, 119]. In the literature, there appears to be an inconsistency in the use of the term, where fully coupled is used to indicate that aerodynamics, hydrodynamics and mooring have all been included in the analysis. Formally speaking, fully or loosely coupled refers to the degree of coupling between models. Matthies [98] explains this difference anecdotally using an example familiar in the offshore field, Fluid Structure Interaction (FSI). Some solvers can determine the sub-problems separately (i.e. fluid and structure). One wants to couple these solvers to prevent having to reinvent the wheel. Solving the problem by separately solving the sub-problems results in a loosely coupled system. For a fully coupled system, the system components must be evaluated at the same time, often requiring iterative methods and hence adding to the computational expense [98]. Ramachandran applies a fully

coupled approach to FOWT by solving all of the system matrices in a single equation at once [119]. All of the other literature reviewed applies a loosely coupled system, as existing solvers for the different components are put together.

5.2. Rigid body formulation

This literature review has concluded that the dynamic behaviour of a FOWT TLP is dominated by aerodynamic, hydrodynamic and mooring loads. The response to these forces is complex and contains non-linearities and hence cannot be represented by a linear model, and must be solved in a time-domain [70, 127]. This also has implications for the formulation of the equation of motion. Cummins derived a direct solution to the equations of motion as a function of time [34]. This model is known as the Cummins equation and takes the form as shown in equation (5.1).

$$(\mathbf{M} + \mathbf{A})\,\ddot{\vec{X}} + \int_0^\infty \mathbf{B}(\tau) \cdot \dot{\vec{X}}(t-\tau)\,dt + \mathbf{C}\vec{X} = \vec{F}(t) \tag{5.1}$$

Where $\vec{X}$ is the motion vector containing the rigid body response in the six considered degrees of freedom. In equation (5.2) it can be seen that two types of notation may be used interchangeably to denote a response in a particular degree of freedom, their order however will always remain as follows; surge, sway, heave, roll, pitch, yaw. An effort will be made to implement the latter notation, however, the first may be implemented to reduce perceived visual clutter from equations.

$$\vec{X} = [X_1(t), X_2(t), X_3(t), X_4(t), X_5(t), X_6(t)]^T = \left[x(t), y(t), z(t), \theta(t), \phi(t), \psi(t)\right]^T \tag{5.2}$$

When a fluid is disturbed, the effects of a disturbance during $(t_0, t_0 + \Delta t)$ affect the fluid at all later time intervals. This also applies to motions. This effect is captured by the term $\mathbf{B}(\tau)$ known as the retardation, or memory function [34, 110, 127]. The process of determining the matrices in equation (5.1) will be described in sections 5.2.1 to 5.2.4 below.

5.2.1. Potential added mass and damping matrices

The derivations for the added mass and damping matrices follow from the radiation contribution from the potential approach, as described in section 4.2.2.3. This allows for the frequency-dependent added mass and damping to be calculated as shown in equations (5.3) and (5.4) [70, 145].

$$a_{ij}(\omega) = -\Re\left[\rho \iint_{S_0} \phi_j n_k \cdot dS_0\right] \tag{5.3}$$

$$b_{ij}(\omega) = -\Im\left[\rho\omega \iint_{S_0} \phi_j n_k \cdot dS_0\right] \tag{5.4}$$

All variables on the right-hand side are either known or can be derived using a potential solver. If the above is repeated for all ω in wave spectrum $S(\omega)$, a $6 \times 6 \times \omega$ matrix for a and b will be produced describing the coupled response for all incident wave frequencies.

5.2.2. Inertia contribution

The mass matrix is the simplest matrix to form and directly takes shape from the substructure, tower and RNA mass and inertia and centre of gravity.

Determining the added mass directly through the potential is quite complex, Ogilvie derived a solution for this based on existing frequency domain calculations [110]. This method allows for the matrices **A** and **B** to be determined based on the hydrodynamic added mass and damping. Without diving into the mathematical derivation, the results are presented below;

$$\mathbf{A} = a(\omega) + \frac{1}{\omega}\int_0^\infty \cancel{\mathbf{B}(\tau)\sin(\omega\tau)\,d\tau} = a(\omega = \infty) = \mathbf{A}^\infty \tag{5.5}$$

As this expression is true for all ω, the integral can be disregarded, and the hydrodynamic added mass can be evaluated at the high-frequency limit (HFL) according to equation (5.3) [70]. Notation varies between literature but is often denoted with a combination of matrix **A** and ∞ or HFL. Any added mass contributions above the waterline, in the air, are neglected. No literature was found that implemented

added mass of the structure above water. This is probably due to the much higher density of water than air. Thus, it is assumed that any added mass effects due to the displacement of air are negligible.

5.2.3. Damping contribution

Although there are multiple sources removing energy from the system in the form of damping, not all of these sources are quantified on the left-hand side of the equation. For this system, only hydrodynamic damping is included, consisting of a potential and viscous part. The aerodynamic damping will be included in the aerodynamic force, as calculated by the BEM model, as described in section 4.1.4. Although the mooring lines do carry a degree of damping, due to the modelling choice as quasi-static, mooring-induced damping cannot be included.

5.2.3.1 Potential damping

Without diving into the mathematical derivation, the Ogilvie solution for damping can be formulated as follows [110], resulting in a matrix sharing the same dimensions as $b(\omega)$;

$$\mathbf{B}_{\text{potential}}(\tau) = \frac{2}{\pi}\int_0^\infty b(\omega)\cdot\cos(\omega\tau)\,d\omega \tag{5.6}$$

5.2.3.2 Quadratic damping

By means of experiments, Stewart has shown that quadratic damping due to viscous drag is important for low-frequency excitation, as for TLP structures, radiation damping decays to near zero [133]. In section 4.2.5, Morison's formulation for force was already discussed, as well as the importance of including the viscous force term. This term is referred to both as a viscous drag force term, as well as the quadratic damping term (due to it being proportional to the square of the velocity), depending on context. This is not a problem. However, this term must be included **either** in the left-hand side of the equation **or** the right-hand side of Cummins equation equation (5.1).

$$F_{\text{drag}} = B_{\text{visc}}\dot{\vec{X}} = \frac{1}{2}\rho C_D D(u-v)|(u-v)| \tag{5.7}$$

5.2.4. Stiffness contribution

Apart from the mass matrix, the stiffness matrix can also be determined directly, however, requires some extra computational effort as the stiffness matrix is entirely dependent on the shape of the submerged body. The buoyancy of the TLPWT is larger than its weight. It is pulled downwards into the water by tendons which are fixed to the seabed. Together, the weight and the tendon tension equilibrate the buoyancy [13, 70]. Formally, for ships, the stiffness matrix may only be considered for infinitesimally small waves and motions as a ship has a rapidly changing waterline area in a vertical direction [145]. However, as the TLP under consideration in this literature review has a constant diameter surface piercing column extending significantly below and above the waterline, this is not an issue [13, 45].

As established in section 4.3.3, a quasi-static mooring approach is sufficient for the scope of this investigation. Due to the linear approach of each mooring line, the mooring stiffness matrix depends on the number of lines, mooring configuration and angle of the lines.

5.3. Flexible body formulation

As opposed to the rigid body assumption, as the name suggests, the flexible body approach allows for structural elements to deform. Due to the frequency of the loads, dynamic structural analysis is required [33, ch. 11]. The governing equation for structural dynamics follows from the conservation of energy, requiring that the work done by the sum of external forces is equal to the work absorbed by inertial, dissipative and internal forces [33, p. 375]. The governing structural equation is presented in equation (5.8) and is used in FEA.

$$\mathbf{M}\ddot{\vec{U}} + \mathbf{B}\dot{\vec{U}} + \mathbf{R}^{\mathbf{int}} = \vec{F^{ext}} \tag{5.8}$$

with

$$\mathbf{R}^{\mathbf{int}} = \mathbf{K}\vec{U} \tag{5.9}$$

Equation 5.8 is a system of coupled second-order differential equations that are continuous in time and discretised in space [13]. It is very important to note that the mass, stiffness and damping matrices here are not related to those discussed above. Here, M is the continuous mass matrix, B is the continuous damping matrix, K is the stiffness matrix and $\vec{U}$ is the displacement vector. The internal forces are implicitly expressed as the product between the stiffness and displacement, whereas external forces are explicitly expressed as $\vec{F_{ext}}$. The term 'consistent' asserts that these matrices follow from the FEA discretisation and use the same shape function as the stiffness matrix.

5.3.1. Mass matrix

There are multiple methods of formulating the mass matrix, of which two are lumped and consistent mass, each with its own set of benefits and drawbacks. As the details are out of the scope of this investigation, Cook's conclusion can be directly considered. Cook states that neither lumped nor consistent mass is better overall. Instead, consistent mass matrices are more suited for flexural problems such as beams and plates and allow for the computation of the upper bound resonance frequencies. Lumped mass matrices are more suited for impact loading [33]. For implicit time integration, the mass matrix does not need to be diagonal, as a consistent mass matrix follows from the shape function of the stiffness matrix [13]. This is executed by FEA software.

5.3.2. Damping matrix

Damping dissipates energy from the system and can be added or removed by design to influence dynamic response to an external influence [33]. This holds for both the aforementioned equation of motion in section 5.2.3 and for the structural equation. Three types of damping influence structural dynamics and hence loading and response [33].

- **Viscous damping:** Movement of the structure through a fluid, dissipating energy through frictional losses.
- **Hysteresis damping:** Deformation of material and dissipating energy as it returns to its original state. We commonly know this in, for example, washing machine damping pads used to reduce the noise and vibration of the machine.
- **Coulomb damping:** Also known as frictional damping it dissipates energy through dry friction between parts. This may be neglected in the substructure as there are no free-moving parts.

According to Cook, damping forces are quite small relative to other forces on the structure, of which viscous damping is dominant if the structure is loaded in the elastic range [33]. Hence, hysteresis damping may be dismissed. Rayleigh damping defines a global frequency-dependent matrix and consists of a linear combination of the mass and stiffness matrices as follows [13];

$$\mathbf{B} = \alpha\mathbf{M} + \beta\mathbf{K} \tag{5.10}$$

Where α and β are coefficients are frequency dependent coefficients. The contribution of $\alpha\mathbf{M}$ dominates low-frequency damping contributions, whereas $\beta\mathbf{K}$ dominates high-frequency damping. This low-frequency component can be imagined as an imaginary fluid whose viscosity becomes infinite for rigid body motions. As Bachynski points out, for FOWT applications, it is important to consider rigid body motions. Hence, this term should be as small as possible, or zero [13]. This means that the structural damping is frequency and stiffness-dependent. As the global damping matrix does not represent a structure that has components of different stiffnesses, Bachynski recommends specifying damping coefficients on an element-by-element basis for the different flexible components [13]. In practice, this can simply realised with finite element analysis.

5.3.3. Stiffness matrix

As stated previously, the Newmark relations should be applied in this investigation, which for the displacement vector are as follows [33, p. 418]:

$$\vec{\dot{D}}_{n+1} = \vec{\dot{D}}_n + \Delta t \left[\gamma \vec{\ddot{D}}_{n+1} + (1-\gamma)\vec{\ddot{D}}_n\right] \tag{5.11}$$

$$\vec{D}_{n+1} = \vec{D}_n + \Delta t \vec{\dot{D}}_n + \frac{1}{2}\Delta t^2 \left[2\beta \vec{\ddot{D}}_{n+1} + (1-2\beta)\vec{\ddot{D}}_n\right] \tag{5.12}$$

Where γ and β are constant depending on the type of Newmark method used and are textbook values. These equations can be plugged into the structural equation 5.8 resulting in;

$$\mathbf{K^{eff}}\vec{D}_{n+1} = \vec{R}^{ext}_{n+1} + M\left[\frac{1}{\beta\Delta t^2}\vec{D}_n + \frac{1}{\beta\Delta t}\dot{\vec{D}}_n + \left(\frac{1}{2\beta} - 1\right)\ddot{\vec{D}}_n\right] + \mathbf{B}\left[\frac{\gamma}{\beta\Delta t}\vec{D}_n + \left(\frac{\gamma}{\beta} - 1\right)\dot{\vec{D}}_n + \Delta t\left(\frac{\gamma}{2\beta} - 1\right)\ddot{\vec{D}}_n\right] \quad (5.13)$$

with

$$\mathbf{K^{eff}} = \frac{1}{\beta\Delta t^2}\mathbf{M} + \frac{\gamma}{\beta\Delta t}\mathbf{B} + \mathbf{K} \quad (5.14)$$

Where $\mathbf{K}$ is a linear stiffness matrix, this is not necessarily representative as the geometric stiffness of the system is a function of the internal force of the system and the change in the location of nodes. These internal forces change due to deformations. To adhere to the law of conservation of energy, on which FEA is built, it is more accurate to solve the static equilibrium of the system in the deformed configuration [78]. In practice, this means that for each timestep, a new tangential stiffness matrix must be calculated using an iterative approach, such as the Newton-Raphson method [13, 33]. This tangent stiffness matrix is the linearised solution to a geometrically non-linear problem and contains both linear elastic and geometric stiffness contributions [78].

5.4. Hybrid flexible-rigid formulation

The hybrid flexible-rigid formulation allows for the previously discussed rigid body and flexible body methods to supplement the weaknesses posed by the methods. When a structure is considered very stiff, such that the excursions are much larger than the deformations, a combination of separately determined rigid body dynamics and FEA may be applied. This drastically reduces the computational load as the solver no longer needs to consider internal stress and strain, but only the surface mesh [91]. Stepping back from marine and offshore publications, this is a field that affects many industries, such as aerospace and automotive engineering and is known as flexible multibody dynamics, and it considers the modelling and analysis of constrained deformable bodies that undergo displacements containing rigid body and elastic deformations [126]. Luan spearheaded a new time-domain method that can easily be implemented into current state-of-the-art modelling code to expand on existing functionality [91]. His proposition was validated for a semi-submersible FOWT, however, the methodology was explicitly developed for floaters, in general, [91]. It is also relevant to note that the submerged structure bears a striking resemblance to the structure that is to be considered in this literature review, as can be seen in figure 5.3.

In the flowcharts below, the proposed changes by Luan are clearly shown. In figure 5.1 on the left, it can be seen that the substructure is modelled as a rigid body, whereas the blades, tower and mooring lines are modelled as flexible elements. This approach is referred to as a hybrid frequency-time domain method, as the hydrodynamic loads and motions of the substructure are evaluated in the frequency domain, whereas the blades, tower and mooring are solved in the time domain. This method was also used in many of the sources evaluated for mooring modelling purposes [12, 13, 127]. It is loosely coupled in all respects, as the motions are solved using separate aero-hydro-mooring solvers, and the structural response is also solved in a separate procedure from the motions.

On the right, in figure 5.2, the proposed changes for a time domain method are presented. Here, the hull of the floating structure is considered a rigid body, however, the loads are evaluated at n nodes. The external loads are evaluated in the frequency domain according to potential theory and Morison's drag formulation (see sections 4.2 and 4.2.5 for more information) as though the body can be modelled as rigid. Next, these loads are mapped onto the FEA model by lumping the distributed loads over the panels onto the corresponding locations on the FEA model. These nodes are rigidly connected in the dynamics model and, hence, do not deform. This complete FEA model can subsequently be solved at each timestep.

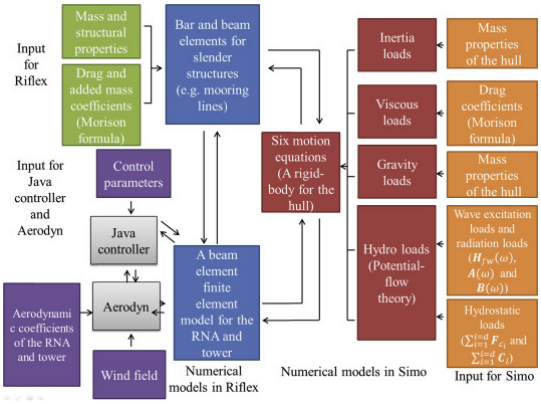


Figure 5.1: Flow chart of general approach as presented by Luan et al ([91, p .89])

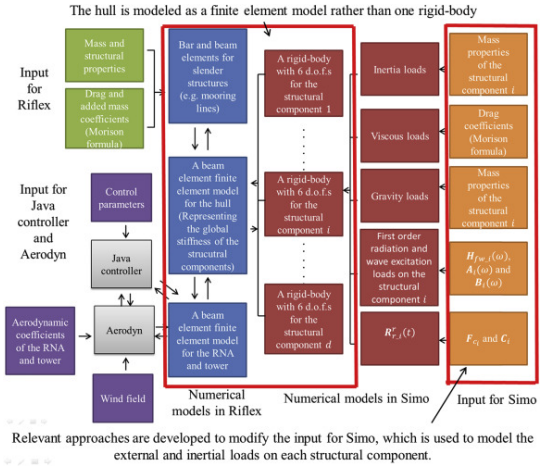


Figure 5.2: Flow chart of proposed changes to the analysis approach as presented by Luan et al ([91, p .91])

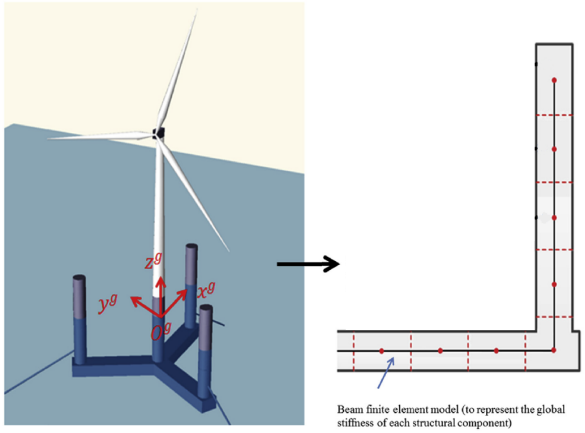


Figure 5.3: Discretization of FOWT. Shown is one of three pontoons and surface piercing columns (adapted from [91, p .92])

5.4.1. Drawbacks of Hybrid Method

This approach was validated in separate studies by Luan [92] where it was concluded that there was a very good agreement between simulated and measured results for normal operational tests. However, for measurements in extreme conditions, the spread in measured vs predicted values increased drastically. The author comments on the cause of the discrepancies in the normal operational conditions. He demonstrated that this source of error is not due to the aerodynamic modelling as the simulated and measured results were in very good agreement with each other. For the hydrodynamics, however, only first-order components were considered in the simulated model. As was established in section 4.2, second-order loading is also an important component. As it is not possible to '*turn off*' second and third-order loading in the experiment, there is a discrepancy between measured and calculated data. The author also explicitly states this as a recommendation in both validation studies [89, 92].

Another concern identified in this review, which is not addressed by Luan [89, 90, 91, 92] is the implications of quasi-static FEA. As discussed in section 4.3.2, quasi-static considers a dynamic problem as n number of static '*time frames*'. The issue with this is that dynamic effects are not considered, which is especially relevant when a shock load is applied to an element. A shock wave will travel through the material at the speed at which sound propagates through that material. The quasi-static approach cannot consider this and assumes that the shockwave instantly propagates through the material and reaches equilibrium. Therefore, quasi-static is not an appropriate approach if local structural dynamic problems are considered involving wave propagation, such as slack line events in the mooring followed by snap loading of the tendons. However, as established, this literature review will not consider slack

line events, and hence, this source of loading is not of concern.

The second concern related to the hybrid approach is also connected to the lack of loading onto a deformed body. In parts of the structure, due to the hydrostatic pressure, stiffened panels will already be partially deformed. This is neither included in the evaluation of the rigid body motion matrices nor the FEA analysis.

Finally, due to the implications of rigid body dynamic analysis, internal ballast is modelled as a (set of) solid mass(es). In the physical FOWT system, there is likely to be some solid ballast and/or a fluid in ballast tanks. If the ballast is a fluid, such as seawater, and the tanks are not fully filled, a free surface is present. When the structure moves in the dynamic environment, the fluid ballast will be free to move, thus changing the dynamic response characteristics. In extreme motions, this may cause sloshing in the tanks. The presence of a free surface within the structure is not accounted for in linear frequency domain analysis. However, as a TLP is stabilised through its mooring, the importance of ballast as a source of stability is low.

5.4.2. Benefits of Hybrid Method

As mentioned, the approach was validated in separate studies by Luan [89, 92] with good agreement. Although some of the aforementioned shortcomings are not to be overlooked in the implementation of this literature review, the method Luan proposes is highly promising and allows for the internal structural loads to be determined in time with reasonable computational efficiency, a feat neither of the methods previously discussed can produce. This approach can also easily be implemented in several state-of-the-art software packages and thus does not require the development of new software or complex pre- or post-processing [91].

Although Luan does not explicitly consider this in their research, the method allows for n^{th} order loading terms to be incorporated into calculations. Linear hydrodynamic theory may be used to calculate the rigid body response of the floater, thus eliminating the need for CFD based calculations. This is especially useful when considering the number of simulations that need to be run to determine the motion and structural response in misaligned wind-wave conditions. This reaffirms the gains in computational efficiency stated previously.

This method also allows for the body to be considered in all six degrees of freedom, and the designer can choose between detail and computational speed by discretising the structure in more or fewer nodes. Furthermore, motion and response analysis may be conducted together or separately, either of which is a good option depending on the computational setup of the researcher. For example, if a High Performance Cluster (HPC) is not available, the researcher can run the FEA on a separate system without compromising the dynamic simulation. This may be done as hydroelastic effects may be ignored, and thus, the added computational load of fluid-structure interaction does not need to be considered. This means that there is no coupling from the flexible structure back onto the loading.

5.5. Aero-elasticity

As was hinted in section 4.1 about aerodynamic loading and shown in section 5.1, there is a very strong coupling between aerodynamic loading and the structural behaviour of the blades and tower [57]. Separating the behaviour of the blades from the tower, a blade may deform in a twist (axial direction of the blade), thus changing its angle of attack concerning the incoming wind, thus changing the loading [57]. This change in the angle of attack also occurs when the tower moves up or downstream due to structural deformation of the tower [57]. For onshore and offshore fixed WTGs, this is already an important modelling consideration, but for FOWT, it is not to be neglected due to the extra excitation from the moving substructure.

The inclusion of aero-elasticity has also been demonstrated to be important for the performance of the FOWT. Liu demonstrated that modelling the turbine blades as rigid overpredicted the thrust and power delivered by the WTG [87]. The work of Al-Solihat demonstrated that the modelling of the tower as a rigid body also affects the response in all six degrees of freedom. The amount depended on platform properties [129]. Al-Solihat also showed that modelling the tower as a rigid body neglected

part of the aerodynamic damping, which, according to Hansen, is weak for a composite structure [57, 129]. Chen conducted a more thorough investigation into the effect of modelling different parts of a semi-submersible FOWT as rigid or flexible, testing 4 models in total with an increasing number of flexible parts. One of the most important conclusions Chen draws is that the modelling choice of the tower as rigid or flexible affects natural periods, and hence the response of the entire system [31]. Another conclusion Chen draws is that neglecting aero-elasticity fails to model dynamic stiffening of the bladed, as the blades become increasingly stiff as the rotational speed increases [31]. DNV also requires that any FOWT simulations are run using flexible body dynamics for the tower [9].

In conclusion, as modelling the tower and blades as rigid or flexible has an effect on loading and response, aero-elasticity must be included in the analysis.

5.6. Hydro-elasticity

As briefly mentioned previously, hydro elasticity is a phenomenon where the deformation of the structure due to loads interacts with the incoming wave loads [103]. Although the TLP considered in this investigation is a structure consisting of a slender tower and slender pontoons, the loading may be relatively low compared to a bulky structure. A slender structure is more prone to deformations. The previously mentioned DNV guidelines for coupled dynamic analysis explicitly discourage rigid body analysis for TLPs under the premise that deformations of the structure may influence the dynamic motion behaviour, but do not provide any references for this statement [9, p. 36]. Although hydro elasticity is not a new field, very little research has been done on this topic for FOWT applications. The following literature was found evaluating hydroelastic contributions for various FOWT applications.

Borg investigated the effect of flexibility in a Single Point Anchor Reservoir (SPAR) using a radiation-diffraction solver, thus a linear approach [21]. The author does not comment on the use of taut or catenary mooring in the model, however, the author does state that a linear mooring model is used, which is quasi-static. Borg found that for this particular SPAR type, structure resonance at the first bending mode did not bear a significant effect on the substructure. Therefore, hydro elasticity does not need to be considered for this condition, however, the author does reiterate that not enough data has been gathered to conclude the studied substructure in other conditions nor for SPAR structures as a whole. Despite this, some parallels may be drawn with the TLP considered in this literature review. At the surface (highest concentration of hydrodynamic loads), the TLP shares the same shape as the SPAR, as well as the quasi-static mooring model considered for the TLP.

More recently, though, De Souza published a paper investigating the effects of hull flexibility of a TLP on the structural dynamics [131]. The author concluded that effects on decay are varying, where the rigid body mode significantly underestimated the first heave resonance mode, but other modes to a lesser degree, this was also reflected in the response. The loads at the tower base and tendon fairleads, however, appeared to be unaffected by the hydroelastic model. The author also identifies limitations of their model, the first of which is that larger turbines may cause increased deflections due to the inherently larger loads the TLP is subject to. More importantly, the methodology only considered regular waves, which is, of course, not representative of realistic wind-wave sea states.

Based on the literature above, there is no concrete evidence that the inclusion of hydro-elastic effects is crucial for the dynamic analysis of a TLP. Hence, these effects will not be considered in this investigation for feasibility purposes.

6

Multiaxial Fatigue

As was established, a FOWT is subject to variable multiaxial loading, as the loading of the structure by the environment is typically multiaxial in nature as wind, waves, and current may be incident at different heading angles. Even within wave loading, there is a component of multiaxiality as swell and wind seas may also have different headings. As discussed in chapter 3, the random nature of environmental loading is highly stochastic in terms of amplitude, frequency and phase angle and is hence considered multiaxial non-proportional (random) Variable Amplitude (VA) loading [18]. Apart from motions, the structure will also respond according to the structural equation discussed in section 5.3, resulting in global and local stresses and deformations. Multiaxial loading does not guarantee a multiaxial response, as structure geometry and location also play an important role. For example, the response is multiaxial by definition in the weld notch [18, 118].

This chapter will discuss the process of conducting a fatigue lifetime assessment and any specific considerations when determining lifetime expectation for critical weld seams in a TLP type FOWT. In order to do this, section 6.1 will cover the fundamentals of fatigue, followed by fatigue resistance in section 6.2. Following this, sections 6.3 and 6.4 will cover failure criteria and stress parameters. section 6.5 will discuss damage planes and section 6.6 will cover cycle counting. In sections 6.7 and 6.8, non-proportionality and damage accumulation are covered, and finally, in section 6.9, recommendations from design guidelines regarding fatigue assessment in welded structures will be covered.

6.1. Fundamentals

The cyclical loading and response of a structure below the static strength of the structure induces progressive structural damage at a local scale until fracture. This damage mechanism is known as fatigue [125]. Fatigue is an important factor in the design of any structure designed for long-term offshore deployment, as structures with insufficient fatigue capacity will develop cracks over time. These cracks will need to be repaired offshore at a considerable cost and effort [26], as disconnecting a TLP temporarily for onshore repair is not an option.

Fatigue physics can be divided into four interacting resistance dimensions: material, geometry, loading & response and environment [18]. According to den Besten, material and geometry typically define the reference resistance, whereas loading & response and environment are influence factors affecting the fatigue damage process from crack nucleation up to fracture [18]. This investigation will consider loading & response, and geometry for feasibility purposes.

Fatigue physics covers a range of scales from atomic scale (micro) to structural scale (macro), as can be seen in figure 6.1 below. Fatigue must be understood as a crack initiation process followed by crack growth and propagation [85, 18]. Crack initiation covers short crack growth at the micro and meso scale, whereas crack growth covers long cracks at the macro scale until failure. It is essential to make this distinction as several conditions have a large influence on crack initiation but very limited influence on crack growth [125]. Separating these processes allows for the two processes to be predicted independently.

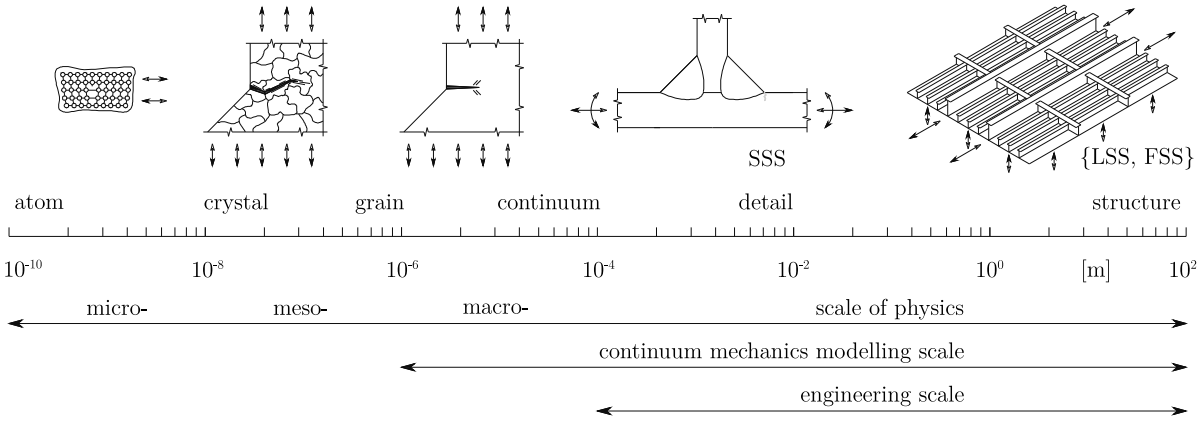


Figure 6.1: Range of scales at which fatigue physics can be considered [20, p. 2].

Fatigue damage requires plasticity of the material, and microscopic research has shown that nucleation may occur almost immediately after the first load cycle is applied above the fatigue limit. The fatigue limit is the stress level below which no damage is done to the material, and hence, it will have an infinite life. It is safe to say that the stress response in the critical weld seams of a FOWT structure due to combined wind-wave loads will exceed this lower limit.

Although fatigue lifetime is dominated by growth, most of the fatigue life of a marine structure is spent in the initiation phase [20, 85]. The initiation phase is driven at a microscopic scale due to cyclic slip [20, 85]. Although cyclic slip occurs at the micro and meso scales and most fatigue assessment methods consider the macro scale, it is an important effect in multiaxial fatigue, as will become evident in section 6.4. As the name implies, cyclic slip requires cyclic shear stress. At the micro-scale, shear stress will not be uniformly distributed. When sufficient stress is reached in grains, cyclic slip will occur due to the plasticity of the material. With repeated cyclic loading, these dislocations will move row by row until the boundary of the grain is reached. As dislocations cannot pass a grain boundary, multiple dislocations will eventually accumulate. These accumulations of dislocations are known as persistent slip bands. At these persistent slip bands, extrusions and intrusions will occur, where the material extrudes with respect to the original parent material boundary or is intruded with respect to the original parent material boundary. These intrusion and extrusion pairs are already considered micro cracks. From this initiation, cracks can start to grow along grain boundaries or along the slip bands across grains [125].

Schijve states that it is very difficult to give a quantitative definition for the transition between crack initiation and growth. Instead, he states that once the crack growth is no longer dependent on material surface conditions, the crack growth phase can be considered [125]. This is because crack growth is, unlike initiation, not a surface phenomenon. Crack growth and propagation take place when stress intensity at the crack tip is high enough to penetrate the grain barrier [125]. It is this process that prevents initiated cracks from growing resulting in infinite fatigue life, as the stress response is insufficient to overcome growth barriers. Crack growth is also a process driven by the opening and closing of the crack as fatigue cracks follow the path of least resistance [85].

6.1.1. Damage modes

Loading and response of a structure can be divided into three modes: I, II, and III. These modes may be considered individually for uniaxial application. Multiaxial loading is a term that has been repeatedly addressed in the sections above but has not yet been defined in the context of this investigation. Response (and fatigue) may be considered as multiaxial when a subject is loaded in two or three directions (modes) depending on thickness [118]. These three directions or modes are normal mode I, in-plane mode II and out-of-plane mode III, as depicted in figure 6.2 below.

For thin-walled constructions, the in-plane shear or sliding mode (mode II) may be neglected as the through-thickness shear forces are negligible [18]. As the considered structure is a thin-walled structure, this thesis will only consider mode I (σ_s) and mode III (τ_s) responses.

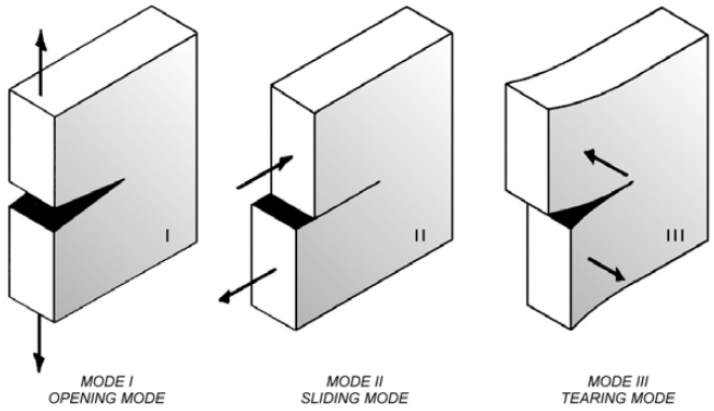
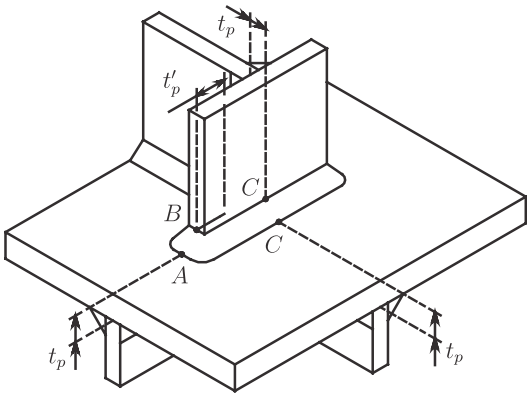


Figure 6.2: Crack surface displacing modes [66, p. 25].

Fatigue damage criteria are usually developed for application for a certain plane and lifetime phase (initiation or propagation) [84]. This is a challenge for modelling multiaxial fatigue as the loading plane shifts (see section 6.5). When the total response is dominated by the response in a single plane/mode this is not an issue as uniaxial fatigue assessment methods may be applied [18].

6.1.2. Welded joint hotspot types

Structural hotspots at weld toe notches can be classified based on location [48], which are used for hotspot stress assessment, see section 6.4.2. Hotspots can be classified as shown in figure 6.3 below.



(a) At the weld toe on the plate surface at an ending attachment
(b) At the weld toe around the plate edge of an ending attachment
(c) Along the weld of an attached plate

Figure 6.3: Hotspot types as defined by Fricke [48] (higher resolution figure adapted from [117, p. 5]).

6.1.3. Weld notch stress distribution

The through-thickness notch stress is not uniform, instead, it follows a distribution. This distribution differs for weld toe and weld root. As this investigation concerns critical weld seams, it can be assumed that the construction and inspection process will ensure full penetration weld. Hence this investigation will consider stress at the weld toe, as will become evident by the stress assessment methods presented in section 6.4. At the weld toe, assuming linear elastic behaviour, the total through-thickness stress distribution can be considered a linear superposition of an equilibrium (σ_s) and self-equilibrating (σ_{nlp}) stress part. The former can be further separated in a membrane (σ_m) and bending (σ_b) stress component, and the latter can be separated into a v-shaped notch and weld load-carrying component [20]. This is illustrated in figure 6.4 for reference, showing both mode-{I,III} stress distribution in a DS welded T joint and DS cruciform joint.

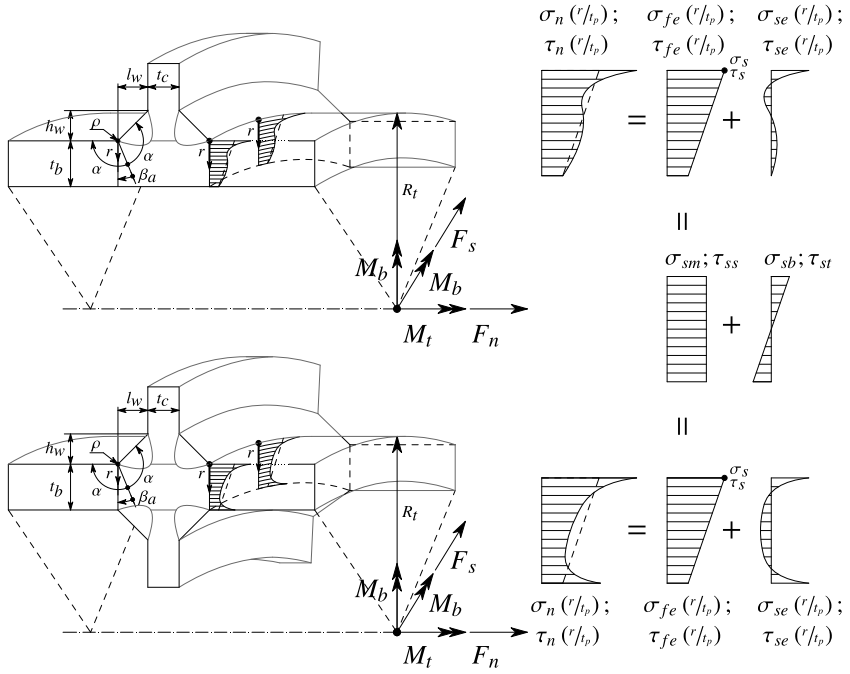


Figure 6.4: Weld toe notch stress distribution of a DS welded T-joint and DS welded cruciform joint in a tubular structure. The total resulting stress can be decomposed into an equilibrium equivalent (membrane and bending component) and a self-equilibrating stress part, for both mode-{I,III} [23, p. 7].

6.1.4. Mean stress

Mean stresses are caused by stationary loads such as the structure's weight, cargo, etc. or due to the mean component of the stress response in time [125]. A common convention to quantify the mean stress is through the load or stress ratio r_{lr} (see figure 6.5) [19, 85]. As fatigue considers the loading of a structure in the elastic region, loading and stress response are linearly related. Van Lieshout [85] comments on the use of two sets of terminology ('*load ratio*' and '*stress ratio*') by stating that although they are numerically indistinguishable from one another, the terminology may be misleading. This is because the term '*stress ratio*' implies that mean stresses are governed by the stress response, whereas mean stresses are actually governed by loading. Van Lieshout states that the use of '*load ratio*' is less ambiguous, and should hence be used. This convention will also be applied in this investigation. Trivially, if the structure is loaded such that the stress response is above yielding, the load and stress ratio are no longer equal.

6.1.5. Residual stress

During the fabrication process of both the parent material as well as the structure, residual stresses are induced in the material. It is defined as the stress distribution in a material when it is not subject to external loading [125]. Residual stress does not always need to be detrimental to fatigue resistance. For example, compressive residual stress can significantly improve fatigue resistance, whereas residual tensile stress accelerates fatigue issues. This can be explained when considering that crack growth is driven by the opening and closing of a crack [125]. If there is residual compressive stress in the material, a higher tensile stress must be applied to open the crack. However, to satisfy equilibrium, any residual compressive stresses must be opposed by tensile stress [125]. A classic example of a source of residual stress is welding. The heat added to the material in the process, along with the fast cooling produces a highly tensile stress at the weld toe [85].

Residual stress is distinctly different from mean stress as, unlike mean stresses, residual stresses can be relaxed by heat treatment, machining (grinding or ultrasonic impact treatment), or repeated loading [19, 85, 125]. These processes allow for the dislocations at a crystal scale to rearrange, relieving stress on the material. A specimen can be referred to as as welded (AW) or stress relieved (SR) [23]. However, when considering mean or residual stresses in fatigue strength parameters, no distinguishment is made in the methodology.

S-N curves can be converted using a mean stress correction in order to better represent the mean stress-induced load levels [85]. DNV applies an engineering approximation by means of a mean stress correction factor in a predefined stress range [10]. More scientific approaches include Walker or Smit-Watson-Topper (SWT) mean stress correction models. SWT considers an equal contribution between mean stress and stress amplitude, whereas Walker applies an unequal contribution, requiring a material-dependent calibration coefficient [84]. Walker's correction has shown to be the most effective for welded joints [23, 24, 84].

6.1.6. Multiaxial sources

Multiaxial stress response can be attributed to sources that can be allocated into three categories, as will be discussed in sections 6.1.6.1 to 6.1.6.3.

6.1.6.1 Material

Using the works of Chai and Laird [29], van Lieshout describes the dependence of fatigue resistance under non-proportional loading in ductile materials as a consequence of cyclic hardening [85] (see section 6.7). Due to the rotating glide plane, cross-hardening takes place due to interactions between dislocations. This interaction causes the dislocations to block each other. As the propagation of persistent slip bands serves to relieve stress, a higher stress concentration will be realised as a consequence. This higher stress concentration has a negative consequence for fatigue resistance [84].

6.1.6.2 Geometry

Geometry concerns the type of weld, joint connection, and plate thickness. Discontinuous geometries cause an inhomogeneous stress distribution, resulting in a stress increase at the joint connection [85, 125]. Weld geometry will always induce a stress concentration and the weld toe, and, depending on the weld penetration level, also at the weld root. This is important as stress concentrations are hotspots for fatigue cracks to form [20]. Geometry-induced multiaxial stress is largely proportional, as the principal stresses vary proportionally [101].

Another category of geometry considers *intact* or *cracked* geometry and is used to apply the right type of fatigue assessment method, which will be discussed in section 6.4 below.

6.1.6.3 Loading

Trivially, the effect of applying an alternating normal or shear stress-inducing load can be seen in the stress response signal [42]. Van Lieshout compared the results from a number of experiments considering smooth specimens under combined bending and torsion loading under non-proportional constant amplitude loading [85] (see section 6.7). She shows that the contradicting result of fatigue resistance both increases and decreases under non-proportional loading can be attributed to material ductility. It was also observed that increasing the frequency ratio between loads decreased fatigue resistance. No sensitivity to whether normal or shear stress was applied with higher frequency was observed. Finally, the loading wave also appeared to influence fatigue resistance [85].

6.2. Fatigue resistance

Prediction of fatigue crack nucleation and growth at the scale described in section 6.1 is simply not feasible for large structures. Instead, different approaches are used to quantify fatigue properties, which also consider the fatigue lifetime. Fatigue lifetime can be separated into three ranges; Low Cycle Fatigue (LCF) ($N < 10^4$ cycles), Medium Cycle Fatigue (MCF) ($10^4 < N < 10^7$ cycles) and High Cycle Fatigue (HCF) ($N > 10^7$ cycles) [19]. Different fatigue assessment criteria exist to evaluate the effects of cyclical loading on a structure and can be categorised as follows [18]:

- Global or local information
- Intact or cracked geometry
- Stress, strain or energy-based
- Point, line, or area/volume based

It has been demonstrated that strain-based criteria are particularly well suited for LCF [84, 118]. Energy-based criteria have shown promise for predicting lifespan. However, as energy is a scalar quantity and crack growth is determined by vector properties, this is not sufficient for crack growth models [118]. Finally, stress-based criteria are effective approaches for HCF where the yield strength is not surpassed [84, 118].

As the structure considered in this review is subject to HCF, stress-based criteria are considered, and therefore, fracture mechanics will not be considered. Although energy-based criteria would be a valid choice and intact geometry will be assumed in this thesis, further investigation into cracked geometry would not be possible, whereas stress-based criteria do allow for this in a (possible) subsequent investigation.

Although structural stress response does not inherently include information about the fatigue process, it is often used for fatigue resistance calculations [20]. The accuracy of this approach depends on the amount of local information included in the assessment, as will be discussed in more detail in section 6.4. As shown in figure 6.5 a stress cycle can be expressed by different means.

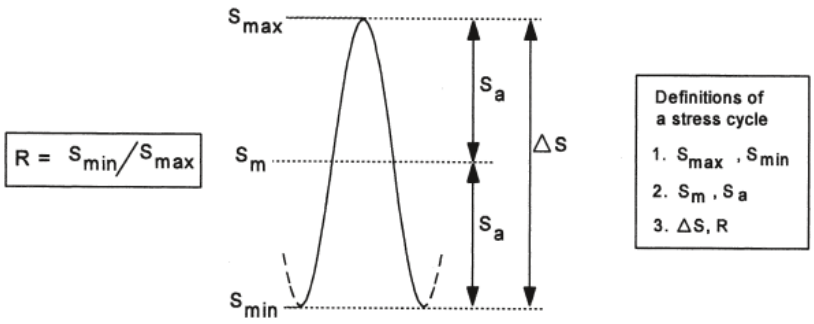


Figure 6.5: Different parameters to characterise a stress cycle [125, p. 142].

As pictured in figure 6.5 there are three different ways of characterising a stress cycle. The first of which is using the maximum and minimum stress reached in a cycle. The second is constant mean stress (section 6.1.4) over which a time-varying cyclical load is superimposed with a characteristic amplitude. The third way is using the loading ratio and change in stress.

6.2.1. Wöhler curves

Wöhler curves, more commonly known as SN curves, are experimentally derived curves used to describe the relationship between stress range S and number of cycles N for Constant Amplitude (CA) data. This is typically done on a log-log scale, for which a linear dependency can be observed (in the MCF-HCF range), which can be described with a Basquin type relation, formulated in equation (6.1) [20]. With number of cycles N, curve slope m and stress range S.

$$\log(N) = C - m \cdot \log(S) \tag{6.1}$$

The relation presented above is for CA loading, which, as established in chapter 4 is not applicable for FOWT. It has been demonstrated that for VA loading, slope m is hardly affected, but $\log(C)$ is. This must be considered appropriately when evaluating fatigue lifetime.

6.2.2. Constant and Variable Amplitude Loading

S-N curves are determined from CA loading specimens subject to a constant mean load and constant loading amplitude. Determining fatigue resistance or accumulated damage is quite straightforward as the loading amplitude and the number of cycles are known. As can be concluded from this literature review, marine structures, including FOWT TLPs, are subject to VA loading. A simple example is the loading due to the irregular waves which have varying amplitudes and periods. For these types of structures, fatigue failure is not an option within the operational lifespan. A simple option would be to design the structure considering the most extreme load as a CA load for the entire lifetime. This would, of course, lead to an unnecessarily heavy and expensive structure [125].

6.2.3. Loading signal shape

Schijve states that if load frequency is an important consideration in crack propagation, it can also be expected that the wave shape of the load cycle can also affect crack growth [125]. This is due to the mechanism behind crack extension, being a gradual process as S_{max} is approached, rather than a discrete process once S_{max} is reached. Hence loading rate is important for crack growth [125]. This effect is not expected to contribute significantly to the fatigue damage for a TLP type FOWT, as it was established in chapter 4 that all loads due to the dynamic environment are sinusoidal in nature, apart from one exception. This is a slack line event, which causes snap loading to the structure, as depicted as a block wave in figure 6.6. These events are, however, subsequent to highly non-linear extreme events with low probability. Furthermore, TLPs are designed to avoid slack line events.

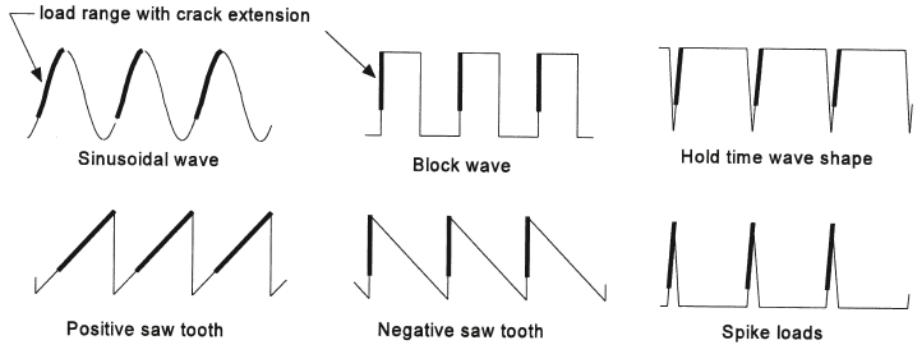


Figure 6.6: Different load signal shapes (adapted from [125, p. 46]).

6.3. Failure criterion

Engineering approaches often reduce stress signals to uniaxial and are processed with the uniaxial fatigue test data. Actual in-service load signals are often multiaxial. There are several failure criteria available in the literature to reduce a multiaxial stress state into an equivalent uniaxial stress condition [28, 113].

Before discussing these criteria, it is important to discuss the fundamentals. Any stress tensor can be decomposed into a hydrostatic (mean) and deviatoric (shear) component. The hydrostatic component is responsible for material volume change only (no deformations), whereas the deviatoric component is responsible for shape change only (no volume change). Ductile materials, such as metals, are sensitive to deviatoric stress, whereas brittle materials, such as ceramic, are sensitive to hydrostatic stress and can fracture under small changes in volume [23, 71, 125].

As this thesis only considers steel, ductile materials will be considered henceforth. Ductile material comprises grains varying in size, shape and orientation [23, 125]. For any load, each grain is subject to a different degree of slip, which is a volume-conserving process that changes the shape due to shear. As discussed previously as well, cyclic shear (deviatoric) causes cyclic slip. At fracture, these slip bands are visible at the fracture surface, thus suggesting that the Tresca maximum shear stress criterion is decisive [23]. Experimental evidence, however, indicates that ductile materials (steels) do not fail under pure hydrostatic stress, thus the distortion (shape change) is based on von Mises's maximum deviatoric stress criterion [23].

Provided that the mode-{II} contribution is negligible in shell structures, two types of failure criteria can be formulated, both of which are independent of hydrostatic stress.

$$S = \max(\tau_{III}) \leq \sigma_y \qquad \text{Tresca, linear type} \tag{6.2}$$

$$S = \max\left(\sqrt{\sigma_I^2 + \beta\tau_{III}^2}\right) \leq \sigma_y \qquad \text{von Mises, non-linear type} \tag{6.3}$$

If initiation dominates fatigue lifetime, shear stress is the controlling parameter, and thus a Tresca-type criterion should be considered. On the other hand, if growth dominates fatigue lifetime, a von

Mises-type criterion should be adopted [23]. From shipbuilding practices, we know that weld toe lifetime is growth controlled, and hence a von Mises-type criterion should be considered. Although there is no scientific consensus regarding an all-encompassing method, however, a number von Mises based failure criteria are discussed below.

6.3.1. Von Mises

Relative stress range can also be expressed using the von Mises equivalent stress. This approach is widely applied [85] and recommended by the IIW for proportional loading, including significant shear effects [60, 113]. It does, however, suffer from a number of shortcomings. The first of which is that severe overestimation of fatigue life was observed under combined out-of-phase torsion and bending (non-proportional loading) [85, 113]. Next, the von Mises equivalent stress is strictly positive, hence (partially) compressive stress states do not contribute to stress range [113]. Furthermore, the von Mises equivalent stress formulation appears to be insensitive to phase shifts between normal and shear components [109]. In engineering practices this can be compensated for by setting the maximum damage $D \neq 1$ [130]. For proportional narrow band spectrum (CA) loading, Sonsino [130] recommends a maximum damage parameter $D_{PM} = 0.5$. For wide band spectrum (VA) loading a maximum damage $D_{PM} = 0.2$ is recommended. Another issue is that a constant ratio between uniaxial fatigue resistance between normal and shear components is taken β, which has been demonstrated to not always be true. This is because the normal and shear uniaxial fatigue resistance curves are not always parallel to each other [23, 109], as illustrated in figure 6.7. A recent approach offers a solution to this issue and is discussed in section 6.3.6.

$$\Delta\sigma_{vM} = \sqrt{\Delta\sigma_x^2 + \Delta\sigma_y^2 - \Delta\sigma_x\Delta\sigma_y + 3\Delta\tau_{xy}^2} \tag{6.4}$$

6.3.2. Modified Gough Ellipse

The first interaction equation was proposed by Gough and Pollard and is well known as the Gough-Pollard interaction equation as presented in equation (6.5) [52].

$$\left(\frac{\sigma_a}{\sigma_{a,f-1}}\right)^2 + \left(\frac{\tau_a}{\tau_{a,f-1}}\right)^2 = 1 \tag{6.5}$$

It can be rewritten as a fatigue effective stress range $\Delta\sigma_{f,eff} = \sqrt{\Delta\sigma^2 + k \cdot \Delta\tau^2}$ with $k = \sigma_{a,f-1}^2/\tau_{a,f-1}^2$, which takes the familiar von Mises based form, assuming mode-{II} is negligible. As σ_{af-1}^2, τ_{af-1}^2 are the respective pure mode-{I,III} fatigue limits for fully reversed loads ($r_r l = -1$), the Gough-Pollard interaction equation implicitly includes a constant resistance-dependent correlation factor [85, 113].

Most multiaxial fatigue assessment methods in design codes apply an interaction equation to relate the contribution of different stress components to the damage accumulation. Interaction equations define a region of infinite life as long as the bounds are not exceeded. These equations are derived empirically from experimental data. Hence, the capacity of the interaction equation is closely related to the quality and completeness of the parent dataset [85]. As will become evident in section 6.9, many multiaxial fatigue criteria are based on a (modified) Gough-Pollard interaction equation. If the stress state remains within the bounds of this ellipse the fatigue life is expected to be infinite [52, 85]. The modifications to the original Gough-Pollard ellipse by Dong et al. [39] are to include a dimensionless parameter as a function of the out-of-phase angle in order to include proportional and non-proportional damage processes.

6.3.3. Effective Equivalent Stress Hypothesis

Effective Equivalent Stress Hypothesis (EESH) is a von Mises-based equivalent stress, critical plane integral failure criterion proposed by Sonsino [130], developed for multiaxial fatigue assessment for welded structures. EESH seeks to include the effects of non-proportional loading by including shear stress interaction effects in multiple material damage planes [83].

This is done by means of a non-dimensional parameter, which is a function of the phase angle [83]. EESH appears to be successful at correlating fatigue testing data but demonstrated a poorer correlation

of data than the Modified Gough Ellipse [41]. The implications of EESH on cycle counting for multiaxial fatigue are yet to be considered [113, 130]. It will hence not be considered further in this thesis.

6.3.4. Modified Carpinteri and Spagnoli

The Modified Carpinteri-Spagnoli (MCS) method is a multiaxial von Mises stress, critical plane-based method. The modified methodology distinguishes itself from previously discussed methods by explicitly including mean stress effects [28]. It can be rewritten as the fatigue-effective stress range of the Gough-Pollard equation:

$$\Delta\sigma_{MCS} = \sqrt{\Delta\sigma_{eq}^2 + \left(\sigma_{a,f-1}^2/\tau_{a,f-1}^2\right)\cdot\Delta\tau^2}, \quad \Delta\sigma_{eq} = \Delta\sigma + \Delta\sigma_{a,f-1}\cdot\left(\frac{\sigma_{\text{mean}}}{r_{lr}}\right) \tag{6.6}$$

This method is based on the physical observation that the fracture plane is closely related to the principal stress direction and maximum shear stress [85, 113]. The MCS method also determines the critical plane from principal stresses. MCS can be combined with the cycle counting methodologies presented in this literature review.

6.3.5. Minimum Circumscribed Ellipse

The previously described failure criteria have demonstrated a varying level of accuracy in regards to relating normal and shear stress into uniaxial equivalent stress but are not successful in including non-proportional effects of the load path. The Minimum Circumscribed Ellipse (MCE) was first proposed [81, 120] as an improvement of the Minimum Circumscribed Circle (MCC) method, which sought to define the effective stress amplitude as the minimum radius of the circle enclosing the load path in the von Mises space, assuming a constant shear stress coefficient. Hence it takes the form.

$$\sigma_{vM} = \sqrt{\Delta\sigma + \beta\Delta\tau} \tag{6.7}$$

Adding to this, the MCE method allowed for the effective shear amplitude to be determined. An issue that was not resolved with MCE is that load path information is lost, and no distinction can be made between the different load paths that share the same MCE.

Donk [42] demonstrated that the application of MCE provides an excellent screening tool for multiaxial stress response and also allows for the level of mean stress to be captured. MCE did not provide a perfect indication of fatigue damage but did allow for hotspots subject to multiaxial stress response to be isolated for further analysis. This is especially interesting for large-scale FEA models, such as required for FOWT. In Donk's investigation, Khachiyan's algorithm [72, 136] was applied to determine the MCE. Although Khachiyan's algorithm (referred to as Minimum Volume Enclosed Ellipse (MVEE)) was not developed specifically for multiaxial fatigue, it provides a proven mathematical model accomplishing the same mathematical operations as MCE.

6.3.6. Response level dependency

In previous fatigue criteria, the shear strength coefficient β was considered constant. This constant was set $\beta = 3$, following from the original von Mises formulation, or resistance-based $\beta = \sigma_{af-1}^2/\tau_{af-1}^2$. Recently, Bufalari and den Besten [23] proposed a response level-dependent coefficient to incorporate the mode I and mode III contributions as a response representative, rather than a mode III representative, resistance curve. This is because, in the finite lifetime, the ratio between mode-{I,III} fatigue strength ratio depends on the number of cycles until failure [23]. In this paper, further considerations regarding the implications of cycle counting methodologies (see section 6.6) and choice of failure criterion are analysed in detail. Assuming that the stress response is multiaxial and non-proportional (as may be expected from the loading) and a failure criterion with the least amount of stress information lost, an equivalent normals stress von Mises type criterion should be adopted. More specifically, in the following form:

$$S = \max\left(\sqrt{\sigma_{I,max}^2(\phi) + \beta\{\sigma_I(N), \tau_{III}(N)\}\cdot\Delta\tau_{III}^2(\phi)}\right) \tag{6.8}$$

Bufalari et al. [23] combines this methodology with a path-dependent cycle counting method (see section 6.6.3) and moment of load path (see section 6.7.1) in order to establish a mode-I equivalent von

Mises type of failure criterion at the critical plane, based on effective notch stresses. This proposed methodology is used to conduct multiaxial fatigue analysis.

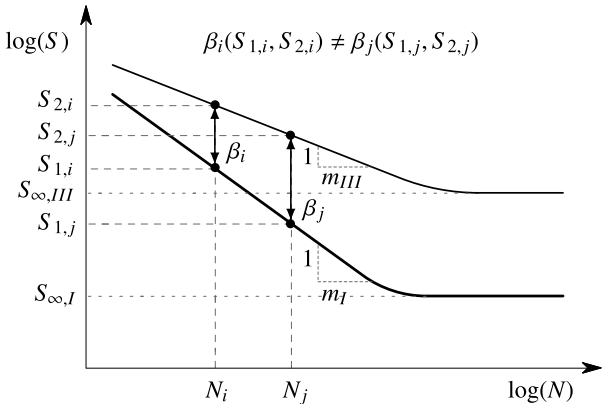


Figure 6.7: Response level dependent shear strength coefficient [23, p. 4].

6.3.7. Summary

In the previous sections, it was established that due to the type of stress signal that may be expected, and hence processed preserving as much information as possible, a von Mises-based failure criterion should be adopted. Given the scale at which stress signals must be processed efficiently in this thesis, it is justified to apply a MCE based approach, employing a constant $\beta = 3$ as neither resistance nor response level dependent shear stress coefficient is available ahead of time.

6.4. Assessment Concepts

As was established in section 6.2, stress-based assessment methods are effective tools for determining fatigue life expectations for HCF loaded structures. Stress assessment methods are however only one piece of the puzzle, as cycle counting is also required to make a meaningful fatigue life expectancy assessment, this will be discussed in more detail in section 6.6. Fatigue resistance curves (as discussed in section 6.2.1) are lifetime relations that empirically provide integrity and longevity information. For an intact or cracked geometry, this is expressed by Basquin or Paris type relations, respectively [18].

As a marine structure spends most of its lifetime in the crack initiation phase (weld notch affected region) instead of the crack growth phase, it makes sense to apply an intact geometry parameter. Referring to the overview in figure 6.8 a number of fatigue assessment methods are categorised based on a number of criteria, including intact and cracked geometries. The methods discussed in this section are highlighted in green for reference.

A fatigue assessment concept consists of a fatigue damage criterion and a corresponding resistance curve [19]. The first of which will be considered in this section. A fatigue damage criterion seeks to strike a balance between an assessment of the following components [19].

1. Total life: Account for contributions to the initiation and growth phase. Correctly correlate parameters to intact or cracked geometry.
2. Incorporate the four fatigue resistance dimensions mentioned in the introduction of chapter 6.
3. Include information at global and local scale

Each fatigue assessment criterion strikes a different balance between the accuracy and complexity of the assessment method. In this review, four methods will be considered, the first three assessment methods of which are commonly applied in engineering standards [38, 85]. These methods will be specifically reviewed for multiaxial fatigue applications. In section section 6.4.1 the Nominal Stress Concept will be discussed, followed by the Hot Spot Structural Stress Concept in section 6.4.2. Finally, the Effective Notch Stress Concept will be discussed in section 6.4.3.

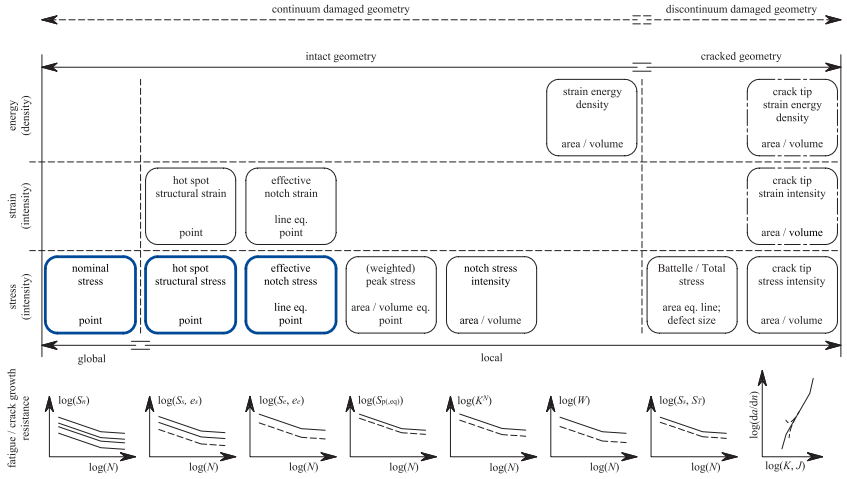


Figure 6.8: Overview of fatigue assessment methods grouped by stress, strain and energy-based methods for intact or cracked geometries. The assessment methods considered in this thesis are outlined in blue (adapted from [18, p. 5]).

6.4.1. Nominal Stress Concept

The Nominal Stress Concept (NSC) is a stress criterion calculated at a point, disregarding local stress raisers such as welds, but including stress-raising effects of large geometries in the vicinity (e.g. large cutouts such as doorways or portholes [60]. From a design perspective, this is very attractive as the exclusion of local information, thus only considering the far-field response, makes this method computationally inexpensive [19, 85]. Evaluation of MCF and HCF requires the nominal stress range $S_n = \Delta\sigma = 2\sigma_n$, as pictures in figure 6.9.

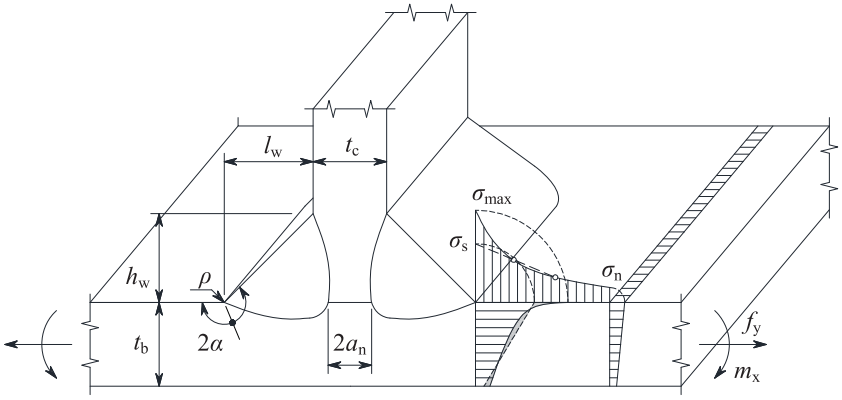


Figure 6.9: Welded joint normal force and bending moment induced stress distributions, clearly separating the nominal stress distribution and structural hotspot stress distributions [18, p. 6]. Only mode-{I} is depicted here.

As this parameter does not contain any local information on the joint, no meaningful assessment can be made regarding the fatigue lifetime of the joint. In order to make a fatigue assessment of a particular structural detail, the CA fatigue resistance information available is expressed in FATigue classes or detail CATegories, which define the intercept log(C), as per the Basquin relation [18]. In order to do this, fatigue resistance (S-N) curves are used for structural details. As there is a large variety in welded joint geometries, dimensions and load combinations, there is theoretically an infinite number of unique structural details and an infinite number of fatigue resistance curves [19]. However, in marine structures, most of the variation in joint geometry is a matter of dimensions rather than diversity in weld geometry [18]. There are currently about 80 different classes defined by IIW or CEN [18]. This stress criterion is valid as long as material, geometry, loading & response, environment (i.e. corrosive or not), weld failure location (toe or root) and quality (metallurgical quality as well as the offset of welded components) fit the FAT or CAT requirements [18].

As S_n is evaluated at a single point local effects are not taken into account explicitly and must be

corrected for. More importantly, the NSC does not account for the interaction between mode I and mode III. Both the IIW and CEN prescribe an interaction equation at the reference plane in the finite lifetime region based on the Gough-Pollard relation (which will be further discussed in section 6.3.2).

6.4.2. Hot Spot Structural Stress Concept

Reducing the uncertainty concerning the previously discussed concept is the Hot Spot Structural Stress Concept (HSSSC), by explicitly including material, geometry, loading & response and environmental conditions. The structural stress at the hotspot included all stress raisers at a structural detail, apart from the weld itself [18, 60, 116]. The dimensions of the welded geometry are however not incorporated in this assessment concept, and hence, an infinite number of S-N curves is still required [18, 116]. To reduce this number of curves a distinction between Load Carrying (LC) and Non Load Carrying (NLC) is made based on engineering judgement, as there are no explicit rules defining the two. The weld load carrying level is however defined by two mechanisms: stiffness-attracted load (joint geometry dimensions) and enforced load path (weld penetration level) [38, 19]. This distinction between LC and NLC allows for a reduction to two S-N curves, one for each.

As with NSC, the interaction between mode I and mode III is not considered, however, these stress components are evaluated in the (critical) fracture plane [18]. IIW and CEN prescribe an interaction equation. Furthermore, HSSSC does not consider the stress contribution caused by the weld notch itself, which, as established, is multiaxial by nature.

Calculation of the hotspot structural stress S_s can be done in one of three ways, as described in sections 6.4.2.1 to 6.4.2.3.

6.4.2.1 Surface extrapolation

Conducting a HSSSC assessment following IIW or CEN is restricted to weld toes, due to the practical restrictions of detecting weld root cracks [60]. HSSSC is a surface extrapolation calculated in FEA using shell elements. It is hence a mesh-sensitive method, and appropriate care must be taken. The surface extrapolation method can be further divided into a linear and non-linear type of extrapolation, respectively based on a two or three-point extrapolation. In figure 6.10 an indication is given of a linear extrapolation based on two points. These points are typically defined as a fractional distance of the plate thickness from the weld toe. The fractions differ depending on the type of hotspot (see section 6.1.2) considered, the regulations followed and the shell element type (4-node or 8-node) [60].

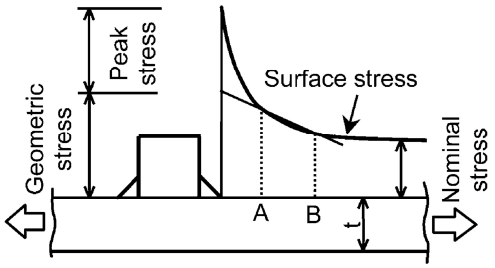


Figure 6.10: Linear HSSSC extrapolation based of two reference points. This figure also clearly shows that although it includes more local information than NSC, the weld stress contribution is still ignored [147, p .3].

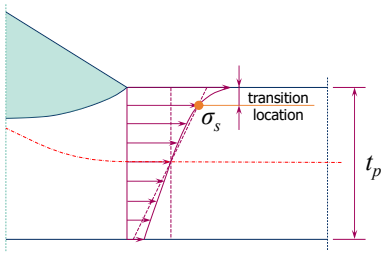


Figure 6.11: Crosssection, zoomed in perspective from figure 6.9 showing subsurface extrapolation method to determine hotspot structural stress. Clearly shown is the transition from weld notch to far-field stress-dominated region, at which S_n is calculated [19, p .26].

6.4.2.2 Subsurface identification

Alternatively, a subsurface extrapolation may be employed. This method requires a solid model of the geometry and is hence also mesh sensitive. S_s is calculated at a depth in the baseplate, where a transition from notch governing (zone 1 and 2) to far-field dominated (zone 3) stress takes place, typically at 1mm below the surface. However, as den Besten points out, this transition typically takes place at $0.1t_p$, below the surface [18, 19], as pictured in figure 6.11. For a 10mm plate, typically used in

marine and offshore structures, as used in the original publication by Xiao [147], this corresponds to 1mm. It should be noted that for different plate thicknesses, the subsurface depth considered must be reevaluated as the transition point shifts.

This method is however not appropriate for the application considered in this investigation as a solid FEA model with an appropriate mesh density will be detrimental to computational expense.

6.4.2.3 Traction-based structural stress

The traction-based structural stress method has been shown to consistently characterise stress concentration effects at weld toe for continuous welds while achieving good mesh and element type insensitivity [39, 40, 41]. This method is built on two assumptions, the first of which is that the stress state in the weld toe can be represented as a (far field) equilibrium equivalent stress state and a self-equilibrating part (as discussed in section 6.1.3). The second assumption is that for displacement-based finite element methods, the balanced nodal forces and moments always satisfy the equilibrium conditions at every nodal position. Stress does not have to satisfy this equilibrium condition [39].

The traction-based structural stress method can deal with both uniaxial and multiaxial loading conditions [39]. As shown in figure 6.12, weld node forces are extracted per element in the global axis system. In order to calculate stress using these nodal forces, they must first be expressed in a local elemental axis system [40].

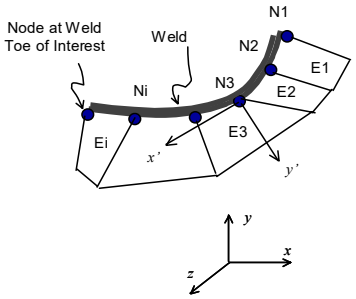


Figure 6.12: Curved weld in space depicting global and local axis systems [40, p .2]

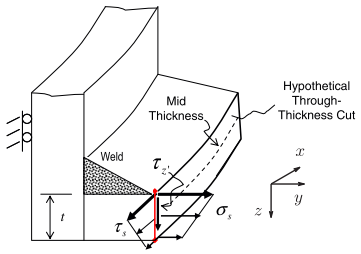


Figure 6.13: Structural stress definitions at weld toe with respect to local coordinate system (adapted from [41, p .3])

For linear shell elements, the work done by the nodal forces along the nodal displacements is equal to the line force over the same distance. Applying this principle, the following formulation can be devised to determine the line forces f_i using the known nodal forces F_i and line matrix, representing the element edge length projected onto the weld toe line. This matrix also depends on whether the weld considered is closed (start and end points are the same) or open. These are described with equations equations (6.9) and (6.10) [39, 40]. The difference between weld seams can be seen in the start/end node contribution in the first and last term on the main diagonal, as well as a difference in the $L_{n,0}$ and $L_{0,n}$ terms.

$$\begin{Bmatrix} F_1 \\ F_2 \\ F_3 \\ \vdots \\ \vdots \\ F_{n-1} \end{Bmatrix} = \begin{bmatrix} \frac{(l_1+l_{n-1})}{3} & \frac{l_1}{6} & 0 & 0 & \cdots & \frac{l_{n-1}}{6} \\ \frac{l_1}{6} & \frac{(l_1+l_2)}{3} & \frac{l_2}{6} & 0 & \cdots & 0 \\ 0 & \frac{l_2}{6} & \frac{(l_2+l_3)}{3} & \frac{l_3}{6} & 0 & \vdots \\ 0 & 0 & \ddots & \ddots & \ddots & 0 \\ \vdots & \ddots & 0 & \frac{l_{n-3}}{6} & \frac{(l_{n-3}+l_{n-2})}{3} & \frac{l_{n-2}}{6} \\ \frac{l_{n-1}}{6} & \cdots & 0 & 0 & \frac{l_{n-2}}{6} & \frac{(l_{n-2}+l_{n-1})}{3} \end{bmatrix} \begin{Bmatrix} f_1 \\ f_2 \\ f_3 \\ \vdots \\ \vdots \\ f_{n-1} \end{Bmatrix} \tag{6.9}$$

$$\begin{Bmatrix} F_1 \\ F_2 \\ F_3 \\ \vdots \\ \vdots \\ F_n \end{Bmatrix} = \begin{bmatrix} \frac{l_1}{3} & \frac{l_1}{6} & 0 & 0 & \cdots & 0 \\ \frac{l_1}{6} & \frac{(l_1+l_2)}{3} & \frac{l_2}{6} & 0 & \cdots & 0 \\ 0 & \frac{l_2}{6} & \frac{(l_2+l_3)}{3} & \frac{l_3}{6} & 0 & 0 \\ 0 & 0 & \ddots & \ddots & \ddots & 0 \\ \vdots & \ddots & \ddots & \ddots & \frac{(l_{n-2}+l_{n-1})}{3} & \frac{l_{n-1}}{6} \\ 0 & \cdots & \cdots & 0 & \frac{l_{n-1}}{6} & \frac{l_{n-1}}{3} \end{bmatrix} \begin{Bmatrix} f_1 \\ f_2 \\ f_3 \\ \vdots \\ \vdots \\ f_n \end{Bmatrix} \tag{6.10}$$

Each of the line forces in equations (6.9) and (6.10) consists of 3 line force and 3 line moment components $f_i = \begin{bmatrix} f_{x'} & f_{y'} & f_{z'} & m_{x'} & m_{y'} & m_{z'} \end{bmatrix}$. This allows for the stress and shear along each line segment to be calculated as follows [39, 40, 41].

$$\sigma_s = \sigma_m + \sigma_b = \frac{f_{y'}}{t} + \frac{6m_{x'}}{t^2}, \qquad \text{and} \qquad \tau_s = \tau_m + \tau_b = \frac{f_{x'}}{t} + \frac{6m_{y'}}{t^2} \tag{6.11}$$

6.4.3. Effective Notch Stress Concept

Welded notch radii are small and highly stochastic. This notch reduces both the stress concentration and strength at the notch [38]. The theoretical stress concentration derived using the methods presented above is not fully effective, adopting the maximum stress as a fatigue criterion would be too conservative [18, 38, 116].

Instead, an effective structural stress parameter can be derived by averaging the notch stress distribution over the expected crack path, over a characteristic length ρ^*, which represents the length in which the majority of fatigue lifetime is spent [23]. This parameter no longer needs to be derived by means of solid FE models [24, 116, 117]. This methodology allows for the geometry, loading & response and notch geometry to be taken into account.

For fatigue damage accumulation, engineering practices apply one resistance curve. Due to the formulation of this curve, and a number of underlying assumptions regarding weld notch radius, the plate thickness must be larger than 5mm due to artificial cross-sectional weakening/strengthening at the weld root/toe notches [18]. This should, however not be an issue for application in critical weld seams for any floating structure, as these connections are likely to be much thicker than 5mm.

Although this methodology allows for an increased level of detail, due to the inclusion of local (geometry) effects, this literature review seeks to establish an assessment method for far-field multiaxial stress response. The Effective Notch Stress Concept (ENSC) provides detailed information, which is not required at the added expense of computational effort. ENSC will therefore not be considered further.

6.4.4. Summary

Provided the information in this subsection, and considering the scale of the considered FOWT model, a stress assessment concept that provides as much detail as possible at minimal computational expense, the HSSSC is chosen. More specifically, the traction-based structural stress method was deemed most appropriate due to its computational efficiency and mesh insensitivity. Assuming that the crack plane propagates in the plate through the thickness direction, the critical plane can be assumed, thus saving further on computational expense. This methodology allows for independent mode-{I,III} stress signals to be derived and processed using the appropriate toolsets downstream. As an added benefit, the work of [117, 24, 23] allows for effective notch stresses to be determined using far-field stresses. Therefore, this methodology also allows for further, more detailed analysis to be conducted at a later time using the same dataset.

6.5. Damage plane selection

For proportional multiaxial loading the magnitude of the stress tensor varies over the stress cycle. As a consequence of non-proportional loading, the principal stresses vary in magnitude as well as directions (ϕ), over time [23, 85]. For each principle stress direction a corresponding plane exists to which the principle stress tensor is normal. In order to consider the damage contribution of each individual plane an integral method must be incorporated [23, 85]. Alternatively, a critical plane method can be considered.

The critical plane is determined through an iterative process. For each iteration, a fatigue criterion is evaluated, either maximum shear stress amplitude or range on the plane, maximum damage on the plane or specific inclination towards another fracture plane [67, 83, 85]. Depending on the criterion, the plane that expects the lowest fatigue life, as indicated by the criterion is the critical plane. Van Lieshout concludes that a critical plane approach is most successful with a damage parameter, as a damage parameter allows for the damage mechanism and fatigue strength to be accounted for properly, allowing for the fatigue resistance to be determined correctly [85]. Given that this methodology only supplies information at a single point in space, it is extremely computationally expensive to apply for

large-scale structures. Hence, it is also important to isolate locations that are subject to multiaxial stress before applying a critical plane damage evaluation model.

However, as the stiffness distribution of stiffened panels in maritime structures (such as FOWT) is predominantly orthotropic, cracks at weld notches generally propagate in through-thickness direction, i.e. the fracture plane [23]. This information can be easily extracted from an FEA model, thus providing a computationally efficient method of evaluating a damage plane.

6.6. Cycle counting

The first part of assessing fatigue damage accumulation is cycle counting. A common (uniaxial) cycle counting method is the rain flow counting algorithm. This algorithm defines a load cycle by the closed hysteresis loops in the cyclic stress-strain behaviour. It considers one input parameter and is hence unsuitable for multiple variable input parameters, such as when considering a joint subject to mixed mode I and mode III response. In the subsections below an overview of multiaxial cycle counting methods is presented.

6.6.1. Multiaxial rainflow

Bannantine and Socie proposed a multiaxial rain flow counting method in which the normal and shear strain components are evaluated separately, in the critical plane [16]. This approach suffered from several shortcomings, most notably that maximum normal and shear strain may not coincide [77]. Langlais proposed an extension to a rainflow-based multiaxial cycle counting method by considering two input parameters. The first of which is the governing fatigue contributor in the chosen plane, to which rainflow counting is applied. For the second signal, the strain fluctuations for each primary cycle are tracked [77, 85]. As this method considers two signals separately, interaction effects between modes are not considered, nor is the response path.

6.6.2. Virtual

Virtual cycle counting methods do not consider hysteresis loops like (multiaxial) rainflow counting. Instead, a load-block is defined between two zero up-crossings of shear stress [4]. Within each load block the number of load cycles is counted using equivalent shear stress as defined by the Stress Scale Factor method [4]. For the considered application, the virtual cycle counting method suffers from a detrimental flaw. This is because virtual cycle counting does not account for any mean stress effects [85]. As non-zero mean stress is expected in the critical weld seams of a TLP type FOWT, it is important that a cycle counting method is able to resolve possible mean stress effects. It will hence not be considered any further.

6.6.3. Path-dependent maximum range

The Path-dependent-maximum range (PDMR) methodology was proposed by Dong [41] to evaluate components subject to (non-proportional) VA multiaxial loading. PDMR seeks the maximum possible distance/range (in the stress or strain space) between two points for a given time trace. The total path length is computed from the path length along a monotonically increasing distance in time, between the two points in the stress space, as shown in figure 6.14 [41]. Starting at point **P** and following the stress path (solid line) until point **R** is reached, referred to as the turning point. This point lies a distance of r_0 from point **P**, just as $\mathbf{R}^*$, the *projected* turning point. The search along the loading path will be continued from $\mathbf{R}^*$ until **Q** is reached. Afterwards, all other loading segments such as $\mathbf{RR}^*$ will be considered using the same methodology described above. Once the entire load path **PQ** has been considered, the path-dependent effective stress range (path length) of the considered half-cycle can be computed as the sum of all the individual paths considered. This process is repeated until the entire stress signal has been processed.

The PDMR method can be applied to 3D stress states (σ_s,$\sqrt{\beta_{II}}\tau_{II}$,$\sqrt{\beta_{III}}\tau_{III}$) as well , however, as established in section 6.1.1, mode II response is negligible in thin-walled marine structures. Furthermore, this method can be applied to traction-based stress components, which makes PDMR cycle counting an excellent option for analysis of fatigue critical weld seams in FOWT as traction-based structural stress allows for full-scale structural analysis to be conducted without mesh sensitivity issues.

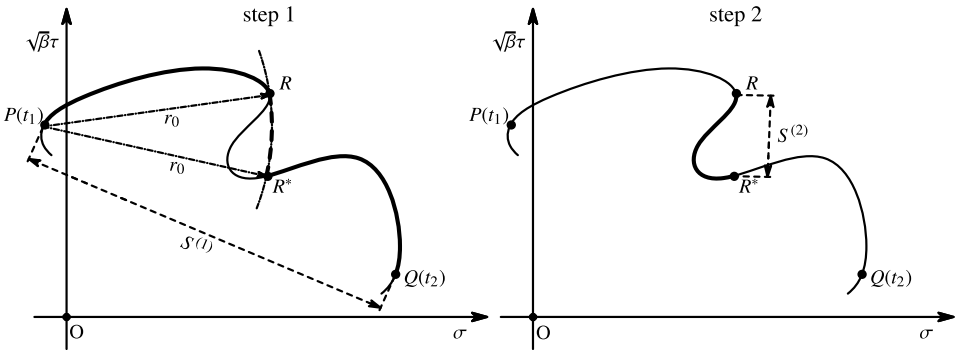


Figure 6.14: PDMR cycle counting methodology (adapted from [23, p .5]).

6.7. Non-proportionality

Loading and response may also be divided into proportional and non-proportional loading, depending on whether the principal stress/strain directions rotate throughout a loading cycle [102]. As this review only considers mode I and mode III for reasons explained in section 6.1.1 the following explanation is valid, if a third mode needs to be considered the stress can no longer be represented in a 2D stress plane. It is important to make the distinguishment between proportional and non-proportional loading as the rotational principal stress and strain axes under non-proportional loading cause extra hardening, causing non-proportional loading to be more damaging [102]. Van Lieshout conducted a detailed comparison between multiaxial fatigue assessment methods and demonstrated that a two-component non-proportional stress signal could produce 1.3-3.4x greater damage than when considering a single load component [83]. Any load path can be mapped from a nominal stress-based plane ($\sigma_n - \sqrt{\beta}\tau_n$) to a structural stress-based plane ($\sigma_s - \sqrt{\beta}\tau_s$). Here, $\sqrt{\beta}$ represents a fatigue equivalent parameter between S-N data of pure torsion and pure bending [102]. It typically takes on a value of $\sqrt{3}$ [102], following from the von Mises stress criterion, showing to be an effective criterion [39], provided it is applied in the finite lifetime region [18]. However, as was established previously, this shear stress coefficient is not always equal to 3, but rather

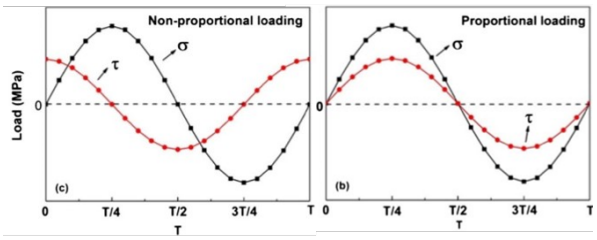


Figure 6.15: Proportional and non-proportional CA load paths for mode I and mode III (adapted from [62]).

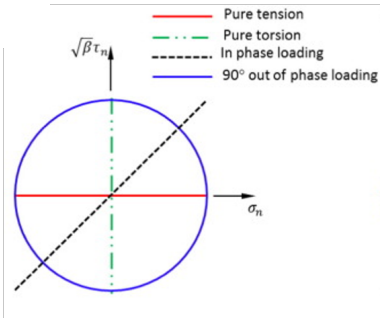


Figure 6.16: Load paths plotted in nominal stress plane (adapted from [102]).

In figure 6.15, a fully reversed proportional and non-proportional CA load path is plotted for a single period. Plotting the response to these loads on the nominal stress plane produces different results, as shown in figure 6.16. For the proportional load, the response is also proportional, i.e., it lies along a linear line (black dashed line). As the load is fully reversed, the in-phase loading line passes through the origin, as seen in figure 6.16. If the loads are of the same frequency and 90° out of phase, the principal strain direction changes over time, resulting in a circle being plotted in the stress plane. For reference, a pure tension and torsion response is also plotted, both of which are uniaxial.

The load paths and stress response presented in figures 6.15 and 6.16 are examples of ideal conditions. By varying the waveforms (effect discussed in section 6.2.3), phase difference and geometry of the

structure while applying CA loading, different stress responses can be expected. For reference, some examples are plotted in figure 6.17. Also shown in paths 7-11 is what the response looks like if the load applied is not fully reversed ($r_{lr} \neq -1$), more information in section 6.1.4), and hence a mean stress component is present. As wind and wave loading is likely to contain out-of-phase (non-proportional) and VA components, the response is also likely to take on these characteristics. For reference, some VA, non-proportional, multiaxial stress responses are plotted in figure 6.18.

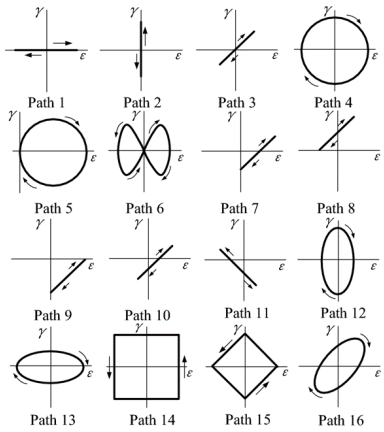


Figure 6.17: Different types of proportional and non-proportional CA load paths for mode I and mode III (adapted from [82]). Note that strain is plotted.

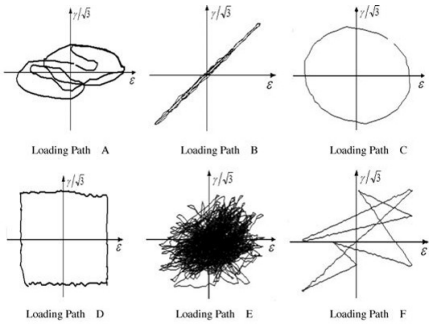


Figure 6.18: Different types of proportional and non-proportional (random) VA load paths for mode I and mode III [30]. Note that strain is plotted.

6.7.1. Moment of Load Path

As has been established, non-proportional loading is more damaging than proportional loading. Several methods have been proposed to account for load path effects in fatigue damage calculations (see section 6.3), however, none have been shown as effective a Moment of Load Path (MLP). MLP was developed as an extension to PDMR cycle counting and considers the stress path length and shape. Consider two points in a stress space, such as figure 6.19. Here, points **P** and **Q** represent the start and end points of a single stress cycle, between which many different stress paths can be taken, just as plotted in figure 6.14. Path A is a semi-circular path with radius R, and path B is a series of semi-circular load paths with radius R/n; both paths share the same length. As one can imagine, as n increases, the fatigue damage of path B should approach that of path C, a straight line between points **P** and **Q**. To address this deficiency Mei et al. [101] proposed a path-dependent method based on the accumulative strain energy density of normal and shear stresses.

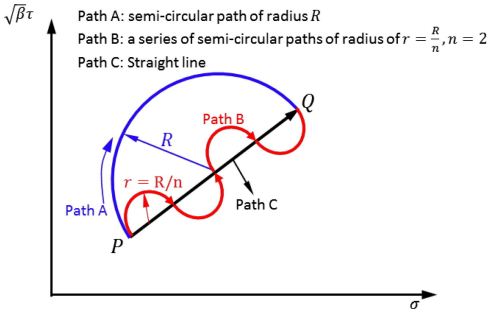


Figure 6.19: MLP concept visualized [101, p. 3].

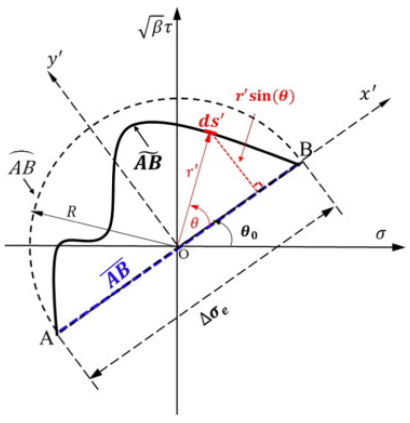


Figure 6.20: MLP method for an arbitrary non-proportional stress path between two points in a stress cycle [101, p. 4].

MLP considers the total damage of a non-proportional load path as $D = D_P + D_{NP}$, where the proportional damage component is derived for segment $\overline{AB}$ and corresponding effective stress range $\Delta\sigma_e$, as can be seen in figure 6.20. On the other hand, the non-proportional damage contribution $D_{NP} = \int_{\tilde{AB}} r' \cdot |\sin\theta| ds'$. MLP has been demonstrated to be an effective tool for considering non-proportional load path contributions to fatigue damage accumulation.

6.8. Damage accumulation

Fatigue damage is a progressive process in which response history is important. This is referred to as sequence effects and explains why a high-low load cycle produces lower damage than a low-high cycle [23, 38]. Deul [38] and Hectors et al. [59] compounded and reviewed current literature for a large array of different damage accumulation models which can be split up into three categories:

1. Continuum mechanics: Material is modelled as an intact geometry
2. Fracture mechanics: Material is modelled as a cracked geometry
3. Damage mechanics: Material is modelled as a deteriorating continuum

As established in section 6.4, a stress-based, intact geometry stress parameter is the most suitable approach for a multiaxial stress response investigation as described in this literature review. Hence, only continuum mechanics-based damage accumulation models will be considered from this point onwards.

Within continuum mechanics-based damage models a further distinction can be made between linear ($D = \sum \{n_i(S_i)/N_i(S_i)\} \leq 1$) and non-linear models $\left(D = \sum \left[C_i \cdot \{n_i(S_i)/N_i(S_i)\}^{f(S_i)}\right] \leq 1\right)$ [23, 38, 59], although D may take on a smaller value depending on recommendations from design guidelines to account for various processes that affect fatigue lifetime (e.g. mean stress, design factors, environmental exposure). Comprehensive comparisons and reviews have been done of linear and non-linear damage accumulation models, however, a model that is able to outperform linear damage accumulation is not available at the time of writing [23, 59].

6.8.1. Palmgren-Miner

Palmgren first introduced the notion of linear summation of fatigue damage, and Miner was the first to express this notion in the mathematical form [46, 125]. This methodology can be referred to as the Palmgren-Miner rule, Miner Rule or Linear Damage Rule (LDR) and is the best-known damage accumulation model and is often recommended by design guidelines (see section 6.9). The LDR assumes that constant work is absorbed per cycle and a characteristic amount of work is absorbed at failure [46]. It can mathematically simply be expressed as the cycle ratio. The relation between damage and cycle ratio can be captured in an S-N curve (see section 6.2.1).

$$D = \sum \{n_i(S_i)/N_i(S_i)\} \leq 1 \tag{6.12}$$

It is worth noting though, that a linear damage model can contain a resistance-induced damage accumulation non-linearity if a 2-slope SN curve is applied. This is relevant when considering MCF and HCF, as the two slopes account for different fatigue mechanisms [19, 23].

Despite the wide implementation of the Miner rule, it is important to be mindful of the shortcomings posed by this method, such as neglecting load interaction and load sequence effects. Load interaction effects mean that the damage induced by a load cycle is not only dependent on the amplitude of the load cycle but also the damage caused by previous cycles. This is caused by plasticity at the weld root notch, which may be larger or smaller depending on previous load cycles [125]. Furthermore, as discussed in section 6.1.4, the loading of a specimen can redistribute mean stresses, thus affecting the damage contribution of further cycles [38, 125].

Load interaction effects are responsible for load sequence effects, which are the effect of the order of loads on a specimen. For example, a high-low load sequence does not produce the same damage as a low-high load sequence. This makes a sensible damage prediction for VA loading a lot more difficult. There are, however, models available to improve damage prediction for VA loaded structures described in Deul [38], Fatemi et al. [46], and Hectors et al. [59], which will not be covered in this literature review as it is out of the scope of a subsequent investigation.

6.9. Recommendations in design guidelines

In this section, a brief review will be conducted of current design guidelines applicable to offshore or marine structures. Starting with Bureau Veritas in section 6.9.1, ABS in section 6.9.2 and Eurocode 3 in section 6.9.3. Next IIW design code will be reviewed in section 6.9.4 and finally DNV in section 6.9.5.

6.9.1. Bureau Veritas

Bureau Veritas (BV) has released a classification guideline for FOWT [139, 140] and recommends the use of NSC and HSSSC using both prescribed Stress Concentration Factor (SCF)s and the method described with linear surface extrapolation for fatigue assessment. Interestingly, BV does not make a distinction between a hotspot type A and hotspot type C, i.e. a notch along the weld end or a notch along the weld seam respectively, maintaining the definition used by Hobbacher [60]. Damage accumulation is calculated with the Palmgren-Miner method. No measures are taken for multiaxial fatigue.

6.9.2. American Bureau of Shipping

American Bureau of Shipping (ABS) has a certification guide available for FOWT, access was not available, however. For offshore structures in general, ABS recommends NSC, HSSSC using both prescribed SCFs and the method described in section 6.4.2 with linear surface extrapolation. No comment on ENSC is made. Furthermore, no indication is made that hotspot types have an effect on fatigue assessment. ABS also applied the Palmgren-Miner method for damage accumulation. No measures are taken for multiaxial fatigue [128].

6.9.3. European Committee for Standardization: Eurocode 3

Eurocode is a series of 10 European Standards for the built environment, of which number three is related to steel structures. It is written by the European Committee for Standardization (CEN). The section considered here is EN 1993-1-9: Fatigue [132]. Although not specific for marine or offshore structures, it is a guideline for all steel structures.

Eurocode 3 recommends the use of NSC and HSSSC using prescribed SCFs. No indication is made that hotspot types affect fatigue assessment, and the Palmgren-Miner rule is used for damage accumulation. Eurocode 3 does specify separate criteria for uniaxial, CA multiaxial and VA multiaxial fatigue. For multiaxial fatigue, a modified Gough-Pollard (see section 6.3.2) is applied, as shown in equation (6.13). The denominators represent the fatigue strength at 2×10^6 cycles (as defined by CAT class), which is the number of cycles in the fatigue resistance that shows a slope change. Both CA and VA loading can be included in this criterion in the numerator by converting the VA loading of both stress and shear components to a CA equivalent load, resulting in the same amount of damage at 2×10^6 cycles [85, 132].

$$\left(\frac{\sigma_a}{\sigma_{a,N_{CAT}}}\right)^3 + \left(\frac{\tau_a}{\tau_{a,N_{CAT}}}\right)^5 \leq 1 \tag{6.13}$$

However, as the total fatigue damage is a result of the linear summation of the damage contributions of the two modes, interaction is not accounted for after all [18].

6.9.4. International Institute of Welding

The International Institute of Welding (IIW) recommends the use of NSC and HSSSC using both prescribed SCFs and the method described with linear surface extrapolation, and ENSC for fatigue assessment. IIW also does not make a distinction between a hotspot type A and hotspot type C, i.e. a notch along the weld end or a notch along the weld seam respectively [60]. IIW also distinguishes between uniaxial, CA multiaxial and VA multiaxial fatigue. IIW differentiates between multiaxial fatigue CA and VA loading, using separate Gough-Pollard based equations. Much in the same way as defined in Eurocode 3, the denominators are equal to the fatigue resistance at 2×10^6 cycles as defined by the FAT class. For both CA and VA loading CV is set to 1 for proportional loading and 0.5 for non-proportional loading. For VA loading an equivalent damage stress $\sigma_{eq}(D)$ for specified damage D_{spec}. However, as the total fatigue damage is a result of the linear summation of the damage contributions of the two modes, interaction is not accounted for after all [18].

IIW CA loading:

$$\left(\frac{\sigma_a}{\sigma_{a,N_{FAT}}}\right)^2 + \left(\frac{\tau_a}{\tau_{a,N_{FAT}}}\right)^2 \leq CV \tag{6.14}$$

IIW VA loading:

$$\left(\frac{\sigma_{eq}(D)}{\sigma_{a,N_{FAT}}}\right)^2 + \left(\frac{\tau_{eq}(D)}{\tau_{a,N_{FAT}}}\right)^2 \leq CV \tag{6.15}$$

Damage accumulation is calculated with the Palmgren-Miner method, with a slight modification. As the IIW code is still relatively new and under development, the guidelines are quite conservative [44, 60, 85]. IIW recommends that for variable amplitude a damage sum $D_{spec} = 1$ may be too conservative and a damage sum $D_{spec} = 0.5$ is recommended instead. For situations with high mean stress fluctuations, a $D_{spec} = 0.2$ is recommended.

An aspect at which the IIW guidelines are unique with respect to the aforementioned design codes is a specification on what response conditions constitute multiaxial stress response. The effect of shear (mode III) stress may be neglected if either:

- The nominal shear stress range is less than 15 % of the normal stress range.
- The fatigue damage sum due to the shear stress range is lower than 10 % of that due to the normal stress range.

6.9.5. Det Norske Veritas

DNV also has a certification guide available for FOWT, which does not specify any fatigue assessment methods, DNV-CG-0129 and DNV-RP-C203 however do [8, 10]. In the fatigue assessment guide for ship structures NSC, HSSSC using both prescribed SCFs and the method described in section 6.4.2 with linear surface extrapolation and finally ENSC are recommended. Furthermore, DNV explicitly distinguishes between hotspots of type A, B and C, unlike BV and IIW. Finally, Palmgren-Miner damage accumulation rules are used.

In order to assess multiaxial fatigue, DNV adopts a maximum principal stress definition, as fatigue cracks tend to grow perpendicular to the maximum principal stress, as pictured in figure 6.21 [10]. As previously established, for uniaxial and CA multiaxial loading the direction of the maximum principal stress remains constant, however, for VA multiaxial loading this direction changes [85]. DNV recommends different fatigue resistance curves depending on the angle ϕ between the principal stress direction and the normal to the weld. In order to assess the total damage caused, the damage due to stresses normal and parallel to the weld toe is evaluated separately ($D_\perp$ and $D_\parallel$).

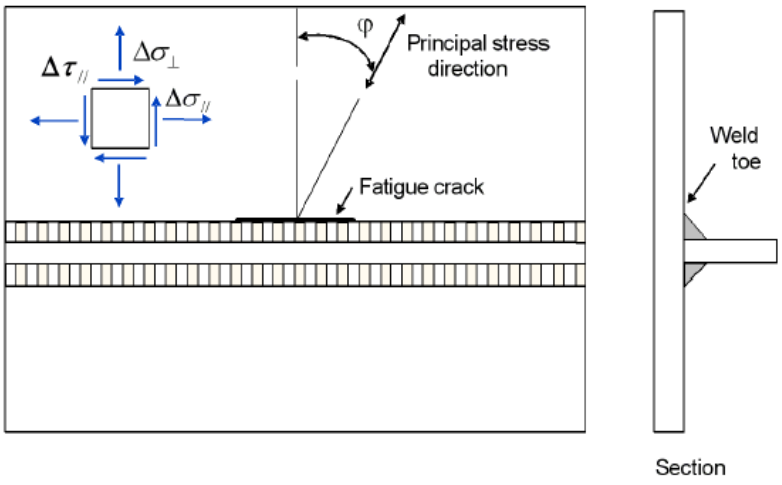


Figure 6.21: Maximum principal stress used by DNV regulations for multiaxial stress states. Also clearly showing direction of crack propagation [10, p .23].

This methodology has four major flaws;

1. Interaction between components is not considered as $D_{\perp}$ and $D_{\parallel}$ are determined separately.
2. This method cannot account for changing the direction of maximum principal stress, as is expected for non-proportional loading. DNV recommends a bandaid solution of splitting up the time series into chunks which have a $\delta\phi \approx 5°$. If the time series exhibits significant variation of principal stress direction, this approach will no longer be valid as fatigue damage is no longer dominated by principal stress direction. A Critical Plane Method must hence be adopted (see section 6.5).
3. The entire methodology assumes that maximum principle stress is a valid method of correlating multiaxial stress. Bäckström et al. [14] and Dong et al. [39] demonstrated that the maximum principle stress range fails to provide a reasonable correlation for both proportional and non-proportional multiaxial loading.
4. Method does not distinguish between phase shift or frequency-induced proportionality. Furthermore, as the fatigue resistance curve is selected based on principal stress directions and mode-I-based slope, torsional loading results in lower damage, due to the difference in power coefficients [83].

7

Methodology

The literature review conducted in the previous chapters on coupled dynamic motion and stress response analysis, in combination with subsequent fatigue analysis, provided the information required to conduct an investigation to answer the research question and provided the following scope definitions. In section 7.1 the research gap will be identified, followed by the hypothesis in section 7.2. Finally, in section 7.3, a structural approach to the investigation will be outlined.

7.1. Research gap

As became evident from the literature review, very little research has been conducted regarding the fatigue analysis of FOWT substructures in general. Most of the floating wind fatigue-related research has been conducted on the tower and blades. As explained in section 5.4 this largely has to do with complications in the modelling process and the implications of the rigid body assumption on structural analysis. No (published) investigations have been conducted regarding multi-axial fatigue in FOWT.

This defines a large research gap, which is realistically too large to fill within the timeframe of a subsequent investigation in the form of a thesis. Hence, subsequent work will focus on an aspect within multi-axial fatigue for FOWT application. As a substructure of the considered size may end up containing hundreds of meters of welds, not every weld requires the same level of scrutiny; hence, a distinction between critical and non-critical can be made. An example of critical weld seams in the considered TLP are the welds connecting the pontoons to the central column. This means 8 welded connections in total, 2 closed, and 6 open, as illustrated in figure 7.1.

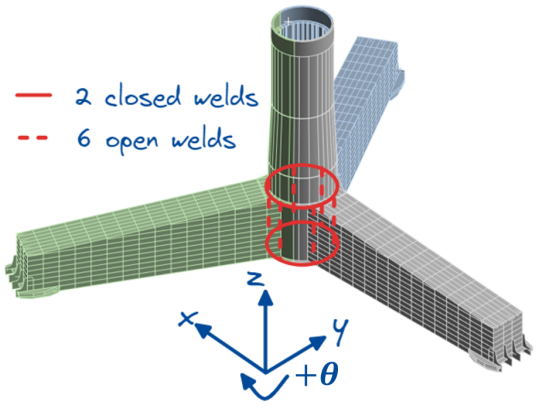


Figure 7.1: The considered research will investigate the structural stress response in 8 critical weld seams, 2 closed and 6 open.

7.2. Research hypothesis

Given the number of rules and regulations in regard to fatigue design for offshore focused on uniaxial stress assessment, mode-{I} response is expected to be governing. That being said, engineering of FOWT, substructures, in particular of the TLP type presents a new challenge of a restrained floating structure subject to large excitation forces both from the wave and wind environment. It is, therefore, expected that a degree of multi-axiality might also occur due to the multiaxial non-proportional (random) VA loading the structure is subject to. The locations with these complex stress states are, however, not expected to be the driving areas for fatigue failure.

7.3. Research setup

In the literature review conducted in part I, it was concluded that in order to achieve the research goals posed in chapter 2 and answer the main research question, a specific type of model needs to be constructed. The various subsystems are to be coupled by means of a loosely coupled dynamic model that considers separate models for aerodynamic, hydrodynamic, and mooring response. A novel hybrid flexible-rigid formulation is applied to account for both rigid body motions and local elastic deformations. This model is to be evaluated in the time domain, such that a traction-based structural stress assessment model can be applied to derive time domain mode-{I,III} stress response signals.

The process of building, validating and applying such a model can be split up into distinct phases, which allows for the work to be split into distinct parts, to which this thesis will be structured.

7.3.1. Phase 1: Coupled System Dynamics

This phase will revolve around familiarization with the TLP system and its subcomponents from a rigid body dynamics perspective for both loading and motion response. The work performed in this phase seeks to take the numerical representation of the metocean environment as input, simulate the motion response and provide the loading input to perform structural response analysis. This is done using a loosely coupled dynamic model.

7.3.2. Phase 2: Dynamic Structural Analysis

In this phase, a hybrid flexible-rigid model must be constructed. Using the input from phase 1, loads are mapped to the structural model to allow for a structural response analysis to be conducted. By applying the traction-based structural stress method, the stress can be resolved from the nodal forces and moments. The resulting temporal stress signals must be processed to assess the extent of multiaxiality at various levels of detail (element, node and weld).

7.3.3. Phase 4: Application

Having constructed a model that can take an environmental representation as an input signal and produce a multiaxial stress response signal, this phase will derive and apply a set of environmental conditions compatible with the rest of the model. These environmental conditions are to test the performance of the substructure in variation loading conditions.

7.3.4. Phase 5: Results and evaluation

In the final phase, the various load cases applied to the derived system will be applied and analysed using the proposed post-processing methods. The resulting data will be evaluated to answer the research question and subquestions.

Part II

Modelling

8

Coupled System Dynamics

The literature review conducted in part I concluded that a specific type of model is required to investigate multiaxial stress response for FOWT. This chapter will discuss the first part of this model, the loosely coupled dynamic model, which facilitates the hybrid flexible-rigid formulation. The various subcomponents of this model will be handled separately, and the construction and validation of the model used in this thesis will be presented and discussed. To start, in section 8.1, the structure considered in this thesis is introduced. In section 8.2, the definitions and properties of the rigid body system will be covered. This is followed by the multi-disciplinary submodels for hydrodynamics, aerodynamics and mooring in sections 8.3 to 8.5. Next, in section 8.6, the coupling of these submodels is discussed. Finally, in section 8.7, the key findings in this chapter are reiterated.

8.1. System overview

The structure that will be considered in this thesis is a TLP designed by Bluewater Energy Services (Bluewater), whose focus lies on the substructure and mooring system, as the tower and RNA are outsourced. Pictured in figure 8.1 is the substructure consisting of a central column and three protruding pontoons. At the end of each pontoon are two mooring lines connecting the structure to the seabed by means of tensioned mooring lines. Unlike the catenary mooring, tension-leg mooring has no chain laid out on the seabed to generate a restoring force. Instead, this force is generated by the tensile stretch of the line [93]. As can be seen well, the mooring lines are installed under a small angle between the seabed and the mooring line. This allows the vertical and transverse response to be tuned to the desired behaviour.

The considered turbine is a three-blade, upwind, pitch-regulated, direct drive horizontal axis wind turbine, more specifically, the NREL 15MW Offshore Reference Wind Turbine, which includes a controller, also referred to as IEA-15-240-RWT [49].

8.2. Rigid Body Properties

As discussed in chapter 5, the structure's dynamic motion is considered a superposition of a rigid body motion and a structural deformation. For rigid body motions, the terms of Cummins equation (8.1) must be derived.

$$(\mathbf{M}+\mathbf{A})\,\ddot{\vec{X}}+\int_0^\infty \mathbf{B}(\tau)\cdot\dot{\vec{X}}(t-\tau)\,dt+\mathbf{C}\vec{X}=\vec{F}(t) \tag{8.1}$$

As with any rigid body analysis, static properties are required for the mass matrix [**M**], as shown in equation (8.1). As established previously, the total FOWT system consists of multiple subsystems. The documentation for each of these subsystems expressed rigid body properties within a subsystem-bound local axis system, as can be seen in figure 8.1. In sections 8.2.1 to 8.2.4, these properties are derived for the various subsystems. Important to note that the centre of gravity is expressed in the still water line (swl) bound axis system, whereas component inertia is expressed concerning the component centre

of gravity. The contribution of the Steiner term to the total system inertia is accounted for separately. Finally, in section 8.2.5, the rigid body properties of the combined system are derived.

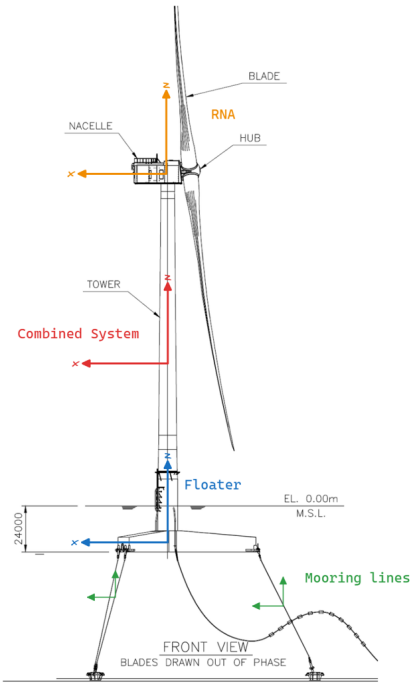


Figure 8.1: Axis system for the different subsystems considered, as well as the total combined system

8.2.1. Floater

The rigid body properties of the floater follow from a 3D CAD model and contain all structural elements. This means that primary, secondary, and tertiary steel have been modelled, including grating. Primary steel is the primary load-bearing material, whereas secondary steel contains items such as the intermediate platforms supporting the grating. Finally, tertiary steel contains items such as ladders, cages and handrailings. Although secondary and tertiary steel and grating do not contribute to the structural strength of the TLP, these items do contribute to the total mass and inertia and must hence be considered for the rigid body properties of the floater. Secondary and tertiary steel will not be modelled in the FEA calculations hereafter.

This information can be presented as follows:

Table 8.1: Substructure rigid body properties

		COG (w.r.t swl			Mass Inertia $\times 10^6$ (w.r.t floater COG) [kgm^2]					
Item	**Mass [t]**	**X [m]**	**Y [m]**	**Z [m]**	**Ixx**	**Ixy**	**Ixz**	**Iyy**	**Iyz**	**Izz**
Floater	2,854.5	-0.01	-0.03	-14.93	1151.22	0.31	1.15	1150.60	3.12	1719.66

8.2.2. Tower

Given the open-source nature of the turbine platform made available by NREL, the system is subject to periodical updates stimulated by community feedback. Although the publication *"IEA Wind TCP Task 37: Definition of the IEA Wind 15-Megawatt Offshore Reference Wind Turbine"* from March 2020 [49] has not been updated since publishing, there have been numerous iterations in the design, some more important than others. In addition to this, NREL has published a reference model for fixed and floating wind applications. In their report NREL state *"Note that when a floating substructure is used, the frequency requirements and boundary conditions will shift such that a stiffer tower is required. Therefore, the tower geometry presented here will be replaced with one better suited for a* [floating] *platform."* [49, p. 21], but subsequently

never update the report to contain the tower properties for floating application. These versions are, however, available in the GitHub repository [17].

Before blindly selecting the floating tower, it is important to consider that the floating tower is designed for a semi-submersible substructure and is considered to be grossly overproportioned to avoid resonance with the floater motions. The current version of the floating tower is a quick fix to an issue raised by another user, demonstrating that the old floating tower design caused significant resonance. This, combined with the Bluewater TLP, which is designed to support the fixed tower, are the reasons that the fixed tower is considered.

There is, however, a small alteration to the NREL design, which is the location of the interface. NREL has designed for an interface height of +15m, whereas the Bluewater TLP considers an interface height of +18m. In order to preserve the design of the rest of the system, the interface geometries at the substructure and nacelle, as well as the hub height, must remain unchanged. This can be done with linear scaling along the z-axis of the tower by a factor of 0.977, which has a near-negligible effect on the structural properties of the tower and allows for seamless integration with the existing nacelle and floater design. The rigid body properties for the scaled tower, as considered in this thesis, are presented in table 8.2.

Table 8.2: Scaled NREL fixed tower rigid body properties

		COG (w.r.t tower base)			Mass Inertia (w.r.t COG) $\times 10^6$ [kgm^2]					
Item	**Mass [t]**	**X [m]**	**Y [m]**	**Z [m]**	**Ixx**	**Ixy**	**Ixz**	**Iyy**	**Iyz**	**Izz**
Scaled Tower	833.7	0	0	75.37	1,057.7	0	0	1,057.7	0	13.3

8.2.3. Rotor Nacelle Assembly

The rotor consists of the blades and hub, and the nacelle houses almost all of the electrical generation systems. Although the nacelle is a term referring to the contents of the entire housing body, the exact components are not of interest in the scope of this investigation and will hence be referred to as the umbrella term *nacelle*. These systems which do not contribute to the structural strength of the floater, do have mass and inertia and must hence be included in the dynamic simulations. In figure 8.2, the RNA for the IEA-15-240-RWT can be seen.

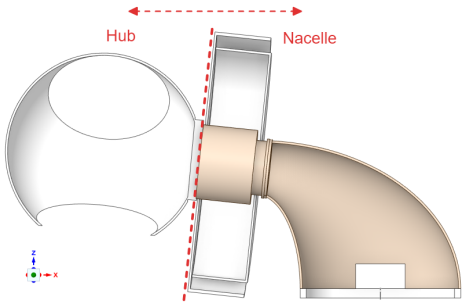


Figure 8.2: Cross section of the IEA-15-240-RWT hub and nacelle, turbine blades are not rendered (based on geometry from GitHub repository [17])

The rigid body properties of the hub and nacelle can be copied from the specifications supplied by NREL. On further inspection of the reported values of the blades, it had to be concluded that these were incorrect for the simple reason that it is geometrically impossible for a cone-shaped rotor plane (due to the upwind pre-curve of the blades) to have its centre of gravity lie at the tip of the cone. This discrepancy has been raised with the developers at NREL and has since been fixed.

Table 8.3: IEA-15-240-RWT RNA rigid body properties [17]

Item	Mass [t]	COG (w.r.t swl)			Mass Inertia (w.r.t component COG) $\times 10^6$ [kgm^2]					
		X [m]	Y [m]	Z [m]	Ixx	Ixy	Ixz	Iyy	Iyz	Izz
Nacelle	675.1	-4.53	-0.14	148.68	9.91	0.43	2.49	10.86	-0.22	10.36
Hub	69.4	-11.42	0.00	150.85	0.97	0.00	0.00	0.62	0.00	0.62
Blades	205.2	-17.4	0.00	174.85	1,039.12	-53.73	87.31	650.52	-83.72	661.35

8.2.4. Tendons

As discussed in section 8.3.1, the geometry of the tendon connectors at the ends of the pontoons is not included in the hydrodynamic diffraction model. The coordinates of their connection points, however, are. These are reflected in table 8.4, as well as the anchor coordinated.

Table 8.4: Coordinates of tendon connectors and anchors, expressed in body boud coordinate system with the origin at SWL

Type	Pontoon number	Item number	X [m]	Y [m]	Z [m]
Connector	Pontoon 1	1	-45.99	-2.08	-23.07
		2	-45.99	2.08	-23.07
	Pontoon 2	3	24.79	-38.78	-23.07
		4	21.19	-40.86	-23.07
	Pontoon 3	5	21.19	40.86	-23.07
		6	24.79	38.78	-23.07
Anchor	Pontoon 1	1	-75.73	-2.08	-135.00
		2	-75.73	2.08	-135.00
	Pontoon 2	3	39.66	-64.54	-135.00
		4	36.06	-66.62	-135.00
	Pontoon 3	5	36.06	66.62	-135.00
		6	39.66	64.54	-135.00

Once the coordinates of pontoon-tendon connectors and anchors are known, the stretched tendon length can be determined as the shortest distance between coordinates in 3D space:

$$L = \sqrt{(x_a - x_c)^2 + (y_a - y_c)^2 + (y_a - z_c)^2} = 115.891 \text{ m} \tag{8.2}$$

The mass follows from the tendon-specific mass of 108.5 kg/m (internal data reference) as suspended in water, as the entire tendon remains submerged at all times. As the tendons are homogeneous in axial direction, it can be assumed that the centre of gravity will be located halfway along each line. Each tendon also has a negligible influence on the total system inertia [68].

Table 8.5: Tendon rigid body properties, expressed in body boud coordinate system with the origin at SWL

Item	Mass [t]	COG (w.r.t swl)			Mass Inertia (w.r.t COG) [kgm^2]					
		X [m]	Y [m]	Z [m]	Ixx	Ixy	Ixz	Iyy	Iyz	Izz
Tendon 1	12.6	-61.41	-2.10	-79.03	0	0	0	0	0	0
Tendon 2	12.6	-61.41	2.10	-79.03	0	0	0	0	0	0
Tendon 3	12.6	32.52	-52.14	-79.03	0	0	0	0	0	0
Tendon 4	12.6	28.89	-54.24	-79.03	0	0	0	0	0	0
Tendon 5	12.6	28.89	54.24	-79.03	0	0	0	0	0	0
Tendon 6	12.6	32.52	52.14	-79.03	0	0	0	0	0	0
Total	**75.4**	**0**	**0**	**-79.03**	**0**	**0**	**0**	**0**	**0**	**0**

8.2.5. Total FOWT System

Using the rigid body properties derived in sections 8.2.1 to 8.2.4, the total mass and centre of gravity for the FOWT system can be determined as summarized in table 8.6.

Table 8.6: Summary of rigid body properties, expressed in body boud coordinate system with the origin at swl of the complete FOWT system

		COG (w.r.t SWL)		
Item	**Mass [t]**	**X [m]**	**Y [m]**	**Z [m]**
Floater	2,854.5	-0.01	-0.03	-14.93
Tower	833.7	0.00	0.00	75.37
Nacelle	675.2	-4.53	-0.14	148.68
Blades	205.2	-17.43	0.00	150.85
Hub	69.4	-11.42	0.00	150.74
Tendons	75.4	0.00	0.00	-79.04
Total	**4,713.3**	-1.61	0.00	34.9

Given that the inertia of each subsystem is expressed with respect to the subsystem Center of Gravity (COG), the total system inertia cannot be considered as just the sum of all components. Using the Parallel Axis theorem, inertia with respect to a body-bound coordinate system can be expressed in terms of a global fixed axis system. In equations (8.3) and (8.4) below the coordinate vector $[x_g, y_g, z_g]$ is the position of the body-bound coordinate system relative to the global fixed axis system, i.e. the position of each component's COG relative to the total system COG, as determined in table 8.6.

Applying the formulations in equations (8.3) and (8.4) results in the total inertia contribution.

$$(I_{xx})_O = I_{xx} + m(y_g^2 + z_g^2), \quad (I_{yy})_O = I_{yy} + m(x_g^2 + z_g^2), \quad (I_{zz})_O = I_{zz} + m(x_g^2 + y_g^2) \tag{8.3}$$

$$(I_{xy})_O = (I_{yx})_O = I_{xy} + m x_g y_g, \quad (I_{xz})_O = (I_{zx})_O = I_{xz} + m x_g z_g, \quad (I_{yz})_O = (I_{zy})_O = I_{yz} + m y_g z_g \tag{8.4}$$

8.2.6. Tendon elastic stiffness

The tendons are modelled as linear springs in the dynamic motion analysis; hence the stiffness for each tendon must be determined. Manufacturers of offshore mooring lines specify tendon axial stiffness $[EA]$, which can be used to calculate the spring stiffness in equation (8.5) based on the unstretched length of the tendon.

$$k = \frac{E \cdot A}{l_0} \tag{8.5}$$

In order to determine the unstretched length of each line, first, the force on each line must be determined. Assuming static hydrostatic conditions,

$$\Sigma F_z = \nabla \rho g - mg - \frac{6 \cdot T_{\text{tendon}}}{\cos\theta} = 0 \tag{8.6}$$

$$T_{\text{tendon}} = \cos(15°) \cdot (97.07 - 46.43) \times 10^6 = 8.74 \text{ MN} \tag{8.7}$$

Hence, the unstretched line length and line stiffness follow from solving the below with the mooring line length of 115.89m (8.2);

$$F_{\text{tendon}} = k \cdot L = k \cdot (l_0 + \delta l) \tag{8.8}$$

This results in an unstretched length of 115.00m and a line stiffness of 19.83 MN/m. It should be noted that this approach does create a minor circular dependency, as the mass of the tendon is calculated using the stretched length of the line instead of the unstretched length. Therefore, the true stiffness of the mooring line is slightly larger. This difference is, however, negligible concerning the total system mass. A second consideration is that this approach only considers a balance in vertical forces. As the centre of gravity of the total system does not lie along the z axis of the system, it will pitch forward, resulting in an uneven mooring line tension in static conditions. The difference in tension entirely depends on the azimuth angle of the yaw bearing between the nacelle and tower, i.e. if the rotor

plane has a yaw angle relative to the tower and substructure, the centre of gravity will lie elsewhere. Hence, the mooring pretension does not consider this *'imbalance'*. This results in the first few timesteps in a dynamic simulation requiring the real static equilibrium to be found. This comprises a part of the transient effects further discussed in section 10.3.3.

8.2.7. System Natural Modes

The TLP FOWT system, as presented here, has natural frequencies for the different degrees of freedom. These frequencies were derived from a spectral modal analysis using AQWA and presented in table 8.7. Notably, the natural frequency for heave is significantly higher than the rest due to the high mooring stiffness, particularly in the heave direction.

Table 8.7: Frequency and period for first natural frequency for the rigid system modes

DOF	Frequency ω_n [Hz]	Frequency ω_n [rad/s]	Period T_n [s]
x	0.031	0.195	32.142
y	0.031	0.195	32.142
z	0.496	3.114	2.017
θ	0.273	1.715	3.663
ϕ	0.273	1.715	3.663
ψ	0.422	0.067	14.906

8.3. Hydrodynamic model

In this section, the various components of the hydrodynamic model are covered. Starting with the mesh in section 8.3.1 and followed by the first order forces in section 8.3.2. Next, in section 8.3.3, an explanation will be offered regarding the exclusion of the second order hydrodynamic forces. Finally, in section 8.3.4, the combination of potential-based hydrodynamic loading with a viscous correction will be explained.

8.3.1. Hydrodynamic mesh

The first type of mesh that will be considered in this thesis is the hydrodynamic mesh of the structure. To maintain the same geometrical baseline for both the structural and hydrodynamic models, the structural geometry will be used as a starting point. The structural model contains stiffeners and bulkheads, which do not contribute to the hydrodynamics of the structure and will interfere with the hydrodynamic mesh. Other components do not need to be included either, as their hydrodynamic contribution may be considered negligible, as well as their negative influence on the meshing process. These components are the structural supports for the electrical export cable, which also serve as a connection between pontoons, as well as the tendon connectors, as pictured in figures 8.3 and 8.4 respectively.

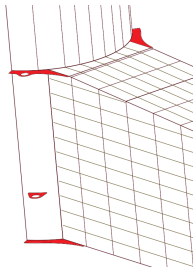


Figure 8.3: Radial flanges between pontoons, connected to the central column. Also, serves as structural support for power export cables.

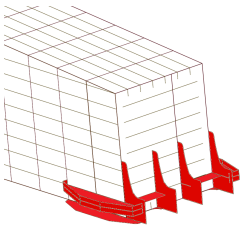


Figure 8.4: Tendon connectors structural configuration.

Removing these features results in the hydrodynamic shell geometry as shown in figure 8.5. In this thesis, the meshing functionality offered by ANSYS will be used to generate meshes. Although different software packages offer meshing functionality that is available for use in the scope of this thesis

(including open-source packages), ANSYS meshing is well-known to be sophisticated and user-friendly. An added benefit is the integration of ANSYS meshing in all other ANSYS software packages, allowing for effortless data flow downstream.

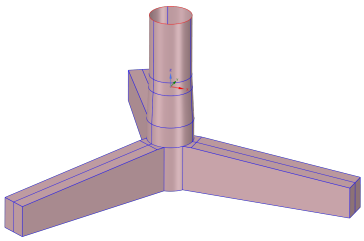


Figure 8.5: Hydrodynamic plate structure used for the meshing process

Although the ANSYS mesher is immediately capable of generating a complete mesh of the structure pictured in figure 8.5, some additional mesh controls must be implemented to obtain a mesh fit for hydrodynamic applications. This is because asymmetries in the mesh may cause unexpected coupling terms in the diffraction analysis, resulting in inaccurate motions. These issues are identified as follows:

1. Slanted mesh edges on surfaces, as can be seen in figure 8.6. This is caused by the taper of this section, resulting in all vertical edges running at a slant instead of perfectly vertical. This was solved by applying face meshing controls.
2. Forced triangular elements in unexpected locations caused by poor mesh control on surrounding surfaces.
3. Asymmetrical mesh on surfaces where the mesh is expected to be symmetrical. This can be solved by decreasing the mesh size or adding face meshing controls. The latter increases computational time.
4. Non-uniform element size as a result of the mesh of the lid of the centre column. This may cause unexpected coupling terms in the diffraction analysis.
5. Asymettrical meshing of the lid of the centre column. This was solved using mesh controls, as well as exploiting the symmetry of the plate, as can be seen in figure 8.6, resulting in a symmetrical mesh.

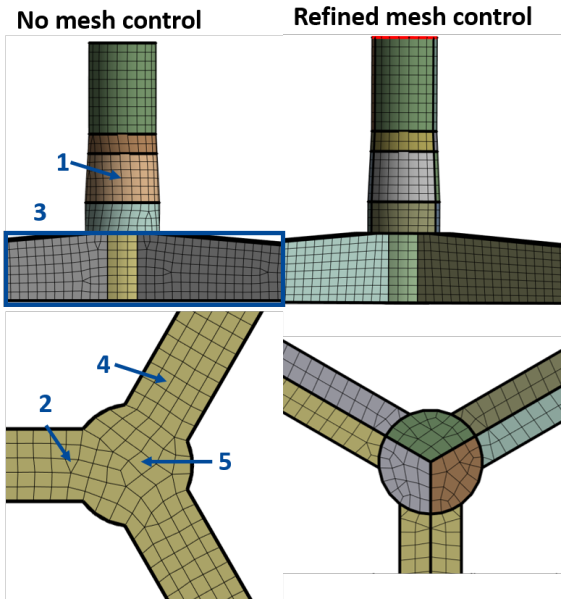


Figure 8.6: Importance of refined mesh control in order to avoid undesirable mesh behaviour

8.3.2. First Order Hydrodynamics: Diffraction analysis

In this section, the setup and validation of the diffraction analysis will be discussed in order to derive the added mass, damping and stiffness matrices required for dynamic motion analysis. In section 8.3.2.1, the hydrodynamic model is introduced and validated in section 8.3.2.2.

8.3.2.1 Model setup

Using a diffraction analysis, the frequency-dependent matrices in the Cummins equation (8.1) can be derived. The setup of a diffraction model is fairly trivial, and the procedures for different software packages are largely the same. As input, the hydrodynamic geometry, the structure's rigid body properties (see section 8.2) and water depth are required.

Although a TLP is a floating structure, there is a very distinct difference with other freely floating or catenary moored vessels, being that the mass of the fluid displaced is not in equilibrium with the mass of the structure, i.e. $m \neq \rho\nabla$. This is due to the significant loading of the tendons, effectively pulling down the structure. Most diffraction software packages contain functionality to conduct 'sanity' checks automatically, including hydrostatic equilibrium. As a TLP cannot adhere to this principle by design, the software package issues a warning. This warning can, however, be safely ignored as object mass is not of consideration in diffraction analysis, as demonstrated in appendix A as none of the terms of the original set of equations nor the integration boundaries contain any mass-related terms. It is only when computing motion response $(x, \dot{x}, \ddot{x})$ that mass and inertia terms are considered. Hence, the aforementioned warning can be ignored as the underlying physics and mathematics for diffraction are still valid, despite hydrostatic disequilibrium.

There are two important differences to note between ANSYS AQWA and HydroStar. The first of which is that the AQWA solver requires no less than 7 mesh elements over the shortest wavelength in order to guarantee solver convergence as well as the integrity of the output. Hydrostar does not present this limitation. The second important difference is that, unlike Hydrostar, AQWA does not support infinite water depth. This only presents an issue for very long waves, which may no longer be considered using deep water linear wave theory. From the dispersion relation, it follows that the boundary between deep and intermediate water conditions lies at $\omega = 0.956$ rad/s.

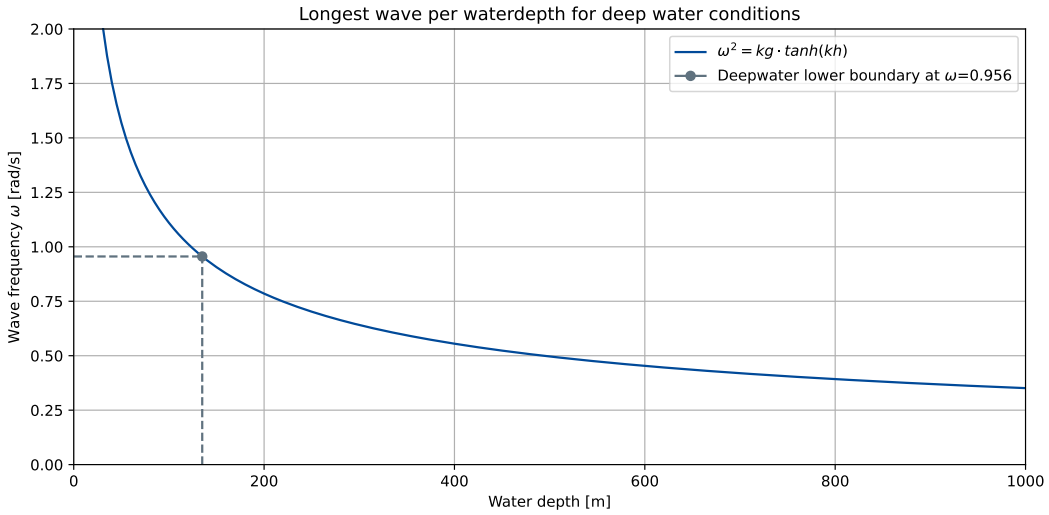


Figure 8.7: Longest wave that can be considered for each water depth using deep water theory

8.3.2.2 Mesh convergence and validation

As discussed previously, the hydrodynamic meshes are generated using the ANSYS meshing capabilities. To allow for a fair comparison, the ANSYS mesh is exported and converted to be used by HydroStar for validation purposes. The global axis system is defined with $+x$ pointing downwind. This convention is chosen as the AeroDyn computation package adopts this orientation. As such, head waves $\theta = 0$ travel in $+x$ direction.

Although formally, the convergence of $A(\omega)$ and $B(\omega)$ is sought after, presenting the convergence of these large matrices requires a very large number of plots to be considered. Instead, motion RAOs are considered, as these inherently include $A(\omega)$ and $B(\omega)$, and allow for a more meaningful interpretation of the convergence data. In appendix B figures B.1 to B.6 the motion response RAO is plotted for various heading angles for each degree of freedom.

The motion RAO results converge almost immediately for each mesh size, independent of the computational software used. Only for heave response was mesh sensitivity constituted around the first natural mode. In figure 8.8, a section of the heave RAO is isolated to provide a better picture of the convergence of the mesh around the first natural frequency of the structure. Here, it can be seen that the natural frequency converges with a mesh element size of 3000mm. Concerningly, though, the response amplitude appears to increase consistently for finer mesh sizes. This can only be explained with a numerical error, as this behaviour is only seen at a frequency of 0.297 rad/s in heave. Also plotted in figure 8.8 are the results of a simulation with a much smaller step size. Here, it can be seen that due to the step size, the natural frequency is not only slightly overpredicted but the maximum amplitude is significantly underpredicted by missing the true natural frequency, as the response is not computed for this excitation frequency. The 500 and 1000mm mesh sizes have, however, converged to the results of the model with the highly refined $\delta\omega$ step size. This approach, however, cannot be realistically applied in the scope of this thesis due to the required frequency range that must be covered using a limited number of step sizes, as the black line is derived for a very small frequency range and the smallest possible step size.

Although there is a non-negligible difference in predicted response behaviour at the first natural frequency, this frequency lies far out of the range of waves seen in the Korean Strait and, hence, does not have any practical implications.

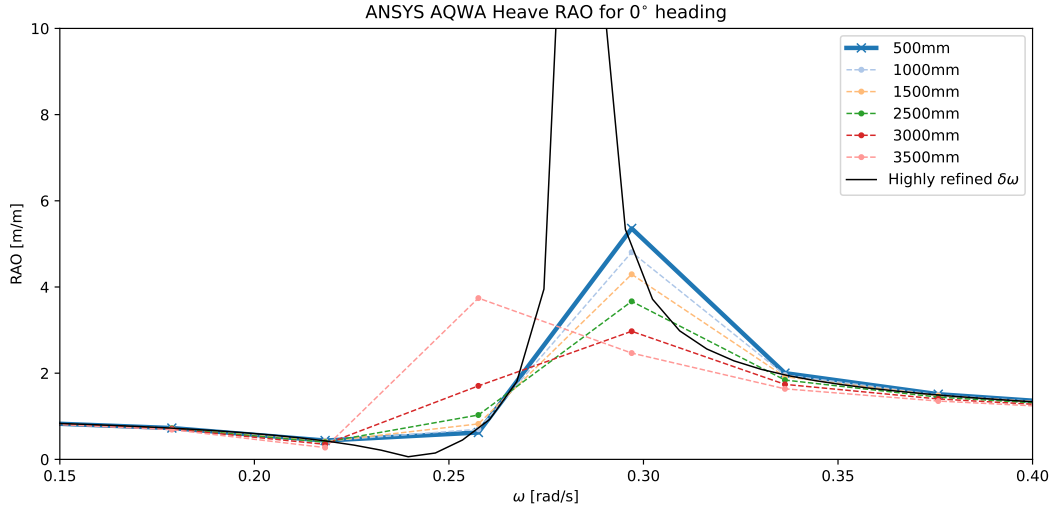


Figure 8.8: Zoomed in mesh heave RAO from AQWA illustrating the mesh convergence

The aforementioned sensitivity of the heave motion to the mesh element size is difficult to resolve due to restrictions imposed by AQWA in the form of a maximum number of diffracting panel elements that can be modelled, as well as a maximum number of frequencies considered in the calculation. In practice, this means that the mesh is restricted to elements > 475mm and a $\delta\omega$ step size of 0.039 rad/s. This step size is defined by the maximum wave frequency that can accurately be resolved for a given mesh; the rougher the mesh, the lower the highest resolvable wave frequency. Given environmental site conditions in the Korean Straight, a maximum wave frequency of 4 rad/s needs to be resolved. Furthermore, the first natural mode at 0.292 rad/s is far out of the range of the waves considered in the Korean Strait, as discussed in chapter 10. Hence, a mesh element size of 1000mm may be considered converged and validated using the independent HydroStar calculation. The natural frequency considered here is that of the pure hydrodynamic system, whereas the data presented in table 8.7 is for the total system. This provides further proof that the stiffness of the moored system significantly lowers the natural frequency.

Table 8.8: Maximum resolvable frequency depending on mesh element size

Mesh element size [mm]	Maximum resolvable frequency [rad/s]
3500	1.48
3000	1.61
2500	1.81
2000	2.05
1500	2.27
1000	2.96
500	4.18

8.3.3. Second-order Hydrodynamics: QTF analysis

In section 4.2.3, it was established that a FOWT is subject to second-order hydrodynamic loading. Not discussed in the literature review is the computational implementation of the QTF. The QTF is calculated using the first-order motion RAO resulting from a diffraction analysis [5]. To illustrate this, a simplified version of the applicable motion equation can be used to derive the RAO for a monochromatic incoming wave.

$$RAO(\omega) = \frac{x_a}{\zeta_a} = \frac{F_0}{C - [M + A(\omega)]\,\omega^2 + i\omega B(\omega)} \tag{8.9}$$

From the derivation above it can be seen that all RAOs contain a stiffness contribution. This is not a problem for rigid bodies, as the stiffness originates from the hydrostatic stiffness terms. However, for a non-diffracting flexible body, there is an extra term contributing to overall system stiffness. This is an issue for for most commercial diffraction software as the mathematical and physical derivations used require a rigid structure. Technically, it would be possible to run a diffraction analysis for rigid structures representing every possible deformation and choose the right submodel for each simulation. This is, however, not a realistic solution for practical implementation.

There are two feasible engineering solutions that allow for flexible tower effects to be considered in diffraction analysis, which consider the frequency independent terms in equation (8.9). The frequency-dependent terms $A(\omega)$, $B(\omega)$ follow from diffraction analysis. The proposed solution is to tune the mass and inertia matrix $[M]$ in order to shift the natural frequency of the approximated rigid system to a predetermined natural frequency of the flexible system. This is an iterative approach that must be redone for any changes to the system.

The second solution is to divide the flexible parts of the system into rigid subsystems interconnected with springs and dampers. Depending on the number of subdivisions of the system, the stiffness coefficients k_i, $k_{T,i}$ and damping c_i must be determined such that the flexible behaviour at the TLP-tower interface and tower-RNA is preserved. This process, as opposed to the previous solution presented, does not need to be redone unless changes to the tower are made.

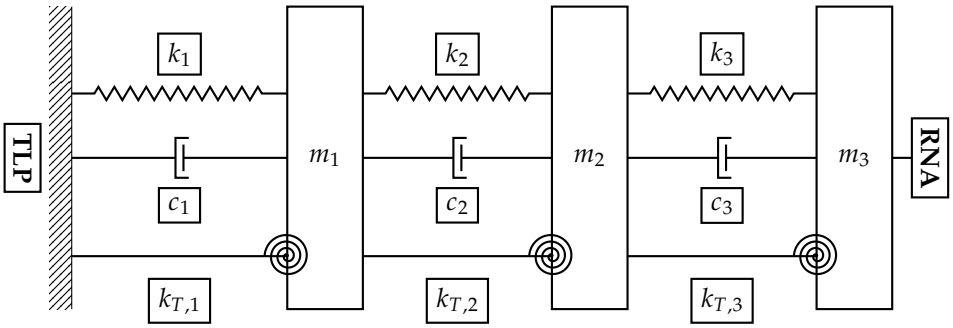


Figure 8.9: Approach for integrating flexible tower effects into diffraction analysis by replacing rigid tower by a number of subsystems connected by springs and dampers.

In a previous investigation conducted on the Bluewater TLP, [79] concluded that although second-

order forces are expected on the structure, hydrodynamic behaviour is dominated by first-order motions. There is no further literature that supports (or counters) this conclusion. Therefore, given the scope of this investigation, the conclusions of [79] as well as downstream technical issues discussed in section 8.6.1, it is deemed justifiable to exclude second-order hydrodynamic forces from this investigation.

8.3.4. Viscous damping

As was discussed in section 4.2.5, potential theory-based approaches cannot consider the effects of viscous damping due to the fluid being considered inviscid. However, as was concluded in section 4.2.5, the case study location, in the Korean Strait, most of the metocean spectrum is neither dominated by Morison loading nor potential loading, but rather a mixture of both. This poses an interesting modelling challenge.

As the hydrodynamic load model requires panel pressures to be available at a mesh element level for load mapping, the base of the hydrodynamic load model must be of potential theory type. Consider Morison's formulation for a moving cylinder in equation (8.10) from section 4.2.5. As can be seen, Morison loading consists of an inertia load and viscous load term. As the inertia term is already included in the potential theory approach, only the viscous drag term is required.

$$f = \underbrace{\frac{1}{2}\rho C_D D(u-v)|(u-v)|}_{\text{Viscous drag}} - \underbrace{(C_m - 1)\frac{\rho\pi D^2}{4}(\dot{u}-\dot{v})}_{\text{Inertia}} \tag{8.10}$$

This seems like a simple solution on paper; however, AQWA does not allow for individual terms to *'turned on'* or *'turned off'*. Instead, diameter (D), mass inertia coefficient (C_m) and damping coefficient (C_d) can be changed. By setting $C_m = 1$, the inertia term disappears, isolating the viscous drag contribution with unknowns D and C_d. These coefficients can be derived from model tests or CFD calculations and physically represent the diameter of a cylinder producing an equal resisting force to an incoming flow at an angle, as indicated in figure 8.10.

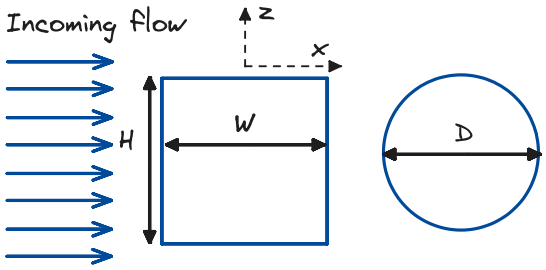


Figure 8.10: Illustration of the challenge of assigning an equivalent drag diameter for non-cylindrical bodies

As one can see, changing the inflow angle for a rectangle in a flow field results in an incoming flow angle-dependent equivalent diameter D. It is, however, not possible with the current toolset available in AQWA to define a flow angle-dependent equivalent diameter. Hence, a representative constant diameter must be chosen along sections of the structure. The TLP structure considered in this thesis can be split up into different components with independent Morison element diameters, such as the column and pontoons. As the column has a uniform diameter along the entire wetted height of the component, the column can be modelled with a uniform Morison element diameter. This is not the case for the pontoons, as its profile tapers down radially away from the column. To account for this change in profile, each pontoon is considered as 4 separate Morison elements. As shown in figure 8.11 the viscous forces upon the TLP are modelled using 5 different Morison elements.

Due to Morison elements being uncapped, the main column's bottom surface and pontoon end plates (which sit perpendicular to the Morison elements defined) do not provide any damping resistance to axial motions. This can be resolved using end plates (more commonly implemented as heave plates for other marine structures). The cylindrical plates only provide a damping force to the flow component normal to the end plate element. The end plate at the bottom of the main column is equal in diameter to the column Morison element, whereas the pontoon end plate diameter is equal to the width of the pontoon end.

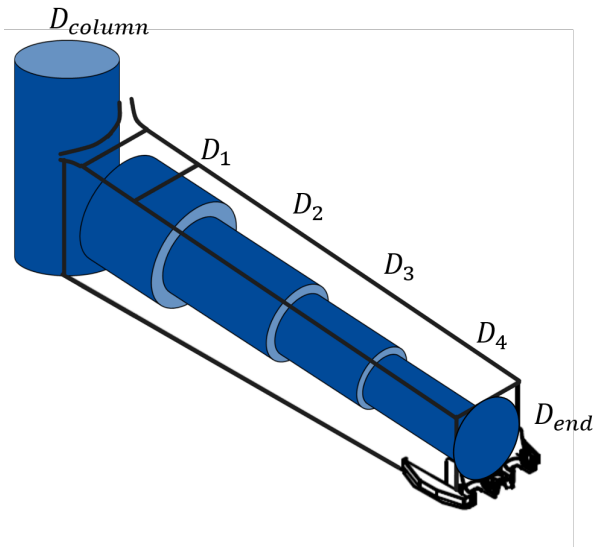


Figure 8.11: Different Morison element diameters modelled along the length of the pontoon to account for the structure's taper, as well as a separate element for the central column.

Table 8.9: Morison element diameter and drag coefficients

Morison element	Diameter D [m]	Drag coefficient C_d [-]
Column	11.00	1.400
1	9.50	2.488
2	8.88	2.194
3	8.40	2.111
4	7.92	2.023
End	6.5	1.14

Implementing the previously described into the AWQA model allows for a potential pressure-based approach to solving hydrodynamic problems while including viscous damping contributions without considering inertia or drag contributions double.

8.4. Aerodynamic model

In this section, the various aspects of the aerodynamic model considered for the coupled dynamics are discussed. Starting with the AeroDyn model in section 8.4.1. Next, implications regarding the aerodynamic controller are discussed in section 8.4.2, after which in section 8.4.3 a solution is proposed.

8.4.1. BEM Model: AeroDyn

As was discussed in section 4.1.4, this thesis integrates the functionality of open source aerodynamic loading package AeroDyn v3.0.0, developed by NREL. AeroDyn is a BEM package which offers a suite of simulation tools, as covered in section 4.1.4, and is connected to the rest of the simulation model covered in this thesis as will be covered in section 8.6. In the sections below, the setup of AeroDyn, as considered in this thesis, will be covered.

8.4.1.1 Blade

The blade model used in this thesis is freely available as a part of the IEA-15-240-RWT turbine [17]. Each blade is discretized into 50 evenly spaced sections along the length of the blade. For each blade section, the spacial geometry, aerodynamic and structural properties are given. The latter of which is not used in this thesis, as blade aeroelasticity is not considered.

Furthermore, the model uses tip and hub loss, as well as skewed inflow and induced wind by including the structure's rigid body motions (see section 4.1.4).

8.4.1.2 Tower

The aerodynamic properties of the tower were modelled from the provided geometry in Barter et al. [17]. The tower was divided into 11 sections of equal length and uniform diameter, with varying diameters between sections to model the gradual taper of the tower along its height. The standard drag coefficient for a circular cross-section is adopted at $C_D = 1$.

8.4.1.3 Turbine

Although the turbine housing does not contribute to the aerodynamic loading of the system, some input parameters are required to determine the orientation of the rotor plane to the horizon. Rotor precone, shaft tilt angle and overhang are design considerations to decrease the risk of a blade striking the tower as it deforms under aerodynamic loading by increasing the distance between the blade and the tower. As can be seen in figure 8.12, rotor precone is achieved by setting the blade root to the nacelle at an angle, whereas shaft tilt is the angle of the spinning rotor shaft to the horizon. Overhang is simply the horizontal projected distance from the blade root to the tower centroid.

8.4.1.4 Azimuth angle

As discussed in section 4.1.4 the incident may not be perfectly normal to the rotor plane, resulting in skewed inflow. This can be caused by a yaw misalignment of the RNA or due to a yaw response in a FOWT. For the application in this thesis, the rotor plane was aligned perfectly upwind, and the yaw mechanism was considered solid. Any skewed inflow effects are hence caused by the yaw response of the entire structure. For very long-term motion analysis, this is not a realistic assumption as the supervisory turbine controller section 4.1.5 may adjust the yaw mechanism to rotate the rotor plane if the wind direction changes. However, for the length of simulations considered in this thesis, no changes to the rotor yaw need to be considered.

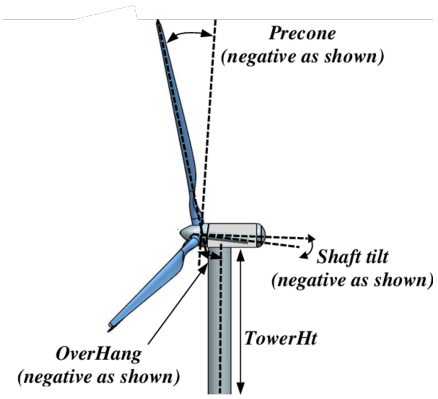


Figure 8.12: Rotor plane precone and shaft tilt angle are two design considerations to increase blade-tower clearance and prevent tower striking [146]

Parameter	Value	Unit
Precone	−6.0	°
Shaft tilt	−4.0	°
Overhang	11.35	m

Table 8.10: Turbine input parameters

8.4.2. Control systems

As discussed in section 4.1.5, the effect of an aerodynamic controller on the dynamic behaviour is significant. It is, however, not realistic to implement and tune a control system in the scope of this thesis. The exclusion of aerodynamic control logic does impose restrictions on the environment that can be simulated using the workflow identified in this thesis. In section 4.1.5, it was discussed that a PRVS controller operates in multiple regions, for each of which different control logic is applied. NREL provides a suggestion for the control system, as shown in figure 8.13. Here, it can be seen that the blade pitch angle (purple) is zero in region 2. This means that between wind speeds of 6.98-10.59 m/s, the control system does not change the blade pitch angle. Therefore, when choosing a range of wind speeds in which the control system has the least effect on the dynamics, the region in which blade pitch remains constant is the best candidate. Hence, this thesis will consider wind speeds of 6.98-10.59 m/s, which will be referred to as the wind window.

Before blindly restricting the investigation to the defined wind window, the implications should be considered as well. As there is no active rotor control, it is not possible to simulate scenarios in which

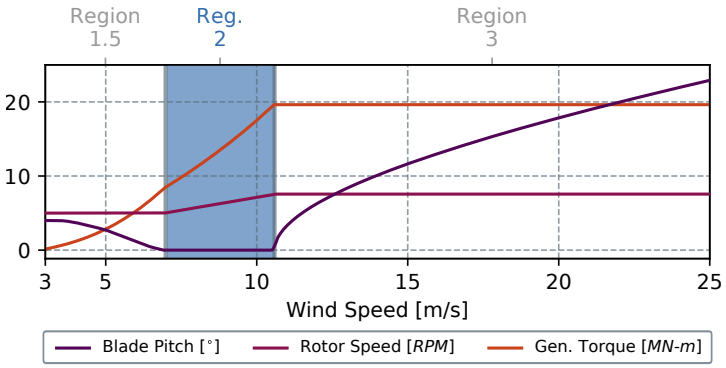


Figure 8.13: NREL controller for the IEA-15-240-RWT turbine considered in this thesis. As can be seen, the pitch controller is inactive in Region 2, between wind speeds of 6.98-10.59 m/s (adapted from [49, p. 19])

above-rated windspeeds are considered. Therefore, it is not possible to consider the implications of active control on structural fatigue.

In addition to this, as can be seen in figure 8.14, the active rotor controls also reduce the lateral load on the turbine at above-rated wind speed conditions. This means that despite not covering the entire wind speed range, the defined wind window still covers the maximum aerodynamic loading scenario. Furthermore, as the rotor angular velocity remains constant in above-rated wind conditions, it is still possible to simulate a scenario with the highest incurred aerodynamic load in combination with the highest loading frequency. Stress response behaviour that can be attributed to aerodynamic load magnitude and frequency should still be observable.

This is also useful for engineering considerations, as simulating the maximum aerodynamic load combination does not require a tuned aerodynamic controller for preliminary modelling. It should be noted, however, that the relationship between wave power and wave height is of the non-linear monotonically increasing type, as shown with an example in figure 8.15.

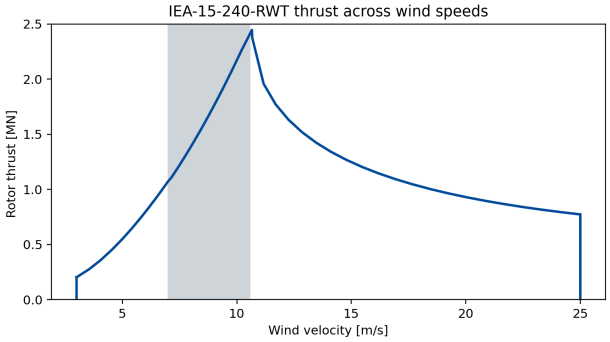


Figure 8.14: Rotor thrust across the wind range. Also depicted is the wind window applied in this thesis (adapted from [49, p. 19])

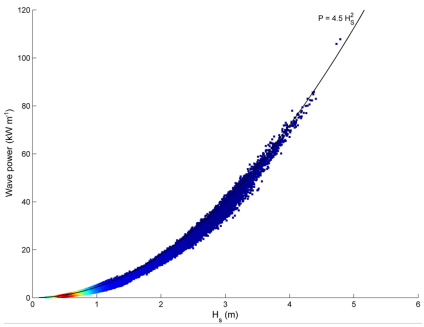


Figure 8.15: Example of the relationship between wave energy and significant wave height [3]

8.4.3. Power take-off

As discussed in section 8.4.2, this thesis does not consider the effects of an aerodynamic controller. This also means that the generator torque control is not included either, effectively removing any outflow of energy from the system. As energy continues to flow into the system, the rotor speed will far exceed the operational limits. This calls for an approach allowing energy to dissipate from the modelled mechanical system as though the system were to be providing electrical energy output.

Let us consider the following energy balance at any time for the enclosed volume of the substructure, tower, and RNA;

$$P_{system} = P_{mechanical} - P_{out} = P_{mechanical} - P_{electrical} \tag{8.11}$$

The generator housed in the nacelle converts the kinetic (mechanical) energy of the spinning rotor into electrical energy. As the model does not consider electrical subsystems, a different approach must be considered. Assuming that the export of electrical energy does not affect the structural dynamics of the system, it may be considered that the form of dissipated energy is not relevant (electrical, mechanical, thermal, sound, etc.). In this case, as long as an equivalent amount of energy is dissipated from the system in another form, the power take-off (PTO) effects are indirectly considered.

As we consider a mechanical system, it is easiest to consider mechanical energy dissipation. From the equation of motion, this can be done with stiffness, damping, and friction, of which friction seems to be the most intuitive. However, due to upstream modelling restrictions for ANSYS dynamic systems, friction is not a suitable dissipator. This is because friction does not consider the influence of torque in the rotor joint type. Hence, friction is not a suitable approach.

Instead, damping should be considered, as this can provide a pure resisting torque, providing an opposing moment to the direction of rotation, thus simulating the resisting generator torque. The power dissipated by this resisting torque can be expressed as equation (8.12).

$$P_{out} = Q_{gen} \times \omega_{rotor} \tag{8.12}$$

As can be seen in figure 8.13, the rotor speed and generator torque share a linear relationship with wind speed, suggesting that generator torque and rotor speed also share a relationship. Using the rotor performance spec sheet from NREL [17], generator torque can, in turn, be defined as a function of an angular velocity-dependent coefficient $C(\omega)$ and the angular velocity, as shown in equation (8.13).

$$Q_{gen} = C_{damping}(\omega_{rotor}) \times \omega_{rotor} \tag{8.13}$$

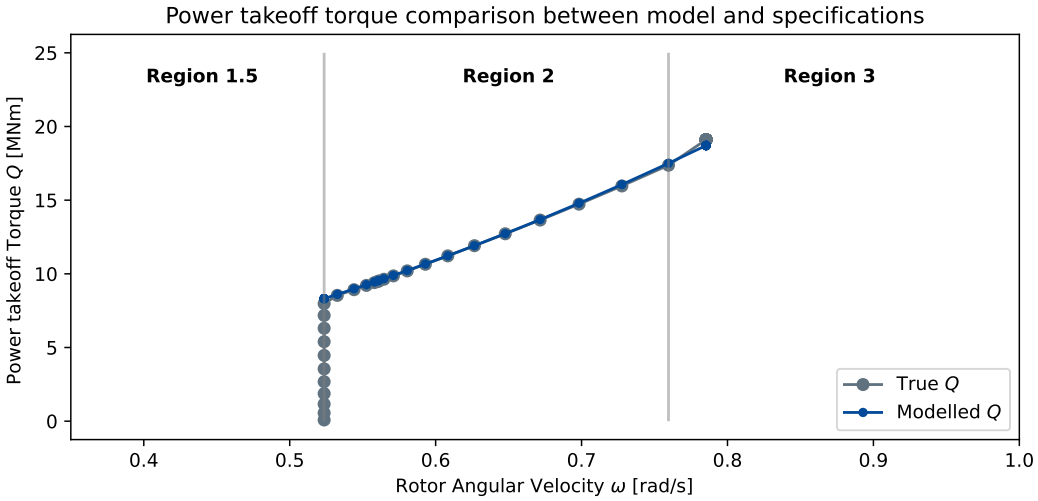


Figure 8.16: True generator torque and modelled torque plotted for angular velocity. Clearly, in Region 2, when the blade pitch remains constant, the rotor torque and rotational speed share a linear relationship

As can be seen in figure 8.16, the correlation between generator torque and angular velocity is linear in control region 2, and as the workflow presented in this thesis considers a restricted operation profile due to the absence of a control system, the identified relationship is sufficient. The generator torque model applied in this thesis considers an angular velocity-independent (constant) damping coefficient and is formulated as follows;

$$Q_{gen} = C_{damping} \times \omega_{rotor} = 30334763 \times \omega_{rotor}^2 \tag{8.14}$$

It should be noted, however, that figure 8.16 presents the impression that the modelled torque is an excellent substitute for a controller. This is, however, not the case, as in control regions 1 and 3, a PRVS controller actively adjusts blade pitch rather than rotor velocity. The effects of active control could not be reflected in figure 8.16. This model is hence bound to control region 2.

8.5. Mooring model

In section 4.3.3, it was established that a quasi-static linear mooring model may be applied for motion analysis of TLP-type FOWT as long as two conditions are met. These conditions are that there are no slackline events, and the tendons are only loaded in the elastic region. The mooring lines were modelled as such in AQWA using the line stiffness $k = 19.83$ [MN/m], as determined in section 8.2.6.

Finally, torsional effects in the tendons due to weave patterns (see section 4.3.1) are not considered in this thesis and were not modelled.

8.6. Coupled Dynamic Model

In the literature review conducted in part I and section 5.4, a novel approach was proposed in order to conduct a structural analysis of a FOWT using a hybrid rigid-flexible model. In this chapter, the various subcomponents of the TLP system were considered and related to the terms of the Cummins equation shown in equation (8.1). In order to conduct an integrated load assessment, these submodels must be coupled to one another. This process can be summarised in a general flowchart, as shown in figure 8.17.

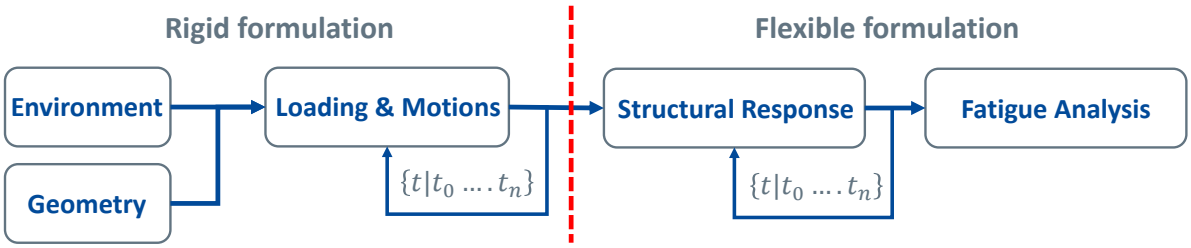


Figure 8.17: Overview of global integrated load analysis process

As can be seen in figure 8.17, the coupled analysis can be split into two distinctly different scopes, both of which contain a separate time-domain calculation, where the structural response calculation is dependent on the loading & motions. This section will cover the rigid part of the analysis. The flexible analysis will be covered in chapter 9.

The rigid formulation, as shown in figure 8.17, can be considered in more detail. As the geometry component of the rigid formulation was covered in detail in section 5.2, figure 8.18 only covers the environment and loading & motions component of the rigid formulation.

In the environment block, the dynamic wind-wave environment is discretized. It is independent of the loading & motions block as the undisturbed wave surface and wind field can be prepared for the entire temporal simulation. This numerical representation of the environment is considered per timestep $\{t|t_0 \ldots . t_n\}$. For each timestep, the external load vector is computed using the theory covered in this chapter. The instantaneous hydrodynamic and aerodynamic loads are dependent on the current system state, which is the acceleration, velocity and displacement.

Using the Cummins equation in equation (8.1), the motion response to the total exciting force can be determined, thus defining the initial system state for the next time step. Before closing the loop and moving on to the next iteration, the external excitation loads and system state are saved in a separate container for later processing.

The process presented here appears to be slightly different from the work presented by Luan et al. [91], but is separated by a fundamental difference. Unlike the work of Luan, this thesis considered hydrodynamic loading as a local pressure on a plate rather than lumped loads acting on a few points on the structure. This change in approach to hydrodynamic loading allows for local loading and structural response phenomena, such as multiaxial stress response, to be observed more accurately.

This process was achieved through a mixture of software packages in the ANSYS environment:

ANSYS AQWA The hydrodynamic modelling software was used to calculate all hydrodynamic and mooring loading & response. By running a new diffraction analysis for each seastate, all hydrodynamic and mooring contributions of the first order are included.

ANSYS TwinBuilder Although this software package is designed for a different type of workload, being the development and deployment of digital twins, TwinBuilder offers a platform for complex multi-physics coupled time domain simulations. As the subsystems may be modelled as separate entities, this platform lends itself very well to the application considered in this thesis. It is, however, important to mention that due to the advanced extra functionality offered by TwinBuilder (which is not necessary for FOWT analysis), it is effectively unavailable for academic use. Hence (further) research is effectively locked behind a paywall. This relates to the scientific relevance mentioned in section 2.5.

AeroDyn Although a separate open-source model, AeroDyn was included in the TwinBuilder analysis through a dynamic link library (DLL), effectively integrating it into the ANSYS environment.

Technical details regarding the implementation of the described workflow can be found in [6]. This manual covers ANSYS software-specific considerations and is hence not of added value to cover in this thesis.

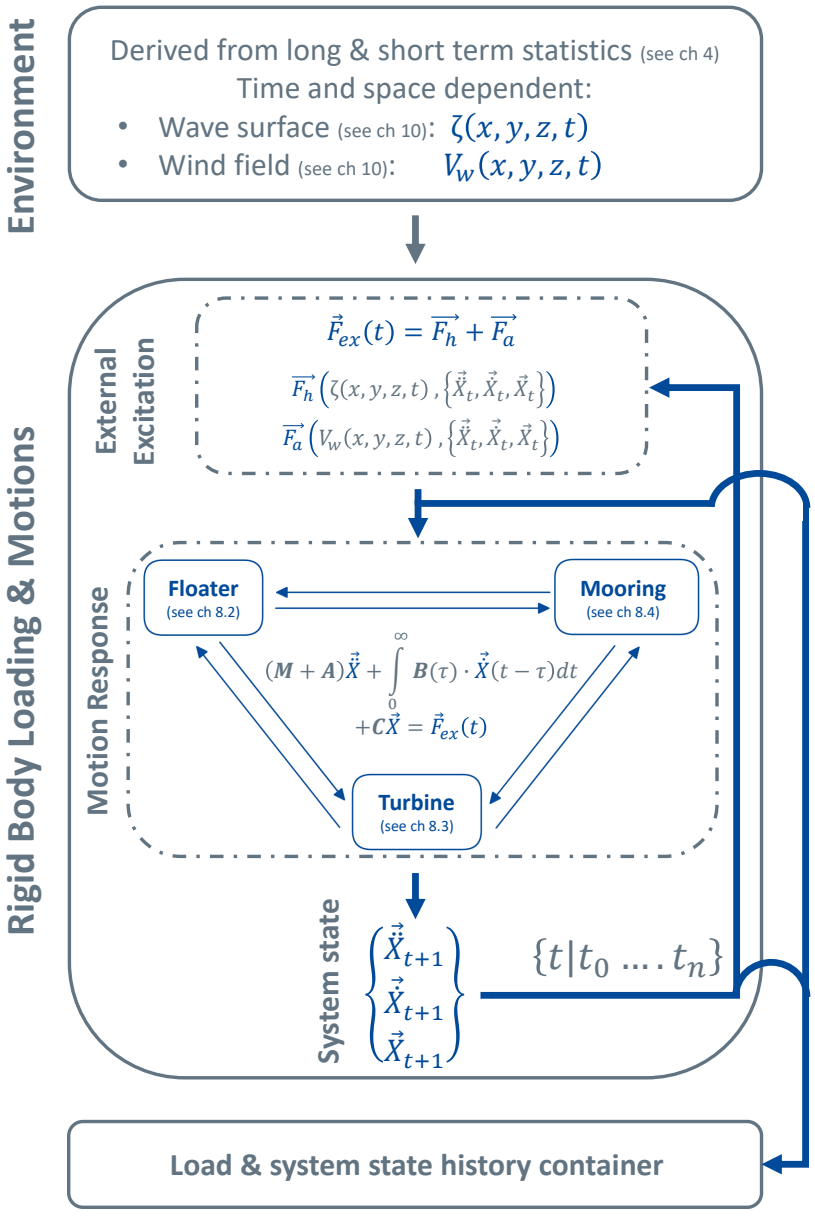


Figure 8.18: Flowchart describing the coupled dynamic model.

8.6.1. Flexible Tower Dynamics

The workflow formulation presented in figures 8.17 and 8.18 is general and offers a platform upon which the investigation presented in this thesis can be expanded, for example, with an aerodynamic controller or second-order hydrodynamics. In section 8.3.3, it was established that second-order hydrodynamics could not be included in the analysis due to the effects of the flexible tower. In hindsight, it was also not possible to include flexible tower effects in the analysis at all. Despite extensive attempts with multiple model types (beam, shell, solid), no successful coupled analysis could be run. As there is no precedent for this type of analysis, there is no supporting documentation. Working together with developers at ANSYS did not produce a validated model in a timely manner either (allowing for sufficient time to conduct the analysis). The root cause of the issue was, however, identified but is not relevant to the discussion presented in this thesis. Once the numerical stability issues of a flexible tower are addressed, a follow-up investigation should be made possible.

8.7. Summarising statement

As discussed in part I, the analysis conducted in this thesis consists of multiple components separated by physics type. In this chapter, a model for the environmental loading and rigid motion response of the TLP-type FOWT system was discussed in detail. The resulting model is capable of considering an input signal depicting a multi-directional mixed wind-wave system and outputting rigid body motions in the system.

This section partially answered **SQ4** by implementing AeroDyn as an aerodynamic BEM model and using AWQA to model the hydrodynamics by introducing a mixed potential pressure-Morison viscous model. This allows for the local hull pressures to be calculated while still considering the viscous damping on the hydrodynamic system. The aero-, hydrodynamic and mooring systems are loosely coupled using Ansys TwinBuilder to solve the temporal system. This allows for the hybrid flexible-rigid model discussed extensively in section 5.4 to be applied. The model presented in this thesis offers some improvements compared to the work presented by Luan [89, 90, 91, 92] is the use of local hydrodynamic pressure rather than lumped loads along the length of the structure and separate mooring lines within a mooring cluster. These improvements come at an additional computational cost but increase the local loading resolution.

9

Dynamic Structural Analysis

The literature review conducted in part I concluded that a specific type of model is required to investigate multiaxial stress response for FOWT. Previously, in chapter 8, the first part of this model was discussed, consisting of a loosely coupled dynamic model which facilitates the hybrid flexible-rigid formulation. This chapter will discuss and validate the components for the subsequent structural analysis. In section 9.1, the setup of and boundary conditions of the structural model are discussed. Next, in section 9.2, the implementation of the traction-based structural stress approach is addressed, followed by a methodology to obtain and process the stress response histories in sections 9.3 to 9.5. After this, a methodology for spectral decomposition is covered in section 9.6. Finally, in section 9.7, the key findings in this chapter are reiterated.

9.1. Structural model

The structural model considers the geometry, mesh and load mapping required to derive a multiaxial structural stress response to the environment. It is distinctly different from the coupled dynamic model used to simulate the motion response to the dynamic environment. In sections 9.1.1 to 9.1.4, the different aspects of the structural model will be discussed.

9.1.1. Geometry

The structural geometry model is derived from 3D CAD engineering models. Unlike the CAD models, the FEA geometry does not contain non-primary load-bearing steel (no deck grating, ladders, etc.). Due to the full-scale nature of the simulations, shell elements are used for all structural elements, including hull and stiffeners.

9.1.2. Mesh

To conduct FE analysis, the shell geometry needs to be meshed. To strike a balance between computational efficiency and result accuracy a suitable mesh size needs to be settled on. DNV [10] requires a mesh size of $t_p \times t_p$ to be implemented for weld hotspot analysis. As computational time scales exponentially with the number of elements, this would be detrimental to computational time. As established in section 6.4.2.3, the traction-based structural stress method is mesh insensitive, provided that the mesh closely follows the weld seam. Furthermore, only the stress behaviour of the eight critical weld seams needs to be considered (see section 9.2.3). This means that a course mesh is acceptable further away from the weld.

For this thesis, a mesh size of 200x200mm was settled upon to model the weld seams and the adjacent material, which is about $4t_p \times 4t_p$. This mesh size also provided a good balance between computation time and output accuracy. In order to have at least 4 elements between the finely modelled weld seam and the transition to a coarser mesh, any shells within at least 1m of the weld seam were modelled with the same 200mm mesh. In some parts of the structure, engineering judgement was applied to extend past the 1m radius to provide a natural mesh transition to nearby structural elements, thus limiting the influence of mesh-induced singularities. Further away from the weld, the mesh is modelled

with elements of 900x900mm, which corresponds to the stiffener spacing in the pontoons. This model corresponds to about 55k nodes and 61k mesh elements.

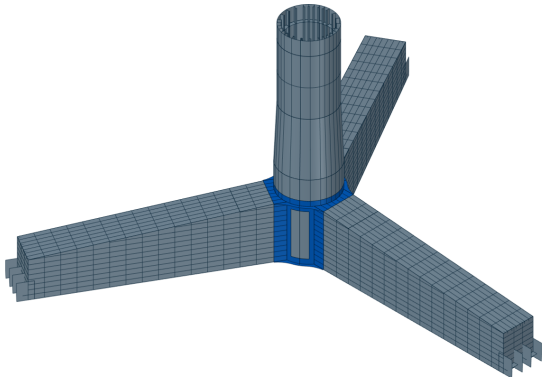


Figure 9.1: FEA model mesh refinement. Gray depicts a rough mesh of 900x900mm, and blue depicts a refined mesh of 200x200mm.

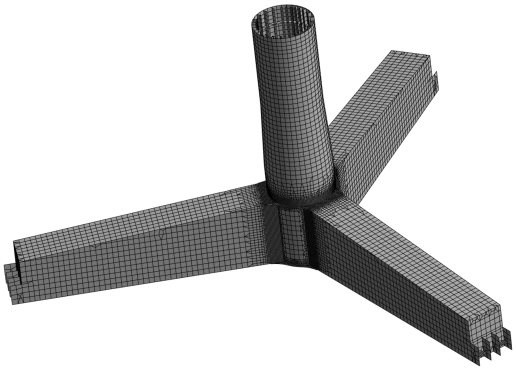


Figure 9.2: FEA model mesh refinement showing rough mesh of 900x900mm and area of refined mesh of 200x200mm.

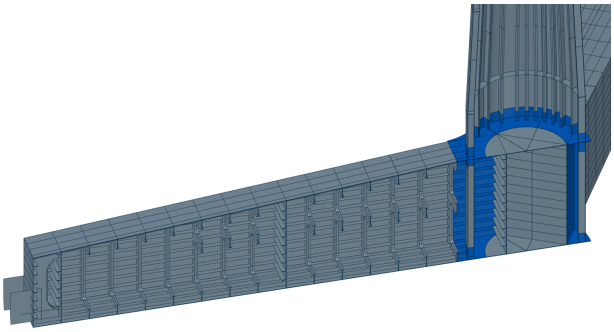


Figure 9.3: Cross section of FEA model mesh refinement. Gray depicts a rough mesh of 900x900mm, and blue depicts a refined mesh of 200x200mm.

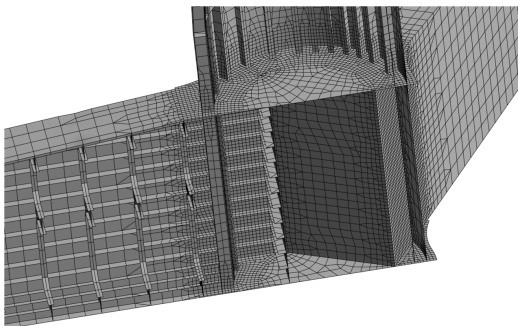


Figure 9.4: Close-up cross-section of FEA model mesh refinement.

A drawback of this relative course mesh size is that traction-based stress can only be applied to the weld seams surrounded by the finer mesh. No conclusions can be drawn regarding the fatigue behaviour of other welded connections in the structure. This is not an issue for the scope of this investigation but may be a consideration when seeking to implement traction-based structural stress analysis into engineering models.

9.1.3. External load mapping

In section 8.6, the process of conduction coupled dynamic motion analysis was covered. At each time step, the total external force acting upon the system is known. This external force can be considered as three distinctly different load sets; TLP-tower interface loads, TLP-tendon interface loads and hydrodynamic pressure loads. The load mapping of each of these components will be considered separately below.

TLP-tower interface loads

At each timestep, the tower loads, consisting of force and moment components, are evaluated at the centre and base of the tower. As there is no load-bearing structure at this point in space, the cumulative interface load needs to be spread out over the interface. In ANSYS Mechanical, this can be done using a remote point. As can be seen in figure 9.5, the remote point corresponding to the TLP-tower interface edge corresponds to the geometric centre. The web depicts how the total load is evenly mapped onto the nodes of the structure.

As will be discussed in section 9.1.4, applying the dynamic forces and moments from the motion analysis allows for a kinematic boundary condition to be applied to the TLP, instead of fixing the substructure at the tower interface line. Although not stated explicitly in a significant amount of

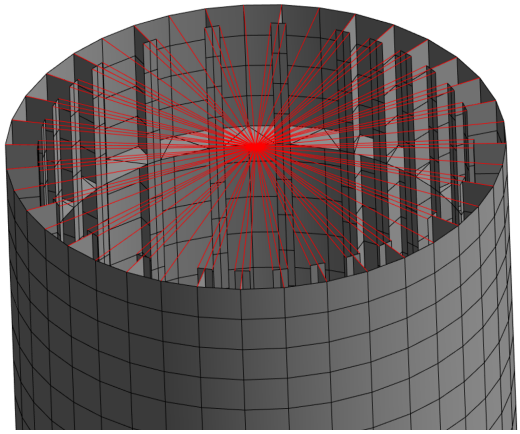


Figure 9.5: Load mapping of forces and moments onto the TLP-tower interface

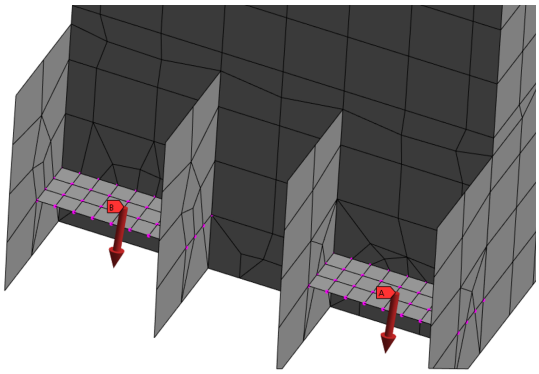


Figure 9.6: Load mapping of forces onto TLP-tendon interface

literature, the lack of a clear interface and load transfers for FEA is indicative of the application of a fixed boundary condition at the interface. Rigidly fixing the interface prevents rigid body motions, which, although seeming desirable, introduces an issue to the simulation model. By fixing the interface condition, all of the energy that would normally act to accelerate and displace the structure must be compensated by an extra resistive force and moment component. This results in more energy being put into the interface and will hence increase the local stresses. Depending on the magnitude of the rigid body accelerations, this extra stress component may become significant and produce a misleading stress signal. The extent to which this effect can be observed in the critical welds considered in this thesis was not investigated.

TLP-tendon interface loads

As was covered in section 8.2.4, all six mooring tendons are modelled separately. Unlike the tower interface, a mooring tendon cannot exert a moment at its end. Furthermore, due to the nature of a tendon, it can only exert a tensile force on the TLP-tendon interface. The force components at the tendon ends are captured at each timestep in the global axis system. This allows for these forces to be simply mapped onto the structure, as shown in figure 9.6. The tendon connector is modelled as a plate, and the force is mapped homogeneously over the surface of the connector.

Hydrodynamic pressure loads

To accommodate for non-linear analysis, AQWA does not relate panel pressure RAOs to only one parameter, such as wave height. Instead, time domain panel pressures are reconstructed based on the instantaneous system state $\{\ddot{x}_i, \dot{x}_i, x_i\}$ as well as instantaneous surface elevation $\zeta(x, y, z, t)$, which are known for all timesteps. This is done for all components of the hydrodynamic pressure (incoming wave, radiation, diffraction, hydrostatic time-varying). This means that the panel pressure for each mesh element can be can simply be reconstructed. In this thesis, the hydrodynamic pressure (sum of all components) will be considered.

As could be deducted from sections 8.3.2.2 and 9.1.2 the hydrodynamic and structural mesh are not equal, hence the panel pressures derived by AQWA cannot simply be transferred to the structural model. Furthermore, by definition, in diffraction analysis, the panel pressure is calculated at the area centroid and is assumed to be equal over the entire surface of the panel. This is a reasonable assumption, provided that the mesh (panels) is fine enough. Mathematically, the pressure at the corners of the panels is undefined. Any form of pressure mapping for FEA requires nodal forces to be known, which are at the corners of the panel by definition.

To solve this issue, ANSYS has implemented a rather intelligent solution. As shown in figure 9.7, for an arbitrary hydrodynamic mesh, there are a number of panels. Each panel shares nodes with its neighbouring panels. Although there is no pressure defined at these points, a load can be assigned to these nodes from the weighted average hydrodynamic pressure of the connected panels. Next, the (finer) structural mesh can be overlaid on the hydrodynamic mesh, and the FEA nodal loads can be

derived using interpolation, as illustrated in figure 9.7. The type of interpolation is not specified but is likely linear.

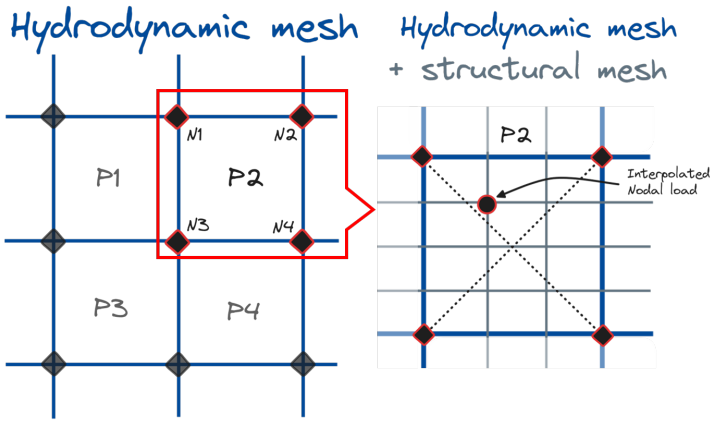


Figure 9.7: Load mapping hydrodynamic pressure to nodal loads for unequal mesh sizes

In figure 9.7, an example of a comparison between the hydrodynamic in AQWA and mapped loads onto the structural model is shown.

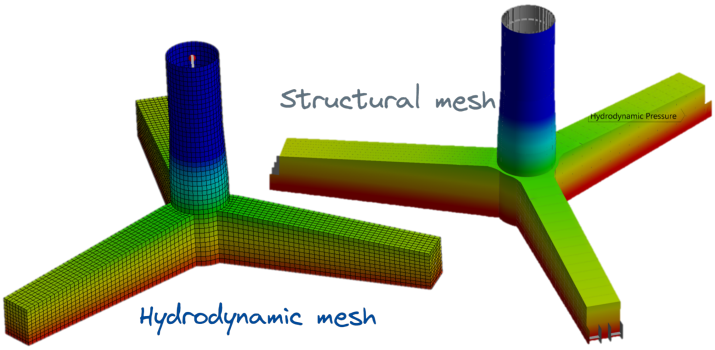


Figure 9.8: Hydrodynamic pressure mapping from 1000mm diffraction mesh to a finer, variable-size structural mesh.

9.1.4. Boundary conditions

For a moored floating structure, ample boundary conditions are required to prevent exaggerated rigid body motions and obtain a realistic structural stress response. Although the loads covered in section 9.1.3 cover most of the boundary conditions, some extra precautions must be taken to allow for model convergence and numerical stability.

Inertia relief

The first of which is inertia relief. Normally, in FE analysis, a structure is considered rigidly fixed, $\Sigma F = 0$, and does not need to consider the inertial contributions of the structure. However, once a non-stationary model is considered, numerical instability is introduced due to the underconstraining of the system. Running the system using inertia relief computes the inertia of the system and allows for realistic accelerations without overconstraining the system.

However, as was covered previously, the structural FEA model does not contain any non-structural steel components (grating, ladders, equipment, etc.). These items do, however, have a mass and inertia contribution. In the context of the FEA model, this means that the mass and inertia are too low, and the motions and accelerations will be too large. This can be solved in one of two ways, the first of which is to model all non-structural steel and equipment with corresponding masses. This is far too complicated to implement and will add a considerable number of unnecessary mesh elements to the structure. Another

option is to add an equivalent point mass to satisfy total mass, inertia and COG, which is much simpler to implement. In table 9.1 the point mass properties are given.

Table 9.1: FEA extra point mass properties

Type	Symbol	Value	Unit
Mass	m_{pm}	137.20	t
COG	x_{pm}	-0.29	m
	y_{pm}	0.00	m
	z_{pm}	-29.00	m
Inertia	$I_{x,pm}$	52.11×10^6	kg m^2
	$I_{y,pm}$	51.48×10^6	kg m^2
	$I_{z,pm}$	192.35×10^6	kg m^2

To account for the distribution of the previously determined point mass, FEA packages such as ANSYS Mechanical require this mass to either be homogeneously distributed over the structure or to be scoped to a part. The homogenous distribution of this mass adds a significant amount of computational load as the partial contribution of the point mass needs to spread out over all nodes, resulting in a recomputation of all elemental masses and inertia contributions. Therefore, if possible, it is preferable to scope the point mass to a surface. In the case for the TLP considered, the non-structural steel items such as deck grating and ladders are concentrated in the central column, as illustrated in figure 9.9. Therefore, the point mass can be mapped to the ring stiffeners in the column carrying these decks.

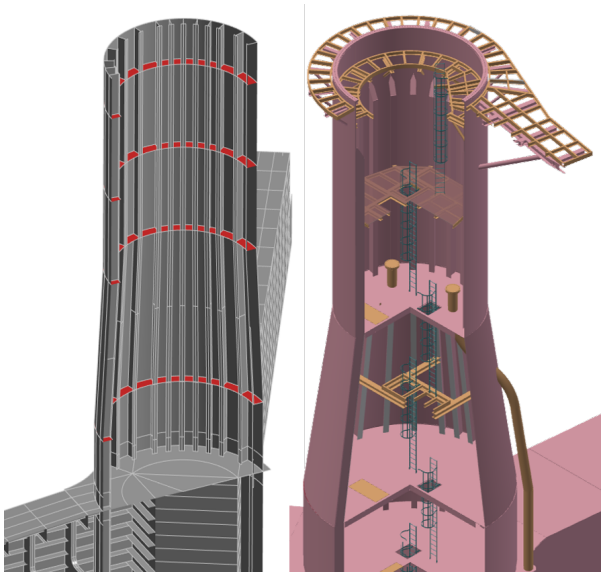


Figure 9.9: Distribution of mass and inertia representing all non-structural steel items in the FEA model. These non-structural steel items are generally items such as ladders, deck grating and supports, which are concentrated in the central column.

Weak springs

Weak springs are automatically created springs distributed across all nodes of the structure, which have just enough stiffness to prevent extra rigid motions. When considering a rigidly fixed model, weak springs prevent all rigid bodies if the model is underconstrained. Conversely, for a model with inertia relief, weak springs prevent excessive rigid body motions that can be caused by low mass or inertia. Hence, for a perfectly tuned model, weak springs are unnecessary. However, as was found when executing simulations, any mass/inertia imbalance causes numerical instability and simulation crash. Consequently, weak springs were applied in all structural models considered in this thesis. In the post-processing, the magnitude of the total weak spring force for all springs was checked for any irregularities. The absolute maximum total instantaneous weak spring force measured was 0.7N, which is negligible considering the magnitude of the mass of the structure and the forces acting upon it.

9.1.5. Time discretisation

In FEA, these types of simulations can be approached quasi-statically or dynamically. The differences between these methods were discussed in section 5.4. Computationally, quasi-static models can run much faster as the workload can easily be spread on multiple cores, as each timestep is independent of load history. To avoid unintentionally discarding information, all simulations were simulated as dynamic models, also an investigation into the application of quasi-static models for the presented application is out of the scope of this investigation.

9.2. Traction based structural stress

After conducting the structural stress analysis using ANSYS Mechanical, the post-processing of information gathered from the coupled dynamic analysis and dynamic structural analysis. This section will discuss the process of extracting information from the FEA model and processing it to a time-variant multiaxial stress response signal.

9.2.1. Nodal forces and moments

Using a number of ANSYS macros, the nodal forces and moments can be exported for each step. At each node, the instantaneous nodal force and moment contributions from the surrounding elements need to be summed. This needs to be done on a weld-by-weld and element set-by-element set basis. This is due to the summation of nodal forces resulting near zero, due to $\Sigma F = M \cdot a \approx 0$ as rigid body motions are maintained (see section 9.1.4). To automate this process, ANSYS macros are applied, which output 3 nodal force and 3 nodal moment components per timestep for each element set per weld. Other necessary parameters, such as nodal coordinates and node-element associativity, are also exported for downstream analysis. This results in 4 element sets + 6×3 element sets = 22 data sets for individual analysis per simulation.

9.2.2. Open and closed welds

Traction-based structural stress assessment makes a clear distinction between open and closed welds. In figure 9.10, an example is given of what a continuous weld seam between a deck plate and outer hull could look like. For clarity, other weld geometries have not been rendered; however, a weld would be expected to be present connecting the web of the stiffener to the hull as well as the web and flange of the stiffener to the deck. As can be seen, due to the weld access holes in the stiffener, the weld is not affected by the presence of the stiffener and, hence, does not contribute to the far-field stress in the weld. For reference, a discontinuous weld seam example is given in figure 9.11. It can be seen that the stiffener is a continuous member and passes through weld access holes in the deck. Due to this, the stiffener does contribute to the far-field stress, and the weld must be considered section by section between the stiffeners.

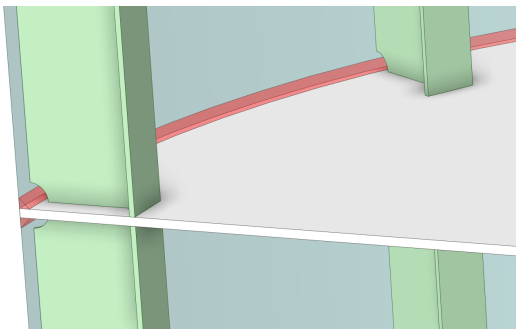


Figure 9.10: Continuous weld seam connecting the deck to hull due to the weld access holes in the stiffeners.

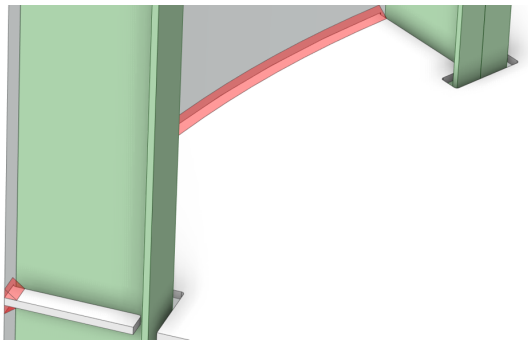


Figure 9.11: Example of a discontinuous weld seam along hull and deck, between stiffeners. The stiffeners are the continuous member and weld access holes are located in the deck plating.

For large-scale production purposes, it is beneficial to adopt shipbuilding practices by building smaller '*blocks*' and assembling at a later stage. This makes the continuous weld geometry presented

in figure 9.10 the most favourable. Hence, for the top and bottom circular welds, a continuous weld geometry will be adopted.

9.2.3. Critical weld seams

The welds connecting the central column to the pontoons are considered critical weld seams in this thesis. Due to the geometry of the weld, as discussed in section 9.2.2, this allows for these welded connections to be considered as two closed and six open welds, as depicted in figure 9.12

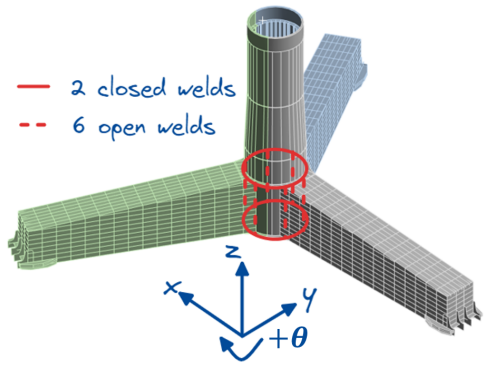


Figure 9.12: Critical weld seams between column and pontoons, considered in this thesis.

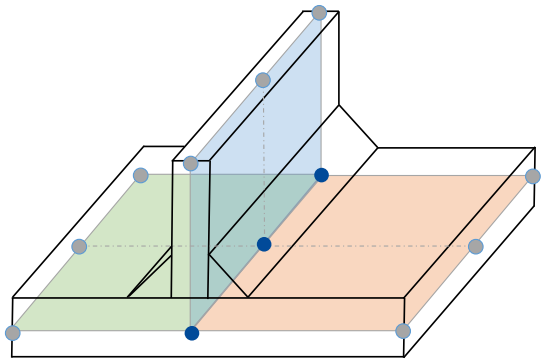


Figure 9.13: Welded geometry represented using shell elements. At the nodes at the centre of the weld seam, 3 shell plates can be seen to come together. These are referred to as element sets of the considered weld

Each weld seam represents the intersection of different plate geometries, which may be modelled as shell elements, provided that the structure is thin-plated. As was established in section 6.1.1, the TLP may be considered as thin-walled. In figure 9.13, an example can be seen of the physical representation of a double-sided T joint, as well as the shell model considered in this thesis. The different colours are used to indicate the parent geometry to which each mesh element belongs. In order to determine the stress behaviour at the weld seam using the traction-based structural stress method discussed in section 6.4.2.3, the line stresses in each elemental set need to be considered separately.

This thesis considers three different welded joint geometries. These can be represented by the weld cross sections in figures 9.14 to 9.16. Each of these figures can be considered as the welded geometry cross section as indicated by the dotted grey line in figure 9.13. The numbers indicate the chosen element set numbering, which shall be applied in this thesis.

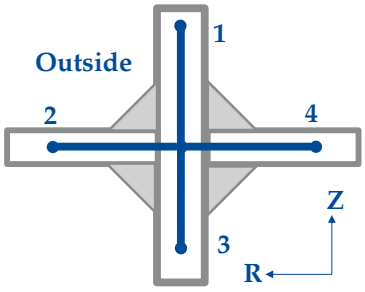


Figure 9.14: Top weld (TW) cross section showing 4 element sets

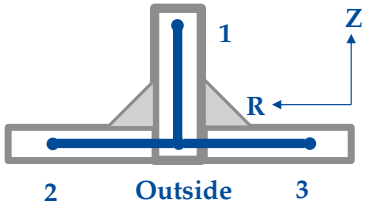


Figure 9.15: Bottom weld (BW) cross section showing 3 element sets

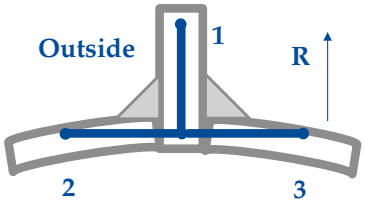


Figure 9.16: Vertical welds (VW1-6) cross section showing 3 element sets

In order to distinguish between the considered critical weld seams, the following weld abbreviations will be used in the rest of this thesis. For example, **VW1** set 3 refers to the element set that is inside of the pontoon (dry section) on vertical weld 3.

Table 9.2: Nomenclature used to refer to critical welds and their location in the structure. The coordinate system is shown in figure 9.12.

ID	Coordinate	Type	# Element sets	Description
TW	$z =$ − 13.0 m	Closed	4	Top circular weld
BW	$z =$ − 24.0 m	Closed	3	Bottom circular weld
VW1	$\theta =$ −126.5°	Open	3	Vertical weld pontoon 1
VW2	$\theta =$ −173.5°	Open	3	Vertical weld pontoon 2
VW3	$\theta =$ 113.5°	Open	3	Vertical weld pontoon 2
VW4	$\theta =$ 66.5°	Open	3	Vertical weld pontoon 3
VW5	$\theta =$ − 6.5°	Open	3	Vertical weld pontoon 3
VW6	$\theta =$ − 53.5°	Open	3	Vertical weld pontoon 1

9.2.4. Nodal sorting algorithm

The nodal forces and coordinates are exported in order of node ID, which is assigned as the mesh is generated, an example of which is shown in figure 9.17. Hence, the output is not necessarily in increasing order along the weld seam, thus complicating the process of computing line forces and moments. As each weld seam requires a separate line matrix as shown in equations (9.5) and (9.6), a nodal sorting algorithm was developed and implemented into the library of code developed in this thesis. Its function is to establish the starting node and every subsequent node in the weld. The individual welds considered in this thesis are in the 2D plane. An arbitrary starting point is selected for closed welds, whereas the upper weld endpoint is selected for open welds. The next node, for open and closed welds, is the closest node in space, which has not yet been selected. To guarantee numerical stability, some boundary conditions are implemented into the model that does not contribute to understanding the problem and will not be discussed here. Proper integration of such a sorting algorithm results in a sorted weld seam order as shown in figure 9.17.

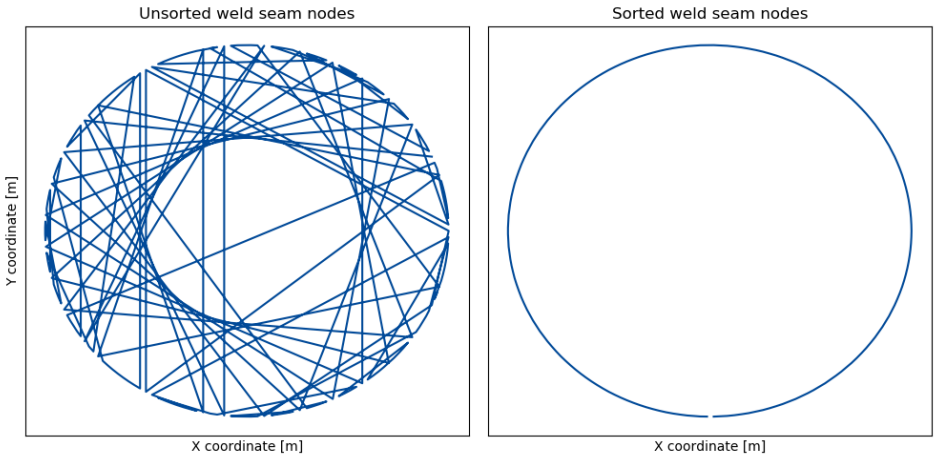


Figure 9.17: Importance of nodal sorting algorithm visualized

9.2.5. Local force and moment transformation

Having established the order of nodes, the local nodal forces can be derived. This, however, requires an extra processing step. In ANSYS FEA, nodal forces are expressed in the global axis system. This means that the nodal forces extracted from FEA need to be expressed in a local, weld seam-oriented axis system. This can be done by means of a rotation matrix R without compromising the data. For the application in this thesis, this process is automated due to the number of times its functionality is called upon. Unlike the nodal sorting algorithm, this process must be repeated for each node and each elemental set in the weld.

The algorithm works as follows, for each arbitrary point P_n in the weld seam (shown in red) belongs to one or more elements. Each element, depending on the element shape (quad/tri), contains either

four or three nodes. These are shown in blue in figure 9.18, and nodes belonging to nearby elements are displayed in grey for reference. Of out of the nodes belonging to this element, there is one other node that lies in the weld seam, P_{n+1}, which is used to construct unit vector U_x,

$$U_x = \frac{P_{n+1} - P_n}{||P_{n+1} - P_n||} \tag{9.1}$$

The local y-axis must point into the element and lie perpendicular to the local x and z-axis and the resulting axis system must be right-handed. In order to achieve this, the local z-axis is computed first. This is done using the cross-product of U_x and an arbitrary construction vector V_c, which lies in the plane of the element. This can be achieved with a unit vector from node P_n to any other node in the element that does not lie in the weld seam.

$$U_z = \pm U_z \times V_c \tag{9.2}$$

Finally, to compute the local y-axis, the cross product between U_x and U_z is taken. To verify that U_y points into the element;

$$U_y \cdot U_z > 1 \tag{9.3}$$

If this is not the case, U_z must be flipped (i.e. sign change). The final rotation matrix can be compounded as,

$$R = [U_x^T, U_y^T, U_z^T] \tag{9.4}$$

This is why sorting of nodal order is important, as local nodal forces are computed using this order.

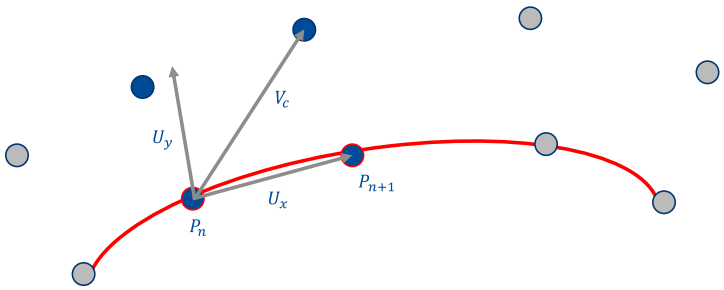


Figure 9.18: Nodal sorting algorithm

A few exceptions exist to the methodology presented above to deal with anomalous behaviour. For example, if an element shares only one node in the weld seam, it cannot contribute to the line matrix, as the force decomposition requires a second node in the weld seam and is hence ignored. However, as the contribution of the force at a node is a property of the node itself and is not related to the element, no information is lost when a single participating node element is ignored. Therefore, as long as the node is part of an element which does have two nodes in the weld seam, this contribution will still be included in the analysis.

This process was tested and validated against the work done by Rick Donk [42] using a tube-flange model, as shown in figure 9.19. Convergence between results was achieved, only separated by an error in the order of 10^{-12}. In order to demonstrate the mesh insensitivity of the presented method, the comparison was repeated using a very coarse mesh, as shown in figure 9.20, which also showed very good convergence.

9.2.6. Weld seam assessment

As discussed in part I, the line matrix must be derived before computing line forces and moments. Furthermore, the works by Dong [39, 40, 41] specify that the presented methodology is only valid for continuous welds, such that there are no large changes in direction from one node to another (reinforcing the importance of a dependable nodal sorting algorithm as discussed in section 9.2.4). This is the case for the open and closed welds. In the previous step, the order of nodes along the weld seam

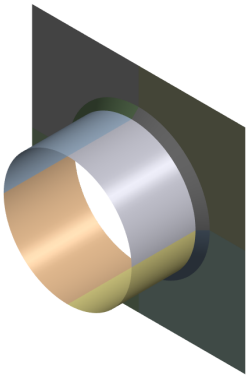


Figure 9.19: Tube to flange model considered by Rick Donk [42] used to validate nodal sorting algorithm and rotation matrix algorithm

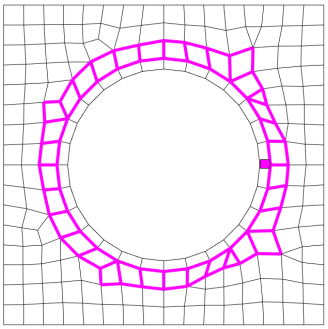


Figure 9.20: Example of a very rough mesh producing a mixture of triangular and quadrilateral mesh elements, which was used to demonstrate mesh insensitivity of implemented algorithms

was established. Using this information, the distance between a nodal pair can be computed as l_n. In physical terms, this represents the length of an element's edge and follows from the sorted nodal order.

For an open weld seam, the line matrix is formulated as follows;

$$L_{m,\text{open}} = \begin{bmatrix} \frac{l_1}{3} & \frac{l_1}{6} & 0 & 0 & \dots & 0 \\ \frac{l_1}{6} & \frac{(l_1+l_2)}{3} & \frac{l_2}{6} & 0 & \dots & 0 \\ 0 & \frac{l_2}{6} & \frac{(l_2+l_3)}{3} & \frac{l_3}{6} & 0 & 0 \\ 0 & 0 & \ddots & \ddots & \ddots & 0 \\ \vdots & \ddots & \ddots & \ddots & \frac{(l_{n-2}+l_{n-1})}{3} & \frac{l_{n-1}}{6} \\ 0 & \cdots & \dots & 0 & \frac{l_{n-1}}{6} & \frac{l_{n-1}}{3} \end{bmatrix} \tag{9.5}$$

As the formulation in equation (9.5) does not consider the contribution the '*first*' and '*last*' nodes have on each other, and vice-versa, a slightly modified line matrix formulation must be applied. These differences can be seen in the $L_{0,0}$, $L_{n,n}$, $L_{n,0}$ and $L_{0,n}$ terms.

$$L_{m,\text{closed}} = \begin{bmatrix} \frac{(l_1+l_{n-1})}{3} & \frac{l_1}{6} & 0 & 0 & \dots & \frac{l_{n-1}}{6} \\ \frac{l_1}{6} & \frac{(l_1+l_2)}{3} & \frac{l_2}{6} & 0 & \dots & 0 \\ 0 & \frac{l_2}{6} & \frac{(l_2+l_3)}{3} & \frac{l_3}{6} & 0 & \vdots \\ 0 & 0 & \ddots & \ddots & \ddots & 0 \\ \vdots & \ddots & 0 & \frac{l_{n-3}}{6} & \frac{(l_{n-3}+l_{n-2})}{3} & \frac{l_{n-2}}{6} \\ \frac{l_{n-1}}{6} & \cdots & 0 & 0 & \frac{l_{n-2}}{6} & \frac{(l_{n-2}+l_{n-1})}{3} \end{bmatrix} \tag{9.6}$$

9.2.7. Line Forces

Using the previously derived nodal forces (f) in the local axis system, as well as the line matrix L_m, the line forces F can simply be computed from equation (9.7). Again, each force component f_i represents a 6 components force and moment vector $\begin{bmatrix} f_{x'} & f_{y'} & f_{z'} & m_{x'} & m_{y'} & m_{z'} \end{bmatrix}$.

$$\begin{Bmatrix} F_1 \\ \vdots \\ \vdots \\ F_n \end{Bmatrix} = L_m \begin{Bmatrix} f_1 \\ \vdots \\ \vdots \\ f_n \end{Bmatrix} \tag{9.7}$$

9.2.8. Line Stresses

Provided that the local nodal forces are computed according to section 9.2.5, a right-handed axis system pointing into the element plane is used. This allows for the line stresses to simply follow from equations (9.8) and (9.9) [39, 40, 41].

$$\sigma_s = \sigma_m + \sigma_b = \frac{f_{y'}}{t_p} + \frac{6m_{x'}}{t_p^2} \tag{9.8}$$

$$\tau_s = \tau_m + \tau_b = \frac{f_{x'}}{t_p} + \frac{6m_{y'}}{t_p^2} \tag{9.9}$$

The methodology used to process stress histories and assess the presence of multiaxial stress response only requires the total stress components σ_s and τ_s. However, for damage assessment using effective notch stress, the far-field stress must be separated into membrane and bending components.

9.3. Stress history

The steps in sections 9.2.5 to 9.2.8 describe a process to derive the structural stress and shear in each point of the weld for a single timestep. To derive a stress history, this process needs to be repeated for every single timestep considered. In figure 9.21, a sample of a multiaxial stress history is shown. Projecting this stress history as a time trace in the stress space produces the characteristic circular trace of a VA non-proportional stress response signal.

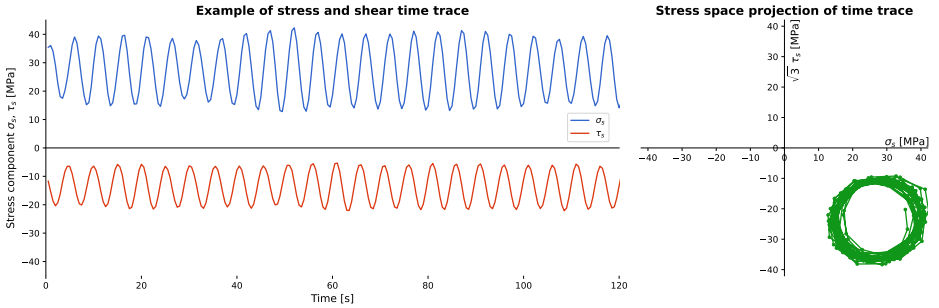


Figure 9.21: Example of a two-component mode-{I,III} stress history as well as the history projection into the stress space. It can be seen that the stress history is of the variable amplitude non-proportional type.

Repeating these steps for every node, in every weld seam, and every timestep allows for the stress behaviour of different sections of various welds to be analysed separately. Ideally, one would compute the accumulated fatigue damage at every single point in the structure. This is, however, computationally expensive and wastes a lot of computational power. Considering figure 9.22, it can be seen that various stress space traces can be expected, which will not necessarily carry equal weight regarding damage importance.

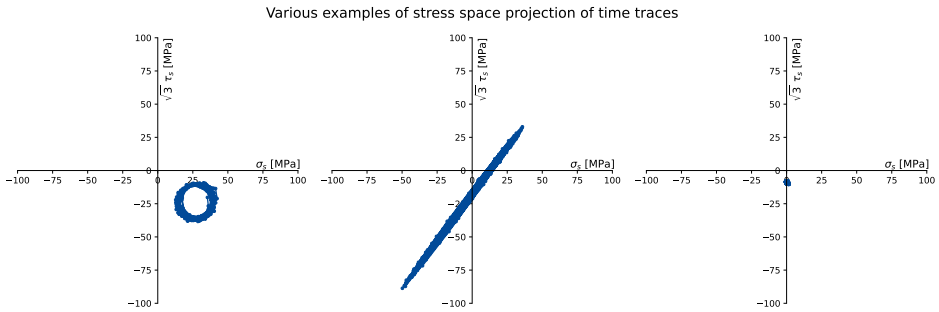


Figure 9.22: Various stress response time traces projected into the stress space, clearly showing different stress response behaviour.

This suggests the necessity for a preliminary screening step based on the structural stress response.

9.4. Minimum Circumscribed Ellipse

In chapter 6, it was demonstrated several important factors need to be considered when examining damage accumulation of a multi-axial stress state. These are as follows: the degree of non-proportionality, CA or VA loading, mean stress and stress range. As damage accumulation for the entire structure is a computationally expensive and potentially unnecessary process, an indicative measure of damage importance is sought after.

As discussed figure 9.22, a qualitative comparison can be made between locations in the structure by visually examining the stress history projected in the von Mises stress plane. A visual examination of results, however, does not allow for qualitative data evaluation and is not scalable to large datasets. This is where the MCE offers a solution. The MCE was first proposed [81, 120] as an improvement of the Minimum Circumscribed Circle (MCC) method, which sought to define the effective stress amplitude as the minimum radius of the circle enclosing the load path. MCE gives very good results for sinusoidal stress waveforms but can be conservative for other load path shapes [4]. As both aerodynamic and hydrodynamic loads are sinusoidal, a good match is expected. This is verified from the stress signal, as discussed in section 9.6.

Donk [42] demonstrated that the application of MCE provides an excellent screening tool for multiaxial stress response and also allows for the level of mean stress to be captured. MCE did not provide a perfect indication of fatigue damage but did allow for hotspots subject to multiaxial stress response to be isolated for further analysis. This is especially interesting for large-scale FEA models, such as required for FOWT. In Donk's investigation, Khachiyan's algorithm [72, 136] was applied to determine the MCE. Although Khachiyan's algorithm (referred to as MVEE) was not developed specifically for multiaxial fatigue, it provides a proven mathematical model accomplishing the same operations as MCE. Khachiyan's algorithm is a mathematical formulation that efficiently finds the MVEE for a given dataset. [136]. It iteratively closes down the size and orientation of the ellipse to find the MVEE for a given dataset. Imelfort [64] published a Python-based open-source implementation of Khachiyan's algorithm, which was modified to accommodate for a 2 component mode-{I, III} stress signal for application in this thesis.

An added advantage of MCE is that an entire loading and response sequence can be reduced to a set of characteristics of its entire stress state. Without considering the entire cycle counting and damage accumulation process, a screening method provides a global overview of expected behaviour.

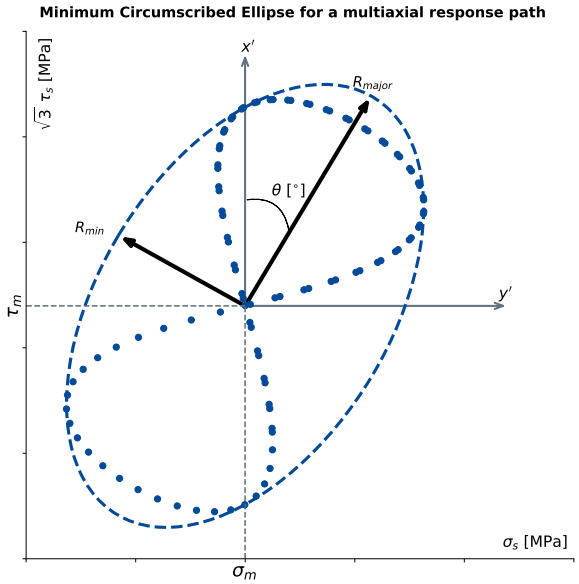


Figure 9.23: MCE applied to a non-proportional multi-axial stress response, enclosing all stress states

9.5. Screening Criteria

Time domain FEA produces detailed structural response information. Using the MCE concept discussed above, a stress response history in a point in a structure can be characterized by a single ellipse in the von Mises stress space. This 'compression' of information allows for a global understanding of the stress behaviour in a point or weld to be understood in a single period, or across seastates. The following screening criteria were proposed by Donk [42], each of which will be discussed in more detail in sections 9.5.1 to 9.5.4.

1. Level of multiaxiality
$$\Theta = 1 - |\cos(2\theta)|, \quad \{0 \leq \Theta \leq 1\} \tag{9.10}$$
2. Level of Non-Proportionality
$$G_{NP} = \frac{R_{minor}}{R_{major}}, \quad \{0 \leq G_{NP} \leq 1\} \tag{9.11}$$
3. Equivalent stress range
$$\Delta\sigma_{eq} = \{\Delta\sigma_{eq,MCE}, \quad \Delta\sigma_{eq,range}, \quad \Delta\sigma_{eq,DNV}, \quad \Delta\sigma_{eq,MCS}, \quad \Delta\sigma_{eq,Walker}\} \tag{9.12}$$
4. Multiaxial damage importance
$$D_{imp} = \left[\Delta\sigma_{eq}(1 + G_{NP})\right]^3 \tag{9.13}$$

9.5.1. Level of multiaxiality

The level of multiaxiality index Θ is an indicator of the dominant stress direction. For $\Theta = 0$ the stress state is pure mode-I, whereas $\Theta = 1$ is pure mode-III. However, as the degree of non-proportionality increases, and the ellipse approaches the shape of a circle $\left(\frac{R_{major}}{R_{minor}} \rightarrow 1\right)$, the orientation of the ellipse becomes irrelevant. Hence, this indicator only has any value for stress states characterized by a low degree of non-proportionality.

9.5.2. Level of Non-Proportionality

The level of non-proportionality can be indexed with the ratio between the major and minor axes of the MCE. As G_{NP} approaches 1, the stress state is characterized by a high level of non-proportional multi-axial fatigue, whereas as G_{NP} approaches 0, the stress state is proportional. As this index contains no information on the orientation of the ellipse in the stress space, the level of multiaxiality indicator must be consulted in order to resolve if the stress state is mode-{I, III} dominant or multiaxial in nature.

9.5.3. Equivalent stress range

Stress range and number of incurred stress cycles are two important indicators for expected fatigue lifetime. For VA non-proportional multiaxial loading stress range can be formulated in a number of ways. For damage accumulation purposes, it is desirable to relate σ_s and τ_s contributions in a single S-N curve. From a screening level, this can be approached by implementing a uniaxial equivalent stress range $\Delta\sigma_{eq}$. In physical terms, this can be thought of as the pure mode-{I} stress range that produces the same damage as a multiaxial stress cycle.

There are different approaches for such an equivalent stress range, containing varying levels of detail, as will be discussed in the sections below.

9.5.3.1 MCE Major axis

Computationally, the easiest equivalent stress range parameter to implement is based on the MCE major axis length. This criterion exhibits a number of flaws, as it does not include any mean stress or non-proportional information. Furthermore, as the MCE method seeks to optimally enclose the data in the stress signal, the resulting ellipse may '*overshoot*' some of the data. As can be seen in figure 9.23, the dimensions of the ellipse exceed the range of the stress signal.

$$\Delta\sigma_{eq,MCE} = 2 \times R_{major} \tag{9.14}$$

The only benefit of this criterion is that no extra computations need to be conducted. However, as this benefit does not outweigh the problems presented by the criterion $\Delta\sigma_{eq,MCE}$ will not be considered further.

9.5.3.2 Maximum stress range

The maximum stress range-based equivalent structural stress operates in the $\sigma_s - \sqrt{\beta}\tau_s$ plane and offers an improvement to the MCE Major axis equivalent stress previously proposed at an additional computational expense. The equivalent stress range is equal to the maximum distance between points in the stress space.

$$\Delta\sigma_{eq,range} = \max\sqrt{(\sigma_s^c - \sigma_s^d)^2 + \beta(\tau_s^c - \tau_s^d)^2} \tag{9.15}$$

This equivalent stress formulation does not consider mean stress or load path effects but does relate normal stress and shear stress contributions to the total stress range through shear stress coefficient β. Due to the simplicity of the stress range formulation, $\Delta\sigma_{eq,range}$ is attractive to implement for screening purposes. In fact Donk [42] demonstrated that $\Delta\sigma_{eq,range}$ based multiaxial screening criteria are good at predicting damage contributions relative to other points in the construction, i.e. what point in the structure will fail first. $\Delta\sigma_{eq,range}$ based multiaxial screening criteria are not very good at predicting absolute damage contributions, i.e. predicting fatigue lifetime.

9.5.3.3 DNV mean stress correction

DNV recommends a mean stress correction based on a stress level correction curve [8, 10]. This correction curve is, however, restricted to post-weld heat-treated connections or welds with low residual stresses. It is not unreasonable to assume that critical welds receive post-treatment to extend fatigue lifetime. In figure 9.24, the empirical correction curve is illustrated and can easily be implemented. As can be seen, stress ranges can only be adjusted to lower values, thus suggesting that the DNV methodology is over-conservative, and a mean stress correction allows for a more favourable, less conservative stress range to be adopted. This reduction of stress range is also conducted for tensile mean stresses, which is problematic as tensile mean stresses are expected to facilitate crack growth, and hence an increase in effective stress range would be expected for large tensile mean stresses.

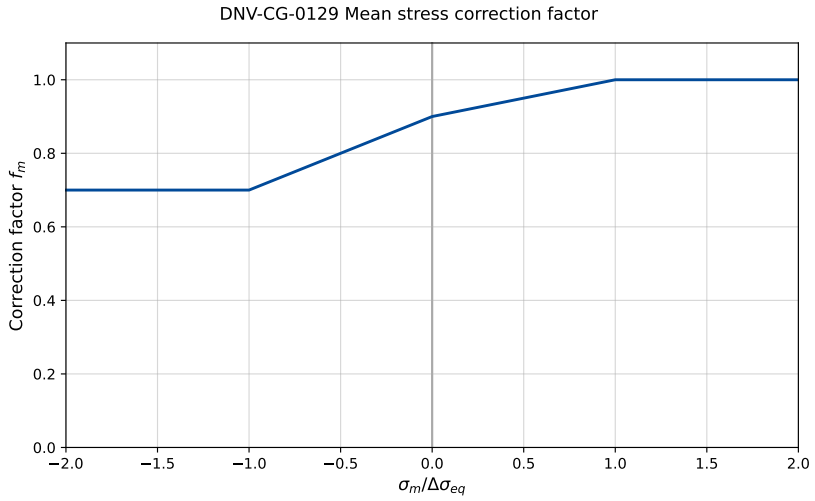


Figure 9.24: DNV mean stress correction, as can be seen only a reduction in effective stress range is realised (adapted from [8]).

9.5.3.4 Modified Carpinteri-Spagnoli

In section 6.3.4, the MCS criterion was identified as a promising equivalent stress range criterion for multi-axial fatigue analysis. During the implementation of this criterion, it was established that MCS is, in fact, a family of criteria. In fact, different formulations exist for all load signals with combinations of CA, VA, proportional, non-proportional, including mean stress contributions, excluding mean stress contributions, fully tensile, and fully compressive and stress reversal. There is, however, no formulation for VA non-proportional loading with mean stress effects, which allows for stress reversals. An attempt was made to implement a modified version of the CA non-proportional stress criterion proposed by Carpinteri et al. [27, 28], which included mean stress effects but could not handle stress reversals. The

proposed modification was to assume that the load path in the stress space could be approximated by the MCE, as presented in figure 9.23. The dimensions of this ellipse in the stress space would be used to formulate an approximate CA stress signal representing the actual VA signal.

The preliminary results from this criterion were inconsistent and inaccurate due to the input load signal containing stress reversals, thus indicating the importance of adhering to the criterion boundaries posed by the original author. Due to the lack of a suitable criterion and conflicting results from the further modified MCS criterion, further attempts to implement a form of MCS were abandoned.

9.5.3.5 Walker's mean stress correction

As established in section 6.1.5, Walker's mean stress correction is shown to be the most effective for welded joints. Walker's mean stress correction model is a uniaxial mode-{I} correction model that considers an unequal contribution of stress range and mean stress contributions to the equivalent stress range. This raises a concern regarding multiaxial stress signals, as considered in this thesis. There are some examples of mean stress correction models for multiaxial fatigue assessment, but there is no scientific consensus on the best approach. Three notable examples found. In the first, Bufalari et al. [23] applies a Walker mean stress correction using $\gamma = 0.9$ in their state-of-the-art multiaxial damage accumulation model. Secondly, a SWT mean stress correction model is included in multiaxial fatigue analysis software Hyperlife by ALTAIR [63], a large FEA distributor. SWT is simply a Walker mean stress correction considering equal contributions of stress range and mean stress. The second notable example is the inclusion of a Walker mean stress correction in NASALIFE, a fatigue lifetime estimation programme developed by NASA [55]. Neither publication offers concrete proof.

An explanation could be offered when considering the contributions of mean stress to crack growth. As $\tau_s \neq 0$ does not affect the fatigue lifetime of a specimen, only crack propagation direction, it would logically not require a mean stress correction. Hence the modified Walker mean stress correction would only need to be applied for the mode-{I} component of the multiaxial signal.

Walker's method also requires a fitted coefficient γ, which captures the previously discussed unequal contribution of stress range and mean stress to the equivalent stress range. This coefficient should be derived from experimental testing [19]. As there is no experimental data available for the considered structure and conducting tests and deriving γ is out of the scope of this thesis, a different approach must be considered. Qin et al. [117] demonstrated that for the generalised randomised fatigue limit model, $\gamma = 0.92$ is a good fit for welded steel connections. This indicates that $\approx 90\%$ of the effective stress contribution comes from the stress range and $\approx 10\%$ from mean stress [117]. Hence this parameter will be adopted. The Walker mean stress correction is formulated as follows with load ratio r_{lr}.

$$\sigma_{I,eq}^{Walker} = \Delta\sigma_I^{\gamma}\sigma_{max}^{1-\gamma} = \frac{\Delta\sigma_I}{(1-r_l)^{1-\gamma}}, \quad \text{with} \quad r_l = \frac{\sigma_{I,min}}{\sigma_{I,max}} \tag{9.16}$$

A typical SN curve is usually a fully tensile fatigue resistance relation ($-\infty < r_l < 1$). In cases of full compression ($1 < r_l < \infty$), a correction needs to be considered, as Walker's model assumes that only the tensile (crack opening) part of the stress cycle contributes to fatigue damage accumulation [20]. Den Besten [20] proposed an equivalent remote mechanical load ratio $r_{l,eq}$ for fully compressive cycles using the tensile case value $r_l^t = 1/r_l$. For tensile cases ($-\infty < r_l < 1$), $r_{l,eq} = r_l$.

$$r_{lr} = -\left[1 + \frac{1}{\frac{1}{2} + 2\left(\frac{r_l^t}{1-r_l^t}\right)}\right], \quad \text{and} \quad r_{l,eq} = 1 - \frac{1-r_{lr}}{1-r_l^t} \tag{9.17}$$

This results in the modified Walker criterion.

$$\sigma_{I,eq}^{Walker} = \Delta\sigma^{\gamma}\sigma_{max}^{1-\gamma} = \frac{\Delta\sigma}{(1-r_{l,eq})^{1-\gamma}} \tag{9.18}$$

The far-field reduction factor can be plotted as a function of the (equivalent) load ratios $r_l, r_{l,eq}$ as shown by the dashed line in figure 9.25. As established by Qin et al. [117], the effective stress range is dominated by the stress range rather than the mean stress. Den Besten [20] proposed that for fully compressive cycles ($1 < r_l < \infty$), an upper bound of $r_{l,eq} = -3$ is adopted due to the limited effect on the

effective stress range. For consistency purposes, the same lower bound is defined for ($-\infty < r_l < 1$). The solid line in figure 9.25 represents this simplified Walker criterion.

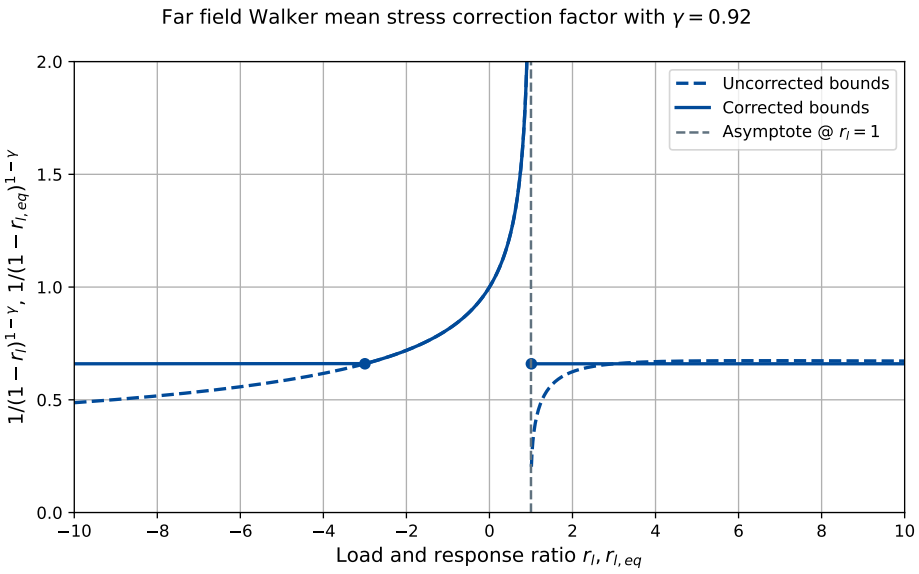


Figure 9.25: Modified correction coefficient used in Walker's mean stress correction as proposed by Besten [20], using $\gamma = 0.92$

To include the mode-{III} stress range contribution, the following is considered. The non-linear failure criterion of the Von Mises type relates normal (σ_s) shear (τ_s) stress components for an equivalent mode-{I} contribution. To include mean stress effects into this relationship, it is proposed to replace the normal stress range ($\Delta\sigma_s$) with the normal stress equivalent parameter $\Delta\sigma_{l,eq}^{Walker}$, resulting in:

$$\Delta\sigma_{eq,Walker} = \sqrt{\left(\Delta\sigma_{l,eq}^{Walker}\right)^2 + \beta(\Delta\tau_s)^2} \tag{9.19}$$

Again, as was discussed previously, this methodology assumes that a lifetime independent coefficient can be used to relate normal and shear stress contributions. Furthermore, the proposed equivalent stress range in equation (9.19) is only used for screening purposes in this thesis.

9.5.4. Damage indicator

Finally, to gain an indication of the importance a particular point in the structure has concerning damage accumulation, damage importance indicator D_{imp} is introduced.

$$D_{imp} = \left[\Delta\sigma_{eq}(1 + G_{NP})\right]^3 \tag{9.20}$$

The damage importance indicator relates the degree of non-proportionality, equivalent stress range and mode-I SN curve slope to screen fatigue-sensitive locations in a structure. In [42], it was demonstrated that the damage importance indicator was effective at predicting the location of fatigue governing points in the construction relative to other points. It was, however, not as effective at predicting lifetime. This is not an issue as long as this criterion is applied to identify hotspot locations.

From section 9.5.3 it was established that maximum stress range based equivalent stress and Walker's mean stress correction are good stress range indicators, either one can be used for damage importance assessment. It must be kept in mind that $\Delta\sigma_{eq,range}$ does not consider mean stress effects.

9.6. Spectral Decomposition

Previously it was established that the environmental loading of a TLP type FOWT is highly stochastic but cyclical. This allows for spectral decomposition to be introduced as a simple but powerful analysis tool and allows for any time-varying cyclical signal to be decomposed into many harmonic signals with varying frequencies. These harmonic components can be used to conduct a Power Spectral Density

(PSD) analysis can be conducted identifying the spectral bandwidth(s) at which energy is concentrated. This information can be used to identify the relationship between (environmental) loading of the TLP and structural stress response.

As will be established in section 10.3.2, the simulations conducted are relatively short. This poses a challenge for Fast Fourier Transform (FFT) as there is relatively little information to accurately determine the spectral distribution. This means that unintended harmonic components will be overrepresented in the spectral plot, resulting in a 'grassy' signal. Ideally, one would have multiple time traces to determine the spectral shape of each. The final spectral plot is determined from the average of all of the time traces. This also identifies the second shortcoming of the data when conducting spectral analysis, as there is only one experiment available per environmental condition.

This is a problem to which Welch [144] devised a solution a long time ago and is widely implemented in engineering tools for spectral decomposition. Named after himself, Welch's method provides excellent noise reduction for finite-time signals. Without diving into the mathematics of Welch's method, this is achieved by splitting up the original time signals into N overlapping sub-signals and conducting a FFT on each sub-signal. The final spectral density is determined by averaging all of the spectra derived.

In figure 9.26, this principle is illustrated using a short arbitrarily generated cyclic signal and applying both FFT and Welch's method. As can be seen, Welch's method provides an overall improvement in signal noise reduction, especially for low-frequency components. Hence, Welch's method will be used hereafter for spectral decomposition.

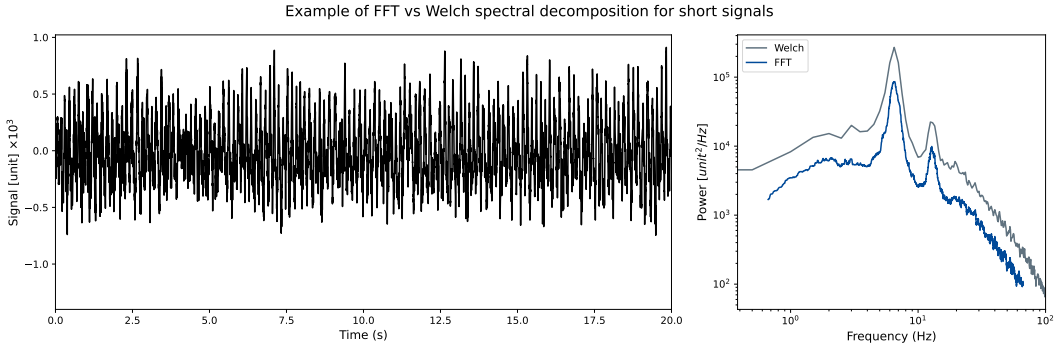


Figure 9.26: Comparison between FFT and Welch's method for spectral decomposition of a short signal.

9.7. Summarising statement

The analysis conducted in this thesis consists of multiple components separated by physics type. In this chapter, a model to determine the multiaxial stress response in a selection of critical weld seams was presented. The resulting model is capable of considering the rigid body response of a TLP-type FOWT in a multi-directional mixed wind-wave system as an input signal and to output multiaxial stress response time traces.

This was achieved with a structural model considering hydrodynamic pressure contributions at a nodal level as well as a kinematic boundary condition for the tower-TLP and tendon-TLP interfaces. This ensures that the rigid body motions are preserved and stress response is not overestimated. This provides the second part of the answer to **SQ4**. After this, the traction-based structural stress method was used to extract nodal forces and moments and to compute multiaxial stress response time histories, providing a worked example to answer **SQ3**. Finally, a multiaxial fatigue screening methodology was presented, building on the work presented by Donk [42] by including mean stress effects in the assessment by applying a modified Walker correction. This screening method allows for multiaxial response to be compared between loading conditions and parts of the structure, thus answering **SQ5**.

10

Case study

In this chapter, the selection process for different load cases in the multiaxial stress response investigation is presented. These load cases are based on a site-specific metocean report. In section 10.1 the environmental conditions on site will be explained, followed by a selection of load cases in section 10.2. Finally, in section 10.3 considerations regarding temporal discretization are handled.

10.1. Environmental conditions

In this thesis, a case study is conducted for a hypothetical installation site in the Korean Strait with a water depth of 135m. Soil conditions are not relevant for this investigation as the assumption will be made that the soil interaction effects with the anchoring installation will not affect the structural response of the TLP. However, as discussed in section 8.3.2.1, the water depth is an important consideration as the water depth must be considered intermediate for long waves. To characterise the metocean conditions hindcast data can be considered. The metocean data used in this thesis is extracted from internal documentation and is not available for public use. It considers hourly measurements for wind, waves and currents from 2002 to 2019.

10.1.1. Wind & Waves

The considered site location is characterized by a fairly bi-directional wave spectrum, propagating along the length of the Korean straight. There are some minor wind wave components originating from different directions. The wind generally blows along the Korean straight, but high winds can also originate from across the channel. Apart from wind speed and direction, the following parameters are available and set:

Wind shear: The parameter α is used to determine the distribution of wind speed using a reference height and depends on the surface. The wind shear exponent is also subject to local variations and should hence be determined from local information. For the considered site, the wind shear component $\alpha = 0.11$ at a reference height of 150m, the height of the rotor hub. Using the power law distribution, the wind speed distribution can be calculated as follows:

$$V(z) = V_{w,r}\left(\frac{z}{z_r}\right)^{\alpha} \tag{10.1}$$

Turbulence intensity: Turbulence in the wind field is subject to a number of input parameters. However, as it was established in section 4.1.1, low turbulence intensity allows for resonant frequencies to build up and be identified, which is important for fatigue analysis. Therefore, for all simulations considered, the turbulence intensity is set $I_t = 0$ [%].

For the wave system, a number of assumptions are also made regarding the simulated conditions:

Spectral shape: The wave system at the considered site is primarily of the developing seastate type. Waves are primarily short-period wind waves characterized by a larger spectral spread than, for example, a developed sea state. Hence, the JONSWAP spectrum will be considered.

Spectral spread: As shown in figure 10.1, the wave mainly propagates in the length of the Korean straight, with little spread. Hence, monochromatic wave systems are considered in this thesis.

Wave order: Due to the application of potential wave theory, only linear waves are considered in this thesis. There is no depth- or steepness-induced wave breaking.

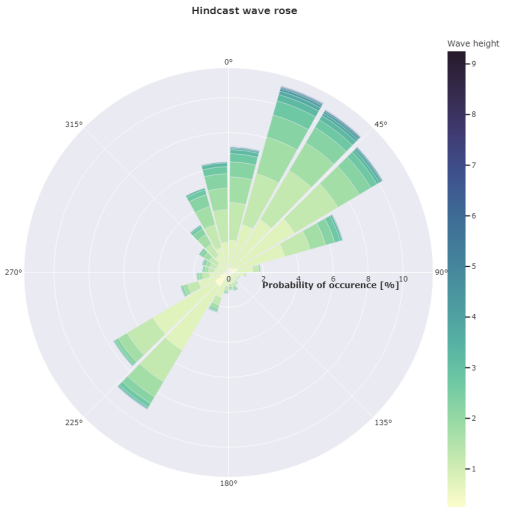


Figure 10.1: Wave rose plot for the case study site in the Korean Straight. The colour gradient is used to indicate wave height. As can be seen, waves predominantly originate from the northeast

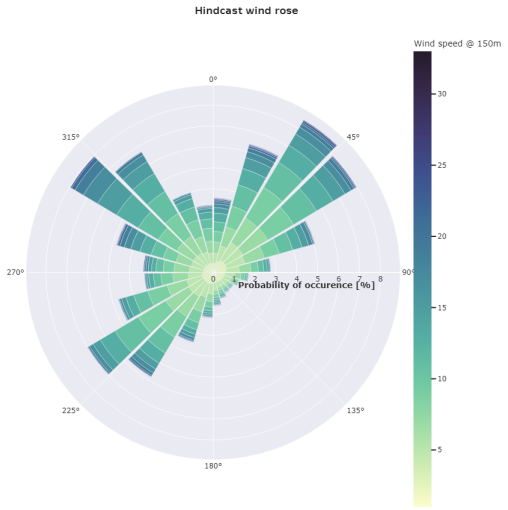


Figure 10.2: Total wind rose plot for case study site in the Korean Straight. The colour gradient is used to indicate wave height. As can be seen, wind predominantly originates from the southwest-northeast hemisphere.

10.1.2. TLP orientation to metocean environment

The first consideration that needs to be made is how the FOWT installation is oriented with respect to the environment. The orientation is dependent on structure, site, and metocean conditions. Ideally, an orientation sensitivity analysis would be undertaken; however, due to scope restrictions, this is not possible. To start, the structure should either be orientated to the dominant wind or wave direction, depending on whether the structural loading is wave or wind-dominated. Important to note is that the nacelle is installed on a yaw bearing, allowing for the rotor to face upwind independently from the substructure orientation. There is no information available regarding an orientation sensitivity analysis, and hence, it cannot be established if the TLP structure considered in the Korean Straight in this thesis is wind or wave-dominated. As can be seen in figures 10.1 and 10.2, waves have a more pronounced dominant direction. Hence, the TLP will be oriented to minimize the wave loading from the dominant wave direction. This is 40° relative to true north. Henceforth, all incoming wind and wave directions will be expressed relative to the substructure orientation.

10.2. Load cases

With an established orientation of the substructure, directional load cases can be derived from the local metocean spectrum. In figure 10.3, the unidirectional wave scatter is presented for all wind speeds.

In section 8.4.2 it was established that it was not possible to include an aerodynamic controller. This means that wind speeds of control region 2 (constant pitch, variable torque) must be adhered to, which are 6.98-10.59 m/s for the turbine considered in this thesis. This wind range will henceforth be referred to as the wind window. In figure 10.4, the wind speed probability distribution is plotted; the green dashed line is indicative of windspeeds falling within the wind window and considers about 29% of measured wind speeds.

Filtering the data presented in figure 10.3 to windspeeds falling within the wind window results in the unidirectional scatterplot presented in figure 10.5. Using this information, a number of representative and realistic environmental conditions can be selected for numerical simulations. As the visual presentation

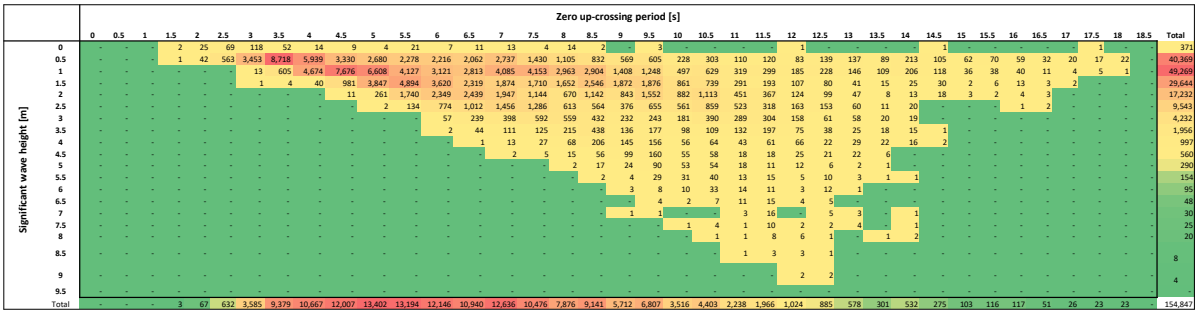


Figure 10.3: Wave scatter plot for all measured seastates, measured at hub height, 150m above sea level

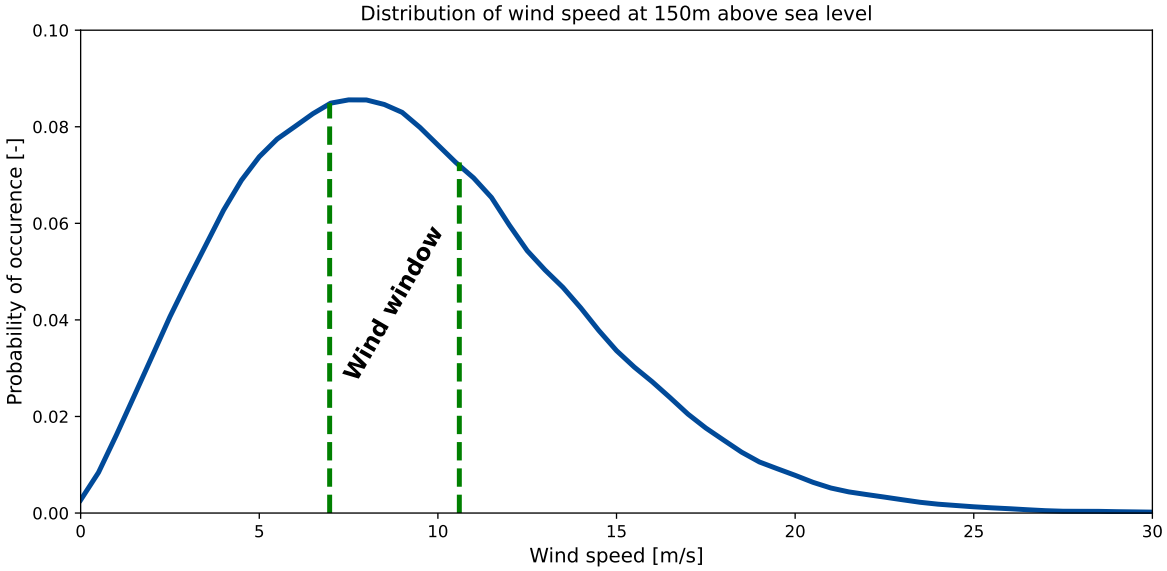


Figure 10.4: Measured wind speed probability distribution 150m above sea level. Also plotted in green is the operational wind window to which simulation must be restricted due to the absence of a controller. Within the green area, 29.8% of measured windspeeds can be found in this window.

of the metocean data in the scatter plot does not contain wind/wave directional information or wind speeds, the original dataset is consulted. Using the bin edges to filter the dataset, a subset of seastates can be considered. Taking the average of the wind speed, wind direction, wave direction along with wave peak period, significant wave height, and peak enhancement factor γ provides all of the required information to simulate a representative combination of wind and waves.

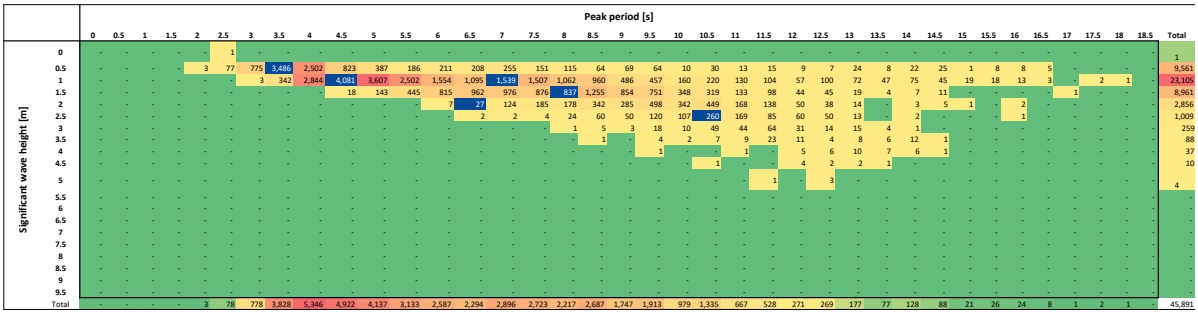


Figure 10.5: Wave scatter plot for sea states that can be simulated without an aerodynamic controller. For the turbine considered in this thesis, this wind window is $6.98 \leq V_{\infty,150m} \leq 10.59$ m/s at the hub height, 150m above sea level. Considered seastates are highlighted in blue.

10.2.1. Seastates

In addition to the assumption discussed in section 10.1.1, the remaining environmental factors considered for each seastate are as follows:

FLS1.1-3: The first seastate chosen is the most likely to occur within the wind window constraint and falls in the bin combination $H_s = 1m, T_p = 4.5s$. Within these bins, the average sea state is characterized by $H_s = 0.918$ m, $T_p = 4.52$ s, $V_{w,150m} = 9.2$ m/s, and both wind and waves are directly incident on the platform in the chosen orientation (no misalignment with respect to the floater). In order to efficiently make use of the computational resources, FLS1 is also used for a wave misalignment study. Therefore, an extra two fictitious seastates are devised with wave misalignment angles of $\theta_{\text{waves}} = 30°$ and $60°$.

FLS2: The second seastate is a relatively frequent occurrence within the wind window constraint and falls in the bin combination $H_s = 0.5m, T_p = 7s$. It was chosen as to provide a spread of chosen conditions in the scatter plot. Within these bins, the average sea state is characterized by $H_s = 1$ m, $T_p = 6.98$ s, $\theta_{\text{waves}} = 120°$, $V_{w,150m} = 8.4$ m/s and $\theta_{\text{wind}} = 156°$.

FLS3: The most likely to occur seastate where the wave spectrum is characterized by a peak period equal to the maximum angular velocity of the rotor, as defined by NREL [49]. This sea state is chosen as it represents the environmental loading spectrum with the narrowest band realistically possible and wave spectrum $H_s = 1.5m, T_p = 8s$. Within these bins, the average sea state is characterized by $H_s = 1.50$ m, $H_s = 8.00$ s, $\theta_{\text{waves}} = 100°$, $V_{w,150m} = 10.58$ m/s and $\theta_{\text{wind}} = 175°$.

FLS4: This seastate was selected as a fictitious seastate in order to test the coupled analysis model. Although not an entirely scientific approach, this seastate allowed for the simulations to be checked by eye to confirm expected behaviour. As each simulation is a significant computational expense, this combination of environmental factors was used to consider the effects of rotor controls, as well as the effect of fatigue brackets as a mitigating measure for peak stresses. Within the bins, the average sea state is characterized by $H_s = 2.50$ m, $H_s = 10.5$ s, $\theta_{\text{waves}} = 0°$, $V_{w,150m} = 9$ m/s and $\theta_{\text{wind}} = 0°$.

FLS5: This seastate came forth from preliminary engineering models with the highest relative damage contribution within the allowed wind window. This seastate is characterized by the bin combination $H_s = 2m, T_p = 6.5s$. It was chosen as to provide a spread of chosen conditions in the scatter plot. Within these bins, the average sea state is characterized by $H_s = 2.18$ m, $T_p = 6.75$ s, $\theta_{\text{waves}} = 60°$, $V_{w,150m} = 9$ m/s and $\theta_{\text{wind}} = 0°$.

FLS6: In order to study the effect of extremely short wavelengths, the most likely seastate to occur with extremely high wave frequency was selected, corresponding to a seastate with bins $H_s = 0.5m, T_p = 3.5s$. Within these bins, the average sea state is characterized by $H_s = 0.61$ m, $H_s = 3.53$ s, $\theta_{\text{waves}} = 150°$, $V_{w,150m} = 8.3$ m/s and $\theta_{\text{wind}} = 150°$.

All of the seastates can be summarized in table 10.1 below.

Table 10.1: Summary of seastates considered in this investigation

Name	H_s [m]	T_p [s]	$\theta_{\text{waves}}[°]$	γ [-]	$V_{w,150m}$ [m/s]	$\theta_{\text{wind}}[°]$
FLS1.1	0.92	4.52	0	1.6	9.20	0
FLS1.2	0.92	4.52	30	1.6	9.20	0
FLS1.3	0.92	4.52	60	1.6	9.20	0
FLS2	1.00	6.98	120	1.6	8.38	156
FLS3	1.50	8.00	100	1.6	10.58	175
FLS4	2.5	10.5	0	1	9.00	0
FLS5	2.18	6.75	60	1.63	9.00	0
FLS6	0.61	3.53	150	1.6	8.30	150

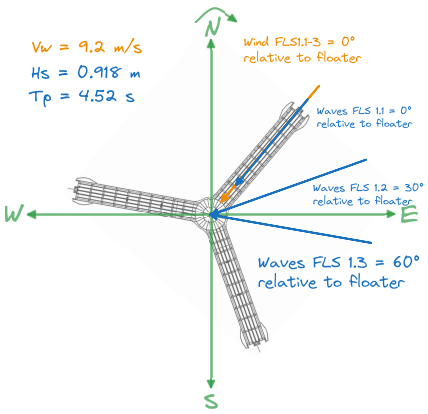


Figure 10.6: FLS 1.1-3 are a set of simulated seastates based on the most likely to occur combination of wind and waves within the wind window.

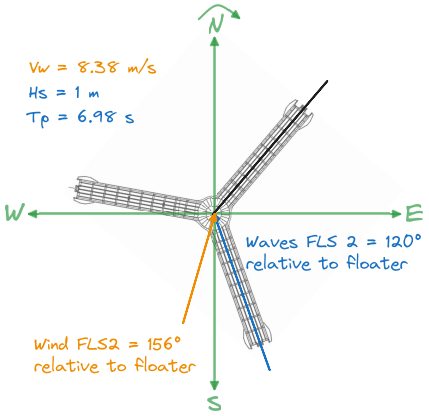


Figure 10.7: FLS 2 is chosen to provide an even spread in the choice of seastates from the site-specific scatter plot.

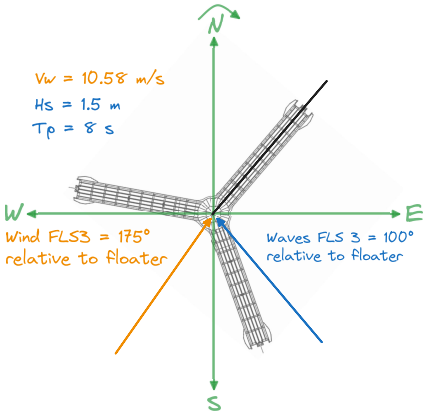


Figure 10.8: FLS 3 aligns maximum angular frequency with the peak frequency of the incoming wave to concentrate external excitation energy in a narrow spectral bandwidth.

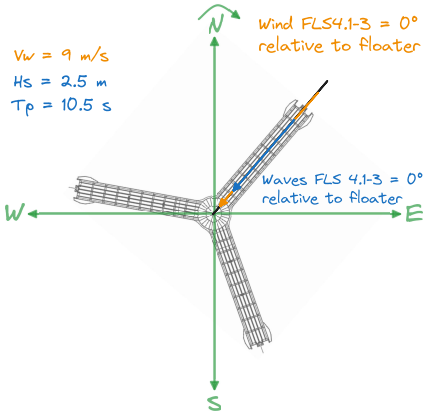


Figure 10.9: FLS 4 provided a baseline to investigate changes to a single parameter in the system.

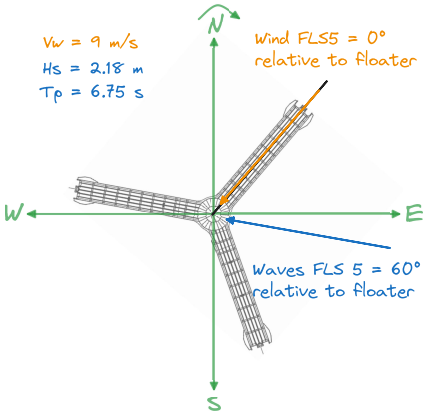


Figure 10.10: FLS 5 is the design case that results in very high statistical damage.

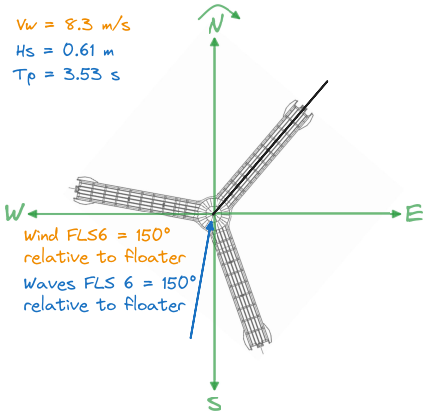


Figure 10.11: FLS 6 studies the effect of short wave systems on structural loading and response.

10.2.2. Special cases

In addition to the seastates introduced in section 10.2.1, several extra cases are considered in order to investigate the effect of particular changes to the system. Although FLS1.1-3 can also be categorised in this way, the special cases in this consider the exact same environmental conditions.

FLS4.1-2 This seastate is used to investigate the effects of rotor controls on the floater motions, as well as the structural stress response. In FLS4.1, the FOWT system will be considered unchanged relative to the other simulations and use the power control system discussed in section 8.4.3. In FLS4.2, no power controls will be considered. In the absence of any resisting force/torque, the rotor is free to rotate as fast as possible until the blade's aerodynamic profile starts to stall, effectively making the turbine a stall-controlled turbine, as briefly covered in section 4.1.5.1.

FLS3FB, FLS4FB, FLS5FB These seastates will consider the effects of fatigue brackets installed between the pontoons and central column. These fatigue brackets seek to reduce hotspot stress, especially at the hard points between the corners of the pontoon-column connection. As can be seen in figure 10.12, these brackets are distributed over the width of the pontoon-column connection. All of the considered brackets are of equal plate thickness and column thickness. Furthermore, as can be seen, the brackets installed at the edges of the pontoons are larger due to the increased magnitude of the stress hotspot at this point.

The three considered seastates are chosen specifically because: FLS3 is a narrow loading spectrum, FLS4 already serves as a platform for comparison and FLS5 is the seastate with the highest expected damage.

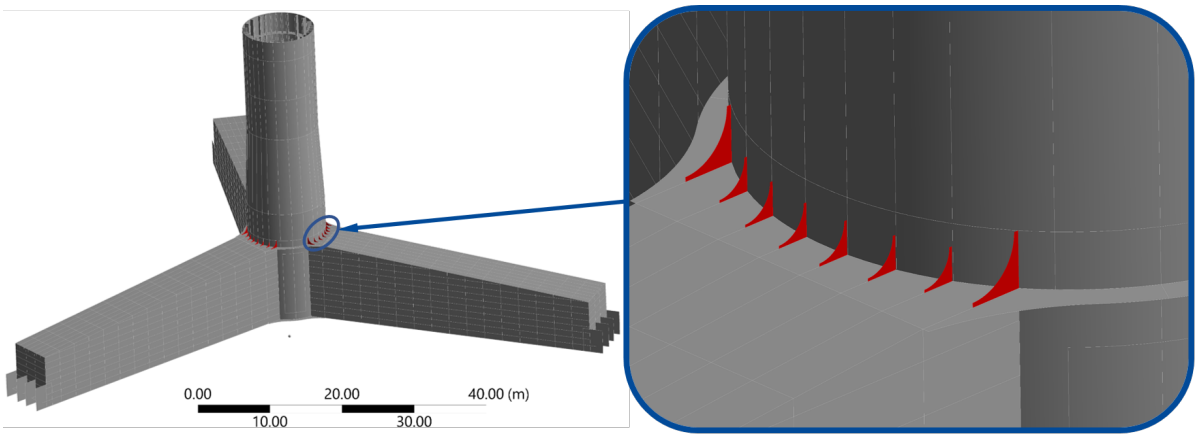


Figure 10.12: Addition of external fatigue brackets installed between the pontoons and column on the outer hull. These fatigue brackets seek to reduce hotspot stress, especially at the hard points between the corners of the pontoon-column connection.

Table 10.2: Summary of special cases

Name	Description of special case
FLS3FB	Including fatigue brackets
FLS4.1	Including PTO
FLS4.2	Excluding PTO
FLS4FB	Including fatigue brackets
FLS5FB	Including fatigue brackets

10.3. Temporal discretization

For temporal analysis, a number of considerations regarding time must be addressed. First of all, simulation time step convergence needs to be achieved, which is addressed in section 10.3.1, and a simulated time frame needs to be established. Next, the total simulation duration, including startup time allowing for transient effects to subside, needs to be covered in sections 10.3.2 and 10.3.3 respectively.

Finally, any artefacts caused by generating temporal signals from the spectral representation of data are considered in section 10.3.4.

10.3.1. Time step

For the type of analysis conducted in this thesis, there are two types of time steps, one for the motion analysis and one for FEA analysis, which do not need to be equal ($\delta t_{motion} \geq \delta t_{FEA}$). As can be seen from figure 10.13, the size of the timestep converges very quickly. As a benchmark, the magnitude of the excursions of the COG is considered. A time stepsize of $\delta t = 1$s was also attempted but could not converge. As can be seen in the window, step sizes of $\delta t = 0.05$s and $\delta t = 0.01$s display almost identical behaviour. A step size of $\delta t = 0.1$s shows the same response but is not able to capture a high-frequency component. The difference in response is in the order of 1cm and should hence suffice. Hence, for the motion analysis, a temporal discretization of $\delta t = 0.1$s is applied.

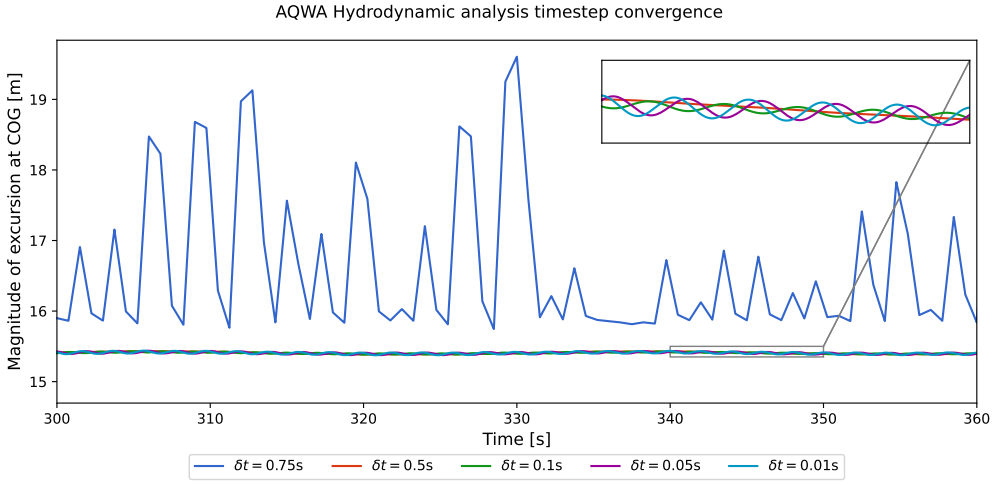


Figure 10.13: Convergence of time step discretisation for an AQWA motion analysis.

For structural response models, a larger time step may be considered as the loads on the floater are generally of lower frequency than at the rotor. This also allows for the model to run more efficiently. Hence, for the structural response analysis, a temporal discretization of $\delta t = 0.5$s is applied.

10.3.2. Simulation duration

In an ideal world, a vast number of hours of simulated time would be computed, providing vast amounts of data and allowing for intricate study of the interaction between subsystems. Sadly, this is not possible, and simulations must be bound to finite blocks of time. Often, blocks of 3 hours are considered as this timeframe usually allows for a storm to build up and subside, providing information on the various phases of the storm. From a computational resource perspective, this timeframe is still too long. Holthuijsen [61] states that the wave period must be short enough to be considered stationary and long enough to provide a reliable average, resulting in the most common compromise of 15-30 minutes. For this reason, a simulation duration of 20 minutes was chosen, plus a period in which the transient effects are allowed to subside.

It should be noted, though, that to properly account for short-term statistics (see section 3.2.4), multiple 20-minute simulations should be run, all of which are generated from the same input data set. The number of simulations that should be conducted depends on how much simulated time is required to achieve convergence between the statistical parameters of the simulated environment and the intended statistical parameters.

10.3.3. Filtering transient effects

Due to the formulation of the simulations, at the time of initialization, all bodies of the structure are at rest, subject to the initial wind speed. As the waves propagate into the simulated volume, the structure begins to interact with its environment. Therefore, the simulation is subject to a period filled

with transient effects before dynamic equilibrium is found. This period with transient effects does not represent the target simulated environment and must hence be filtered out of the dataset. This period is not constant for all simulations and is related to the severity of the seastate to which the structure is subject. Very mild seastates have a short transient period relative to more severe conditions. Through a process of trial and error, it was established that a period of about 300 seconds (5 minutes) is enough time for all transient effects to disappear. Hence, all simulations considered should be of at least 25 minutes in length and should discard the first 5 minutes of data.

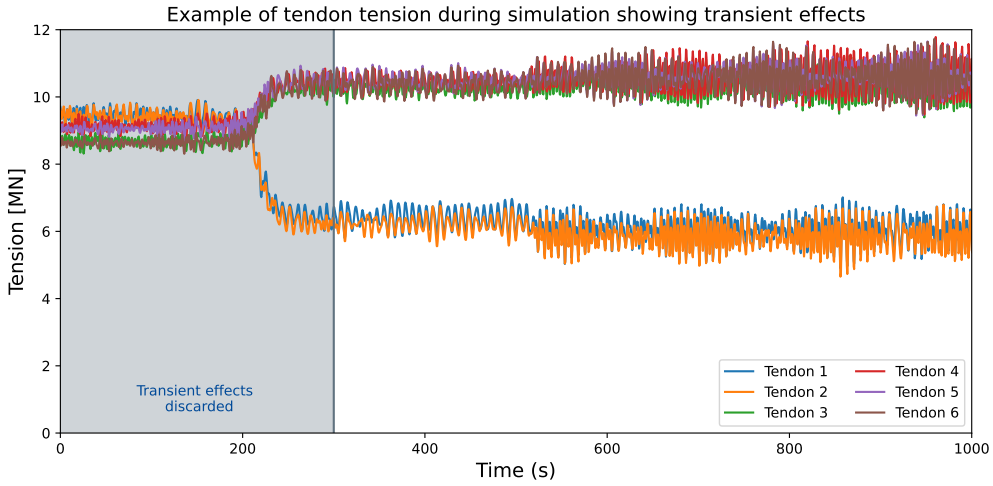


Figure 10.14: Example of a motion analysis conducted, clearly showing startup effects in the first part of the simulation, using tendon tension as an indicator. After a maximum of 300 seconds, the simulation stabilises.

10.3.4. Simulated vs Target spectrum

As was discussed in section 3.2.6, due to the method of reconstructing an irregular sea state signal from long and short-term statistics, the wave spectrum of the generated signal should be statistically indistinguishable from the target spectrum. This is especially relevant to check considering the relatively short wave signals considered, for reasons discussed in section 10.3.2. This can be checked by comparing spectral parameters such as H_s, T_p and γ. As can be concluded from table 10.3, the 20-minute simulated window provides enough cycles to simulate the majority of the spectral input energy accurately, as can be seen by the small difference in H_s, T_p. It can, however, also be seen that 20 minutes is not enough to accurately account for the peak enhancement factor γ. Furthermore, these conclusions are based on a single time trace per seastate, whereas the recommended practice is to simulate enough unique seastates generated from the same spectrum to reach statistical convergence in wave elevation, structure motions and structure loads. Due to computational restrictions, this was not possible within the scope of this thesis.

Table 10.3: Comparison of generated and target wave spectra

	Target			Simulated		
Name	**H_s [m]**	**T_p [s]**	γ [-]	**H_s [m]**	**T_p [s]**	γ [-]
FLS1	0.92	4.53	1.60	0.92	4.49	1.90
FLS2	1.00	6.98	1.60	1.01	7.11	1.57
FLS3	1.50	8.00	1.60	1.50	8.00	1.59
FLS4	2.50	10.5	1.00	2.47	10.24	1.10
FLS5	2.18	6.75	1.63	2.20	6.56	1.62
FLS6	0.61	3.53	1.60	0.61	3.66	1.85

10.4. Summarising statement

In this chapter, the metocean environment was introduced, starting with the general wind and wave environment and how the floater was oriented with respect to the environment. Next, a set of load cases was presented, thus answering **SQ2** with a practical example. The considered seastates are derived from the statistical metocean representation and considered a set of realistic seastates. Another set of seastates was introduced to investigate the effects of specific changes to the system. Finally, the last part of the answer to **SQ4** was provided by discussing the implications of time discretization.

Part III

Results

11

Results

In this investigation, a total of 12 different cases were considered, spread over 6 unique seastates, as discussed in section 10.2. This produced a total of 4 hours of time traces, resulting in a total data footprint of around 1.61TB of data to be processed. For the eight critical weld seams considered, 2343 sets of multiaxial stress time traces are produced per simulation. Each simulation required between 23-27 hours of computational time on a high-performance cluster. Due to the volume of available data, it is simply not feasible to present everything in this chapter. Instead, the key findings will be presented here. In regards to data visualisation, this chapter will highlight several figures. appendix C contains a complete overview of data visualization for all seastates.

First of all, in section 11.1, the results of spectral decomposition on the loading and stress response signals are presented. In section 11.2, the external loading source dominance will be discussed. Next, in section 11.3, a more detailed analysis of the multiaxial stress response signals will be presented. Finally, in section 11.4, the resulting damage accumulation will be presented.

11.1. Spectral decomposition

In section 9.6, the methodology of spectral decomposition was described and will be applied for post-processing in this section. As discussed previously, the temporal simulation approach developed for this investigation can be split up into two distinct parts, loading & response. These components will be handled separately in sections 11.1.1 and 11.1.2. Rigid body natural frequencies from table 8.7 are plotted for reference as well.

11.1.1. Loading

As discussed in part I, the main external loading sources are aerodynamic, hydrodynamic and mooring response types. These sources are considered in the spectral decomposition below. For reference, these plots are quite dense in information and show the PSD for external forces as well as incident wave spectrum on separate y-axes. In addition to this, plotted with vertical lines are the natural frequencies for different rigid body motions, as well as the first three resonance frequencies for the rotor. Furthermore, in the spectral plots below, it may appear as though the structural natural modes are not well aligned with peaks of the PSD; this is an issue that can be attributed to a mismatch in the discretization of the frequency, which was discovered while post-processing.

1. As can be seen in figures C.1 to C.9, there are a couple of key observations that stand out. First of all, across all simulations conducted, a very strong correlation between the spectral density of tendon tension and two specific frequencies. The first of which is the rotor angular velocity (**P**), and the second of which is the natural frequencies of roll (θ) and pitch (ϕ). In figures 11.1 and 11.2 below, it can be seen that there is a significant increase in energy at these spectral bandwidths. This is indicative that aerodynamic loading is a dominant parameter for motion response, along with structural resonance in roll and pitch, which are the constrained DOFs for a TLP. Although z is also a constrained DOF, no spectral peak is observed at ω_z. This could be caused by a lack of excitation in this spectral bandwidth.

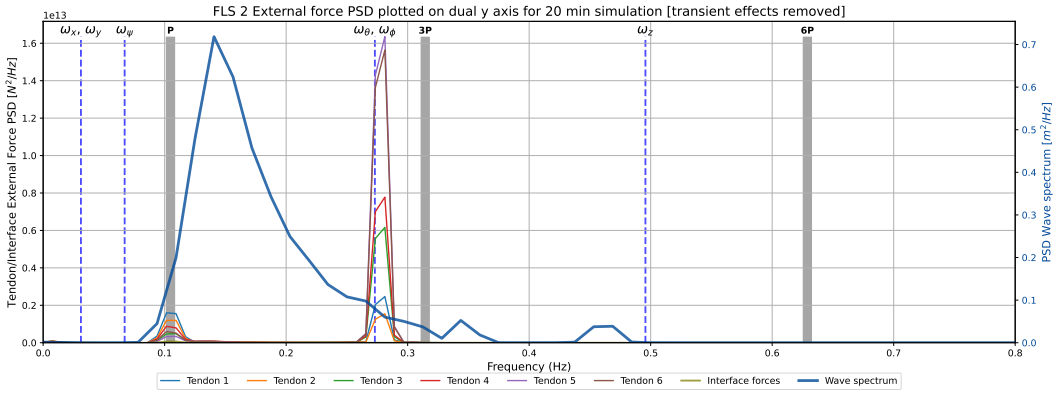


Figure 11.1: Spectral decomposition of external forces for FLS 2

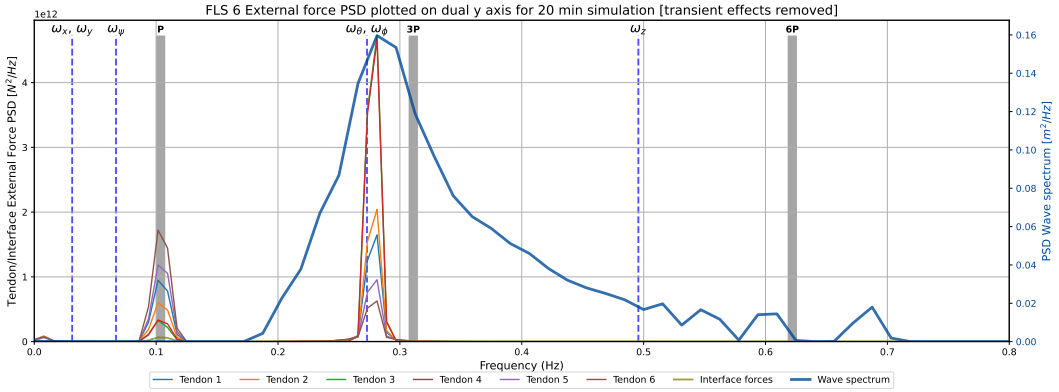


Figure 11.2: Spectral decomposition of external forces for FLS 6

2. The first conclusion can further be tested by considering FLS4.2 (no power controls), which boasts the highest angular velocity. As can be seen in figure 11.3 this confirms this spectral peak is attributed to **P**, and is not a compound effect of a rigid body mode and the wave spectrum. figure 11.3 also reiterates the importance of including power controls when investigating FOWT, as the rigid body motion response is significantly impacted.

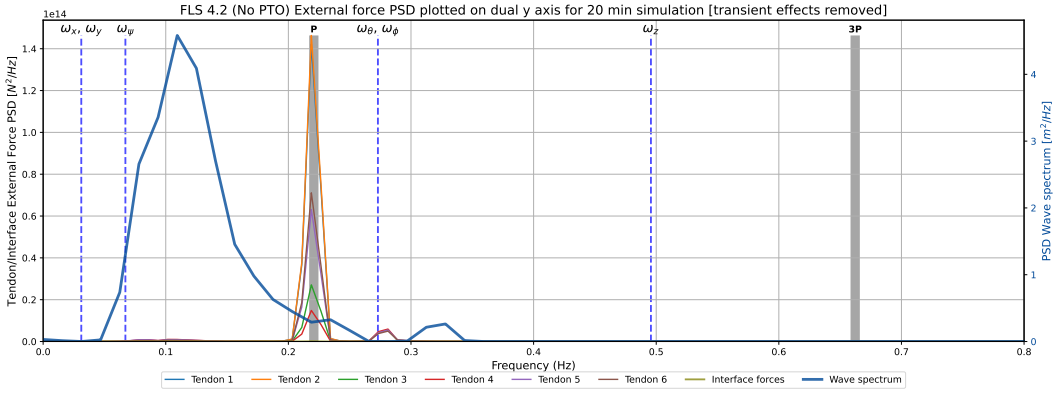


Figure 11.3: Spectral decomposition of external forces for FLS 4 without any rotor power controls, showing a significant increase in rotor angular velocity and corresponding spectral shift in tendon tension.

3. Spectral energy accumulated in specific bandwidths, which can be predicted from rotor angular velocity and natural modes of the structure, both of which are parameters that are known or can easily be calculated ahead of any simulation work. This suggests that the predictability of energy

accumulation in specific spectral bandwidths can be used in screening methods.

4. FLS1.1-3 it can also be concluded that wave misalignment with respect to the floater does not yield a significant impact on the tendon tension PSD, this can be seen in figures C.1 to C.3. As tendon tension is a scalar value this is enough evidence to state that wave heading is not an important factor, as direction must be considered as well. However, this does provide further evidence that wind loading is more dominant than wave loading. This concept is further explored in section 11.2.
5. Another observation from the spectral decomposition is that the spectral shape of the waves is still quite rough and confirms the conclusion drawn in section 10.3.4, which is that the simulations should ideally be longer. However, as discussed, the models are already very computationally heavy.

11.1.2. Response

For reference, these plots are quite dense in information and show the PSD for the total energy density for each weld. This is determined by considering the PSD for σ_s and τ_s for all 2343 time traces separately and considering the total energy spectrum per weld. In this series of figures, the wave load spectrum is not included, as it was established in section 11.1.1 that wave loading does not have a significant influence on mooring line response frequency and hence is not expected to be dominant in structural response.

Again, several observations can be made from the spectral decomposition of the weld node stress signal.

1. As can be seen in figures C.10 to C.21, all simulations display the same very strong correlation between the spectral density of tendon tension two specific frequencies, which again are the rotor angular velocity (**P**) and the natural frequencies of constrained DOFs roll (θ) and pitch (ϕ). In figures 11.1 and 11.2 below, it can be seen that a significant increase in energy is observed at these spectral bandwidths. This is indicative that aerodynamic loading is a dominant parameter for motion response, along with structural resonance in roll and pitch.

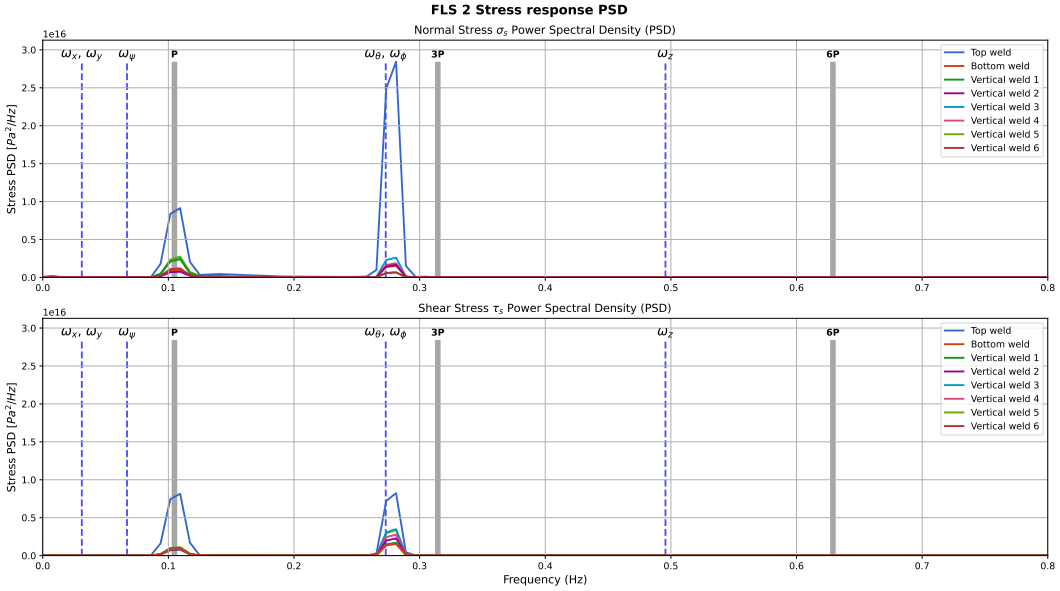


Figure 11.4: Spectral decomposition of weld stress response for FLS 2

2. From the magnitude of the peaks seen in figures C.10 to C.21 it can be seen that mode-{I,III} response are of comparable importance. Hence, there is a degree of multiaxiality in all of the welds considered, especially the top weld. These spectral plots are, however, not definitive proof of multiaxial stress response as this methodology does not distinguish between some parts of the welds subject to uniaxial mode-{I} and uniaxial mode-{III} response and a point that is subject to mixed mode-{I,III} stress response.

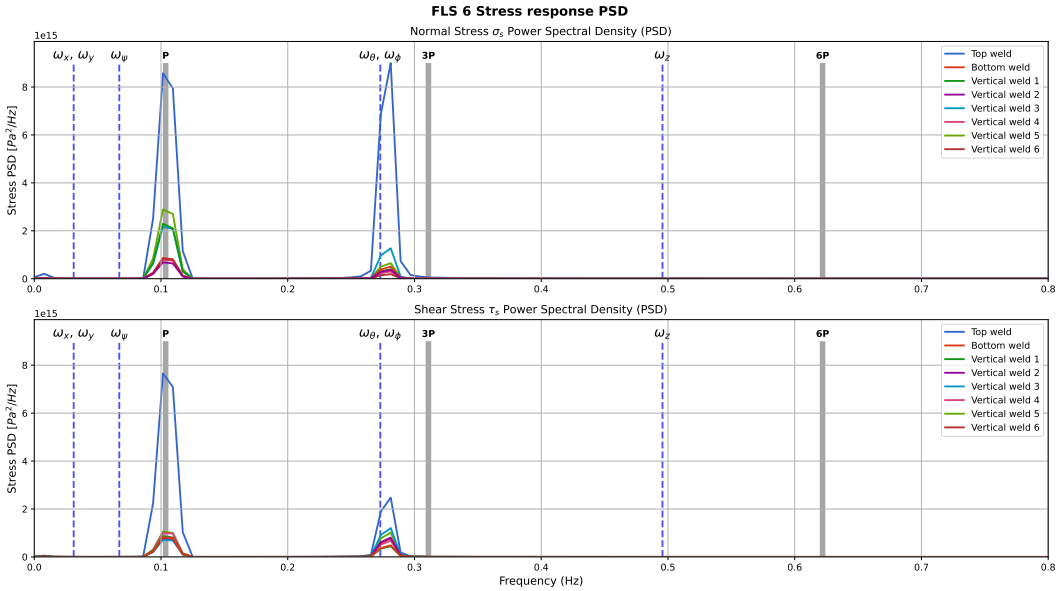


Figure 11.5: Spectral decomposition of weld stress response for FLS 6

3. The spectral accumulation of response energy suggests a degree of predictability in the system. Although no conclusions regarding the degree of multiaxiality can be drawn from this, it does provide valuable insight. For engineering applications, this allows for analysis to be targeted to specific excitation frequencies. For example, if the absolute worst set of loading conditions is applied to the structure, and no multiaxial stress response can be induced, it can be concluded that multiaxial stress response will not be an issue in milder conditions.

11.2. Load dominance

From the simulation output, the relative contribution of various loading sources can be assessed. As a full statistical analysis of the loading information is out of the scope of this thesis, a more straightforward comparison is considered in order to provide more insight into the relative contribution of various load sources.

In table 11.1, all 3D load components are reduced to a magnitude in the global X-Y plane, as this is the plane in which the loads generally propagate. The average magnitude of these loads is expressed as a percentage of the total per seastate. It should be noted that by comparing magnitudes, all directional (and sign) information is lost. As can be seen, the relative contribution of the hydrodynamic load heavily depends on the 'intensity' of the considered seastate, as discussed in section 8.4.3. However, as can generally be seen, the aerodynamic loads are the dominant excitation load, as the mooring loads are a response to said excitation. This provides further evidence for the conclusions drawn from the loading & response spectral decomposition regarding load dominance.

Table 11.1: Comparison of generated and target wave spectra

	Load source contribution		
Simulation	Hydrodynamic	Mooring	Aerodynamic
FLS 1.1	10.8%	45.1%	44.1%
FLS 1.2	11.1%	44.9%	44.0%
FLS 1.3	9.1%	45.9%	45.0%
FLS 2	21.9%	39.6%	38.5%
FLS 3	26.1%	37.3%	36.7%
FLS 4.1	46.6%	27.2%	26.1%
FLS 5	33.3%	33.7%	32.9%
FLS 6	5.8%	47.9%	46.4%
Average	20.6%	40.2%	39.2%

11.3. Multiaxial Stress Response

Multiaxial stress signals can also be analysed in the Von Mises stress plane and allow for different types of stress behaviour to be constituted visually. As discussed previously, due to the volume of time traces, it is not possible to consider them one by one. In figure 11.6, the stress history for all four element sets for a specific node in the top weld are plotted in the same figure. The location of the considered node in the structure is indicated. The behaviour plotted is typical for the structure and provides a lot of information.

Set 1: In this element set there is a significant amount of mean shear and normal stress, relative to the cycle amplitude. Although the signal is technically a multiaxial stress response, the degree of multiaxiality (Θ) and non-proportionality (G_{NP}) is very low (see section 9.5). Hence, the signal can be considered as a mode-III dominant response. This behaviour is expected as the yawing moment applied by the turbine onto the tower-TLP interface results in time-varying shear stress, and the mean shear stress is due to the external loading. The low normal stress range is also expected, and the mean compressive normal stress can be attributed to the weight of the structure above.

Set 2: Weld set 2 displays a completely different type of stress behaviour. The signal still has a low degree of non-proportionality but carries a higher degree of multiaxiality. The mean normal stress component is caused by the pretension in the mooring lines.

Set 3: Weld set 3 experiences the same level of mean normal stress as weld set 1, due to the self-weight of the structure above. However, as it lies in

Set 4: Weld set 4 displays the highest degree of non-proportional multiaxial stress but has low normal and shear stress ranges. There is also very little mean stress because this element set is located inside the column's deck.

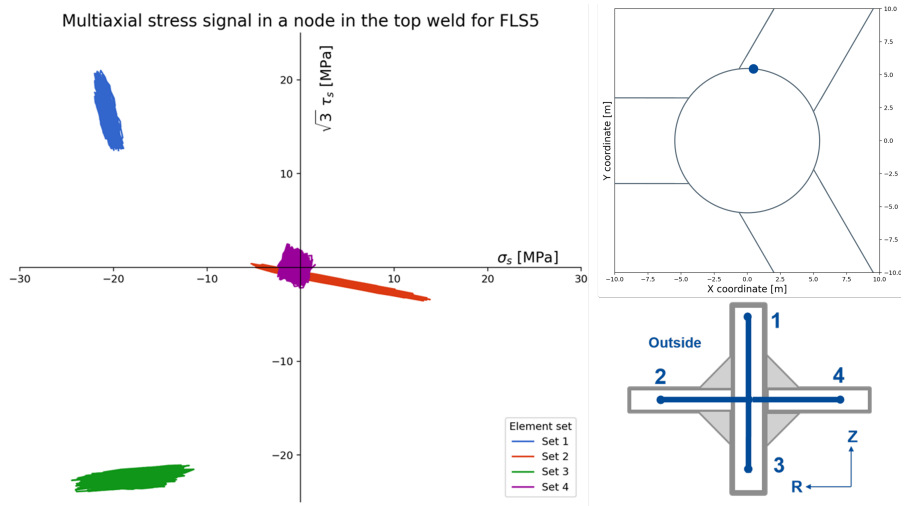


Figure 11.6: Example of varying multiaxial stress state in different weld element sets for the same node in the same weld. This case is in the top weld for FLS5

It can hence be concluded multiaxial stress response is consistently present in all parts of the critical welds but does not present the same level of severity. In order to quantify the severity of the multiaxial stress response, further analysis must be conducted.

11.3.1. General Stress Behaviour

The general behaviour observed in figure 11.6 can be observed in all parts of the critical welds considered. Using the MCE based screening method discussed in section 9.5, individual time traces can be expressed by a number of characteristics of the MCE. The first tool to gain an understanding of the multiaxial stress response behaviour is to consider the $G_{NP} - \sigma_{eq}$ distribution, as shown in figure 11.7 for various considered seastates. In general terms, a high degree of non-proportionality, along with a high equivalent stress range, is an indicator of a low expected lifetime and is problematic.

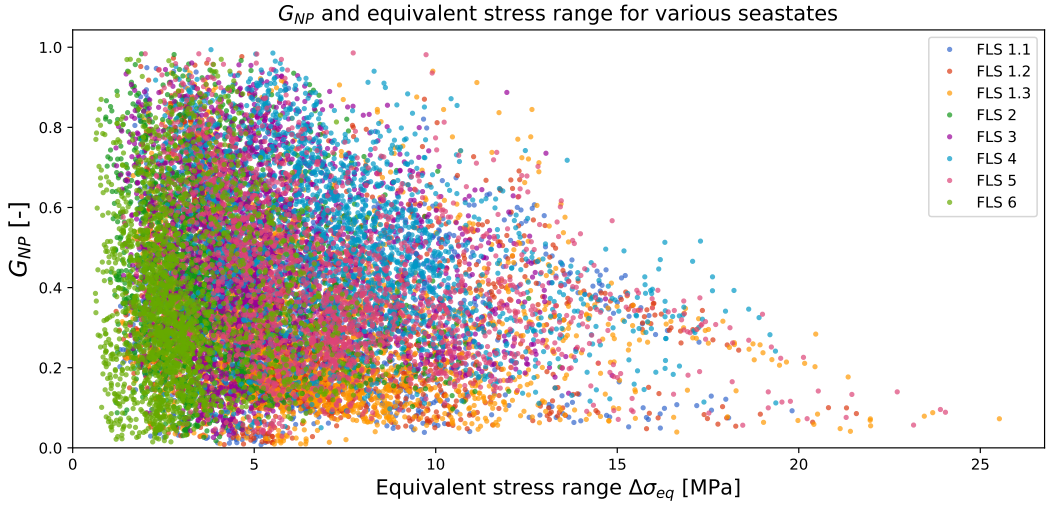


Figure 11.7: Distribution of degree of non-proportionality and equivalent stress range, excluding a mean stress correction.

As shown in figure 11.7, there is a very large spread in the degree of non-proportionality, however, this is not always indicative of a problem, as observed with element set 4 in figure 11.6, which boasts a high level of non-proportionality due to the relatively low stress and shear ranges, i.e. a complex stress state. In order to distinguish between less important and more important fatigue-contributing locations, the damage importance indicator was introduced equation (9.20). As multiaxial stress screening is in early development, no extrapolations to the expected lifetime can be made. Screening parameters such as the damage importance introduced in this thesis should be considered as a tool for relative comparison rather than absolute truth.

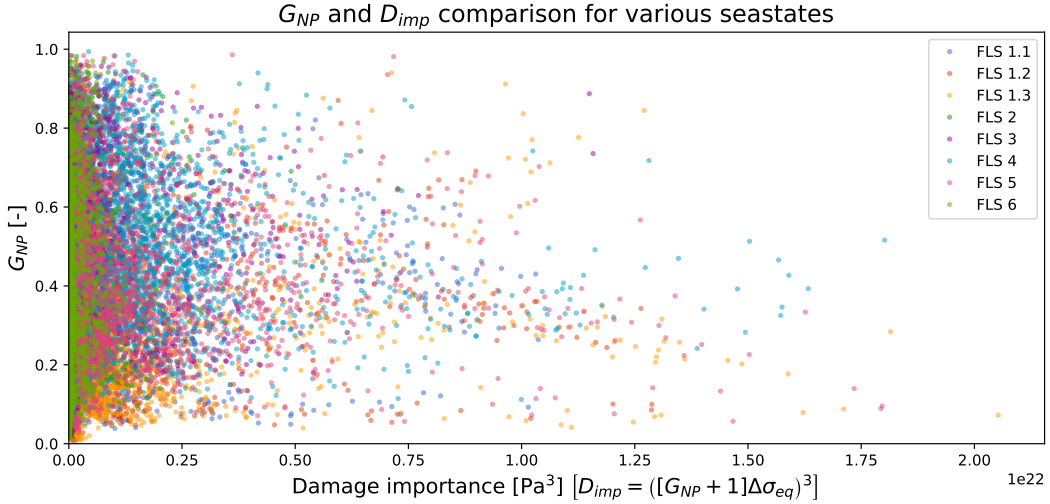


Figure 11.8: Distribution of degree of non-proportionality and damage importance, excluding a mean stress correction.

From figure 11.8, a better distinction can be observed between relative damage importance and non-proportionality. It can also be seen that, generally, the points with the highest relative damage importance have the lowest degree of multiaxiality. Interestingly, FLS1.3, FLS3 and FLS5 result in a selection of highly multiaxial stress states in combination with high levels of non-proportionality despite not being the most violent seastates. The work of Donk [42] demonstrated that the damage importance indicator is a good predictor of fatigue lifetime governing locations. These points will henceforth be referred to as fatigue-governing locations.

11.3.2. Mean stress correction

It was previously mentioned that particular parts of the considered critical weld seams are subject to mean stress, albeit due to varying external loading or structure self-weight. In figure 11.9, the distribution of mean stress in the Von Mises stress space is plotted. A coloured scale is applied to indicate the density of points. As can immediately be seen, the distribution of mean normal and shear stress is clumped, and most of the data has a relatively low mean stress. Interestingly enough, the distribution of shear stress follows a normal distribution, whereas normal stress does not. An explanation for this observation cannot be offered but may serve as an interesting follow-up investigation.

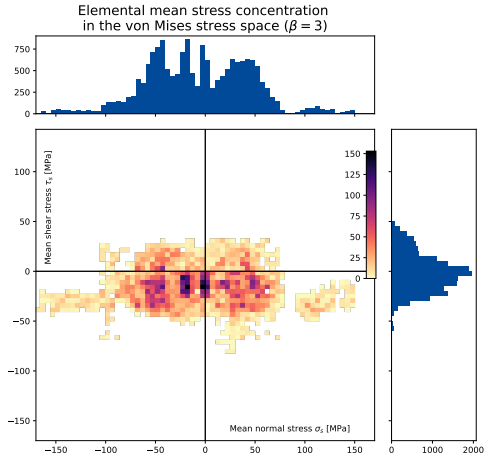


Figure 11.9: Distribution of mean stress concentration

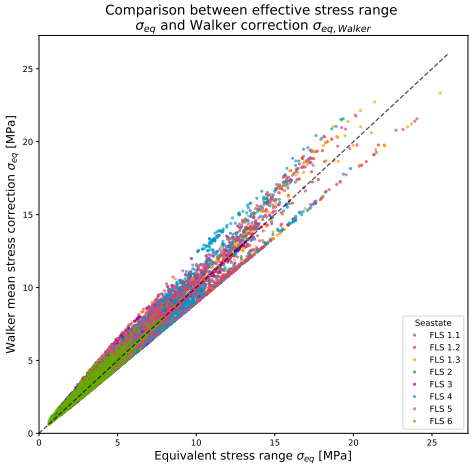


Figure 11.10: Effect of Walker mean stress correction on the equivalent stress range.

In section 9.5.3.5, a methodology to correct for mean stress effects using Walker's model was presented. In figure 11.10, the effects of this correction can be seen, again presented per seastate. For reference a line indicating $\sigma_{eq}/\sigma_{eq,Walker} = 1$ is plotted. Element sets experiencing a compressive mean normal stress have a reduced equivalent stress range and shift to the bottom right of the plot. Elements experiencing a mean tensile normal stress have an increased equivalent stress range to correct for the decreased expected lifespan, attributed to the fatigue crack subjected to variable stress response while being open. About 36% of data is corrected for a mean tensile normal stress, increasing in a larger equivalent stress range $\Delta\sigma_{eq,Walker}$ and D_{imp}.

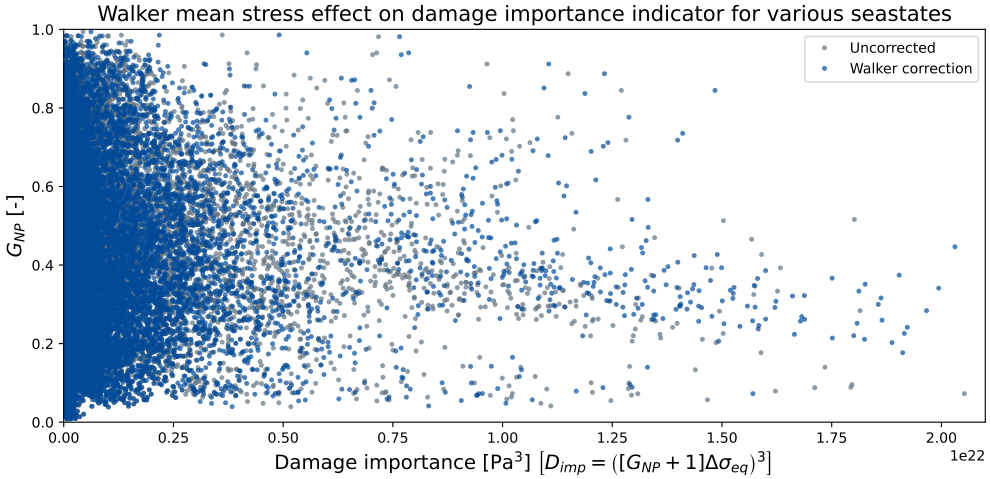


Figure 11.11: Distribution of degree of non-proportionality and damage importance, including a mean stress correction.

Applying this mean stress correction to the data presented in figure 11.8 shows a clear shift in

the data, as depicted in figure 11.11. For reference, the uncorrected dataset is plotted in grey in the background. Although the global effect of the mean stress contribution to the stress behaviour of the critical weld seams was investigated, it is not possible to see the effect of the mean stress effects. In figure 11.12, the effect of mean compressive and tensile stress on the damage importance indicator are evaluated separately, once again relative to the uncorrected dataset.

In the lower window, the effect of Walker's mean stress correction for compressive mean stress is plotted. Generally speaking, most of the points receiving a correction to lower damage importance were already of low damage importance due to a combination of relatively low stress ranges with a wide range of non-proportionality. There is some scatter in the data with a number of elements with high $\{G_{NP}, D_{imp}\}$. No concerning stress behaviour is constituted for $\sigma_m < 0$. This cannot be said for $\sigma_m > 0$, as the elements with existing large $\{G_{NP}, D_{imp}\}$ have shifted into an even more problematic region, indicating that the already highly loaded critical design points are also subject to significant mean stresses. This means that disregard for mean stress effects at the critical design points will lead to an underestimation of the fatigue contribution at these points and an overestimation of life expectancy. As this screening method cannot be used to predict lifetime, an estimate of the incurred error margin can be given. In section 11.4 a brief review of the damage importance criterion is given.

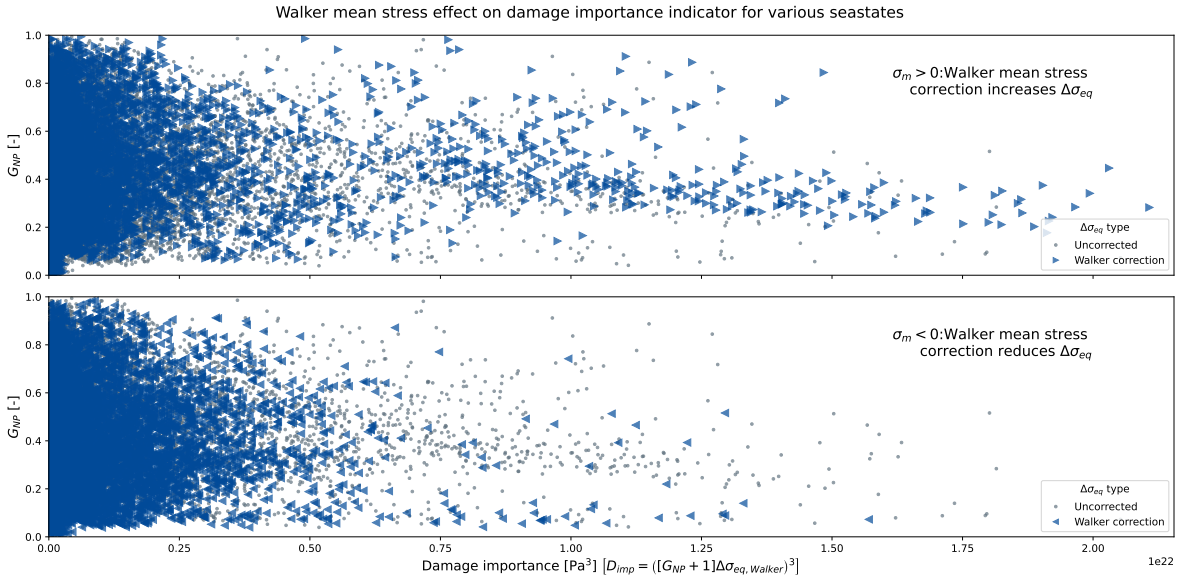


Figure 11.12: Distribution of degree of non-proportionality and damage importance, showing the relative effect of the mean stress correction.

11.3.3. Spatial distribution of stress behaviour

As can be seen in figure 11.13, a strong relationship between D_{imp} and location in the weld seam can be seen. As the top weld is governed by several orders of magnitude, the stress behaviour in the bottom and vertical welds can be found in appendix D.

Taking a step back and considering the behaviour in all critical weld seams. For the top and bottom welds, the level of multiaxial stress response is significantly lower within the pontoons compared to the wetted hull between the pontoons. This pattern can be constituted for all considered seastates, although the magnitude of the data scales with the severity of the seastate considered. Within pontoons 2 and 3, FLS1.3 and FLS5 show a deviation from this pattern, showing higher damage importance than the rest of the data. This deviation can be attributed to the high levels of misalignment between wind and waves for these simulated cases. For the 6 vertical critical welds, a general pattern of increased damage importance near the connection to the top and bottom welds can be seen, along with small increases relative to the rest of the data at the locations of the longitudinal stiffeners. This can be attributed to the stiffness-attracted loading mechanism acting at the hotspot. Again, damage importance in the vertical weld seams is significantly lower than in the top and bottom circular welds.

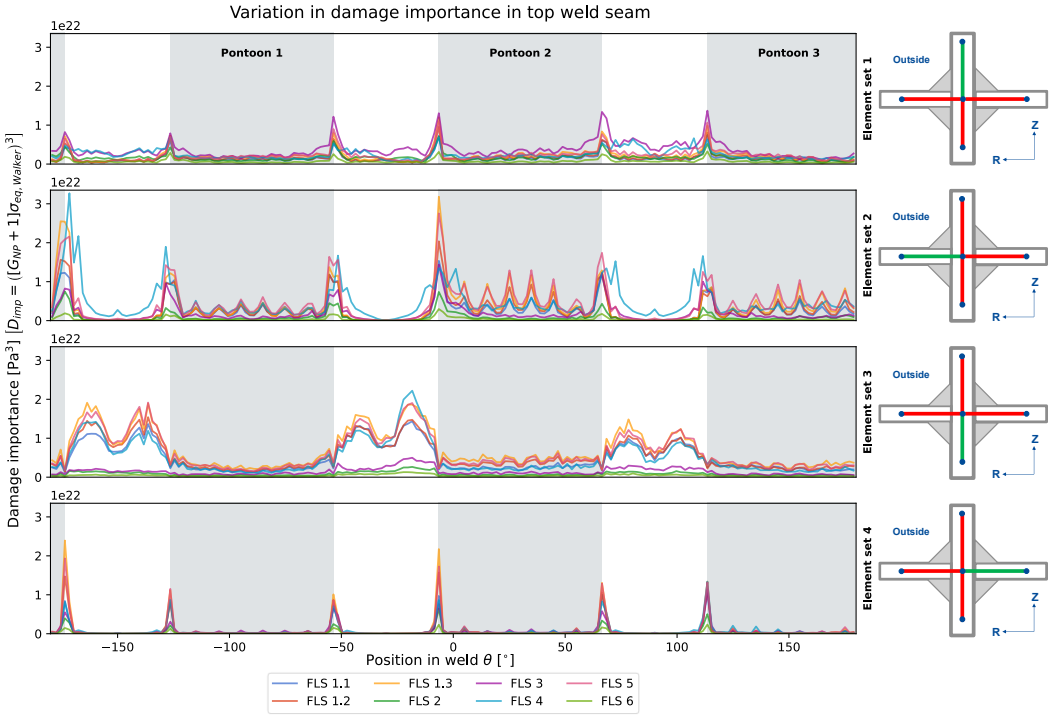


Figure 11.13: Damage importance throughout the top critical weld seam, showing a clear pattern.

The varying stress behaviour between element sets can be attributed to various local loading mechanisms. The most interesting of these loading mechanisms is the scissor effect. This phenomenon is caused by tendon load components that act out of the radial plane of symmetry of the pontoon. As illustrated in figure 11.14, when these components become large enough and point in opposing directions (out of phase), the column between the pontoons (shown in red) is subject to a large compressive, pinching force, just as when closing a pair of scissors. This significantly increases the degree of local non-proportional stress response and may have fatigue lifetime implications. It was found that the transfer of the bending moment from the pontoon to the central column is dominant for this effect.

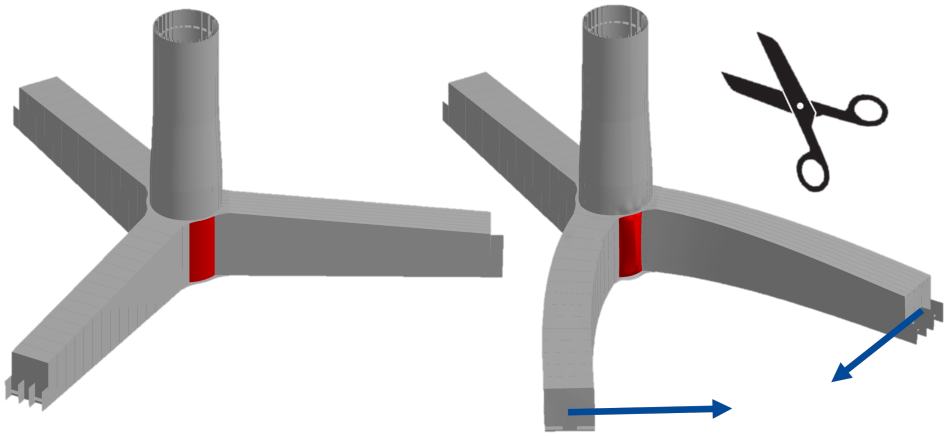


Figure 11.14: Illustration of the scissor effect caused by mooring line loads acting out of the radial pontoon plane of symmetry. Outward buckling of the central column can be seen in the highlighted area. Deformations are exaggerated for illustration purposes

As the stress analysis model considered in this thesis derived mode-{I,III} stress response signals as a '*lump sum*', rather than a linear superposition of responses to individual loads, it is not possible to compare and contrast contribution of the various load mechanisms to the total stress response. This

does not carry any implications regarding the results presented in this thesis, but it does mean that it is not possible to confirm that pressure-based loading is important for multiaxial fatigue analysis of TLP-type FOWT.

11.3.4. Effects of power controls

In section 10.2.2, a scenario in which the effect of power controls on both motion and stress response could be investigated was introduced. These results quickly showed that power controls are very important for the stress response calculation as well. If the angular velocity of the turbine exceeds operational limits, the stress range increases significantly. Therefore it is extremely important to include a form of power/angular velocity control in the engineering models.

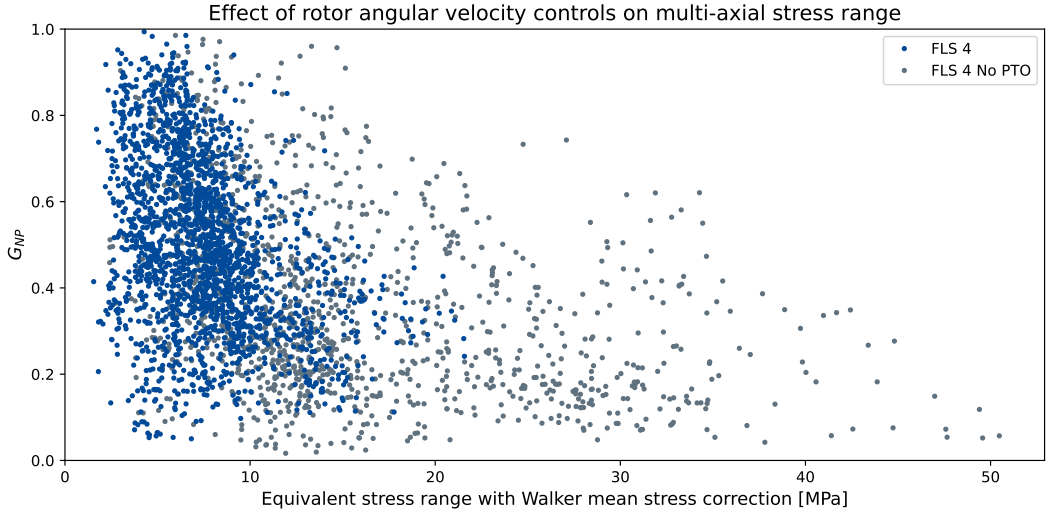


Figure 11.15: Effect of power controls on the damage importance throughout the considered critical welds.

Interesting to note as well is that the increased angular velocity has led to a further increase in the concentration of stress energy at the **1P** spectral bandwidth. This provides further supporting evidence that loading and response are dominated by aerodynamic loading rather than hydrodynamic loading.

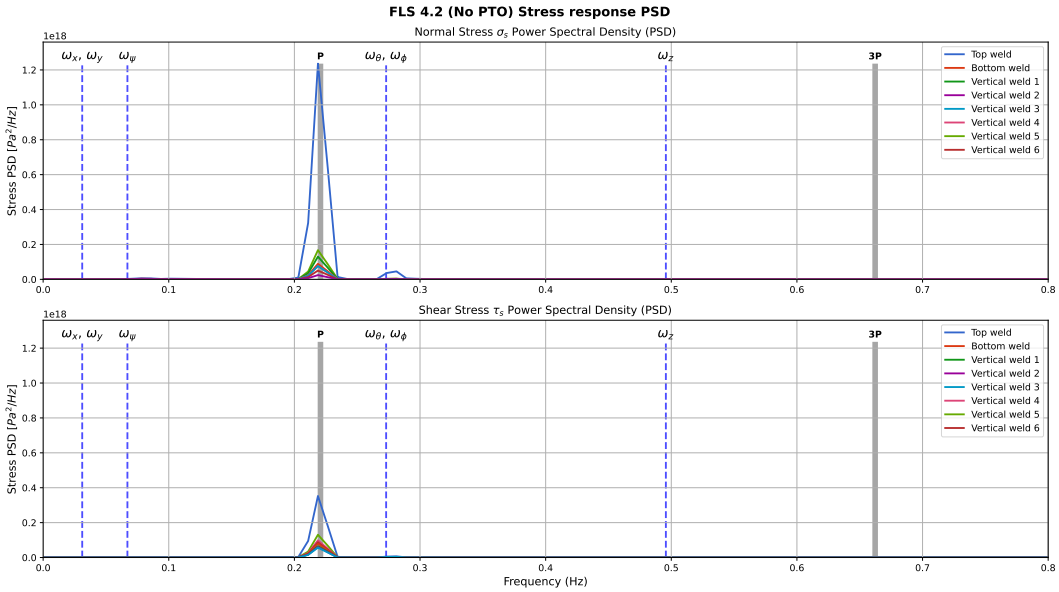


Figure 11.16: Spectral decomposition of normal and shear stress for FLS4 without power controls.

11.3.5. Fatigue conscious design implications

Section 10.2.2 discussed the introduction of a set of load cases in which the effects of introducing fatigue brackets were tested on the fatigue governing weld. In section 11.3.3, it was established that this is the top weld seam. Trivially, as the fatigue brackets connect the pontoon to the column at the height of the top weld seam, the effects of the brackets will only be considered in the top weld seam. As can be seen in figure 11.17, at first glance, it does appear that the average equivalent stress range decreases due to the fatigue brackets. Once again, the presence of longitudinal stiffeners in the pontoons can easily be identified from the spikes. It can also be seen that although the fatigue brackets increase local stiffness in the pontoons, the effect between the pontoons is minor or nonexistent.

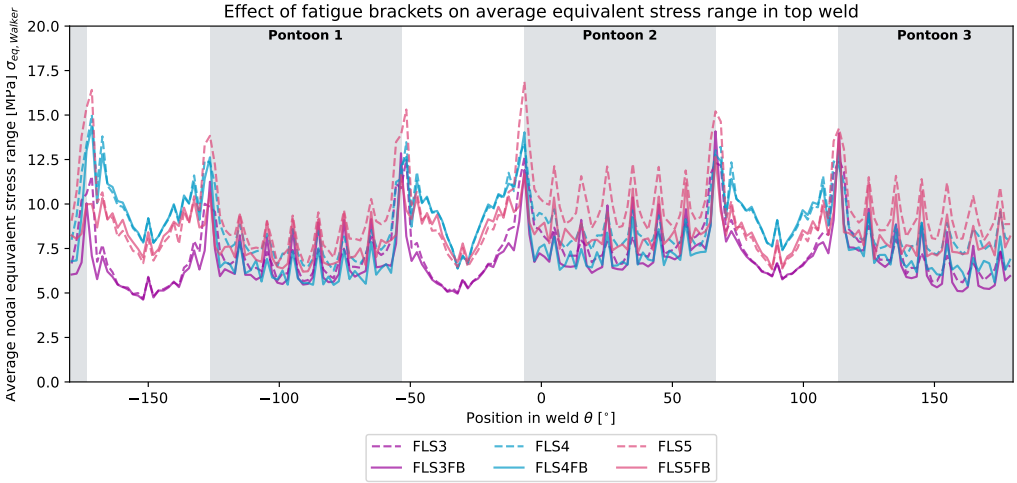


Figure 11.17: Variation of average equivalent stress range $\Delta\sigma_{eq,Walker}$ in the top weld for various seastates, with and without fatigue brackets

Drawing any conclusions from this is, however, premature. When considering figure 11.18, a number of observations can be made. The first of which is that the equivalent stress range and hence damage importance are reduced, thus a relative shift to the left is expected. This is generally true for elements subject to a low-stress range. However, as can be seen in figure 11.18, there are some nodes and element sets with an existing, higher $\{G_{NP}\}$ which have an increased damage importance after the inclusion of fatigue brackets. This observation suggests that the mechanism responsible for the local stress reduction (stiffness-attracted loading) is causing parts of the structure subject to a high degree of non-proportional stress to experience an increased stress range. This means that the addition of fatigue brackets has unforeseen effects on parts of the structure subject to complex stress states.

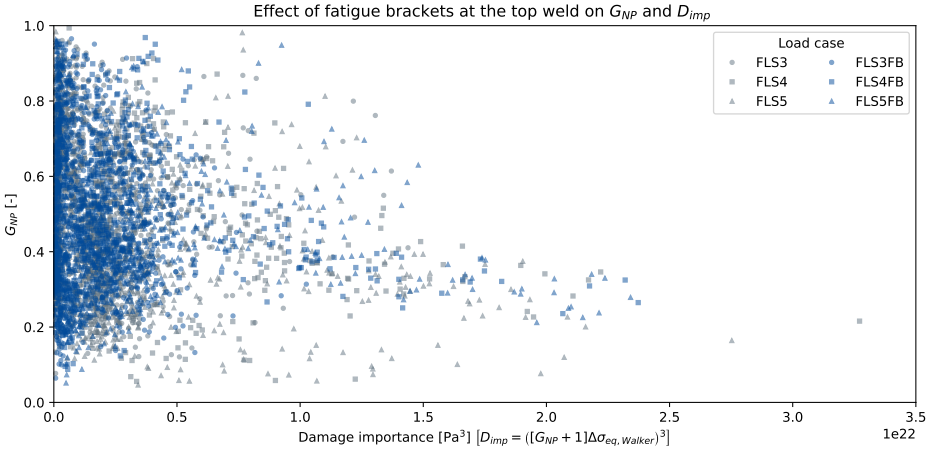


Figure 11.18: Effect of fatigue brackets on the general stress behaviour of nodes in the top fatigue critical weld

This effect is especially obvious when considering the distribution of damage importance throughout the top weld seam. In figure 11.19 this distribution is considered per element set for FLS5. For a complete overview of all of the considered elements, see figure D.4, which exerts the same pattern. Globally speaking, there is very little influence of the fatigue brackets on the damage importance between the pontoons. Considering the following:

Set 1: For the first element set, it can be seen that the inclusion of fatigue brackets generally causes an increase in damage importance, predominantly at the location of the brackets but also between the brackets.

Set 2: In this element set, the fatigue brackets have the desired effect of reducing the effects of fatigue. Reduction of stress range due to fatigue brackets between pontoons is negligible.

Set 3: In the element set on the inside of the pontoon, along the column, the effects of the fatigue bracket are almost negligible. Between the pontoons, an increase in the damage importance is seen.

Set 4: Finally, the supporting deck inside the column generally also experiences a minor decrease in damage importance, reflecting the behaviour seen in element set 2. The overall magnitude is, however, much smaller than the other three element sets and will hence not become governing.

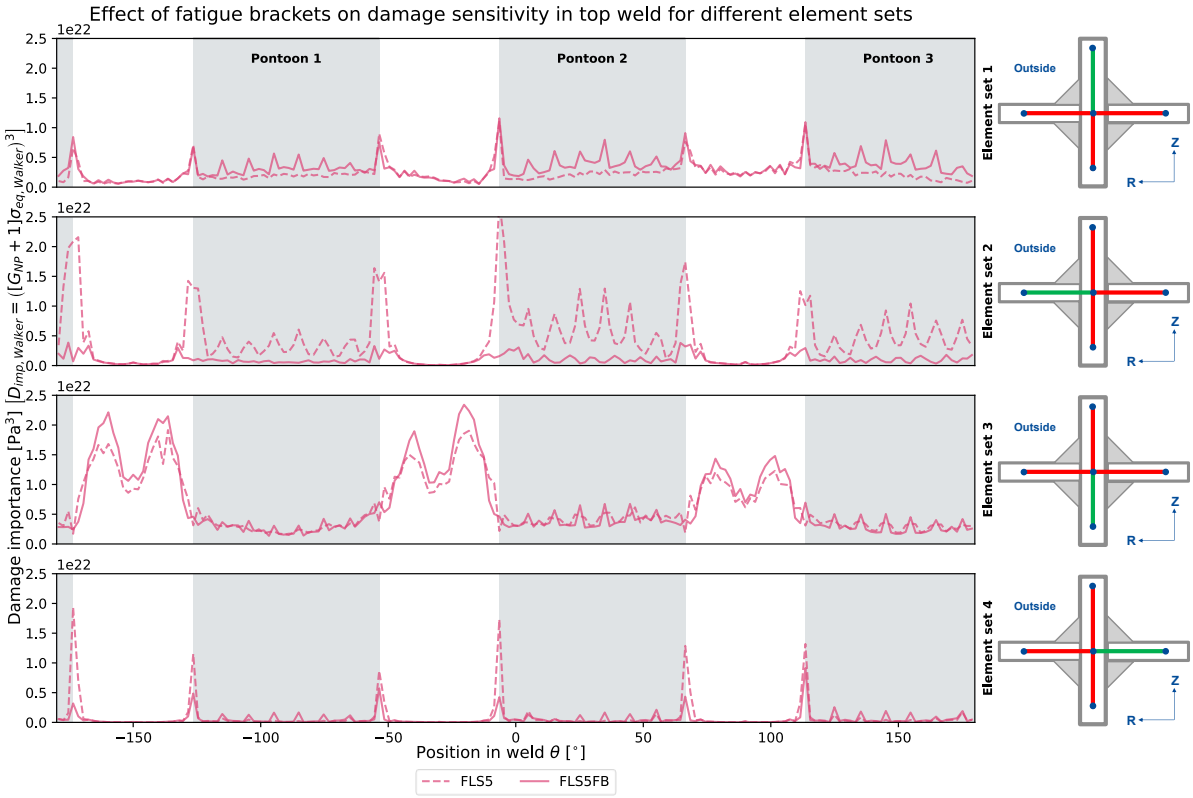


Figure 11.19: Effect of fatigue brackets on the damage importance throughout the top circular weld, broken down by element set.

These emerging patterns are very interesting, especially given that in figure 11.17, it was established that the effective stress generally decreased due to the fatigue brackets. If equation (11.1) is considered, repeated for simplicity:

$$D_{imp} = \left[\Delta\sigma_{eq,Walker}(1 + G_{NP})\right]^3 \tag{11.1}$$

It can be seen that the increase in damage importance observed must have been caused by an increase in the non-proportionality measure G_{NP}, which is supported by the shift observed in figure 11.18. This is concerning as a simple check of the stress range would have completely overlooked this change in loading, potentially underestimating the fatigue lifetime or governing fatigue points. This can be further confirmed if the data plotted in figure 11.17 is broken down by average normal and shear stress range. It should be noted, though, that non-proportional effects cannot be observed in this type of plot.

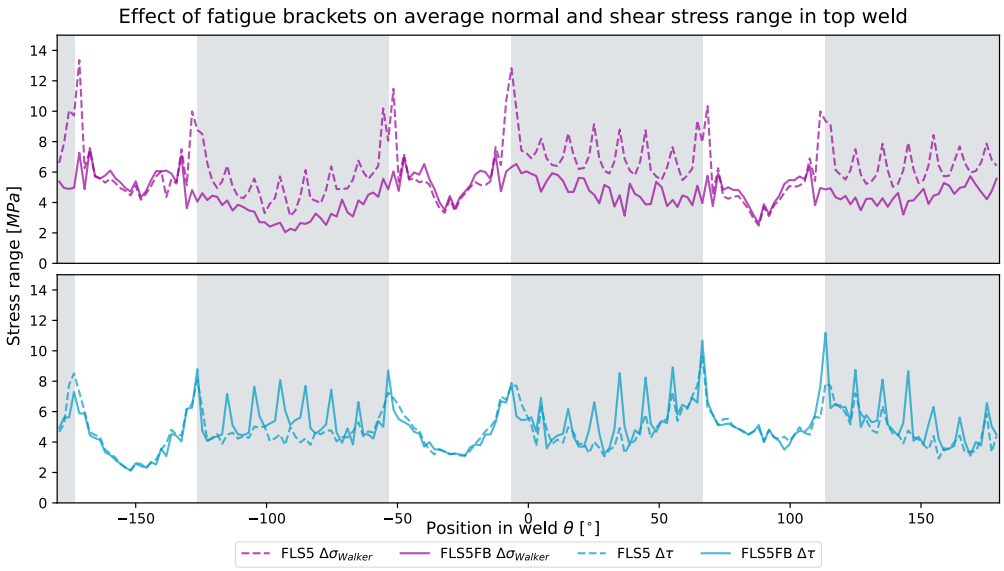


Figure 11.20: Variation of average normal $\Delta\sigma_{Walker}$ and shear $\Delta\tau$ stress range in the top weld for FLS5, with and without fatigue brackets

As a fatigue bracket is a uniaxial structural member, it is expected that the mode-{I} response is predominantly affected. However, when considering the data plotted in figure 11.20, it can clearly be seen that this behaviour is not entirely reflected in the structure. The inclusion of fatigue brackets does indeed reduce the average mode-{I} stress range over the width of the pontoons but do not affect the response of the structure in between the pontoons. On the other hand, the average mode-{III} stress range increases over the width of the pontoon, predominantly caused by the mode-{III} dominated element set 1. This is likely caused by this element set's response being dominated by the turbine yaw moment. The shear stress range of the structure in between the pontoons is unaffected by the inclusion of fatigue brackets.

Therefore, as neither mode-{I,III} experiences an increased stress range due to the inclusion of fatigue brackets, the increase in damage importance seen in figure 11.19, must be caused by an increase in the degree of non-proportionality. For element set 1 it is expected that an increase in the mode-{III} stress range contributes to the observed increase in damage importance as well.

11.4. Damage accumulation

The inclusion of this section was made possible in the final stages of this thesis. Initially, it was never within the scope of the investigation to consider damage accumulation and to focus on dynamic motions, loading & stress response. It was decided to include this section in this thesis due to the extra insight it provides into some of the findings presented above. This section should, however, not become the focal point of this investigation. All credits towards the development and validation of this model go to the relevant persons. In collaboration with the original developer, the model was modified to accommodate the data presented in this thesis. The author of this thesis only supplied derived stress histories presented.

As became evident in part I, multiaxial damage accumulation is a tough field of research without scientific consensus regarding an all-encompassing method. Recently, a state-of-the-art multiaxial damage accumulation model finished development. This validated model is a product of a series of publications [23, 24, 116, 117]. The model is an intact geometry, stress-based assessment model and evaluates local weld notch stress using the ENSC, using far-field stresses (as derived with the traction-based structural stress method). These stress histories are evaluated with a response level dependent shear stress coefficient $\beta\,(S_{e,I}, S_{e,III})$, a path-dependent cycle counting method (see section 6.6.3) and moment of load path (see section 6.7.1) in order to establish a mode-I equivalent von Mises type of failure criterion at the critical plane. This methodology does not suffer from several drawbacks previously addressed as it incorporates load path effects, VA mixed mode-{I,III} signals, and mean stress effect. It, however, is a linear damage accumulation model; thus, load sequence effects are not captured.

This model implements a response level-dependent coefficient to incorporate the mode I and mode III contributions as a response representative rather than a mode III representative resistance curve. By means of an iterative process, the value of β is determined. The model presented by Bufalari et al. [23] adopts single slope (SS) mode-{I,III} resistance curves and has been validated for test data up to $N = 3 \cdot 10^6$ cycles. It does, hence, not account for the change in fatigue damage mechanism, from growth dominant to initiation controlled, as commonly seen for HCF. In the tail end of the data presented by [23], this initial change in fatigue mechanism can be observed as the scatter for $N \approx 10^6 \rightarrow 3 \cdot 10^6$ increases. This change in the mechanism of fatigue damage is commonly modelled in one of two ways, the first of which is by adopting a fatigue limit (infinite slope). For engineering applications, this is not desirable as it may be too optimistic, as all stress ranges below a threshold value are discarded. Another option is to adopt a bi-linear Basquin model [117] or a piecewise continuous dual slope (DS) resistance curve for HCF analysis to account for this change. The latter of which is the common guideline-type solution [10, 60, 128, 132, 139, 140]. As previously discussed, most long-term offshore fatigue analysis, such as for TLP-type FOWT, is in the HCF domain. Hence, a change resistance curve slope can be expected, and a DS slope should be (considered to be) adopted.

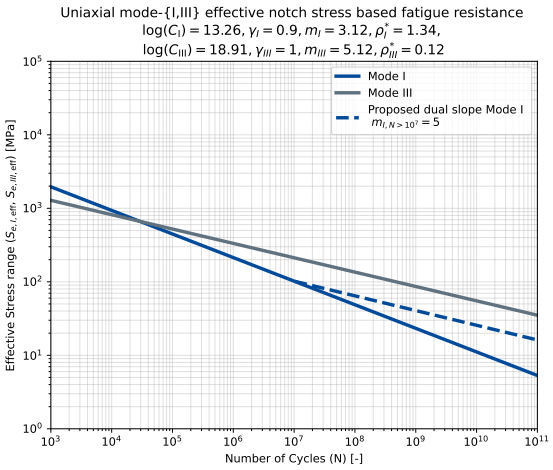


Figure 11.21: Mode-{I,III} single slope SN curves from Bufalari et al. [23], with proposed mode-{I} slope change amendment.

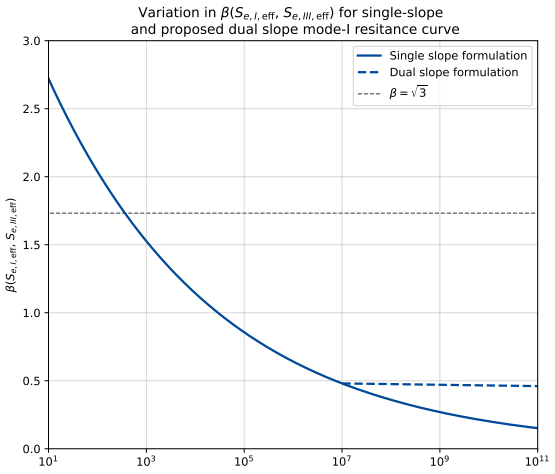


Figure 11.22: Variation in $\beta(N)$ for reference single-slope, and proposed dual-slope resistance curves.

In figures 11.21 and 11.22 the SS mode-{I,III} resistance curves are plotted, and the response level dependent $\beta(N)$, respectively. As can be seen, a SS model results in an infinite exponential decay for $\beta(N)$, thus resulting in all mode-{III} information effectively being lost for HCF analysis. This, along with the shift in damage mechanism seen in the tail end of the data, justifies adopting a mode-{I} slope change. This, however, introduces a problem, as there is no test data to provide exact data. Hence, it is assumed, based on damage guideline recommendations [10, 60, 128, 132, 139, 140] that $m_{I,N>10^7} = 5$ may be expected. Hence, this is adopted, understanding that damage results are subject to changes depending on the true duals slope resistance curve. The conclusions presented in the remainder of this chapter stem from a case study subject to these assumptions and should be evaluated bearing this in mind.

For the application within this thesis, the damage model may be considered as a *black box*, which takes a set of inputs and returns an equivalent effective von Mises stress range S_e and a corresponding lifetime N. The hourly damage accumulation follows from $D_{\text{hourly}} = \Sigma n_i\left(S_{e,i}\right)/N_i\left(S_{e,i}\right) \times 3 \leq 1$, where the factor 3 converts a 20-minute signal to an hour equivalent. This allows for the relative damage contribution of various seastates to be considered. However, due to some of the concerns raised in section 10.3.4 regarding the representation of the considered seastates and extrapolations to the entire scatter diagram, no conclusions on the absolute contribution of various seastates to the total fatigue lifetime will be made, as this would be too speculative.

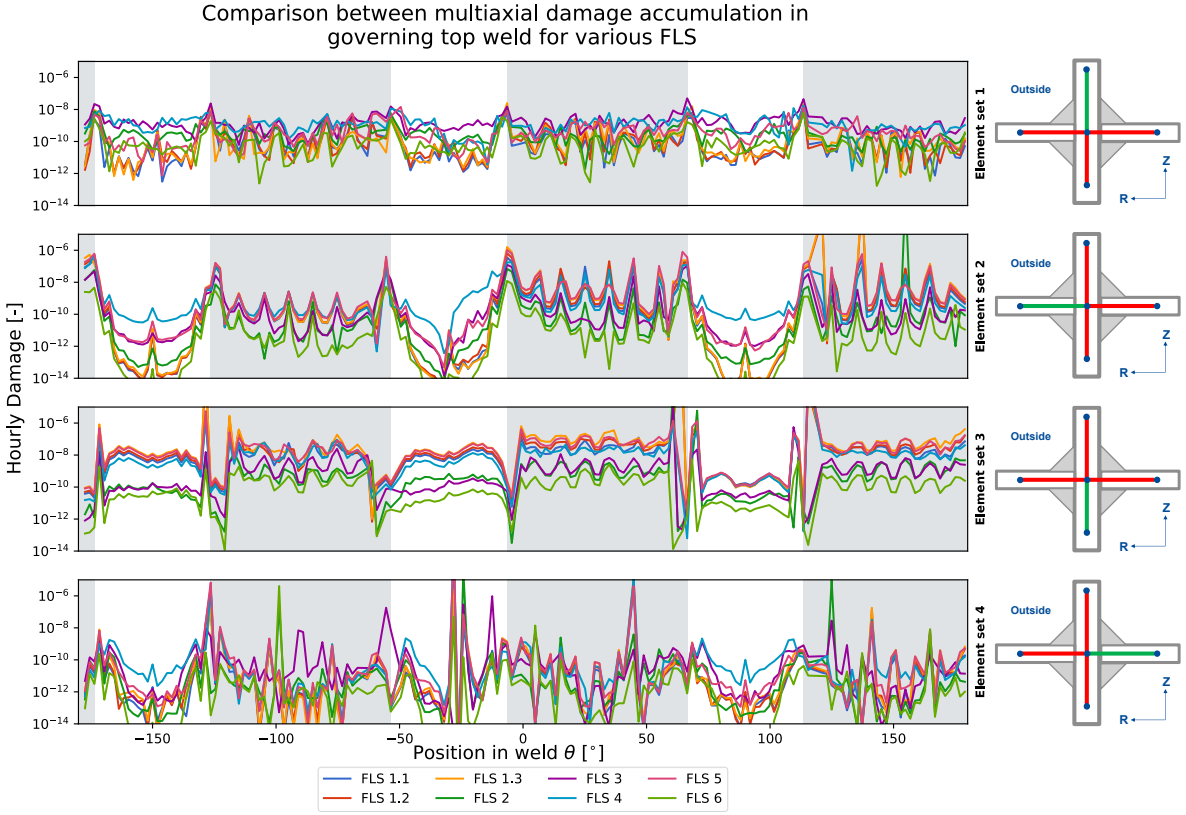


Figure 11.23: Distribution of damage throughout weld fatigue governing top weld seam. Note that distribution is plotted at a logarithmic scale to provide an overview.

When considering damage accumulation in the structure, the relative distribution of damage accumulation is of interest. In figure 11.23, the damage distribution is plotted, allowing for the general trend to be compared. As can be seen from the tight clustering of lines, the damage distribution throughout the welds follows a very predictable pattern regardless of seastate. The hotspots at the longitudinal stiffeners in the pontoons and the corners of the pontoons are subject to the highest damage.

From the distribution plotted in figure 11.23, it appears that hourly damage barely changes between seastates, for element set 1, contrary to what may be expected from conventional fatigue analysis. This can be explained by the observation in section 11.2, where it was found that aerodynamic loading is the

most prominent source of loading. As the research presented in this thesis only considered a part of the operational window (see sections 8.4.2, 8.4.3 and 10.2) in which the aerodynamic controller does not actively regulate pitch (below rated conditions). This means that although a variety of wave conditions were simulated, relatively, a much smaller variety of wind conditions was considered. This results in the tight clustering of hourly damage distributions observed.

The behaviour constituted in section 11.3.5 can also be seen in the hourly damage accumulation in figure 11.24. Again, it can be seen that although the mode-{I} dominant hotspots experience a reduction in accumulated damage, the section of the weld between the pontoons remains virtually unaffected and trends towards becoming the governing hotspot, if the hotspots at the brackets are resolved completely by means of larger bracket.

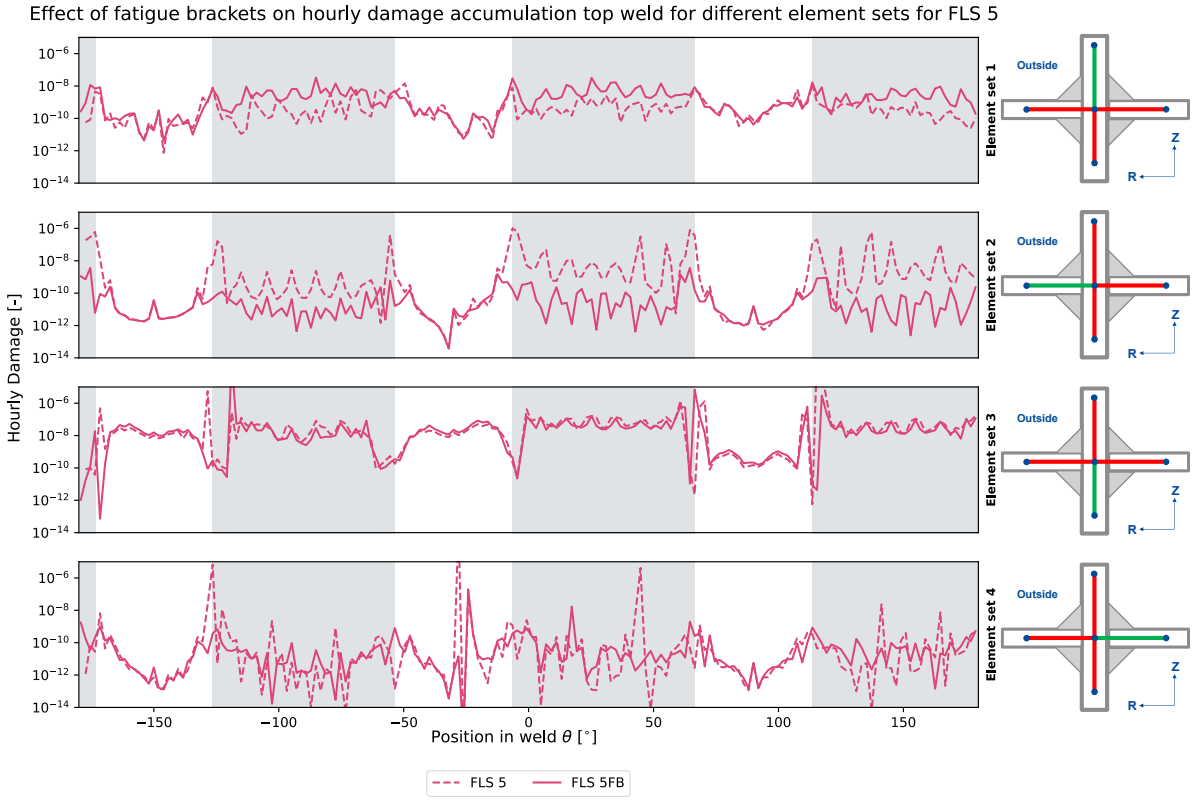


Figure 11.24: Effect of fatigue brackets on hourly accumulated damage.

Another comparison which can be drawn is the spatial distribution of the considered damage importance indicators and the calculated damage, allowing for the quality of the screening method to be tested. In figure 11.25, the damage importance indicators with and without Walker mean stress correction (see section 9.5.4) are compared to the hourly damage. All three datasets are normalised with respect to themselves, as general data trends are more important than absolute values at this stage. In general, it can be seen that both normalised damage indicators do an excellent job of predicting the shape of the damage distribution throughout the top weld. It is, however, incredibly obvious that the damage indicator significantly overestimates the incurred damage by a constant magnitude of $\approx 10^4$. No explanation can be offered as to where this factor originates from. As can be seen from the dotted green line, applying this correction factor to the damage indicator provides an excellent approximation and is accurately able to capture the damage distribution along the weld in between the pontoons, which would be missed by uniaxial screening criteria, as will be demonstrated below.

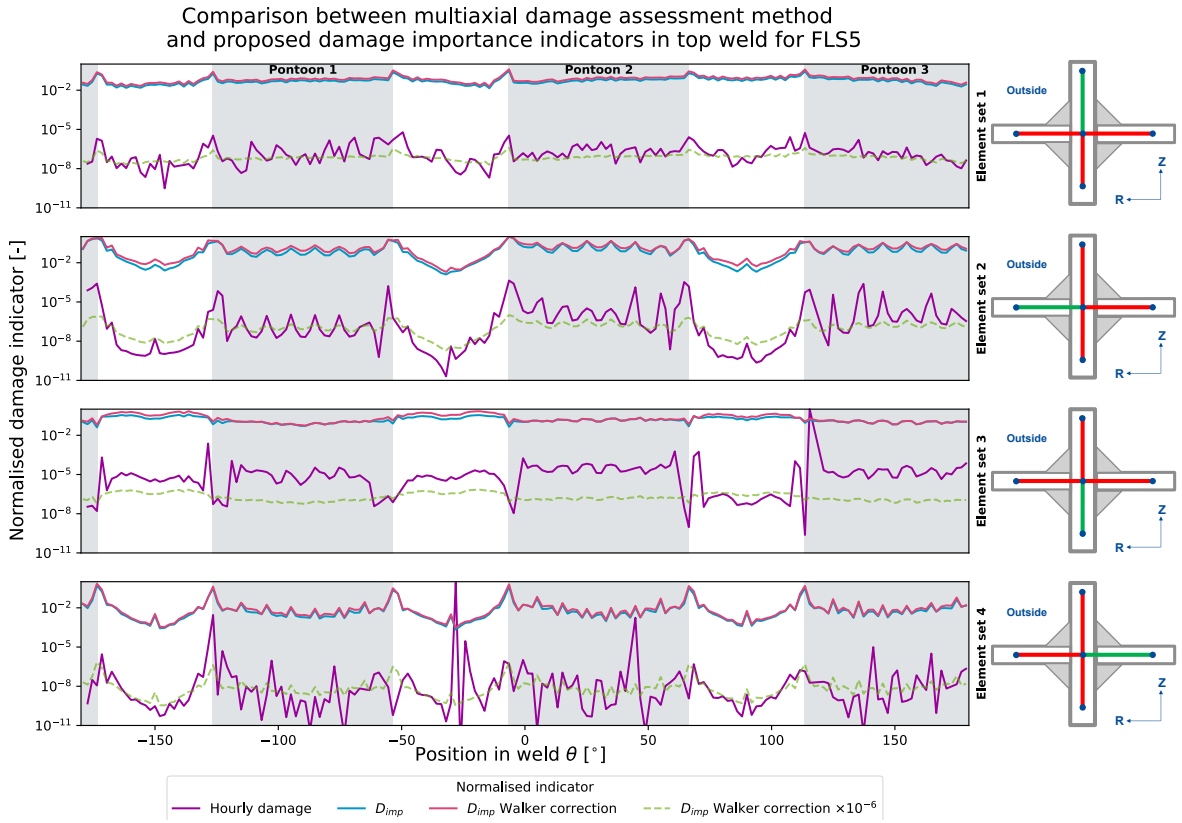


Figure 11.25: Comparison between two proposed damage indicators and multiaxial damage calculation on a normalised scale.

Although the damage indicator provides a good estimation, its formulation may cause discrepancies in trends between approximated damage distribution and calculated damage distribution. As discussed, the multiaxiality indicator (Θ) was not considered in the damage importance. At some locations, the stress may have a low G_{NP} but a very high degree of multiaxiality (for example, stress state 2 in figure 9.22). The stress state property that is considered in the damage importance indicator is G_{NP}. A discrepancy in estimated damage distribution is likely caused by incorrect weighing of the contribution of non-proportional stress response in the damage accumulation mechanism. Another conclusion that can be drawn is that for screening purposes, the shear stress coefficient $\beta = \sqrt{3}$, whereas for the damage calculation, $\beta\,(S_{e,I}, S_{e,III})$ and may be a contributing factor in the difference in the pattern observed between screening indicator and normalised hourly damage. Finally, the screening methodology assumes that the stress trace in the von Mises space follows a perfect ellipse rather than the 'randomized' trace that resembles the likeness of a scoop of spaghetti. This suggests that a spaghetti factor f_s should be considered to capture these effects. These observations suggest that the damage importance indicator can be improved for screening purposes through a weighted contribution of the degree of multiaxiality and degree of non-proportionality in the form of:

$$D_{imp} = \left[\Delta\sigma_{eq} \cdot f\,(\Theta, G_{NP}, f_s)\right]^{\beta(S_{e,I}, S_{e,III})} \times 10^{\alpha} \tag{11.2}$$

Finally, to demonstrate the importance of considering a multiaxial damage accumulation model, a comparison can be drawn between a state-of-the-art damage accumulation calculation, taking all previously discussed aspects into account, and a design guideline-type model. The latter type considers a uniaxial principal stress signal without mean stress effects and reduces it to a peak-valley signal to be processed with rainflow counting. As was established in section 6.3, it is a very poor correlator of multiaxial stress. Therefore, in this comparison, a uniaxial mode-{I} signal will be considered instead. In this type of signal, all multiaxial stress information is lost, as well as mean stress contribution and load path effects. It is, hence, expected that this type of damage model will return a significantly lower total damage.

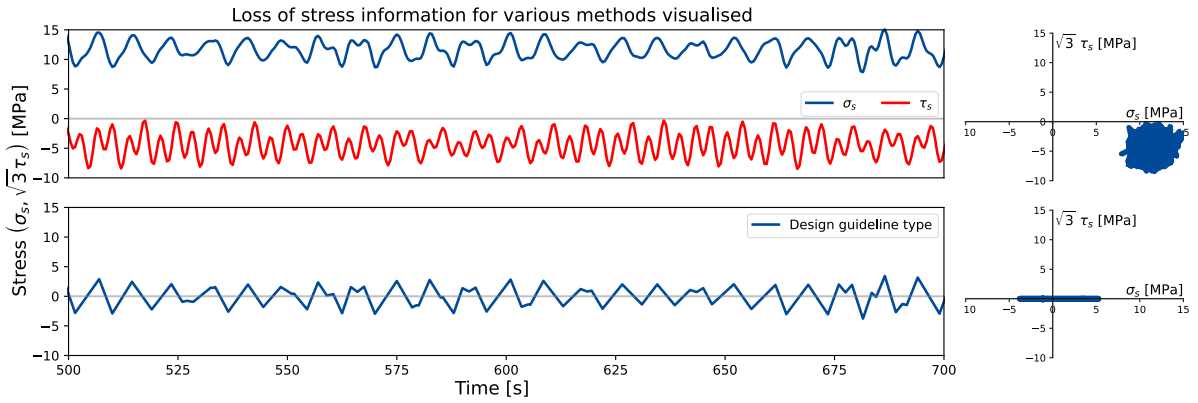


Figure 11.26: Comparison between input signal types for state-of-the-art damage accumulation and design guideline type of stress information.

In figure 11.26, a visual comparison is drawn between the two types of signals. These are both evaluated using the model developed by Bufalari et al. [23], with the named changes. Next, in figure 11.27, the spatial distribution of damage between both types of stress signal processing methods is compared.

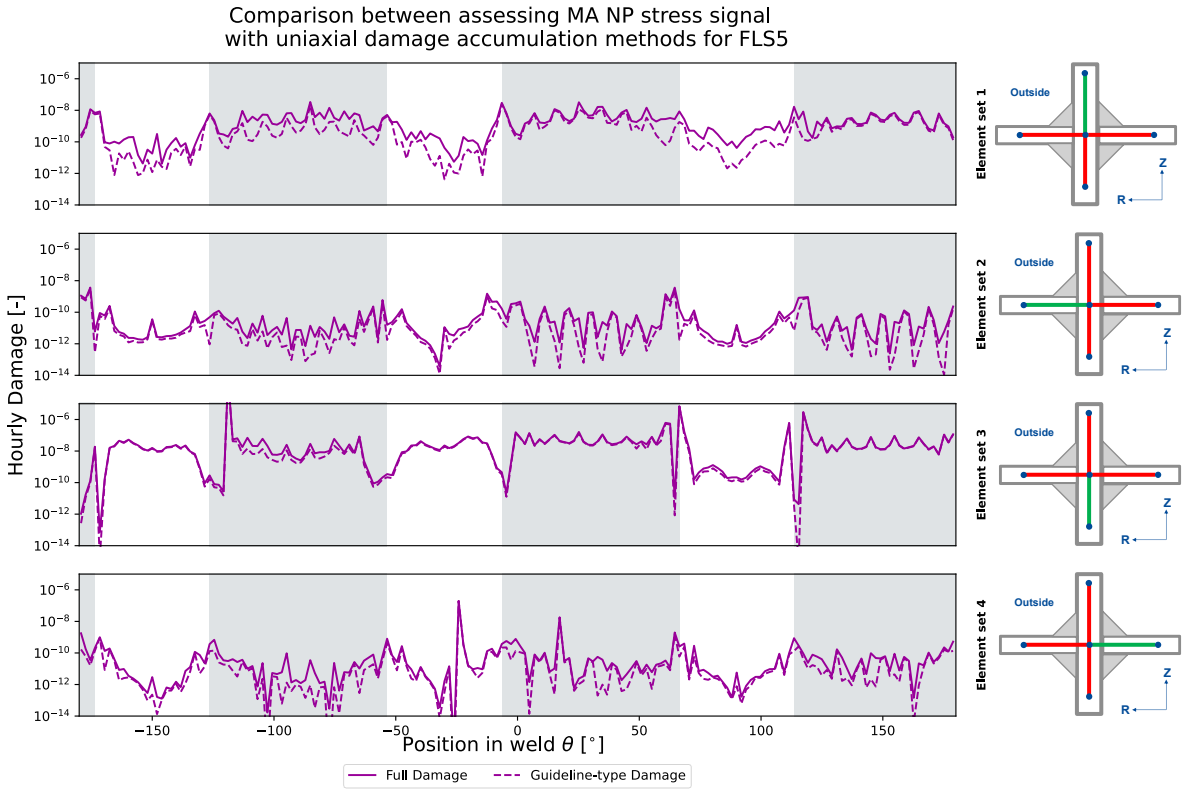


Figure 11.27: Comparison between full MA stress signal processed with a state-of-the-art damage accumulation model, compared to the same signal converted to a design guideline type and processed with a state-of-the-art damage accumulation model.

As can be seen from figure 11.27, the loss of information produces different damage profiles, where the guideline type damage signal always produces a lower damage signal. This can be attributed to one or more combinations of mode-{III} contribution, mean stress effects, stress-response path effects or non-proportionality. In the case of element set 1, it can again be concluded that element set 1 is dominated by mode-{III} stress response, as was found in section 11.3.5. Due to the formulation of the comparison between damage models, the guideline-type damage signal for element set 1 is effectively evaluated on the secondary stress signal, thus returning an hourly damage order of magnitude smaller

than the full multiaxial damage evaluation. Hence, element set 1 should not be considered in this comparison.

For the other element sets, the proximity of the solid and dashed line demonstrates that the hard points at the stiffeners and corners in the pontoons are subject to a dominant mode-{I} stress response. Although the hourly damage at the corners of the pontoons and along the stiffeners of the pontoons is still relatively high in this case, this can be further decreased by implementing larger fatigue brackets (as seen in section 11.3.5), without affecting the structure in between the pontoons. This means that the structure in between the pontoons will carry comparable importance to damage accumulation and may even become the governing hotspot. This is caused by the highly multiaxial stress state found along the weld between the pontoons, caused by the scissor effect. This means that fatigue-conscious design should entail the connection between the pontoon and the central column and the column between the pontoons.

Finally, for element sets 2,3 and 4, a comparison can be made between the factor difference between guideline-type and full multiaxial damage accumulation, $D_{MA} = x \cdot D_{UA}$. In between the pontoons, where a higher degree of non-proportionality is expected relative to inside the pontoons, a factor difference of ≈ 1.4 to ≈ 7.3 at the point exactly in between the pontoons. As this is a significant spread in data, further analysis should be conducted in order to better understand the error that is introduces, by definition, when adopting a uniaxial damage assessment method.

Part IV

Conclusions and Recommendations

12

Conclusion

This thesis has covered a multidisciplinary problem, which was tackled in various phases in the previous sections and was guided by several subquestions. These are reiterated, including answers, below.

SQ1: What types of environmental loading is a FOWT subject to, and what loading components must be considered?
This was addressed in chapter 3 and demonstrated that a FOWT is subject to wind waves and current. Due to the nature of wind and wave loading, these loads are highly stochastic and may be multiaxial and out of phase with respect to or more other loading sources. Current loading, on the other hand, may be considered as a static load. For aerodynamic loading, it was concluded that BEM with supplemental corrections provides sufficient accuracy for the scope of this thesis. For hydrodynamic loading, it was concluded that both potential loading and viscous loading have significant contributions to the system dynamics and should, if possible, both be considered. Especially as it was established that local loading has a contribution to multiaxial stress response, and hence local pressure loading should be considered, which is associated with potential theory.
Talk

SQ2: How can the dynamic wind-wave environment be expressed as input for a fatigue sea state?
As covered in chapter 3 the wind-wave environment can be composed from a combination of long and short-term statistics. Specifically regarding wind, it was shown that for fatigue analysis, it is important to have a low degree of turbulence in order to allow for possible resonant frequencies to build up to be observed. With highly turbulent conditions, there is a risk that any resonance in the structure is eliminated before it has a chance to present itself (see section 4.1.1). Variance in the spatial representation of the wind field in the form of wind shear should be included.

Regarding the wave field, wave elevation signals should be produced using a combination of long-term statistics to select a wave spectrum and short-term statistics to generate a time domain signal from this spectrum. In chapter 10, the considered seastates in this thesis provide an example of how this can be achieved.

SQ3: Which stress assessment parameter and fatigue failure criterion can be used to assess multiaxial stress response in combination with time domain finite element analysis?
In chapter 6, it was established that a stress-based assessment criterion is best suited for HCF analysis for intact geometry. More specifically, the HSSSC in combination with a traction-based stress method. This method is mesh insensitive, allowing for application to large structures while considering mode-{I,III} contributions separately. Furthermore, crack growth is expected to originate from the weld toe notch and propagate in the through-thickness direction. Therefore the critical plane can be predefined, and stresses can quickly be evaluated on the Von Mises stress plane.

SQ4: How can the multi-disciplinary, multi-physics submodels be coupled in order to conduct coupled dynamic analysis consisting of a rigid motion and elastic deformation component?
As was covered in section 8.6 a loosely coupled temporal model was considered to integrate the multi-physics submodels. Separate models for hydrodynamics, aerodynamics and mooring

response were integrated into ANSYS TwinBuilder. The process presented in this thesis appears to be slightly different from some literature but is separated by a fundamental difference. This is due to the hydrodynamic loading being considered as a local pressure on a plate rather than lumped loads acting on a few points on the structure. This change in approach to hydrodynamic loading allows for local loading and structural response phenomena, such as multiaxial stress response, to be observed more accurately. Furthermore, by decoupling the motion analysis from the structural response analysis, the simulation process could be sped up. This did, however, mean that only one-way hydroelastic behaviour could be simulated.

It is not possible to comment on the importance of considering system dynamics rather than a quasi-static method without a comparison with a quasi-static approach. However, it can be said that to accurately transfer tower-TLP and tendon-TLP interface forces, it is important to consider kinematic boundary conditions at these interfaces. Rigidly fixing these interfaces will result in all of the energy that would otherwise rigidly displace the structure to act as an extra loading component. Therefore, this is a conservative method regarding load magnitude, impact on load direction cannot be commented on based on the available data.

On a separate note, a concern regarding the replicability of the presented research was addressed, namely that the TwinBuilder software considered is not included in a standard student licence and hence may not be easily acquired by academia.

SQ5: How can *'the amount'* of multiaxial response be quantified and allow for a comparison between locations in the structure?

Simply put, damage accumulation provides a definitive answer to *'the amount'* of multiaxial stress response and its effects. However, as was discussed as well, damage accumulation was initially not within the scope of this thesis. For this reason, the multiaxial stress screening model introduced in section 9.5 was developed in order to provide an alternative toolset to assess the extent of multiaxial stress response.

For engineering applications, this also means that an assessment of the type of fatigue assessment needs to be considered without conducting a full fatigue analysis.

SQ6: Are critical weld seams in an offshore floating wind TLP-type substructure in mixed wind-wave conditions subject to mean stress effects?

As was established in section 6.1.4, the magnitude of mean stress varies throughout the welds. These mean stress components can be attributed in part to the external load, such as the mean torsional stress in the central column caused by the yaw moment exerted by the turbine. On the other hand, the weld seams are also subject to mean stress components caused by the static loads on the TLP. For example, due to the pre-tension in the mooring line, a significant bending moment is applied to the pontoons, resulting in a mean tensile stress in the top weld and a mean compressive stress in the bottom weld.

SQ7: At what stage in design and analysis can predictions of multiaxial stress behaviour be made?

In short, the entire analysis covered in this thesis must be conducted in order to establish the type of multiaxial stress behaviour in a particular node. However, as was covered throughout chapter 11, there are several signals that can be interpreted at a fairly early stage in regard to multiaxial stress response prediction. To start off, the spectral accumulation of response energy can be predicted before any coupled analysis is run. As was established in section 11.1, the stress response occurs mainly at the first natural frequency of constrained DOFs $\{\theta, \psi\}$ as well as rotor angular frequency $\mathbf{P}$.

Finally, reviewing the mechanics of the loads applied to the system allows for a further narrowing of the investigation to locations in the welds. From the scissor mechanism, it can be seen that pinching of the central column between the pontoons introduces a significant amount of multiaxiality into the welds. The location of the critical point in the weld seam is, however, not only a consequence of the level of multiaxiality but also the stress range. Therefore, full stress analysis must be conducted to pinpoint the fatigue governing location in the weld.

SQ8: What are the effects of fatigue brackets on (multiaxial) stress behaviour of a TLP in mixed wind-wave conditions?

As was covered in section 11.3.5, the fatigue brackets are successful at reducing the local stress range, as intended. However, as was also seen, the fatigue brackets do not reduce the stress level in

the entire weld, such as the sections along the central column between the pontoons. This means that as the stress range decreases at the 'old' fatigue governing location, there will, at some point, be a shift in the location of the fatigue governing location. This is caused by the much higher degree of non-proportionality between the pontoons, caused by the scissor effect. As was covered in chapter 6, non-proportionality is an important factor to consider for damage accumulation, and may result in a relatively lower stress range to produce higher damage than a uniaxial stress response.

12.1. Conclusion

Taking a step back from the findings presented previously, the original research goals can be revisited. The goal formulated in section 2.4 was twofold and was achieved by building a model that takes the numerical characterization of the metocean environment as input and allows for the structural stress response to be derived. This model allowed for the multiaxial stress response in the TLP to be investigated. The goals were achieved by answering the questions posed in section 2.2 and allowing for the main research question to be answered.

Research question:
To what extent are fatigue-critical weld seams in an offshore floating wind TLP-type substructure in multi-directional mixed wind-wave loading conditions subject to a multiaxial stress response?

As hypothesised, the stress in the fatigue-critical weld seams is always multiaxial to a degree. However, the stress state is often complex due to low-stress ranges. Contrary to the hypothesis, the findings of this investigation showed that mode-{I} response was not governing in all parts of the structure. Instead, sections of the structure were found that consistently presented a prevailing mixed non-proportional mode-{I,III} response. It was also demonstrated that not all welds exhibit the same stress response behaviour and that the top weld is governing with respect to fatigue lifetime. The exact extent to which the weld seams are subject to multiaxial stress response could not be expressed numerically. However, from the simulations, it became evident that stress response in parts of the structure is extremely complex and, despite a lower observed stress range, may carry (near) equal weight in damage accumulation due to the degree of multiaxiality and non-proportionality at said location. This is a concerning finding, as this would have been completely missed if a uniaxial fatigue criterion were to be adopted.

In addition to underestimating the accumulated fatigue damage at those locations, the adoption of a uniaxial fatigue criterion would have predicted the governing hotspot *only* at the connection between the central column and pontoon in the top weld. Contrary to this, it was found that the weld in between the pontoons was almost as important. Acting on this original assumption (hotspot on the corner of the pontoon), it would be logical, from a design perspective, to reinforce the pontoon-column connection at the top weld with fatigue brackets. As expected, this reduced the local mode-{III}stress range, however, by means of stiffness-attracted loading, stress response distribution changed in the surrounding structure. This resulted in locations in the weld becoming subject to more complex stress states. This was especially obvious in the section of the weld between the pontoons, where an increase in G_{NP} combined with an unchanged stress range resulted in relatively higher damage compared to a structure without fatigue brackets, which was already predicted from the screening methodology. This is again concerning as it demonstrates that the effects of local changes to reduce stress range should be evaluated locally, but in other parts of the structure as well, which are subject to a more multiaxial stress state.

Taking the above into account, it should be concluded that fatigue-critical weld seams in an offshore floating wind TLP-type substructure are subject to multiaxial stress to the extent that multiaxial damage accumulation models should be applied. If this is not possible, a multiaxial stress response screening should be conducted to identify fatigue governing locations in the welds, as well as locations subject to multiaxial stress.

12.2. Discussion

In this thesis, the basis for conducting multiaxial stress response analysis by means of coupled analysis was described. The coupled dynamics model presented in this thesis is distinctly different from work presented in literature by considering hydrodynamic loading as a local pressure on a plate rather than lumped loads acting on a few points on the structure. This change in approach to hydrodynamic loading allows for local loading and structural response phenomena, such as multiaxial stress response, to be observed more accurately. Furthermore, due to the formulation of boundary conditions for the FEA model, rigid body motions and accelerations were preserved while still allowing for multiaxial stress histories to be extracted. The model presented in this thesis was specifically developed to take environmental data as input and produce multiaxial stress signals. It is the first published instance of a single workflow capable of doing so. That being said, there are also some shortcomings to the model presented here.

First of all, the tower is modelled as a rigid body due to software necessity. As covered in section 5.5, FOWT analysis should consider a flexible tower due to the interaction between the tower bending modes and the system motions. In addition to this, a flexible tower allows for second-order hydrodynamic loading to be modelled.

As there is no precedent for an investigation linking tower flexibility to multiaxial stress response, it is difficult to predict the influence of a flexible tower model on stress response in the critical weld. However, from the literature and findings of this investigation, it is possible to make some predictions regarding stress behaviour. From the literature, it is known that modelling the tower as a rigid body overestimates the system stiffness and underestimates the aerodynamic contribution. This decrease in stiffness and increase in damping is likely to decrease the natural frequencies of the constrained DOFs (z, θ, ψ). This will also be reflected in the spectral decomposition of the loads. Furthermore, as the aerodynamic loads carry a large contribution to the overall loading and stress response, it can be expected that a spectral peak around the tower's natural frequency (ω_{tower}) will occur. From this, it is also likely that this peak will be reflected in the spectral decomposition of the stresses.

Stepping back from the dynamics, the effects of these predictions can also be evaluated on the mechanics of the system based on stress behaviour seen in this thesis. First of all, the torsional deformation of the flexible tower due to the yaw moment exerted by the turbine will cause a decrease in torsional loads at the tower-TLP interface. This will likely be reflected in the shear stress range in the top weld. The magnitude of this reduction is, however, not expected to change the multiaxial stress behaviour in the fatigue-critical welds drastically. This is because the flexible tower has little to no effect on the multiaxial stress behaviour in between the pontoons caused by the scissor effect.

A second shortcoming of the conclusions presented in this thesis ties into a concern raised in section 10.3.4, regarding if the (limited) considered short-term statistics are representative of the target metocean spectrum and, by extension, the entire scatter diagram. Although implementing measures to tackle this is not expected to drastically change the results presented in this thesis, it does have implications for the reliability of the data produced by the presented model/methodology. Decreasing this uncertainty at a fundamental simulation input level will also allow for the certainty to draw broader conclusions regarding (stress) behaviour across the entire scatter diagram.

A third shortcoming of the model presented in this thesis is regarding stress processing. In most of the work presented in this thesis, a constant shear stress ratio $\beta = 3$ was applied, despite literature showing that this value is not constant and is, in fact, response level dependent, as was shown in section 11.4. The relationship between normal and shear stress is very important to establish whether or not a multiaxial stress response occurs. As was seen in section 11.4 as well, for low-stress range, HCF fatigue, $\beta(N)$ returned significantly small values and could in theory, be manipulated to turn mode-{I} dominant stress into mode-{III} dominant and illustrates the sensitivity of the entire analysis presented above to a single parameter.

A fourth concern was raised in section 11.4 regarding the considered resistance curves. In the original mode, SS mode-{I,III} resistance curves were adopted that had been validated for test data up to $N = 3 \cdot 10^6$ cycles. In the tail end of the data, it was observed that the scatter increased, indicating a

change in the fatigue damage mechanism. To model this change, a DS resistance curve for HCF analysis was adopted using a regulation-based assumption. This assumption has implications on $\beta(N)$, which, as established, has significant implications on calculated damage. To solve this, HCF tests should be considered. This is easier said than done as data scatter for initiation controlled fatigue mechanism (second slope) is higher. This means that the data is not only more difficult to acquire due to long test times for HCF, but it also means that more tests are required to attain the required certainty for a DS resistance curve, irrespective of the number of runouts.

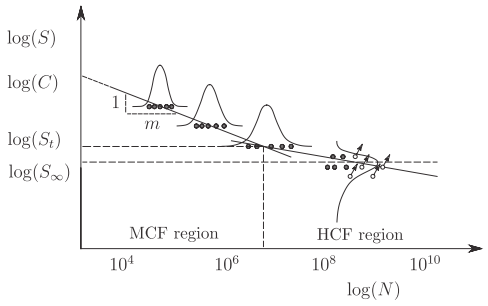


Figure 12.1: Observed data scatter band for growth dominant to initiation controlled [117, p. 3]

Finally, this thesis considered a single TLP design, and although a lot of motion and stress response behaviour could be related back to sources such as structural geometry, the effects of drastic design changes to the structure could not be captured in the scope of this thesis. That being said, dominant multiaxial stress response causes such as turbine yaw moment and the scissor effects, although affected by scale, are bound to the concept.

12.3. Implications

The previously discussed conclusions may raise some eyebrows regarding the implications of these findings. Although it was demonstrated that multiaxial stress response should not be disregarded, the exact effects of this could not be quantified. Without (full) scale testing and the computationally expensive nature of coupled temporal FEA, options for studying multiaxial fatigue in TLP-type FOWT seem slim. However, some questions may already, in part, be answered in literature. Let's consider a hypothetical TLP structure in which the pontoons have become wide enough to overlap. Under the notion that the top weld is governing for fatigue lifetime, this hypothetical TLP can be approximated to a (very large) tube-to-flange connection, as pictured in figure 12.2. The multiaxial stress response of such a geometry under multiaxial loading has been studied in multiple publications (overview can be found in [23]). Specimens subject to variable amplitude and non-proportional loading reflected significantly reduced lifespans. Projecting these findings back onto the hypothetical TLP column allows for predictions to be made for the full-scale structure based on laboratory tests. This may further develop the understanding of the effects of multiaxial stress response in TLPs.

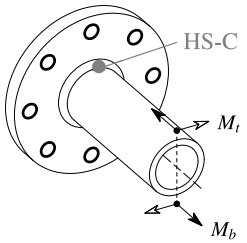


Figure 12.2: Welded tube to flange connection [23]

Another effect identified in this thesis was the scissor effect; the consequences could also not be exactly quantified on the multiaxial stress response. Considering different hypothetical TLP structures, the mechanics of the scissor effect can be studied. The pinching of the central column between the pontoons can be attributed to the bending moment in the pontoons being transferred to the main structure. Assuming all external influences remain the same, the moment exerted at the pontoon-column

connection needs to be reduced to decrease the scissor effect. This can be realised with shorter pontoons. Extending this logic, infinitely short pontoons would be optimal to reduce the pinching effect consequent multiaxial stress response. A structure with infinitely short pontoons is, however, effectively a SPAR. It should be noted that the motion behaviour of a SPAR is significantly different from a TLP.

Rather than tackling the scissor effect at the root, there are also ways to reduce the subsequent effects. As was also demonstrated, increasing the stiffness of the pontoon-column connection effectively increases the pinching of the central column between the pontoons. To reduce the transfer of bending moment to the central column, the most effective measure would be to add bracing between the pontoons, as close to the mooring line interface as possible. Research shows that TLPs are a lighter alternative to other FOWT substructure types, thus theoretically leaving room to increase the strength of the design without surpassing weight or steel cost benchmarks of other solutions on the market while maintaining the attractive motion response behaviour of a TLP.

13

Recommendations

Following the findings of this investigation, the shortcomings of the presented methodology identified in section 12.2 research areas to improve the model can be recommended, as well as investigations into other critical interfaces subject to multiaxial loading.

To start off, the effect of aeroelastic is known on structure motions, however, the effect on stress response in the (sub) structure has not been considered. Hence, it is also unknown if these effects should be taken into account when conducting fatigue analysis. More insight into this topic will also allow for engineering models to be developed with overall process streamlining in mind. Depending on these results, it may be beneficial, computationally, to conduct motion and structural response analysis separately rather than a complete integrated load and response assessment.

The same logic can be applied when considering the effect of second-order hydrodynamics, whose influences on structural stress response are unknown. Therefore, a second, subsequent investigation into the importance of second-order hydrodynamic forces is recommended.

A third recommendation addresses one of the shortcomings identified in this thesis concerning the degree to which the (limited) considered short-term statistics are representative of the target metocean spectrum and, by extension, the entire scatter diagram. It is recommended to address this by conducting enough simulations to reach statistical convergence in for example, the wave elevation and structure loads. This is not (only) a matter of increasing the duration of the simulated time signal but also increasing the number of simulations run with different seastates generated from the same input data, also known as seeding.

A fourth recommended area of research expands upon the previously called-for multiaxial screening practice. In this thesis, previous work was expanded upon by including a mean stress correction. However, as was found in section 11.4, the damage accumulation calculation and screening results revealed that there is still room for improvement. From an industrial application perspective, screening allows for faster implementation of multiaxial stress assessment methods, as the computational expense is a barrier. With efficient screening methods, the search field can be narrowed down to a set of locations to which targeted damage assessment can be applied rather than the entire structure.

A fifth recommendation follows from one of the identified issues regarding resistance curves raised while studying multiaxial damage accumulation and may be addressed with HCF tests in order to determine the characteristics of initiation controlled fatigue mechanism.

Finally, as discussed in part I, fatigue-critical weld seams are not the only part of a TLP subject to multiaxial loading, but also the mooring tendons. As mentioned, due to the weave of a tendon core, the tension on the line will tighten the windings in the line, exerting a multiaxial load on the connecting interface. This means that even axial loading of a tendon will produce a multiaxial stress response in the line, which must also be transferred to the structure. As identified in the literature review, a TLP achieves hydrodynamic restoring force through tendon force. In the worst case, premature mooring

tendon/interface fracture may lead to the loss of an asset due to the instability of the floater on itself. Therefore, an investigation into the (multiaxial) stress behaviour of the tendon/floater interface is recommended.

References

[1] Nikhar J. Abbas et al. "A reference open-source controller for fixed and floating offshore wind turbines". In: *Wind Energy Science* 7 (1 Jan. 2022), pp. 53–73. ISSN: 2366-7451. DOI: 10.5194/wes-7-53-2022.

[2] ABS. *Spectral-based fatigue analysis for floating offshore structures*. American Bureau of Shipping, Mar. 2005.

[3] M. M. Amrutha and V. Sanil Kumar. "Spatial and temporal variations of wave energy in the nearshore waters of the central west coast of India". In: *Annales Geophysicae* 34 (12 Dec. 2016), pp. 1197–1208. ISSN: 14320576. DOI: 10.5194/ANGEO-34-1197-2016.

[4] Vitor Anes, Luis Reis, and Manuel Freitas. "Asynchronous Multiaxial Fatigue Damage Evaluation". In: *Procedia Engineering* 101 (C Jan. 2015), pp. 421–429. ISSN: 1877-7058. DOI: 10.1016/J.PROENG.2015.02.051.

[5] *Aqwa Theory Manual*. ANSYS, Inc., July 2022.

[6] *AQWA User's Manual*. ANSYS, Inc., July 2022.

[7] Muhammad Arshad and Brendan C. O'kelly. "Offshore wind-turbine structures: A review". In: *Proceedings of Institution of Civil Engineers: Energy* 166 (4 Nov. 2013), pp. 139–152. ISSN: 17514231. DOI: 10.1680/ener.12.00019.

[8] DNV AS. *DNV-CG-0129: Fatigue assessment of ship structures*. Det Norske Veritas, Oct. 2021.

[9] DNV AS. *DNV-RP-0286: Coupled analysis of floating wind turbines*. Det Norske Veritas, Oct. 2021.

[10] DNV AS. *DNV-RP-C203: Fatigue design of offshore steel structures*. Det Norske Veritas, Aug. 2021.

[11] DNV AS. *DNV-ST-0119: Floating wind turbine structures*. Det Norske Veritas, June 2021.

[12] Erin E. Bachynski and Torgeir Moan. "Ringing loads on tension leg platform wind turbines". In: *Ocean Engineering* 84 (July 2014), pp. 237–248. ISSN: 0029-8018. DOI: 10.1016/J.OCEANENG.2014.04.007.

[13] Erin Elizabeth Bachynski. "Design and Dynamic Analysis of Tension Leg Platform Wind Turbines". In: (2014). ISSN: 1503-8181. URL: https://ntnuopen.ntnu.no/ntnu-xmlui/handle/11250/238768.

[14] M. Bäckström and G. Marquis. "A review of multiaxial fatigue of weldments: experimental results, design code and critical plane approaches". In: *Fatigue & Fracture of Engineering Materials & Structures* 24 (5 May 2001), pp. 279–291. ISSN: 8756758X. DOI: 10.1046/j.1460-2695.2001.00284.x.

[15] Y. H. Bae and M. H. Kim. "Rotor-floater-tether coupled dynamics including second-order sum-frequency wave loads for a mono-column-TLP-type FOWT (floating offshore wind turbine)". In: *Ocean Engineering* 61 (2013), pp. 109–122. ISSN: 00298018. DOI: 10.1016/J.OCEANENG.2013.01.010.

[16] A. Bannantine and D. F. Socie. "A Multiaxial Fatigue Life Estimation Technique". In: *ASTM Special Technical Publication* (1122 1992), pp. 249–275. ISSN: 00660558. DOI: 10.1520/STP24163S. URL: https://www.astm.org/stp24163s.html.

[17] Garrett Barter et al. "IEAWindTask37/IEA-15-240-RWT: v1.1.6: HAWC2 monopile, VolturnUS-S CAD model". In: (June 2023). DOI: 10.5281/ZENODO.8070464. URL: https://zenodo.org/record/8070464.

[18] J.H. den Besten. "Fatigue damage criteria classification, modelling developments and trends for welded joints in marine structures". In: *https://doi.org/10.1080/17445302.2018.1463609* 13 (8 Nov. 2018), pp. 787–808. ISSN: 17445302. DOI: 10.1080/17445302.2018.1463609. URL: https://www.tandfonline.com/doi/abs/10.1080/17445302.2018.1463609.

[19] J.H. den Besten. *Fatigue Strength of Marine Structures*. 2023.

[20] J.H. Den Besten. "Fatigue resistance of welded joints in aluminium high-speed craft: A total stress concept". Delft University of Technology, Sept. 2015. DOI: 10.4233/UUID:370B3D44-F4A6-403E-9629-D36174C3ACA4. URL: https://repository.tudelft.nl/islandora/object/uuid%3A370b3d44-f4a6-403e-9629-d36174c3aca4.

[21] Michael Borg, Anders Melchior Hansen, and Henrik Bredmose. "Floating substructure flexibility of large-volume 10MW offshore wind turbine platforms in dynamic calculations". In: *Journal of Physics: Conference Series* 753 (8 Oct. 2016). ISSN: 17426596. DOI: 10.1088/1742-6596/753/8/082024.

[22] Donald Brown. *Wind Power Ethics | Ethics and Climate*. 2012. URL: https://ethicsandclimate.org/2012/08/27/wind-power-ethics/.

[23] G. Bufalari, J.H. den Besten, and M.L. Kaminski. "Mode-{I, III} multiaxial fatigue of welded joints in steel maritime structures: Effective notch stress based resistance incorporating strength and mechanism contributions". In: *International Journal of Fatigue* 180 (Mar. 2024), p. 108067. ISSN: 0142-1123. DOI: 10.1016/J.IJFATIGUE.2023.108067. URL: https://linkinghub.elsevier.com/retrieve/pii/S0142112323005686.

[24] G. Bufalari, J.H. den Besten, and M.L. Kaminski. "Mode-III fatigue of welded joints in steel maritime structures: Weld notch shear stress distributions and effective notch stress based resistance". In: *International Journal of Fatigue* 165 (Dec. 2022), p. 107210. ISSN: 01421123. DOI: 10.1016/j.ijfatigue.2022.107210.

[25] Tony Burton et al. *Wind Energy Handbook*. Wiley, May 2011. ISBN: 9780470699751. DOI: 10.1002/9781119992714.

[26] Jeroen J. van der Cammen. "Fatigue prediction and response monitoring on a FPSO". Delft University of Technology, 2008. ISBN: 9789085593454. URL: https://repository.tudelft.nl/islandora/object/uuid%5C%3Aeee952f8-c75f-456b-8860-4a01b68dadf8.

[27] Andrea Carpinteri, Andrea Spagnoli, and Sabrina Vantadori. "Multiaxial fatigue life estimation in welded joints using the critical plane approach". In: *International Journal of Fatigue* 31 (1 Jan. 2009), pp. 188–196. ISSN: 0142-1123. DOI: 10.1016/J.IJFATIGUE.2008.03.024.

[28] Andrea Carpinteri et al. "Structural integrity assessment of metallic components under multiaxial fatigue: the C–S criterion and its evolution". In: *Fatigue & Fracture of Engineering Materials & Structures* 36 (9 Sept. 2013), pp. 870–883. ISSN: 1460-2695. DOI: 10.1111/FFE.12037. URL: https://onlinelibrary.wiley.com/doi/full/10.1111/ffe.12037%20https://onlinelibrary.wiley.com/doi/abs/10.1111/ffe.12037%20https://onlinelibrary.wiley.com/doi/10.1111/ffe.12037.

[29] Hui Fen Chai and Campbell Laird. "Mechanisms of cyclic softening and cyclic creep in low carbon steel". In: *Materials Science and Engineering* 93 (C Sept. 1987), pp. 159–174. ISSN: 0025-5416. DOI: 10.1016/0025-5416(87)90421-6.

[30] H. Chen, D. G. Shang, and E. T. Liu. "Multiaxial fatigue life prediction method based on path-dependent cycle counting under tension/torsion random loading". In: *Fatigue & Fracture of Engineering Materials & Structures* 34 (10 Oct. 2011), pp. 782–791. ISSN: 1460-2695. DOI: 10.1111/J.1460-2695.2011.01572.X. URL: https://onlinelibrary.wiley.com/doi/full/10.1111/j.1460-2695.2011.01572.x.

[31] Jiahao Chen et al. "Comparison of different dynamic models for floating wind turbines". In: *Journal of Renewable and Sustainable Energy* 9 (6 Nov. 2017). ISSN: 19417012. DOI: 10.1063/1.5002750/286319. URL: /aip/jrse/article/9/6/063304/286319/Comparison-of-different-dynamic-models-for.

[32] Xiaohong Chen et al. "Coupled dynamic analysis of a mini TLP: Comparison with measurements". In: *Ocean Engineering* 33 (1 Jan. 2006), pp. 93–117. ISSN: 0029-8018. DOI: 10.1016/J.OCEANENG.2005.02.013.

[33] Robert D. Cook et al. *Concept and Applications of Finite Element Analysis*. 4th ed. John Wiley & Sons. Inc., Oct. 2001, p. 733. ISBN: 978-0-471-35605-9. URL: https://www.wiley.com/en-us/Concepts+and+Applications+of+Finite+Element+Analysis%5C%2C+4th+Edition-p-9780471356059.

[34] W.E Cummins. "The Impulse Response Function and Ship Motions". In: *Schiffstechnik* 47 (Oct. 1962), pp. 101–109.

[35] Yi-Shan Dai, Xiao-Bo Chen, and Wen-Yang Duan. "Computation of Low-Frequency loads by the middle-field formulation". In: *Research Department Bureau Veritas* (2005). URL: https://repository.tudelft.nl/islandora/object/uuid%5C%3A67eb21a7-c1b2-4fb2-8517-ae5914a8a0b4.

[36] Spence Dale. *Statistical Review of World Energy*. BP, June 2022. URL: https://www.bp.com/en/global/corporate/energy-economics/statistical-review-of-world-energy.html.

[37] Josh Davidson and John V. Ringwood. "Mathematical modelling of mooring systems for wave energy converters - A review". In: *Energies* 10 (5 May 2017). ISSN: 19961073. DOI: 10.3390/EN10050666.

[38] Marije Deul. "Fatigue damage accumulation in steel welded joints, subject to (random) variable amplitude loading conditions: An improved fatigue-life model for naval ship structural design". Delft University of Technology, July 2021.

[39] P Dong, JK Hong, and SW Dean. "A Robust Structural Stress Parameter for Evaluation of Multiaxial Fatigue of Weldments". In: *Journal of ASTM International* 3 (7 2006), p. 100348. ISSN: 1546962X. DOI: 10.1520/JAI100348.

[40] P. Dong. "A Robust Structural Stress Method for Fatigue Analysis of Offshore/Marine Structures". In: *Journal of Offshore Mechanics and Arctic Engineering* 127 (1 Feb. 2005), pp. 68–74. ISSN: 0892-7219. DOI: 10.1115/1.1854698. URL: https://dx-doi-org.tudelft.idm.oclc.org/10.1115/1.1854698.

[41] Pingsha Dong, Zhigang Wei, and Jeong K. Hong. "A path-dependent cycle counting method for variable-amplitude multi-axial loading". In: *International Journal of Fatigue* 32 (4 Apr. 2010), pp. 720–734. ISSN: 0142-1123. DOI: 10.1016/J.IJFATIGUE.2009.10.010.

[42] Rick Donk. "Multi-axial fatigue strength assessment of a turret in an FPSO". Delft University of Technology, Oct. 2019.

[43] Espen Engebretsen, Zhiyuan Pan, and Nuno Fonseca. "Second-Order Difference-Frequency Loads on FPSOs by Full QTF and Relevant Approximations". In: *Proceedings of the International Conference on Offshore Mechanics and Arctic Engineering - OMAE* 1 (Dec. 2020). DOI: 10.1115/OMAE2020-18132. URL: /OMAE/proceedings-abstract/OMAE2020/84317/1092585.

[44] N. Exel and C. M. Sonsino. "Multiaxial fatigue evaluation of laserbeam-welded magnesium joints according to IIW-fatigue design recommendations". In: *Welding in the World* 58 (4 May 2014), pp. 539–545. ISSN: 00432288. DOI: 10.1007/S40194-014-0139-6/FIGURES/13. URL: https://link.springer.com/article/10.1007/s40194-014-0139-6.

[45] O. M. Faltinsen. *Sea loads on ships and offshore structures*. Cambridge University Press, 1990, viii, 328 pages : ISBN: 0521372852.

[46] A. Fatemi and L. Yang. "Cumulative fatigue damage and life prediction theories: a survey of the state of the art for homogeneous materials". In: *International Journal of Fatigue* 20 (1 Jan. 1998), pp. 9–34. ISSN: 0142-1123. DOI: 10.1016/S0142-1123(97)00081-9.

[47] Oliver Tierdad Filsoof and Xuping Zhang. "An intuitive representation and analysis of multi-rotor wind turbine whirling modes". In: *Wind Energy* 25 (3 Mar. 2022), pp. 553–572. ISSN: 1095-4244. DOI: 10.1002/we.2686.

[48] Wolfgang Fricke. "Recommended Hot-Spot Analysis Procedure for Structural Details of Ships and FPSOs Based on Round-Robin FE Analyses". In: *International Journal of Offshore and Polar Engineering* 12 (1 Mar. 2002), pp. 89–96.

[49] Evan Gaertner et al. *IEA Wind TCP Task 37: Definition of the IEA Wind 15-Megawatt Offshore Reference Wind Turbine*. Mar. 2020.

[50] Oleg Gaidai et al. "Offshore tethered platform springing response statistics". In: *Scientific Reports* 12 (1 Dec. 2022). ISSN: 20452322. DOI: 10.1038/s41598-022-25806-x.

[51] Hua Geng and Geng Yang. "Linear and Nonlinear Schemes Applied to Pitch Control of Wind Turbines". In: *The Scientific World Journal* 2014 (2014), pp. 1–9. ISSN: 2356-6140. DOI: 10.1155/2014/406382.

[52] H J Gough et al. "The Strength of Metals under Combined Alternating Stresses". In: 131 (1 June 1935), pp. 3–103. ISSN: 0020-3483.

[53] Kurtis R. Gurley and Ahsan Kareem. "Simulation of Ringing in Offshore Systems under Viscous Loads". In: *Journal of Engineering Mechanics* 124 (5 May 1998), pp. 582–586. ISSN: 0733-9399. DOI: 10.1061/(ASCE)0733-9399(1998)124:5(582). URL: https://ascelibrary.org/doi/abs/10.1061%5C%28ASCE%5C%290733-9399%5C%281998%5C%29124%5C%3A5%5C%28582%5C%29%20https://ascelibrary.org/doi/10.1061/%5C%28ASCE%5C%290733-9399%5C%281998%5C%29124%5C%3A5%5C%28582%5C%29.

[54] José E. Gutiérrez-Romero et al. "Non-linear dynamic analysis of the response of moored floating structures". In: *Marine Structures* 49 (2016), pp. 116–137. ISSN: 0951-8339. DOI: https://doi.org/10.1016/j.marstruc.2016.05.002. URL: https://www.sciencedirect.com/science/article/pii/S0951833916300636.

[55] John Z Gyekenyesi, Pappu L N Murthy, and Subodh K Mital. "NASALIFE-Component Fatigue and Creep Life Prediction Program". In: (2014). URL: http://www.sti.nasa.gov.

[56] M. H. Hansen. "Improved Modal Dynamics of Wind Turbines to Avoid Stall-induced Vibrations". In: *Wind Energy* 6 (2 Apr. 2003), pp. 179–195. ISSN: 1095-4244. DOI: 10.1002/we.79.

[57] M. O.L. Hansen et al. "State of the art in wind turbine aerodynamics and aeroelasticity". In: *Progress in Aerospace Sciences* 42 (4 June 2006), pp. 285–330. ISSN: 0376-0421. DOI: 10.1016/J.PAEROSCI.2006.10.002.

[58] M.D. Haskind. "The Exciting Forces and Wetting of Ships in Waves". In: (1957). URL: http://dome.mit.edu/handle/1721.3/51307.

[59] Kris Hectors and Wim De Waele. "Cumulative Damage and Life Prediction Models for High-Cycle Fatigue of Metals: A Review". In: *Metals 2021, Vol. 11, Page 204* 11 (2 Jan. 2021), p. 204. ISSN: 2075-4701. DOI: 10.3390/MET11020204. URL: https://www.mdpi.com/2075-4701/11/2/204/htm%20https://www.mdpi.com/2075-4701/11/2/204.

[60] A. F. Hobbacher. "Recommendations for Fatigue Design of Welded Joints and Components". In: (2016). DOI: 10.1007/978-3-319-23757-2. URL: http://link.springer.com/10.1007/978-3-319-23757-2.

[61] Leo H. Holthuijsen. *Waves in Oceanic and Coastal Waters*. Cambridge University Press, Jan. 2007. ISBN: 9780521860284. DOI: 10.1017/CBO9780511618536.

[62] Yuhui Huang, Shan Tung Tu, and Fu Zhen Xuan. "Pit to crack transition behavior in proportional and non-proportional multiaxial corrosion fatigue of 304 stainless steel". In: *Engineering Fracture Mechanics* 184 (Oct. 2017), pp. 259–272. ISSN: 0013-7944. DOI: 10.1016/J.ENGFRACMECH.2017.08.019.

[63] ALTAIR Hyperlife. *Multiaxial Fatigue Analysis*. 2023. URL: https://help.altair.com/hwdesktop/hlife/topics/solvers/os/analysis_fatigue_multiaxial_r.htm.

[64] Michael Imelfort. *ellipsoid.py*. https://github.com/minillinim/ellipsoid. 2017.

[65] A. K. Jain. "Nonlinear coupled response of offshore tension leg platforms to regular wave forces". In: *Ocean Engineering* 24 (7 1997), pp. 577–592. ISSN: 00298018. DOI: 10.1016/0029-8018(95)00059-3.

[66] Michael Janssen, Jan Zuidema, and Russell Wanhill. *Fracture Mechanics*. 2nd ed. CRC Press, Aug. 2004. ISBN: 9780429076978. DOI: 10.1201/9781482265583.

[67] C. Jiang et al. "A structural stress-based critical plane method for multiaxial fatigue life estimation in welded joints". In: *Fatigue & Fracture of Engineering Materials & Structures* 39 (3 Mar. 2016), pp. 372–383. ISSN: 1460-2695. DOI: 10.1111/FFE.12369. URL: https://onlinelibrary.wiley.com/doi/full/10.1111/ffe.12369%20https://onlinelibrary.wiley.com/doi/abs/10.1111/ffe.12369%20https://onlinelibrary.wiley.com/doi/10.1111/ffe.12369.

[68] J Jonkman and D Matha. "A Quantitative Comparison of the Responses of Three Floating Platforms". In: National Renewable Energy Laboratory, Sept. 2009. URL: http://www.osti.gov/bridge.

[69] Jason M. Jonkman. "Dynamics of offshore floating wind turbines-model development and verification". In: *Wind Energy* 12.5 (2009), pp. 459–492. DOI: 10.1002/we.347. URL: https://www.scopus.com/inward/record.uri?eid=2-s2.0-68149144101%5C&doi=10.1002%5C%2fwe.347%5C&partnerID=40%5C&md5=2509a9b3cb4ead97e57f7a9adf8b3677.

[70] J M J Journée and W W Massie. *OFFSHORE HYDROMECHANICS First Edition*. 2001.

[71] Americo Cunha Jr et al. "Tresca vs. von Mises: Which failure criterion is more conservative in a probabilistic context?" In: (). URL: https://hal.science/hal-04245274.

[72] Leonid G. Khachiyan and Michael J. Todd. "On the complexity of approximating the maximal inscribed ellipsoid for a polytope". In: *Mathematical Programming* 61 (1-3 Aug. 1993), pp. 137–159. ISSN: 00255610. DOI: 10.1007/BF01582144/METRICS. URL: https://link.springer.com/article/10.1007/BF01582144.

[73] Byoung Wan Kim et al. "Comparison of linear spring and nonlinear FEM methods in dynamic coupled analysis of floating structure and mooring system". In: *Journal of Fluids and Structures* 42 (Oct. 2013), pp. 205–227. ISSN: 0889-9746. DOI: 10.1016/J.JFLUIDSTRUCTS.2013.07.002.

[74] Martin Kühn. "Dynamics and design optimisation of offshore wind energy conversion systems". Delft University of Technology, May 2001.

[75] Marit I. Kvittem, Erin E. Bachynski, and Torgeir Moan. "Effects of Hydrodynamic Modelling in Fully Coupled Simulations of a Semi-submersible Wind Turbine". In: *Energy Procedia* 24 (Jan. 2012), pp. 351–362. ISSN: 1876-6102. DOI: 10.1016/J.EGYPRO.2012.06.118.

[76] H Lamb. *Hydrodynamics*. 6th ed. Cambridge University Press, 1932.

[77] T. E. Langlais, J. H. Vogel, and T. R. Chase. "Multiaxial cycle counting for critical plane methods". In: *International Journal of Fatigue* 25 (7 July 2003), pp. 641–647. ISSN: 0142-1123. DOI: 10.1016/S0142-1123(02)00148-2.

[78] Sonia Lebofsky. "Numerically Generated Tangent Stiffness Matrices for Geometrically Non-Linear Structures". University of Washington, 2013.

[79] Kevin Leenders. *Mooring analysis for a TLP supporting a 15MW wind turbine: Identifying critical design parameters that influence the design life of a mooring system regarding higher-order loads for a TLP supporting a 15MW wind turbine*. 2023. URL: https://repository.tudelft.nl/islandora/object/uuid%3A484b963d-81f4-44af-bb03-d001949e4449.

[80] Inga Lehmann. "Deepwater Mooring Systems Design and Analysis – A Practical Overview of Various Calculation Methods". In: *World Maritime Technology Conference, San Francisco, California, USA, 17-20 October 2003, Delft University of Technology, Ship Hydromechanics Laboratory, Department of Maritime Technology* (2003). URL: https://repository.tudelft.nl/islandora/object/uuid%5C%3Ac8a61e43-bec3-477a-a310-ecb9fa97fff9.

[81] B. Li, L. T. Santos, and M. De Freitas. "A computerized procedure for long-life fatigue assessment under complex multiaxial loading". In: *Fatigue & Fracture of Engineering Materials & Structures* 24 (3 Mar. 2001), pp. 165–177. ISSN: 1460-2695. DOI: 10.1046/J.1460-2695.2001.00389.X. URL: https://onlinelibrary-wiley-com.tudelft.idm.oclc.org/doi/full/10.1046/j.1460-2695.2001.00389.x%20https://onlinelibrary-wiley-com.tudelft.idm.oclc.org/doi/abs/10.1046/j.1460-2695.2001.00389.x%20https://onlinelibrary-wiley-com.tudelft.idm.oclc.org/doi/10.1046/j.1460-2695.2001.00389.x.

[82] Jing Li et al. "Prediction of fatigue life under multiaxial loading by using a critical plane-based model". In: *Archive of Applied Mechanics* 89 (4 Apr. 2019), pp. 629–637. ISSN: 14320681. DOI: 10.1007/S00419-018-1478-3/FIGURES/6. URL: https://link.springer.com/article/10.1007/s00419-018-1478-3.

[83] P. S. Van Lieshout, J. H. Den Besten, and M. L. Kaminski. "Comparative study of multiaxial fatigue methods applied to welded joints in marine structures". In: *Frattura ed Integrità Strutturale* 37 (June 2016), pp. 173–192. ISSN: 1971-8993. DOI: 10.3221/IGF-ESIS.37.24. URL: https://repository.tudelft.nl/islandora/object/uuid%5C%3A83dfe882-8a98-4246-89d0-d9dec66d4ee5.

[84] P.S. van Lieshout. "On the assessment of multiaxial fatigue resistance of welded steel joints in marine structures when exposed to non-proportional constant amplitude loading". Delft University of Technology, Jan. 2020. DOI: 10.4233/UUID:AFD39F40-7569-4CC6-AC1A-659342B45F9A. URL: https://repository.tudelft.nl/islandora/object/uuid%3Aafd39f40-7569-4cc6-ac1a-659342b45f9a.

[85] P.S. van Lieshout, J.H. den Besten, and M.L. Kaminski. "Multiaxial fatigue assessment of welded joints in marine structures". In: *International Shipbuilding Progress* 65 (2018), pp. 29–71. DOI: 10.3233/ISP-170141. URL: https://repository.tudelft.nl/islandora/object/uuid%5C%3A82896bc6-6462-4ade-a597-d22226481f4f.

[86] Xiong Liu et al. "Effects of aerodynamic damping on the tower load of offshore horizontal axis wind turbines". In: *Applied Energy* 204 (Oct. 2017), pp. 1101–1114. ISSN: 0306-2619. DOI: 10.1016/J.APENERGY.2017.05.024.

[87] Y. Liu et al. "Aeroelastic analysis of a floating offshore wind turbine in platform-induced surge motion using a fully coupled CFD-MBD method". In: *Wind Energy* 22 (1 2019), pp. 1–20. DOI: 10.1002/we.2265.

[88] Yuanchuan Liu et al. "Establishing a fully coupled CFD analysis tool for floating offshore wind turbines". In: *Renewable Energy* 112 (Nov. 2017), pp. 280–301. ISSN: 0960-1481. DOI: 10.1016/J.RENENE.2017.04.052.

[89] Chenyu Luan, Zhen Gao, and Torgeir Moan. "Comparative analysis of numerically simulated and experimentally measured motions and sectional forces and moments in a floating wind turbine hull structure subjected to combined wind and wave loads". In: *Engineering Structures* 177 (Dec. 2018), pp. 210–233. ISSN: 0141-0296. DOI: 10.1016/J.ENGSTRUCT.2018.08.021.

[90] Chenyu Luan, Zhen Gao, and Torgeir Moan. "Design and analysis of a braceless steel 5-mw semi-submersible wind turbine". In: *Proceedings of the International Conference on Offshore Mechanics and Arctic Engineering - OMAE* 6 (June 2016). DOI: 10.1115/OMAE2016-54848.

[91] Chenyu Luan, Zhen Gao, and Torgeir Moan. "Development and verification of a time-domain approach for determining forces and moments in structural components of floaters with an application to floating wind turbines". In: *Marine Structures* 51 (Jan. 2017), pp. 87–109. ISSN: 0951-8339. DOI: 10.1016/J.MARSTRUC.2016.10.002.

[92] Chenyu Luan et al. "Experimental validation of a time-domain approach for determining sectional loads in a floating wind turbine hull subjected to moderate waves". In: *Energy Procedia* 137 (Oct. 2017), pp. 366–381. ISSN: 1876-6102. DOI: 10.1016/J.EGYPRO.2017.10.361.

[93] Kai Tung Ma et al. "Mooring system engineering for offshore structures". In: *Mooring System Engineering for Offshore Structures* (Jan. 2019), pp. 1–350. DOI: 10.1016/C2018-0-02217-3. URL: http://www.sciencedirect.com:5070/book/9780128185513/mooring-system-engineering-for-offshore-structures.

[94] Pim van der Male, Marco Vergassola, and Karel N. van Dalen. "Decoupled modelling approaches for environmental interactions with monopile-based offshore wind support structures". In: *Energies* 13 (19 Oct. 2020). ISSN: 19961073. DOI: 10.3390/EN13195195.

[95] J. F. Manwell, J. G. McGowan, and A. L. Rogers. *Wind Energy Explained*. 2nd ed. Wiley, Dec. 2009. ISBN: 9780470015001. DOI: 10.1002/9781119994367.

[96] Denis Matha, Jason Jonkman, and Tim Fischer. *Subcontract Report Model Development and Loads Analysis of an Offshore Wind Turbine on a Tension Leg Platform, with a Comparison to Other Floating Turbine Concepts Thesis Supervisors*. 2010. URL: http://www.osti.gov/bridge.

[97] T. Matsui, Y. Sakoh, and T. Nozu. "Second-order sum-frequency oscillations of tension-leg platforms: prediction and measurement". In: *Applied Ocean Research* 15 (2 Jan. 1993), pp. 107–118. ISSN: 0141-1187. DOI: 10.1016/0141-1187(93)90025-S.

[98] Hermann G. Matthies, Rainer Niekamp, and Jan Steindorf. "Algorithms for strong coupling procedures". In: *Computer Methods in Applied Mechanics and Engineering* 195 (17-18 Mar. 2006), pp. 2028–2049. ISSN: 0045-7825. DOI: 10.1016/J.CMA.2004.11.032.

[99] Kevin Mctaggart. "Ship Radiation and Diffraction Forces at Moderate Forward Speed". In: (2015).

[100] B. Le Méhauté. *An introduction to hydrodynamics and water waves*. Springer, 1976.

[101] Jifa Mei and Pingsha Dong. "A new path-dependent fatigue damage model for non-proportional multi-axial loading". In: *International Journal of Fatigue* 90 (Sept. 2016), pp. 210–221. ISSN: 0142-1123. DOI: 10.1016/J.IJFATIGUE.2016.05.010.

[102] Jifa Mei and Pingsha Dong. "An equivalent stress parameter for multi-axial fatigue evaluation of welded components including non-proportional loading effects". In: *International Journal of Fatigue* 101 (Aug. 2017), pp. 297–311. ISSN: 0142-1123. DOI: 10.1016/J.IJFATIGUE.2017.01.006.

[103] Torgeir Moan et al. "Recent Advances in Integrated Response Analysis of Floating Wind Turbines in a Reliability Perspective". In: *Journal of Offshore Mechanics and Arctic Engineering* 142 (5 Oct. 2020). ISSN: 1528896X. DOI: 10.1115/1.4046196.

[104] P.J. Moriarty and A.C. Hansen. *AeroDyn Theory Manual*. National Renewable Energy Laboratory, Jan. 2005.

[105] E. Muljadi and C.P. Butterfield. "Pitch-controlled variable-speed wind turbine generation". In: *IEEE Transactions on Industry Applications* 37 (1 2001), pp. 240–246. ISSN: 00939994. DOI: 10.1109/28.903156.

[106] Ali Nematbakhsh et al. "Comparison of wave load effects on a TLP wind turbine by using computational fluid dynamics and potential flow theory approaches". In: *Applied Ocean Research* 53 (Oct. 2015), pp. 142–154. ISSN: 0141-1187. DOI: 10.1016/J.APOR.2015.08.004.

[107] John Nicholas Newman. "Second-order, slowly-varying Forces on Vessels in Irregular Waves". In: *Department of Ocean Engineering* (19 1974). URL: https://repository.tudelft.nl/islandora/object/uuid%5C%3A740c99a2-8545-475b-8c6a-5a098e987521.

[108] John Nicholas Newman. "The exciting forces on fixed bodies in waves". In: *David W. Taylor Model Basin, Washington DC, USA, Navy Department, Research and Development, Published in: Journal of Ship Research, December 1962, SNAME* (1962). URL: https://repository.tudelft.nl/islandora/object/uuid%5C%3A0dddfbf6-1fdf-416b-8b65-618dea56440f.

[109] Adam Niesony. "A critical analysis of the Mises stress criterion used in frequency domain fatigue life prediction". In: *Frattura ed Integrità Strutturale* 10 (38 Oct. 2016), pp. 177–183. ISSN: 19718993. DOI: 10.3221/IGF-ESIS.38.24.

[110] T Francis Ogilvie. "Recent progress toward the understanding and prediction of ship motions". In: *Symposium on Naval Hydrodynamics* 5 (Sept. 1964). URL: https://repository.tudelft.nl/islandora/object/uuid%5C%3A5accdabd-b484-4450-9613-e1d2c5ee211e.

[111] Orcina. *Orcaflex documentation*. 2023. URL: https://www.orcina.com/webhelp/OrcaFlex/Default.htm.

[112] H. Ormberg and K. Larsen. "Coupled analysis of floater motion and mooring dynamics for a turret-moored ship". In: *Applied Ocean Research* 20 (1-2 Feb. 1998), pp. 55–67. ISSN: 0141-1187. DOI: 10.1016/S0141-1187(98)00012-1.

[113] M. M. Pedersen. "Multiaxial fatigue assessment of welded joints using the notch stress approach". In: *International Journal of Fatigue* 83 (Feb. 2016), pp. 269–279. ISSN: 0142-1123. DOI: 10.1016/J.IJFATIGUE.2015.10.021.

[114] João Pessoa and Nuno Fonseca. "Investigation of depth effects on the wave exciting low frequency drift forces by different approximation methods". In: *Applied Ocean Research* 42 (Aug. 2013), pp. 182–199. ISSN: 0141-1187. DOI: 10.1016/J.APOR.2013.06.003.

[115] J.A. Pinkster. "Low frequency second order wave exciting forces on floating structures". Delft University of Technology, 1980. URL: https://repository.tudelft.nl/islandora/object/uuid%5C%3Ad6d42e9c-c349-47e5-8d63-5c6454196b04.

[116] Y. Qin et al. "Fatigue design of welded double-sided T-joints and double-sided cruciform joints in steel marine structures: A total stress concept". In: *Fatigue and Fracture of Engineering Materials and Structures* 42 (12 Dec. 2019), pp. 2674–2693. ISSN: 8756-758X. DOI: 10.1111/FFE.13089. URL: https://repository.tudelft.nl/islandora/object/uuid%5C%3Adb4e2934-57be-4916-bf40-1b1a3a56235b.

[117] Y. Qin et al. "Mid- and High-Cycle Fatigue of Welded Joints in Steel Marine Structures: Effective Notch Stress and Total Stress Concept Evaluations". In: *International Journal of Fatigue* 142 (Jan. 2021), p. 105822. ISSN: 0142-1123. DOI: 10.1016/J.IJFATIGUE.2020.105822.

[118] V. M. Radhakrishnan. "Multiaxial fatigue - An overview". In: *Sadhana* 20 (1 Feb. 1995), pp. 103–122. ISSN: 02562499. DOI: 10.1007/BF02747286/METRICS. URL: https://link.springer.com/article/10.1007/BF02747286.

[119] G. K.V. Ramachandran et al. "Fully coupled three-dimensional dynamic response of a tension-leg platform floating wind turbine in waves and wind". In: *Journal of Offshore Mechanics and Arctic Engineering* 136 (2 Mar. 2014). ISSN: 1528896X. DOI: 10.1115/1.4025599.

[120] L. Reis, B. Li, and M. de Freitas. "Biaxial fatigue for proportional and non-proportional loading paths". In: *Fatigue & Fracture of Engineering Materials & Structures* 27 (9 Sept. 2004), pp. 775–784. ISSN: 1460-2695. DOI: 10.1111/J.1460-2695.2004.00769.X. URL: https://onlinelibrary-wiley-com.tudelft.idm.oclc.org/doi/full/10.1111/j.1460-2695.2004.00769.x%20https://onlinelibrary-wiley-com.tudelft.idm.oclc.org/doi/abs/10.1111/j.1460-2695.2004.00769.x%20https://onlinelibrary-wiley-com.tudelft.idm.oclc.org/doi/10.1111/j.1460-2695.2004.00769.x.

[121] Nianxin Ren, Yugang Li, and Jinping Ou. "Coupled wind-wave time domain analysis of floating offshore wind turbine based on Computational Fluid Dynamics method". In: *Journal of Renewable and Sustainable Energy* 6 (2 Mar. 2014), p. 23106. ISSN: 19417012. DOI: 10.1063/1.4870988/285430. URL: /aip/jrse/article/6/2/023106/285430/Coupled-wind-wave-time-domain-analysis-of-floating.

[122] Yajun Ren, Vengatesan Venugopal, and Wei Shi. "Dynamic analysis of a multi-column TLP floating offshore wind turbine with tendon failure scenarios". In: *Ocean Engineering* 245 (Feb. 2022), p. 110472. ISSN: 0029-8018. DOI: 10.1016/J.OCEANENG.2021.110472.

[123] Zhihao Ren, Bin Teng, and Longfei Cong. "Time-domain simulation of sum-frequency hydrodynamic performance of a TLP-type floating wind turbine in multidirectional seas". In: *Applied Ocean Research* 135 (June 2023), p. 103565. ISSN: 0141-1187. DOI: 10.1016/J.APOR.2023.103565.

[124] Amy N. Robertson and Jason M. Jonkman. "Loads analysis of several offshore floating wind turbine concepts". In: *Proceedings of the International Offshore and Polar Engineering Conference* (2011), pp. 443–450. ISSN: 10986189.

[125] Jaap Schijve. *Fatigue of structures and materials*. Springer, 2008. ISBN: 9781402068089.

[126] A.A. Shabana. "Flexible Multibody Dynamics: Review of Past and Recent Developments". In: *Multibody System Dynamics* 1 (2 1997), pp. 189–222. DOI: 10.1023/A:1009773505418.

[127] Macheng Shen, Zhiqiang Hu, and Geliang Liu. "Dynamic response and viscous effect analysis of a TLP-type floating wind turbine using a coupled aero-hydro-mooring dynamic code". In: *Renewable Energy* 99 (Dec. 2016), pp. 800–812. ISSN: 0960-1481. DOI: 10.1016/J.RENENE.2016.07.058.

[128] American Bureau of Shipping. *Fatigue Assessment of Offshore Strucutres*. ABS, June 2020.

[129] Mohammed Khair Al-Solihat and Meyer Nahon. "Flexible multibody dynamic modelling of a floating wind turbine". In: *International Journal of Mechanical Sciences* 142-143 (July 2018), pp. 518–529. ISSN: 0020-7403. DOI: 10.1016/J.IJMECSCI.2018.05.018.

[130] C. M. Sonsino. "Multiaxial fatigue assessment of welded joints – Recommendations for design codes". In: *International Journal of Fatigue* 31 (1 Jan. 2009), pp. 173–187. ISSN: 0142-1123. DOI: 10.1016/J.IJFATIGUE.2008.06.001.

[131] Carlos Eduardo Silva De Souza and Erin E. Bachynski. "Effects of hull flexibility on the structural dynamics of a tlp floating wind turbine". In: *Proceedings of the International Conference on Offshore Mechanics and Arctic Engineering - OMAE* 10 (2018). DOI: 10.1115/OMAE2018-77310.

[132] European Committee for Standardization. *Eurocode 3: Design of steel structures - Part 1-9: Fatigue*. CEN, May 2005.

[133] Gordon M. Stewart et al. "Calibration And Validation of a FAST Floating Wind Turbine Model of the DeepCwind Scaled Tension-Leg Platform". In: *International Offshore and Polar Engineering Conference* 22 (June 2012). URL: /ISOPEIOPEC/proceedings-abstract/ISOPE12/All-ISOPE12/12421.

[134] J. van der Tempel. "Design of support structures for offshore wind turbines". Delft University of Technology, Apr. 2006.

[135] C. Tibaldi et al. "An investigation on wind turbine resonant vibrations". In: *Wind Energy* 19 (5 May 2016), pp. 847–859. ISSN: 10991824. DOI: 10.1002/WE.1869.

[136] Michael J. Todd and E. Alper Yildirim. "On Khachiyan's algorithm for the computation of minimum-volume enclosing ellipsoids". In: *Discrete Applied Mathematics* 155 (13 Aug. 2007), pp. 1731–1744. ISSN: 0166-218X. DOI: 10.1016/J.DAM.2007.02.013.

[137] Thanh Toan Tran and Dong Hyun Kim. "A CFD study into the influence of unsteady aerodynamic interference on wind turbine surge motion". In: *Renewable Energy* 90 (May 2016), pp. 204–228. ISSN: 0960-1481. DOI: 10.1016/J.RENENE.2015.12.013.

[138] *Transforming our world: the 2030 Agenda for Sustainable Development*. UN General Assembly, Oct. 2015.

[139] Bureau Veritas. *NI 572: Classification and Certification of Floating Offshore Wind Turbines*. Bureau Veritas, Jan. 2019.

[140] Bureau Veritas. *NI 611: Guidelines for Fatigue Assessment of Ships and Offshore Units*. Bureau Veritas, Oct. 2020.

[141] Axelle Viré. *Floating wind turbines change everything*. May 2022. URL: https://www.tudelft.nl/en/2022/tu-delft/floating-wind-turbines-change-everything.

[142] Axelle Viré et al. *Introduction to wind turbines: physics and technology*. Sept. 2022.

[143] Lin Wang, Xiongwei Liu, and Athanasios Kolios. "State of the art in the aeroelasticity of wind turbine blades: Aeroelastic modelling". In: *Renewable and Sustainable Energy Reviews* 64 (Oct. 2016), pp. 195–210. ISSN: 1364-0321. DOI: 10.1016/J.RSER.2016.06.007.

[144] Peter D. Welch. "The Use of Fast Fourier Transform for the Estimation of Power Spectra: A Method Based on Time Averaging Over Short, Modified Periodograms". In: *IEEE Transactions on Audio and Electroacoustics* 15 (2 1967), pp. 70–73. ISSN: 00189278. DOI: 10.1109/TAU.1967.1161901.

[145] Peter Wellens and Peter Naaijen. *Motions and Loading of Structures in Waves*. 2023.

[146] Daniel Wu. "The Effect of Blade Aeroelasticity and Turbine Parameters on Wind Turbine Noise". In: 2017. URL: https://api.semanticscholar.org/CorpusID:115887875.

[147] Zhi Gang Xiao and Kentaro Yamada. "A method of determining geometric stress for fatigue strength evaluation of steel welded joints". In: *International Journal of Fatigue* 26 (12 Dec. 2004), pp. 1277–1293. ISSN: 0142-1123. DOI: 10.1016/J.IJFATIGUE.2004.05.001.

[148] De Guang Zhang et al. "A method to avoid negative damped low frequent tower vibrations for a floating, pitch controlled wind turbine". In: *Journal of Physics: Conference Series* 75 (1 July 2007), p. 012073. ISSN: 1742-6596. DOI: 10.1088/1742-6596/75/1/012073. URL: https://iopscience.iop.org/article/10.1088/1742-6596/75/1/012073%20https://iopscience.iop.org/article/10.1088/1742-6596/75/1/012073/meta.

[149] Yang Zhou et al. "Numerical modelling of dynamic responses of a floating offshore wind turbine subject to focused waves". In: *Energies* 12.18 (2019). Cited by: 26; All Open Access, Gold Open Access, Green Open Access. DOI: 10.3390/en12183482. URL: https://www.scopus.com/inward/record.uri?eid=2-s2.0-85072541295%5C&doi=10.3390%5C%2fen12183482%5C&partnerID=40%5C&md5=bd9283a093b5fec78f8c47a5edd13ab8.

A

Potential theory

A.1. Deriving the potential

A flow potential is a mathematical expression whose derivative in any direction equals the flow velocity in that direction [145]. As explained in section 3.2 any sea can be decomposed into a set of linear waves that interact with one another. Potential theory is also considered to be linear.

Suppose that the fluid dynamics are dominated by pressure, viscous effects are negligible, the fluid is incompressible and flow is irrotational a potential flow formulation may be used. In an actual viscous fluid, viscosity causes friction, vortices and flow separation, resulting in non-linear damping [70]. It is important to note that it has been found that for large voluminous structures, potential theory gives accurate results compared to model tests. However, discrepancies can be found near resonance frequencies of for example roll, due to the unaccounted viscous effect in potential theory [70]. For relatively slender objects, such as the surface penetrating column of a TLP these effects may be important for all excitation frequencies, and hence cannot be ignored. A potential function may be considered for n^{th} order terms, however, as this thesis will consider only first and second-order terms, a second-order potential is needed.

The velocity potential is a solution of Laplace's equation fulfilling the continuity condition, seabed boundary condition, free surface kinematic boundary condition and free surface dynamic boundary condition. Equation A.1 below shows the full velocity potential including first and second-order terms. The superscript $^{(1)}$ and $^{(2)}$ respectively represent the first and second-order contributions to the total potential. The variable ε is a small number $\varepsilon << 1$ representing the order of the subsequent variable.

$$\Phi = \varepsilon\Phi^{(1)} + \varepsilon^2\Phi^{(2)} \tag{A.1}$$

with;

$$\Phi^{(1)} = \Phi_w + \Phi_r + \Phi_d \tag{A.2}$$

Where Φ_w represents the undisturbed incoming wave potential, Φ_r is the radiation potential and Φ_d is the diffraction potential. The total velocity potential must adhere to a set of boundary conditions [70].

1. **The continuity condition or Laplace equation:**

$$\nabla^2\Phi^{(1)} = 0 \quad \text{and} \quad \nabla^2\Phi^{(2)} = 0 \tag{A.3}$$

2. **Seabed boundary condition:** No flow through seabed therefore at the seabed:

$$\frac{\partial\Phi^{(1)}}{\partial z} = 0 \quad \text{and} \quad \frac{\partial\Phi^{(2)}}{\partial z} = 0$$

3. **Free surface boundary condition:** Fluid particles at the free surface remain at the free surface. No leak through the dynamic free surface. This produces a homogeneous and particular solution of the boundary condition for the first- and second-order potential components respectively.

$$g\frac{\partial\Phi^{(1)}}{\partial z} + \frac{\partial^2\Phi^{(1)}}{\partial t^2} = 0 \tag{A.4}$$

and;

$$g\frac{\partial\Phi^{(1)}}{\partial z}+\frac{\partial^2\Phi^{(1)}}{\partial t^2}=2\cdot\left(\vec{\nabla}\Phi^{(1)}\cdot\vec{\nabla}\frac{\partial\Phi^{(1)}}{\partial t}\right)+\frac{\partial\Phi^{(1)}}{\partial t}\cdot\left(\frac{\partial^2\Phi^{(1)}}{\partial^2 z^2}+\frac{1}{g}\frac{\partial^2}{\partial t^2}\left(\frac{\partial\Phi^{(1)}}{\partial z}\right)\right) \tag{A.5}$$

4. **Kinematic boundary condition on the oscillating body surface:** Watertight hull surface must be satisfied at the instantaneous position of the hull.

$$\vec{\nabla}\Phi\cdot\vec{N}=\vec{V}\cdot\vec{N}$$

This results in the following for the first and second-order potential;

$$\vec{\nabla}\Phi^{(1)}\cdot\vec{n}=\vec{V^{(1)}}\cdot\vec{n} \tag{A.6}$$

and

$$\vec{\nabla}\Phi^{(2)}\cdot\vec{n}=-\left(\vec{X^{(1)}}\cdot\vec{\nabla}\right)\cdot\left(\vec{\nabla}\Phi^{(1)}\cdot\vec{n}\right)+\left(\vec{V^{(1)}}-\vec{\nabla}\Phi^{(1)}\right)\cdot\vec{N^{(1)}} \tag{A.7}$$

where the last term represents the difference between the two velocity vector caused by the first-order change of the directional normal.

Combining equation (A.2) and equation (A.6) results in the following ;

$$\left(\vec{\nabla}\Phi_w^{(1)}+\vec{\nabla}\Phi_d^{(1)}+\vec{\nabla}\Phi_r^{(1)}\right)\cdot\vec{n}=\vec{V^{(1)}}\cdot\vec{n}$$

And considering that the radiated wave component only carries outgoing potential the below distinction can be made;

$$\left(\vec{\nabla}\Phi_w^{(1)}+\vec{\nabla}\Phi_d^{(1)}\right)\cdot\vec{n}=0\quad\text{resulting in}\quad\vec{\nabla}\Phi_w^{(1)}=-\vec{\nabla}\Phi_d^{(1)} \tag{A.8}$$

$$\vec{\nabla}\Phi_r^{(1)}\cdot\vec{n}=\vec{V^{(1)}}\cdot\vec{n} \tag{A.9}$$

The solution for the unknown radiation and diffraction potentials will be discussed in appendix A.2

Finally, when substituting the first-order potential into the particular solution of the second-order free surface boundary condition the following expression holds;

$$\Phi^{(2)}=\Phi_w^{(2)}+\Phi_d^{(2)} \tag{A.10}$$

The solution of $\Phi_w^{(2)}$ and $\Phi_d^{(2)}$ poses a problem due to the complexity of the surface boundary condition as shown in equation (A.5). Some solutions for this have been devised but no exact solution [70].

5. **Boundary condition at infinity** A radiation condition for the radiation potentials $\Phi_w^{(1)}$, $\Phi_r^{(1)}$ and $\Phi_d^{(2)}$ states

$$\lim_{R\to+\infty}\Phi=0$$

A.2. Solving for the unknown potential

The derivation of this unknown potential ϕ_i follows from a three-dimensional boundary element method [99] and the Green function for zero speed. As the Green function only satisfies the free surface boundary at zero forward speed, on the mean wetted surface, this method is a linear approach and can thus be conducted in the frequency domain, as well as time domain. Without going into detail about the mathematics of Green's theorem, as this is out of the scope of this thesis and readily available in textbooks, there are some important consequences of applying this theory to take note of.

1. The implementation of Green's second theorem considers the wetted surface of the body only and due to the boundaries in the derivation, is formally only valid for deep water.
2. The application of the Haskind relations (also out of the scope of this investigation) is only valid for a floating body with a zero time-averaged speed in all directions [70, 58]. Newman derived a generalized version of the Haskind relation for a body with constant forward speed [108]. Although the time-averaged speed of a FOWT is zero by definition, when subject to a current, implementation of the Newman relation should be considered.

As demonstrated in the sections above, the total potential can be expressed as a time and space-dependent part;

$$\Phi = \Phi_0 + \Phi_7 + \sum_{j=1}^{6} \Phi_j = \sum_{j=0}^{7} \Phi_j = -i\omega \sum_{j=0}^{7} \phi_j \zeta_j \tag{A.11}$$

Here $\phi 1 - 7$ are unknowns which can be determined using Lamb's method [76]. According to Lamb, a potential function in 3D space can be represented by a continuous distribution of single sources on the body surface, provided that the appropriate boundary conditions are satisfied [70]. The potential and radial velocity due to a singularity (point source) in 3D space with strength σ is given by equation (A.12);

$$\phi = \frac{-\sigma}{4\pi r}, v_r = \frac{\partial \phi}{\partial r} = \frac{\sigma}{4\pi r^2} \tag{A.12}$$

Of course, it goes without saying that this flow does not satisfy the aforementioned boundary conditions. To address this Green's function $G()$ can be used, distinctly **different** from Green's theorem and should not be confused.

$$\phi(x, y, z) = \frac{1}{4\pi} \iint_{S_0} \sigma(\hat{x}, \hat{y}, \hat{z}) \cdot G(x, y, z, \hat{x}, \hat{y}, \hat{z})\, dS_0 \tag{A.13}$$

It can be shown that if the source strength for each source can be chosen correctly, the free surface and bottom boundary conditions are satisfied. However, satisfying the watertight hull surface condition proves to be more challenging. In order to satisfy this condition the flow velocity due to the singularity needs to be equal but opposite to the normal velocity on the hull. As this normal velocity is a harmonic function in time, the source strength σ needs to be a harmonic function. This is referred to as a pulsating source and is a function of forcing frequency or the harmonic wave frequency for radiation and diffraction respectively. Addressing another issue the influence of a source on itself cannot be determined, the following expression holds;

$$\frac{\partial \phi}{\partial n}(x, y, z) = -\frac{1}{2}\sigma(x, y, z) + \frac{1}{4\pi} \oiint_{S_0} \sigma(\hat{x}, \hat{y}, \hat{z}) \cdot \frac{\partial G(x, y, z, \hat{x}, \hat{y}, \hat{z})}{\partial n}\, dS_0 \tag{A.14}$$

As a hull shape is generally complex, it cannot be described by an analytical function. Equation A.14 above can be discretized for a number of panels in space, each with its own source as;

$$\frac{\partial \phi_{r,m}}{\partial n} = -\frac{1}{2}\sigma_m + \frac{1}{4\pi} \sum_{n=1}^{N} \sigma_. \frac{\partial G_m n}{\partial n} \Delta S_n \tag{A.15}$$

As the above does not include dependence on time, and hence frequency, equation (A.15) must be repeated for each excitation (incoming wave) frequency.

B

Hydrodynamic Mesh Convergence

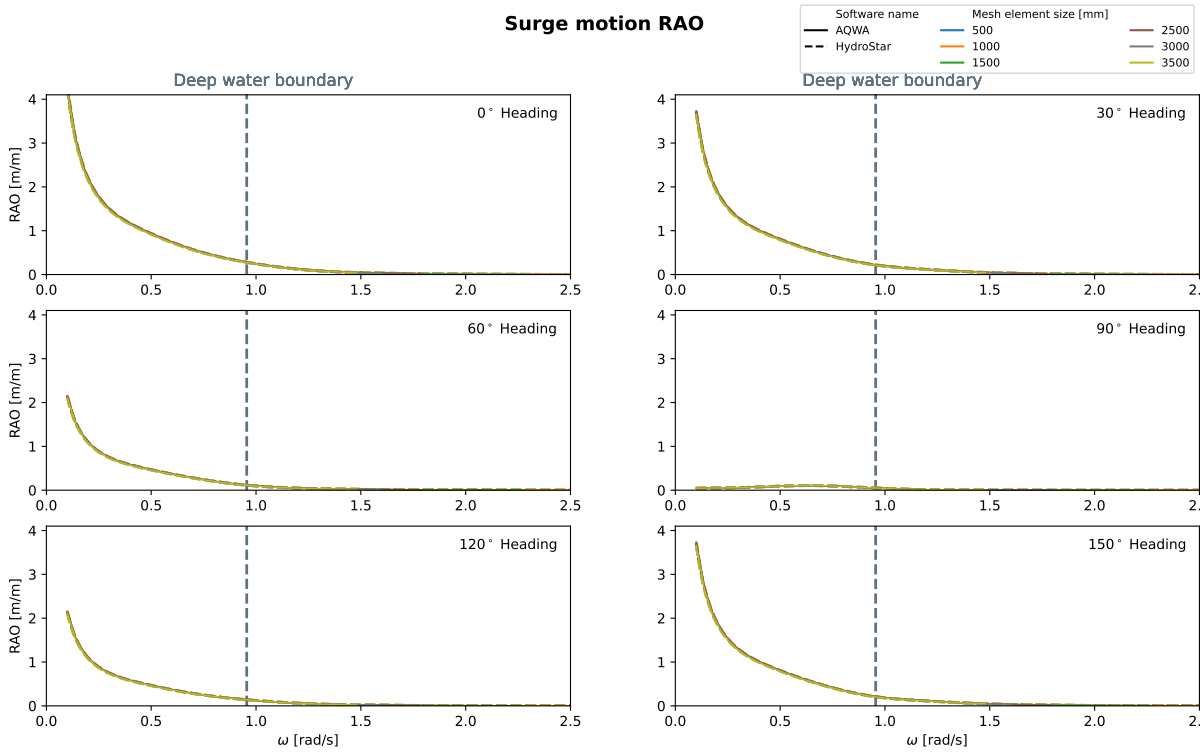


Figure B.1: Mesh convergence study and comparison between ANSYS AQWA and HydroStar for surge motion RAO

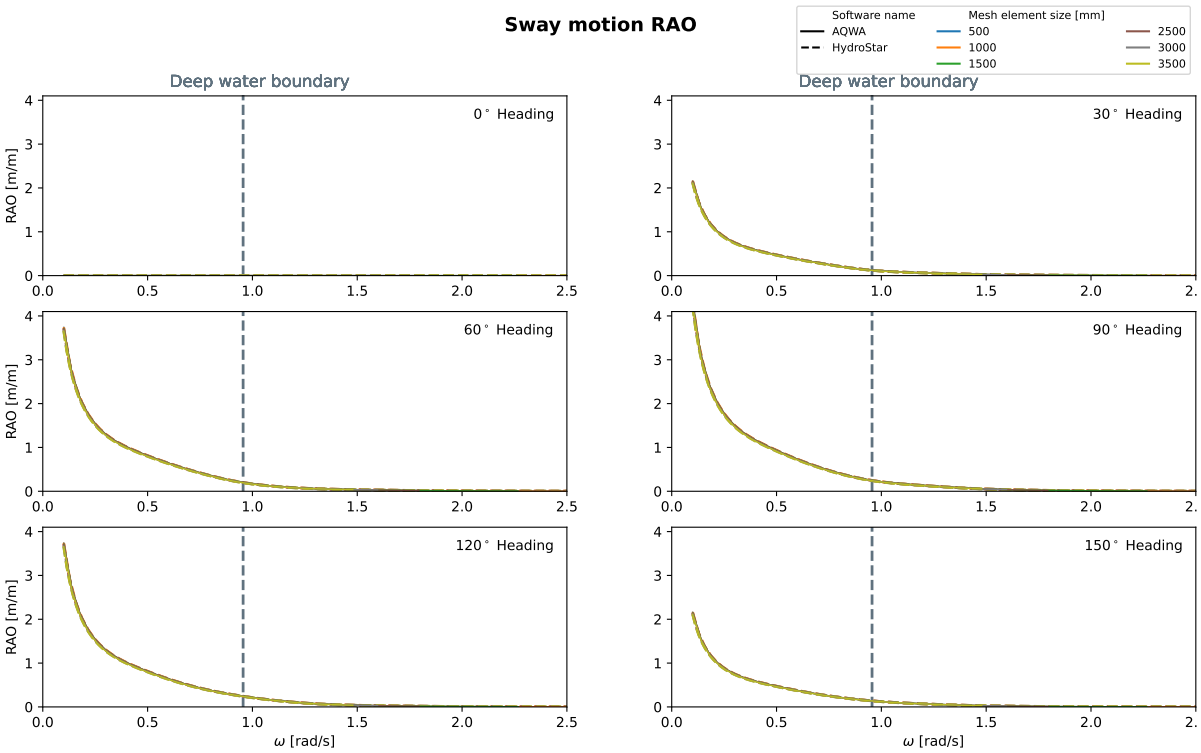


Figure B.2: Mesh convergence study and comparison between ANSYS AQWA and HydroStar for sway motion RAO

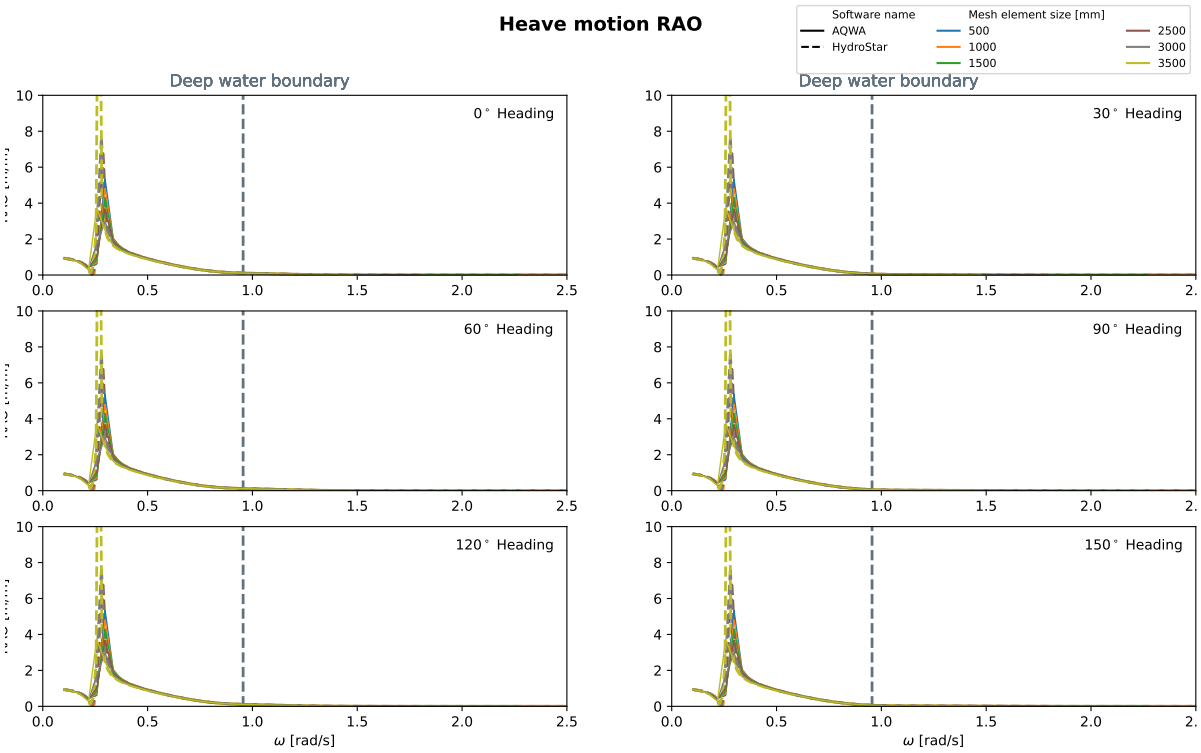


Figure B.3: Mesh convergence study and comparison between ANSYS AQWA and HydroStar for heave motion RAO

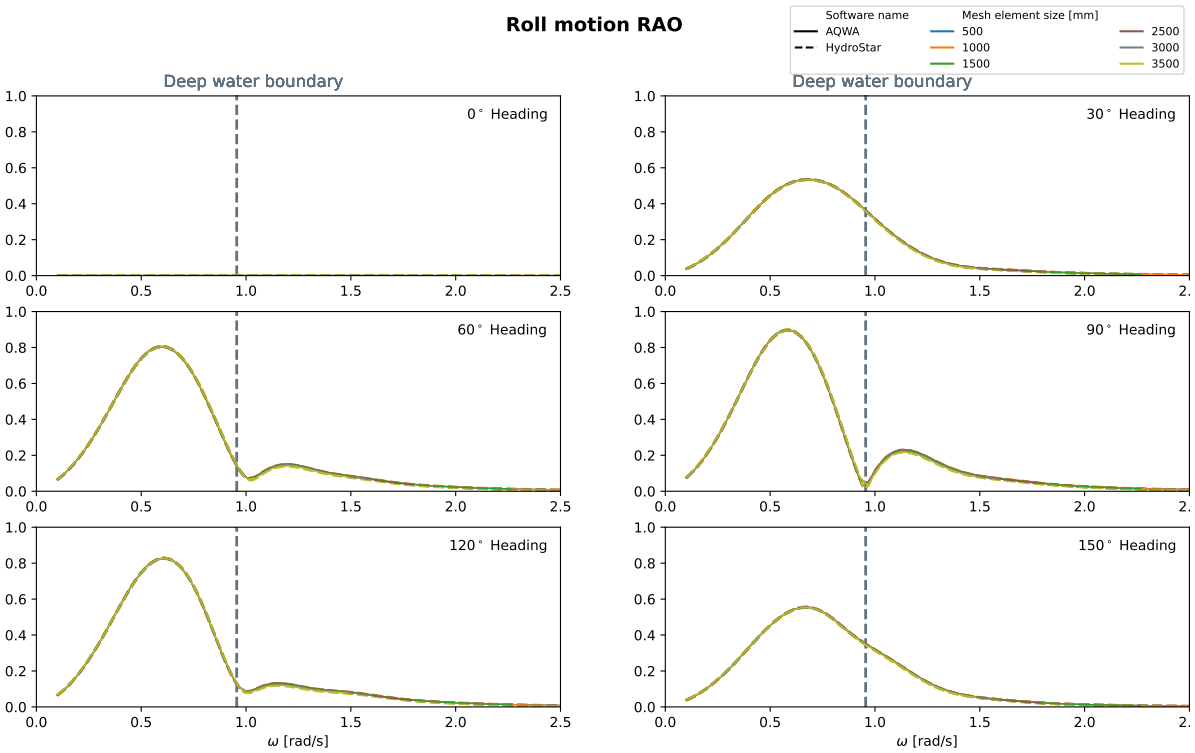


Figure B.4: Mesh convergence study and comparison between ANSYS AQWA and HydroStar for roll motion RAO

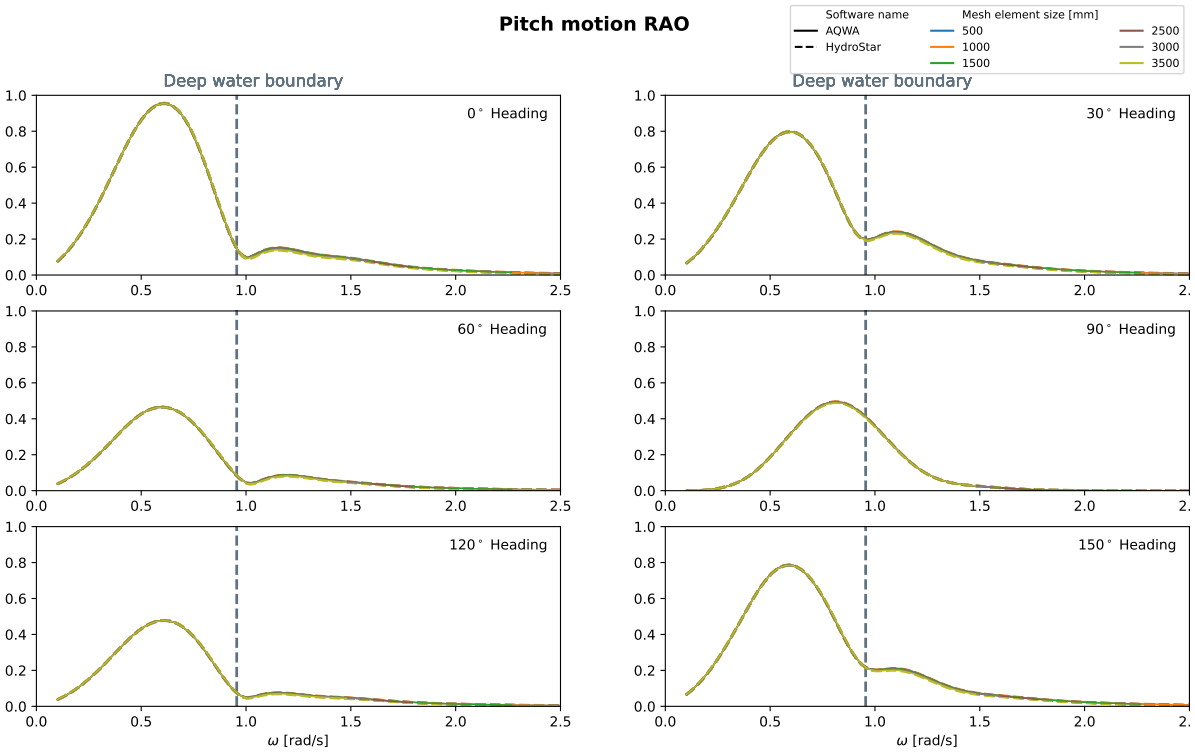


Figure B.5: Mesh convergence study and comparison between ANSYS AQWA and HydroStar for pitch motion RAO

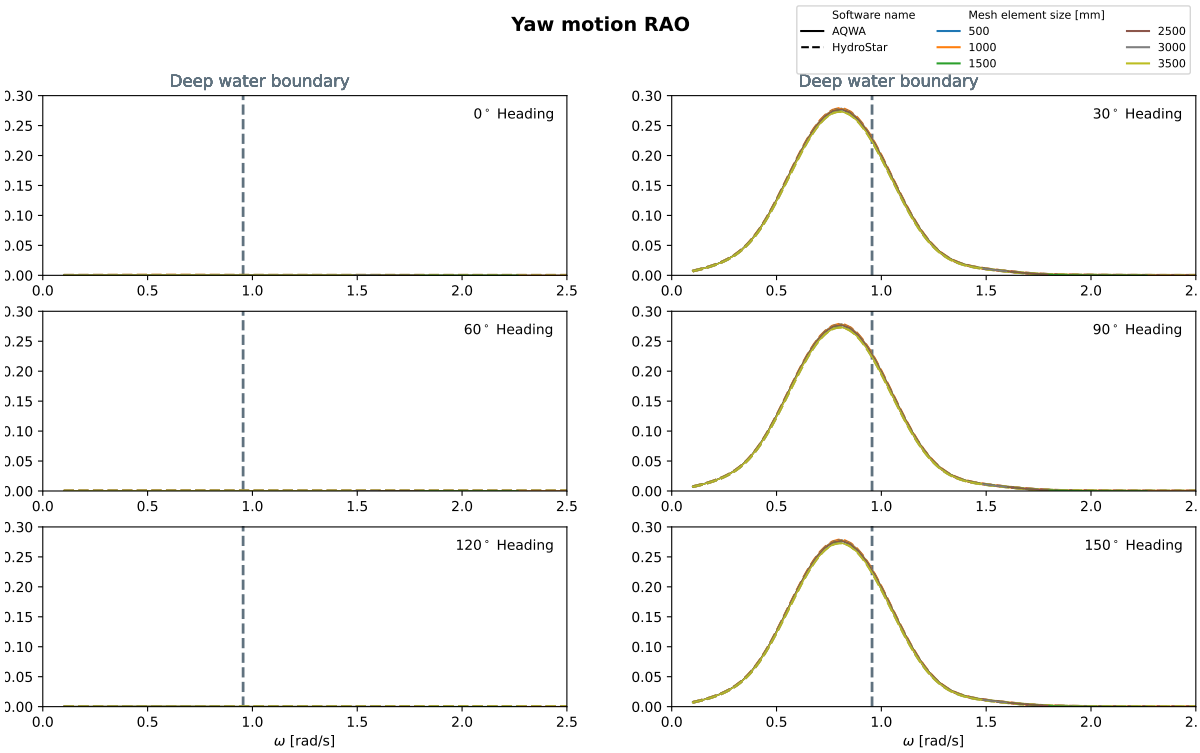


Figure B.6: Mesh convergence study and comparison between ANSYS AQWA and HydroStar for yaw motion RAO

C

Spectral Decomposition Results

C.1. Loading

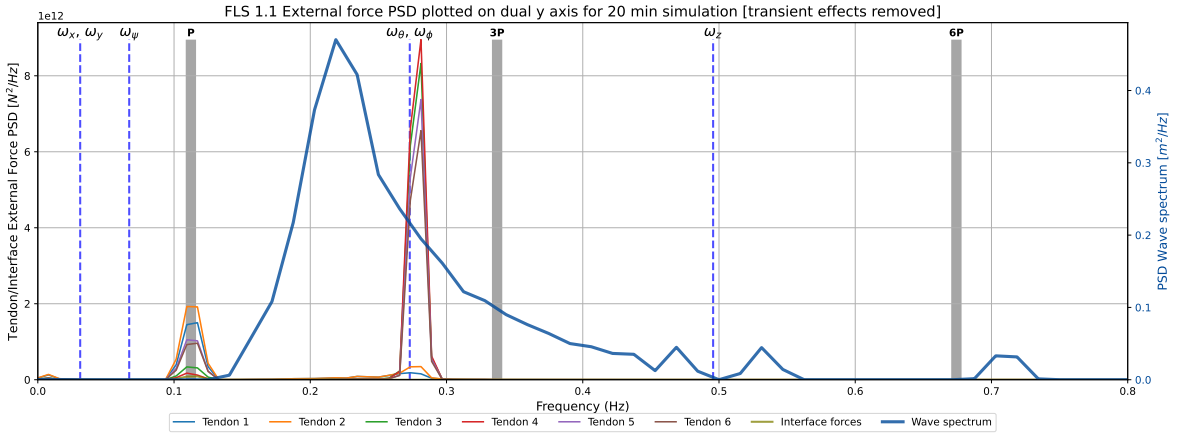


Figure C.1: Spectral decomposition of external forces for FLS1.1

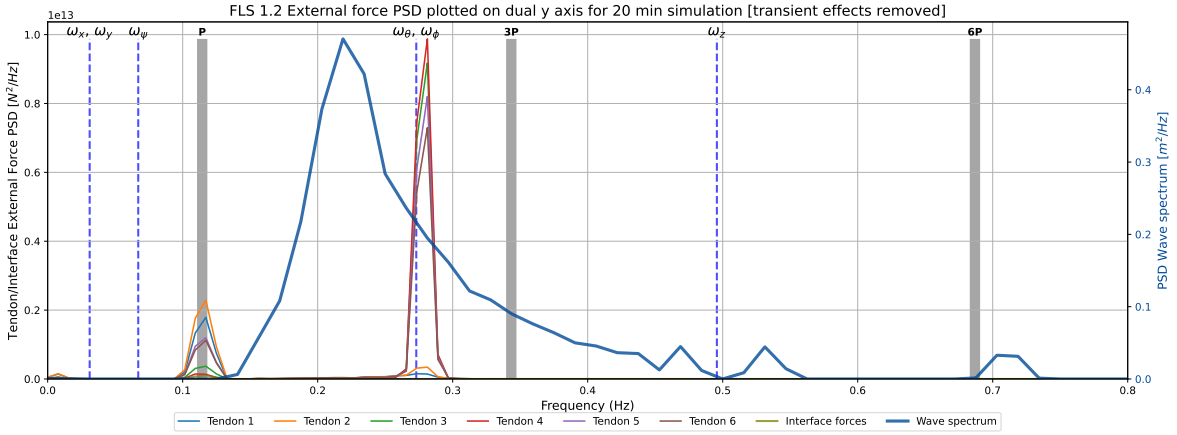


Figure C.2: Spectral decomposition of external forces for FLS 1.2

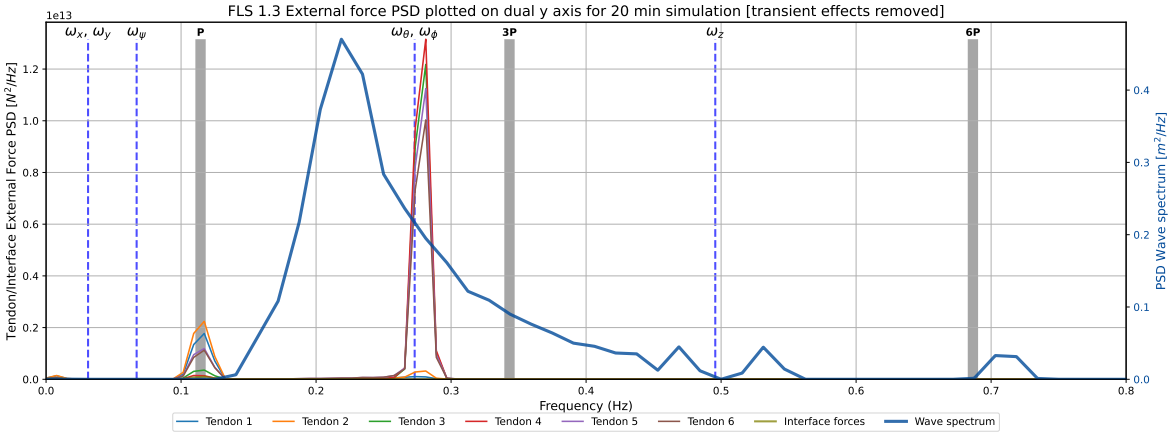


Figure C.3: Spectral decomposition of external forces for FLS 1.3

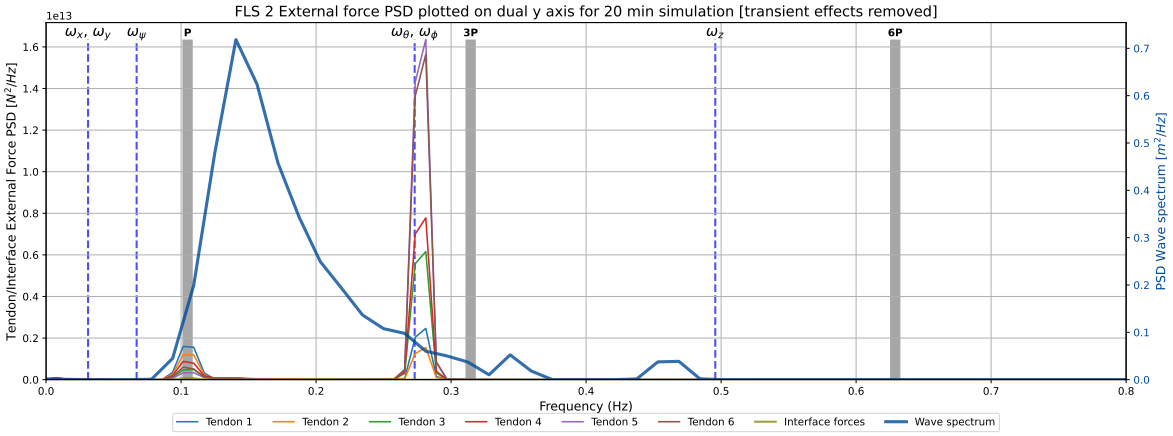


Figure C.4: Spectral decomposition of external forces for FLS 2

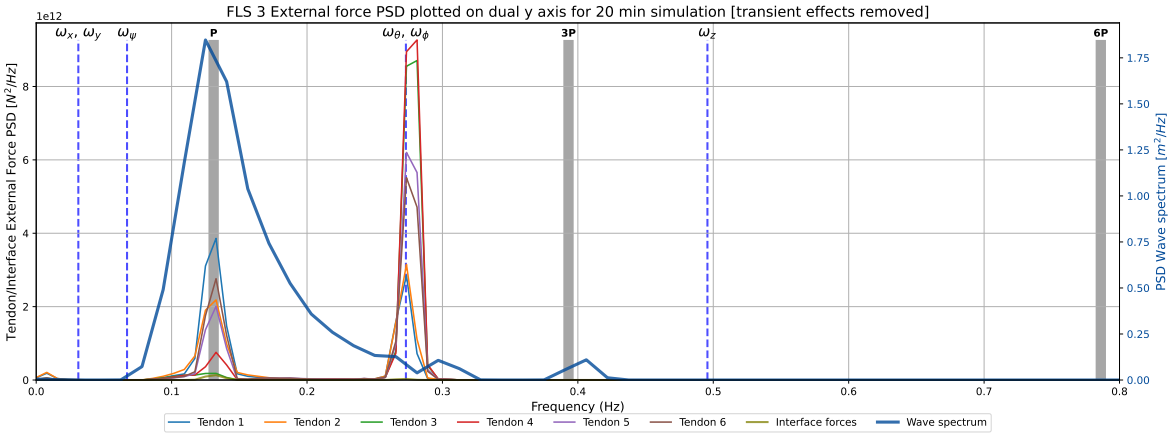


Figure C.5: Spectral decomposition of external forces for FLS 3

C.2. Response

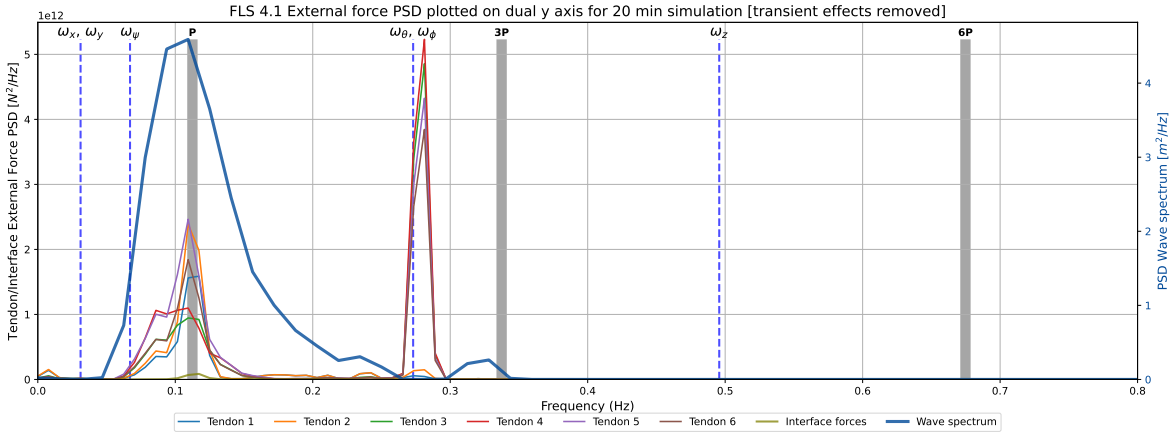


Figure C.6: Spectral decomposition of external forces for FLS 4

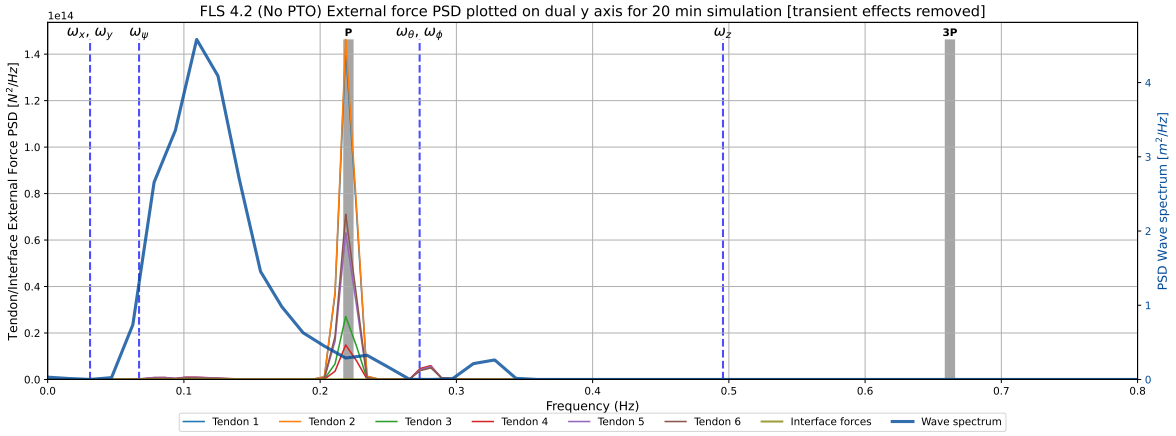


Figure C.7: Spectral decomposition of external forces for FLS 4 without power take off

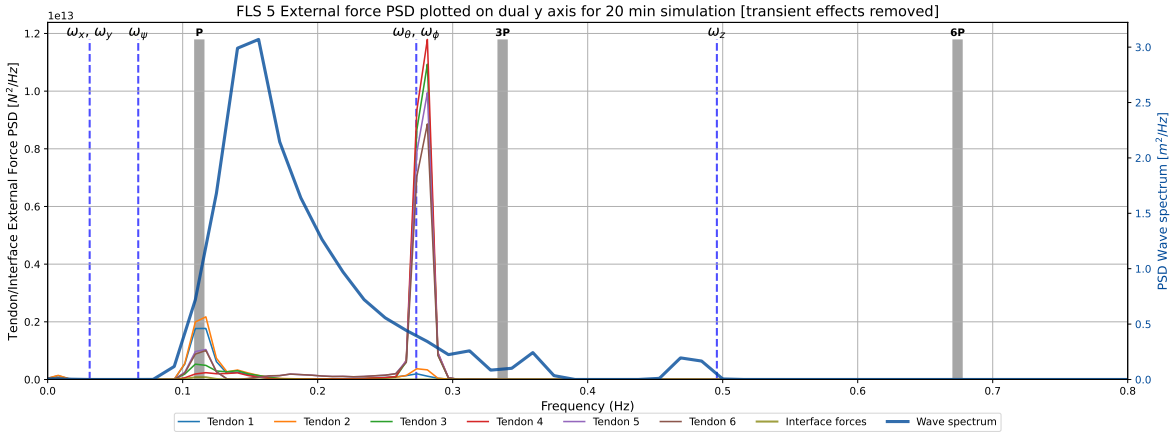


Figure C.8: Spectral decomposition of external forces for FLS 5

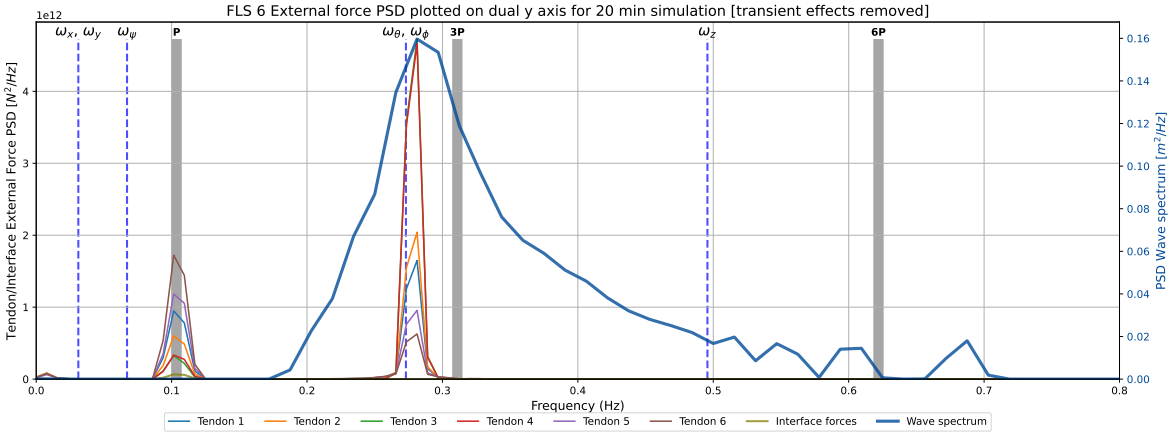


Figure C.9: Spectral decomposition of external forces for FLS 6

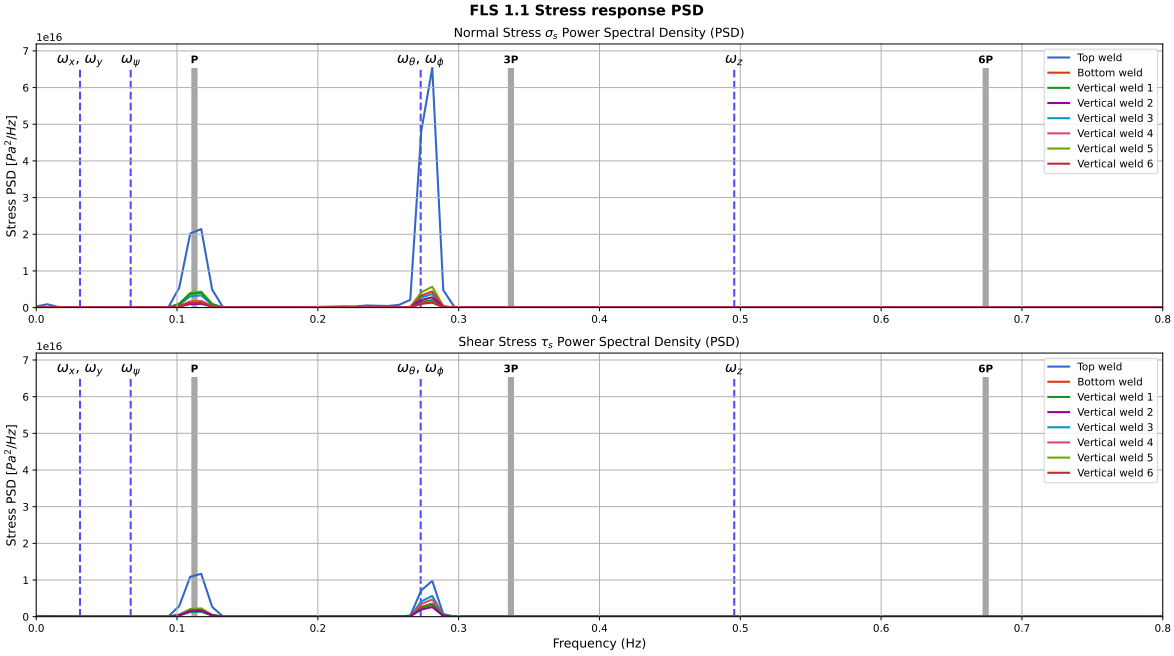


Figure C.10: Spectral decomposition of normal and shear stress response for FLS1.1

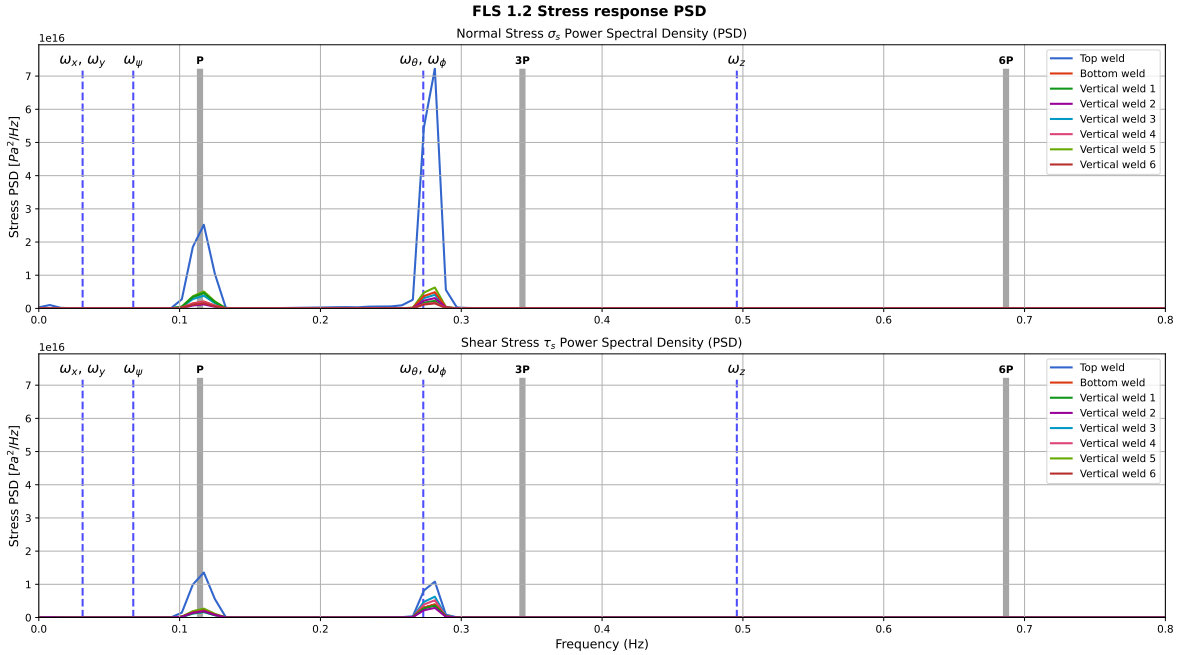


Figure C.11: Spectral decomposition of normal and shear stress response for FLS 1.2

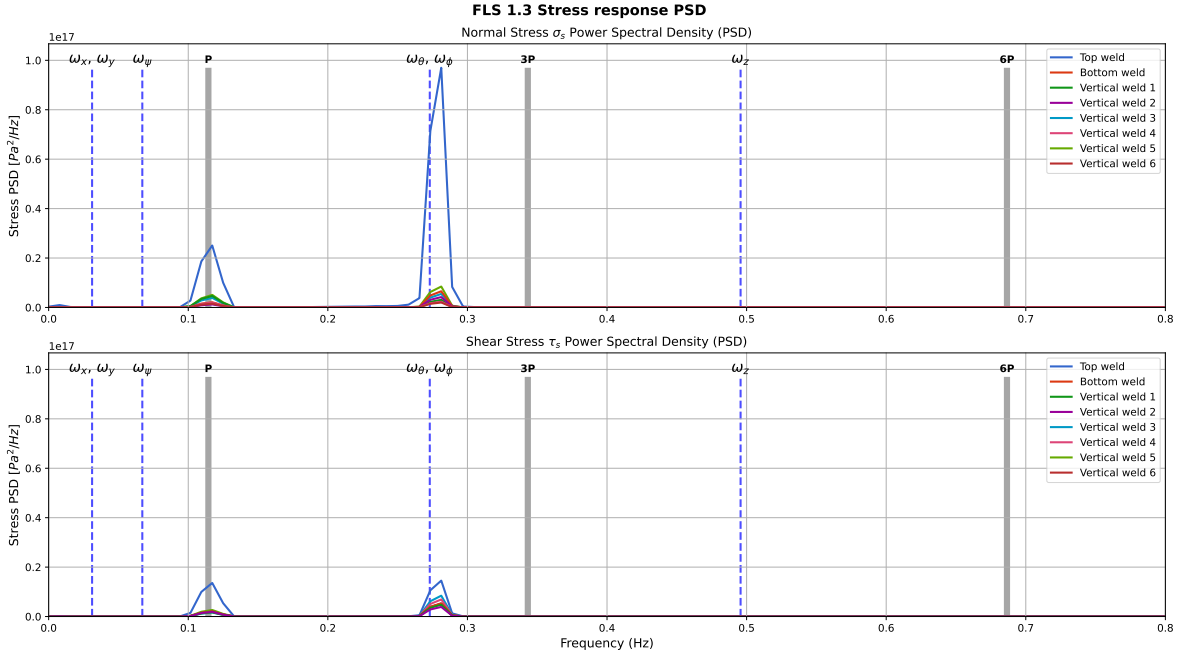


Figure C.12: Spectral decomposition of normal and shear stress response for FLS 1.3

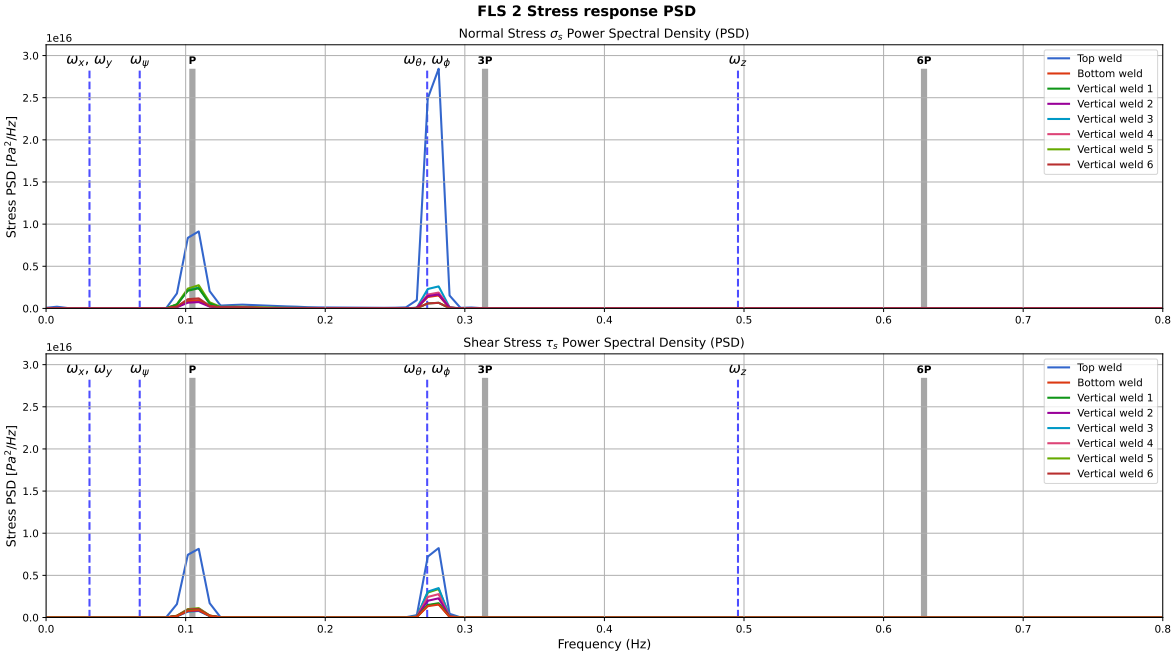


Figure C.13: Spectral decomposition of normal and shear stress response for FLS 2

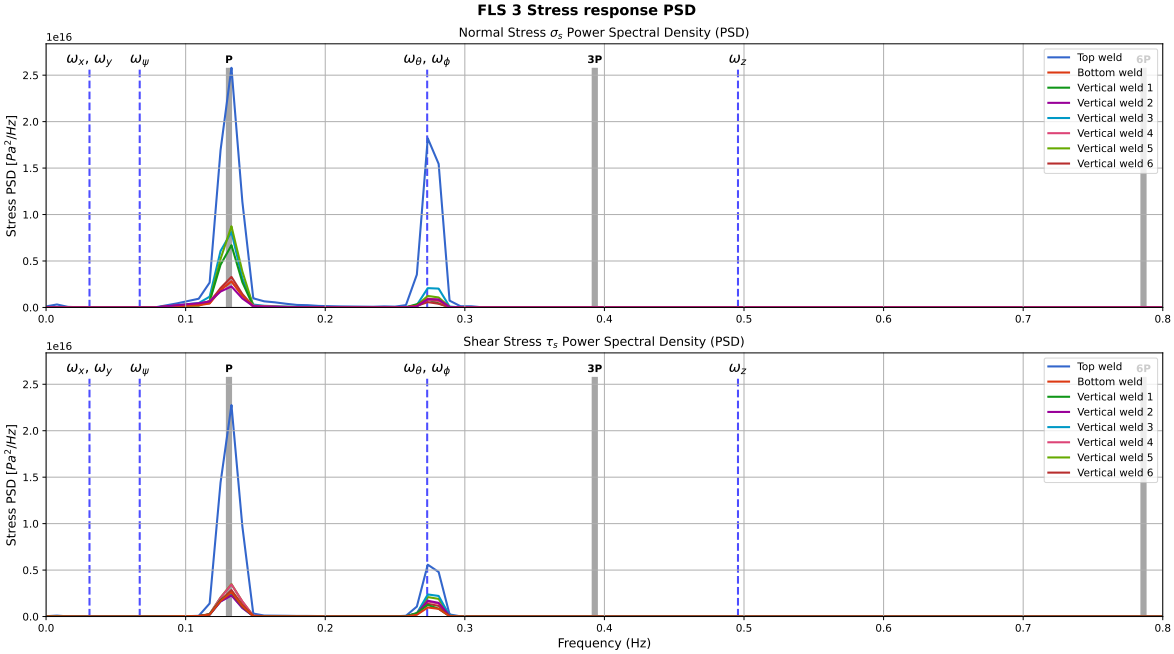


Figure C.14: Spectral decomposition of normal and shear stress response for FLS 3

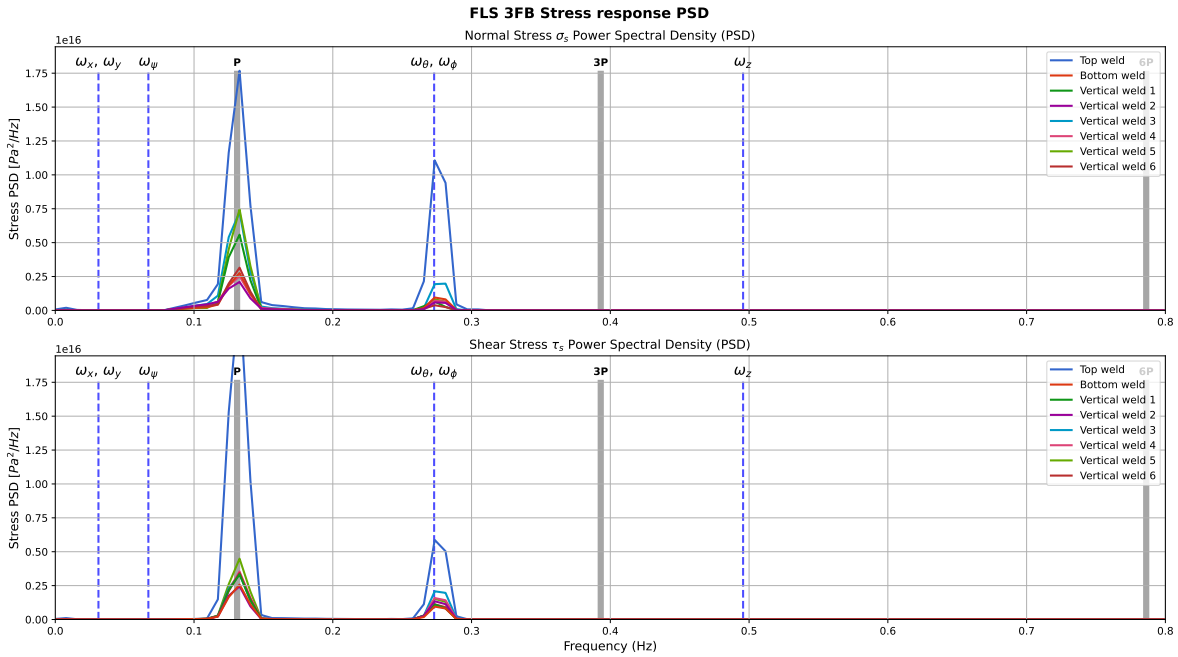


Figure C.15: Spectral decomposition of normal and shear stress response for FLS 3 with fatigue brackets

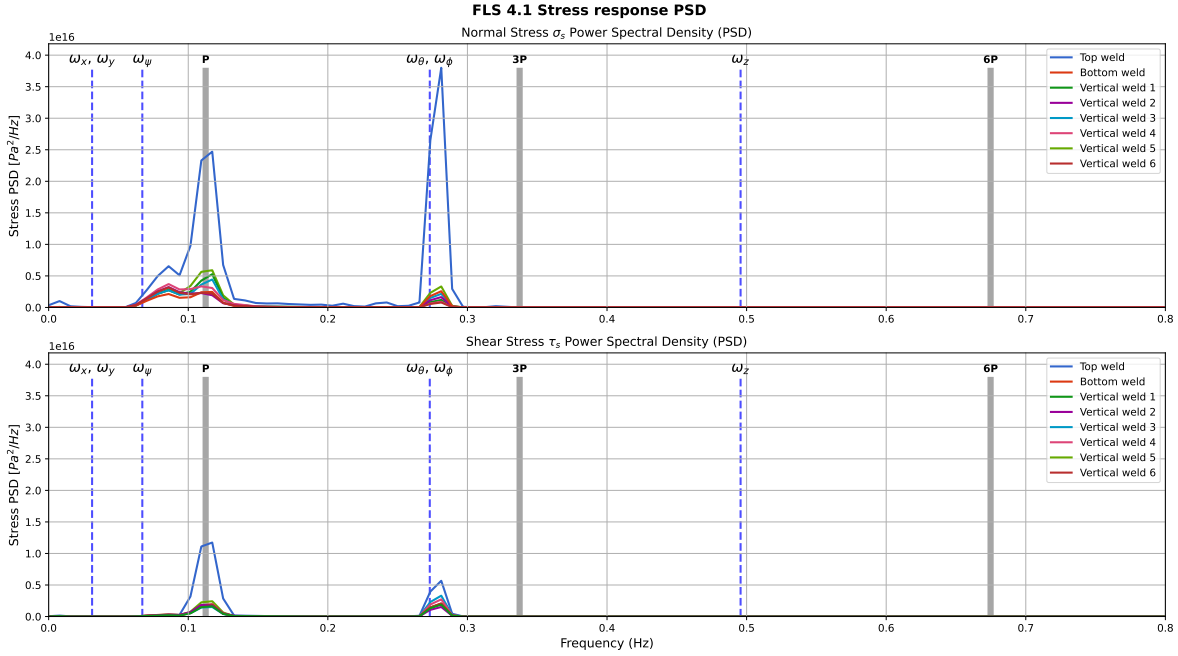


Figure C.16: Spectral decomposition of normal and shear stress response for FLS 4

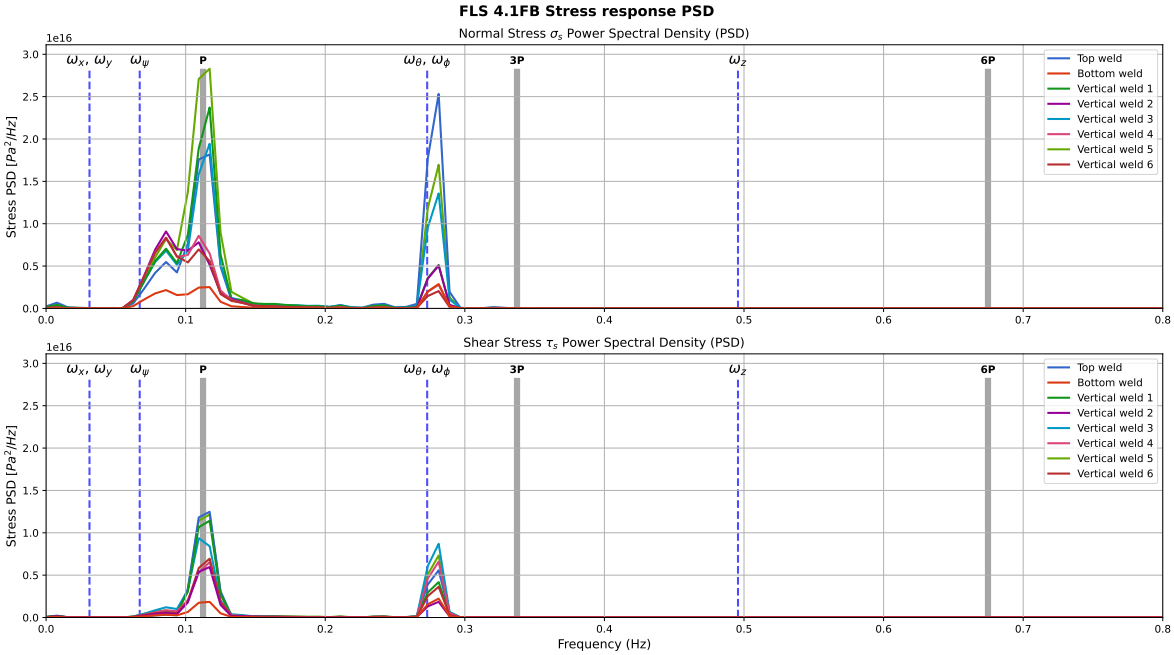


Figure C.17: Spectral decomposition of normal and shear stress response for FLS 4 with fatigue brackets

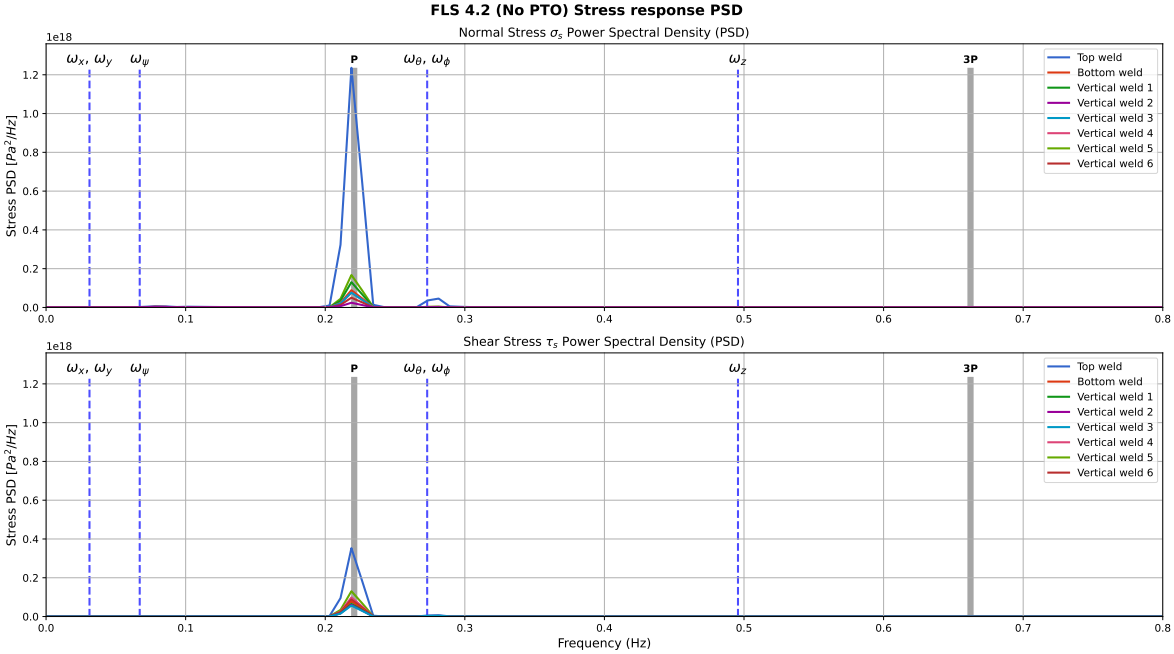


Figure C.18: Spectral decomposition of normal and shear stress response for FLS 4 without power take off

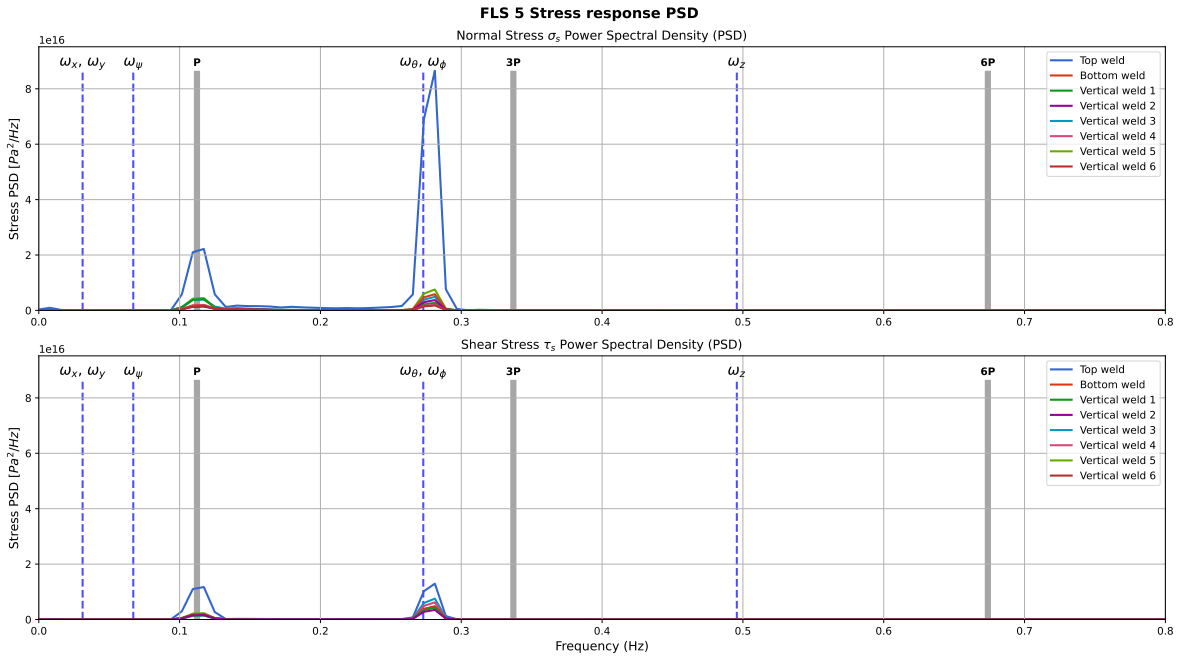


Figure C.19: Spectral decomposition of normal and shear stress response for FLS 5

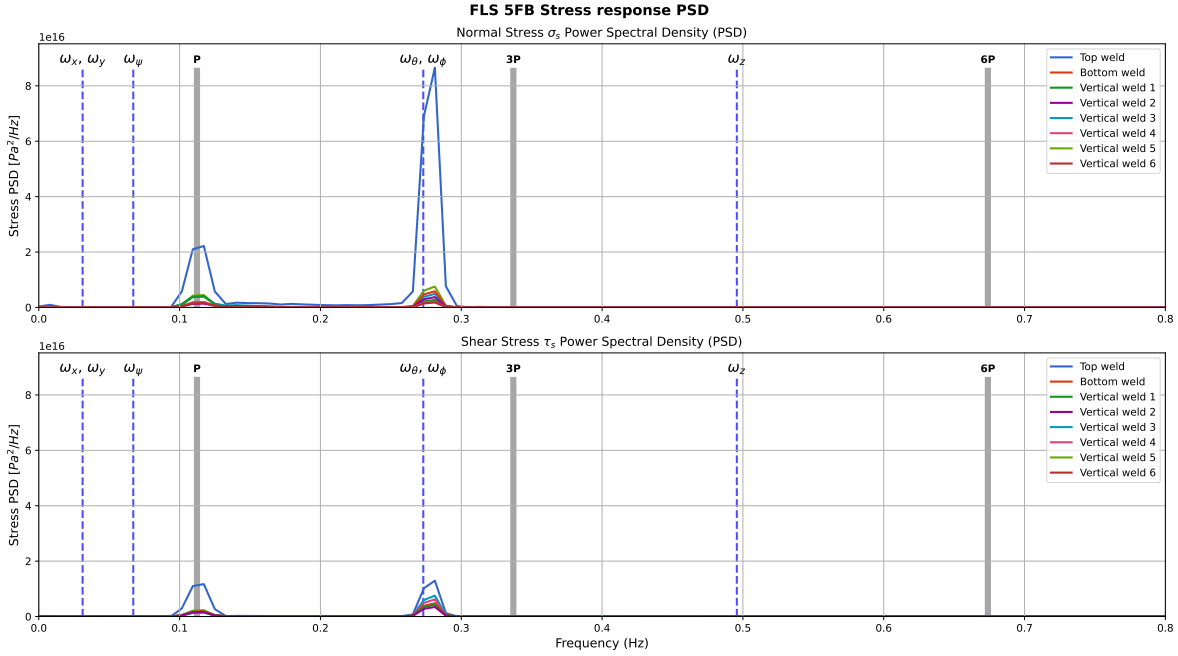


Figure C.20: Spectral decomposition of normal and shear stress response for FLS 5 with fatigue brackets

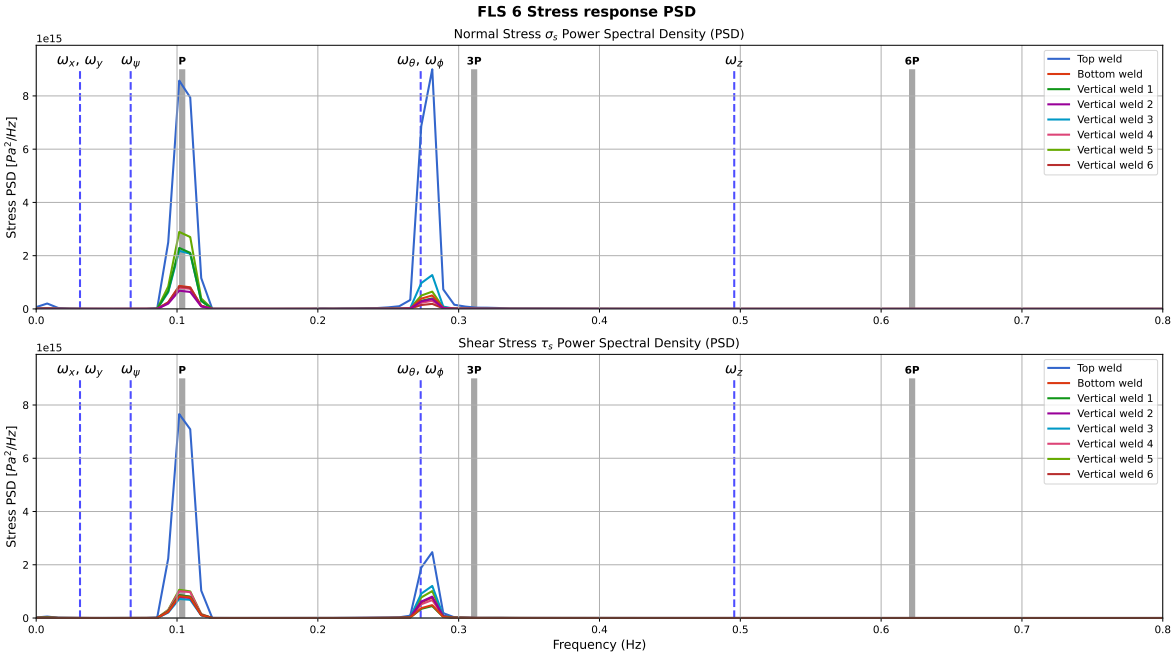


Figure C.21: Spectral decomposition of normal and shear stress response for FLS 6

D

Stress behaviour in weld seams

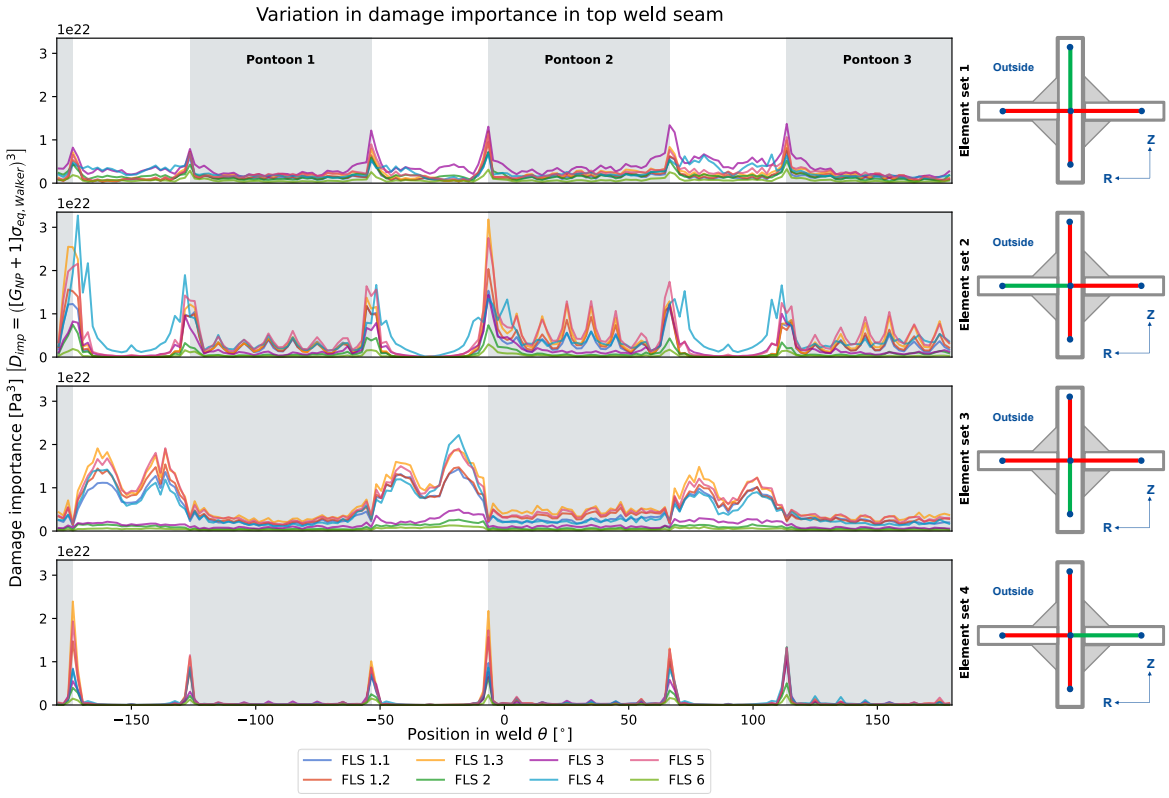


Figure D.1: Damage importance throughout the top critical weld seam, showing a clear pattern.

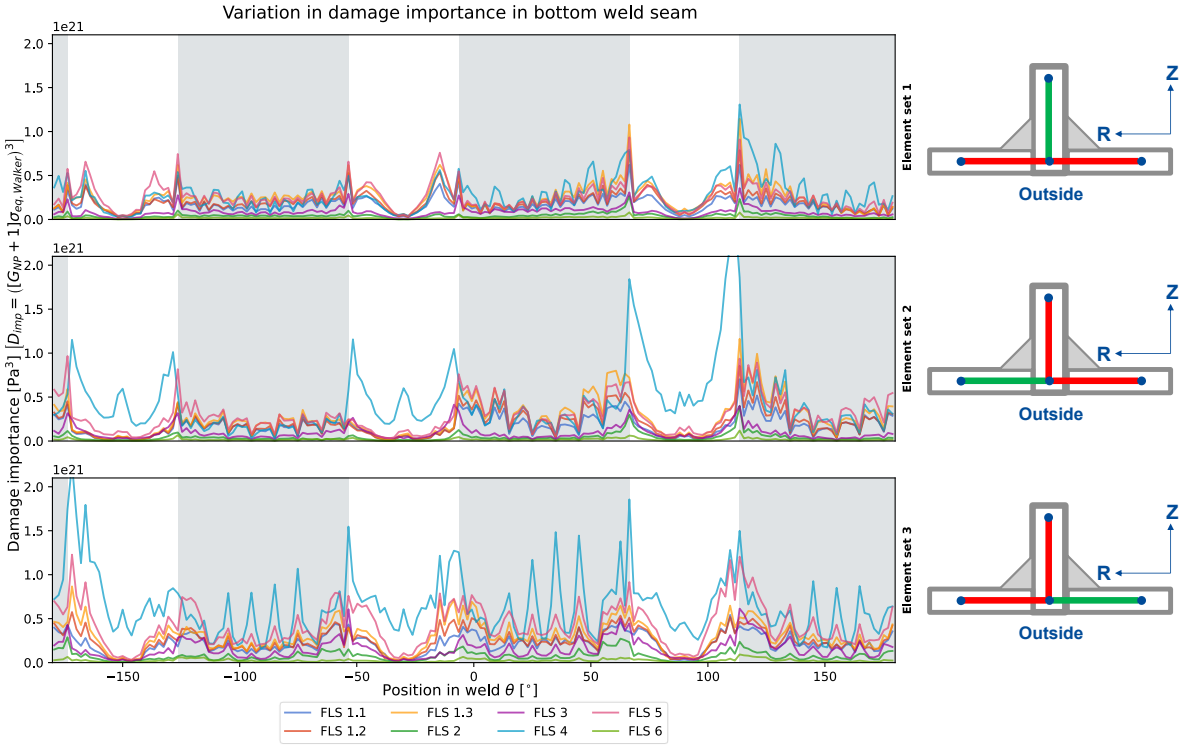


Figure D.2: Damage importance throughout the bottom critical weld seam, showing a clear pattern.

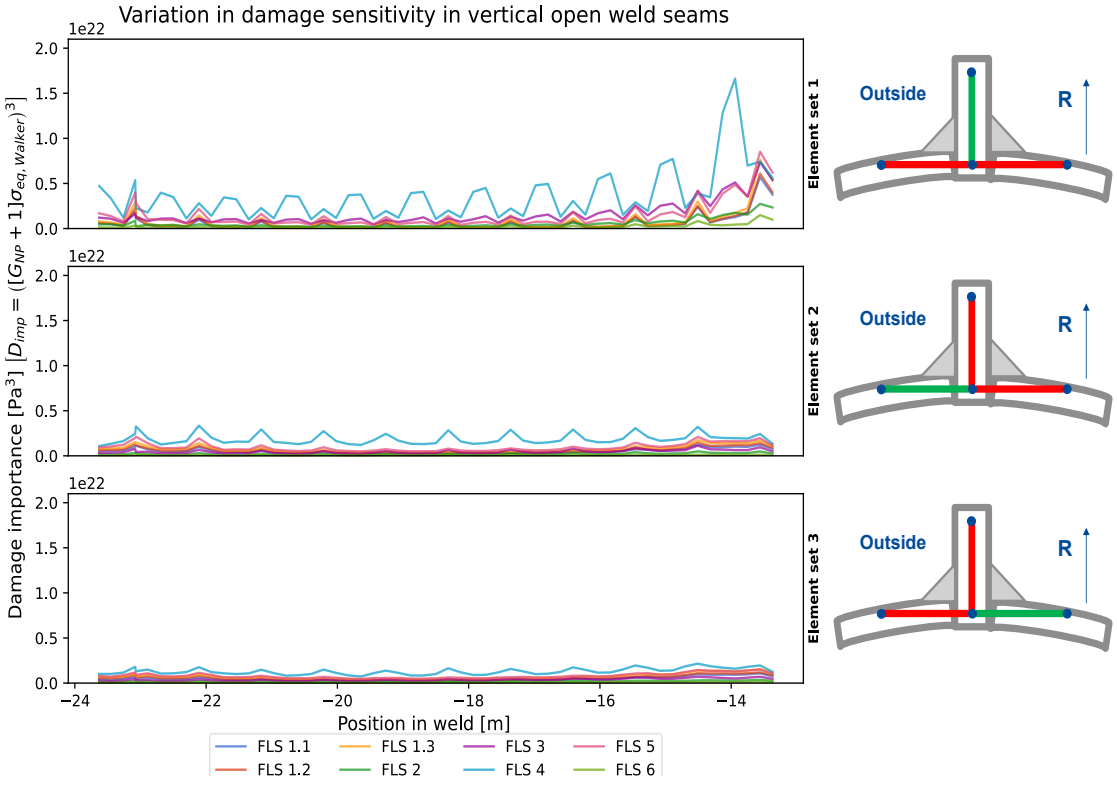


Figure D.3: Damage importance throughout the vertical critical weld seams, showing a clear pattern.

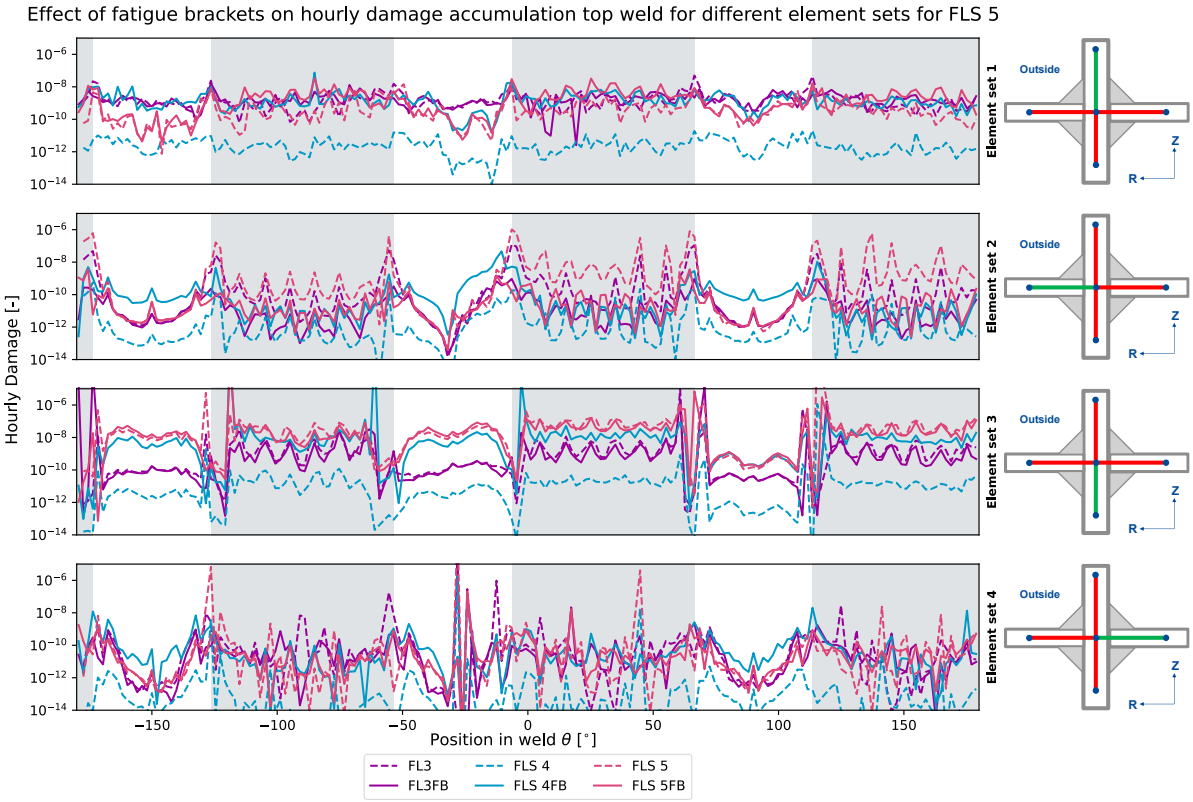


Figure D.4: Effect of fatigue brackets on the damage importance throughout the top circular weld, broken down by element set.